

SGP-TR-177

Liquid-Gas Relative Permeabilities in Fractures: Effects of
Flow Structures, Phase Transformation and Surface
Roughness

Chih-Ying Chen

June 2005

Financial support was provided through the
Stanford Geothermal Program under
Department of Energy Grant No. DE-FG36-02ID14418,
and by the Department of Petroleum Engineering,
Stanford University



Stanford Geothermal Program
Interdisciplinary Research in
Engineering and Earth Sciences
STANFORD UNIVERSITY
Stanford, California

© Copyright by Chih-Ying Chen 2005

All Rights Reserved

Abstract

Two-phase flow through fractured media is important in petroleum, geothermal, and environmental applications. However, the actual physics and phenomena that occur inside fractures are poorly understood, and oversimplified relative permeability curves are commonly used in fractured reservoir simulations.

In this work, an experimental apparatus equipped with a high-speed data acquisition system, real-time visualization, and automated image processing technology was constructed to study three transparent analog fractures with distinct surface roughnesses: smooth, homogeneously rough, and randomly rough. Air-water relative permeability measurements obtained in this study were compared with models suggested by earlier studies and analyzed by examining the flow structures. A method to evaluate the tortuosities induced by the blocking phase, namely the channel tortuosity, was proposed from observations of the flow structure images. The relationship between the coefficients of channel tortuosity and the relative permeabilities was studied with the aid of laboratory experiments and visualizations. Experimental data from these fractures were used to develop a broad approach for modeling two-phase flow behavior based on the flow structures. Finally, a general model deduced from these data was proposed to describe two-phase relative permeabilities in both smooth and rough fractures.

For the theoretical analysis of liquid-vapor relative permeabilities, accounting for phase transformations, the inviscid bubble train models coupled with relative permeability concepts were developed. The phase transformation effects were evaluated by accounting for the molecular transport through liquid-vapor interfaces. For the steam-

water relative permeabilities, we conducted steam-water flow experiments in the same fractures as used for air-water experiments. We compared the flow behavior and relative permeability differences between two-phase flow with and without phase transformation effects and between smooth-walled and rough-walled fractures. We then used these experimental data to verify and calibrate a field-scale method for inferring steam-water relative permeabilities from production data. After that, actual production data from active geothermal fields at The Geysers and Salton Sea in California were used to calculate the relative permeabilities of steam and water. These theoretical, experimental, and in-situ results provide better understanding of the likely behavior of geothermal, gas-condensate, and steam injection reservoirs.

From this work, the main conclusions are: (1) the liquid-gas relative permeabilities in fractures can be modeled by characterizing the flow structures which reflect the interactions among fluids and the rough fracture surface; (2) the steam-water flow behavior in fractures is different from air-water flow in the aspects of relative permeability, flow structure and residual/immobile phase saturations.

Acknowledgments

I truly admit that it is not possible to express my sincere appreciation to all the people that have made my life at Stanford so fruitful and enjoyable, especially with my limited English and the limited pages. However, several people must be acknowledged for their special contributions to this work and to my life.

The members of my reading and examination committees, Khalid Aziz, Tony Kovscek, Ruben Juanes, Roland Horne, and the chair of my examination committee, Jerry Harris, all made significant contributions to this work. Their continuous and constructive critiques and suggestions have made this work more mature and thicker. Dr. Aziz and Dr. Kovscek were the two who led me to explore some originally missed key points in this work, and made this work more rigorous and practical.

My academic advisor, Roland Horne, deserves most credits for making Mr. Chen become Dr. Chen. Not only is he my academic advisor, but he is my life mentor and good friend. Were it not for his patience and encouragement during my most struggling first-year, I would have dropped my doctoral dream. His advising philosophy certainly inspires most of this work, as well as my thoughts on research and life.

Additional contributors to this work are Mostafa Fourar, Gracel Diomampo and Jericho Reyes. Mostafa Fourar is by all means a significant contributor to this work. During his 4 months stay at Stanford as a visiting scholar, his expertise in fracture flow experiments and fluid mechanics helped me overcome many bottlenecks in this work. Gracel and Jericho helped me a lot in experimental design and field data analysis. I am

also very thankful to Kewen Li and other members in Stanford Geothermal Program for their valuable research discussion.

There are several people who help me out before and after I arrived at Stanford. My MS advisors, Tom Kuo and Edward Huang, first encouraged me to go to Stanford and extend my study from single-phase groundwater to multi-phase petroleum. James Lu was the one who inspired me the idea of study abroad from my teen-age and pushed me into the airplane when I hesitated in the dilemma of staying or leaving Taiwan. Bob Lindblom is not only my lecturer but also my partner for watching ball games. Their friendship and warmth will be kept in my mind.

I always appreciate the life in Green Earth Sciences Building. My royal officemate Todd Hoffman has become my best American friend. He certainly is the one who reduced my cultural shock. I have learned a lot of good American spirit from him. Greg Thiesfield and Yuanlin Jiang were my constant companions during late night in Room 155 where many enjoyable things happened.

I am also grateful for the support from Taiwan Government that allowed me to pursue my doctoral studies at Stanford University. Financial support during the course of this work was also provided by the U.S. Department of Energy under the grant # DE-FG36-02ID14418 and Stanford Geothermal Program, which are gratefully acknowledged.

Lastly and most importantly, the biggest thank you goes to my family. During these 5 years at Stanford, a lonely single man became a husband, a father, and now a doctor. These would not have happened without my wife Hsueh-Chi (Jessica) Huang coming into my life. To Jessica, my true love, thanks for sharing your life with me; I am definitely in debt to you. Your courage as a responsible pregnant wife and a full-time student simultaneously always reminds me how great you are. To baby Derek, thanks for coming to this world in the right time. Watching your sound sleep at late night when

daddy struggled for research, always relieved my stress and reminded me what is most important. This dissertation is dedicated with love to you two.

Contents

Abstract	iv
Acknowledgments	vi
1 Introduction	1
1.1 Problem Statement	5
1.1.1 Conventional Liquid-Gas Flow in Fractures	5
1.1.2 Unconventional Liquid-Vapor Flow in Fractures.....	7
1.2 Outline of the Dissertation	8
2 Relative Permeability in Fractures: Concepts and Reviews	10
2.1 Introduction of Relative Permeability.....	10
2.2 Porous Media Approach.....	12
2.3 Reviews of Air-Water Relative Permeabilities.....	17
2.4 Reviews of Steam-Water Relative Permeabilities	21
3 Experimental Study of Air-Water Flow in Fractures	26
3.1 Experimental Apparatus and Measurements.....	26
3.1.1 Fracture Apparatus Description	28
3.1.2 Pressure Measurements.....	34
3.1.3 Flow Rates Measurements	34

3.1.4 Saturation Measurements.....	38
3.2 Experimental Procedure and Data Processing	42
3.3 Experimental Results	44
3.3.1 Hydraulic Properties of the Fractures	44
3.3.2 Description of Flow Structures	48
3.3.3 Calculations of High-Resolution Relative Permeabilities	57
3.3.4 Average Relative Permeabilities: Prior versus Posterior.....	60
3.3.5 Relative Permeabilities Interpretation	62
3.4 Chapter Summary.....	66
4 A Flow-Structure Model for Two-Phase Relative Permeabilities in Fractures	67
4.1 Motivation	67
4.2 Model Description.....	72
4.3 Channel Tortuosity in Fractures.....	79
4.4 Reproduction of Relative Permeabilities	83
4.5 Tortuosity Modeling	88
4.6 Applicability and Limitations	91
4.6.1 Fitting Results from Earlier Studies.....	92
4.6.2 Effects of Flow Rates on Flow Structures	94
4.6.3 Suggestions	97
4.7 Chapter Summary.....	97
5 Theoretical Study of Phase Transformation Effects on Steam-Water Relative Permeabilities	99
5.1 Introduction	100
5.2 Inviscid Bubble Train Model	101
5.2.1 Model Description	101

5.2.2	Interfacial Flux for Vapor Bubbles in a Capillary	108
5.2.3	Modeling Results	111
5.3	Discussion	114
5.4	Chapter Summary.....	119
6	Experimental Study of Steam-Water Flow in Fractures	121
6.1	Apparatus, Measurements and Procedure	122
6.1.1	Steam and Water Rates Measurements.....	124
6.1.2	Pressure Measurements.....	126
6.1.3	Experimental Procedure.....	127
6.2	Results and Discussion.....	130
6.2.1	Effects of Non-Darcy Flow.....	130
6.2.2	Flow Structures and Relative Permeabilities	132
6.2.3	Effects of Phase Transformation.....	139
6.2.4	Effects of Surface Roughness	142
6.3	Comparison with Earlier Results from Porous Media	143
6.4	Relative Permeability Interpretations Using Known Models	145
6.5	Modeling Steam-Water Relative Permeability Using Modified Tortuous Channel Model (MTCM)	148
6.6	Chapter Summary.....	153
7	Verification and Improvement of a Field-Scale (Shinohara) Method	155
7.1	Background	156
7.2	Method	156
7.3	Laboratory Verification.....	159
7.4	Reservoir Applications.....	165
7.5	Discussion	174

7.6 Chapter Remarks	178
8 Conclusions and Future Work	179
8.1 Conclusions	179
8.2 Future Work	183
Nomenclature	185
References	189

List of Tables

2.1	Previous experiments relevant to steam-water relative permeabilities.....	22
3.1	Reported contact angle of aluminum and silica glass.....	29
3.2	The analysis results of gas and water fractional flows from Figure 3.7.	37
4.1	Averages of tortuous-channel parameter obtained from CAAR image processing program and the relative permeability values for the tortuous-channel approach and experiment.....	84
5.1	Fluid properties and parameters used in the inviscid bubble train model	113
6.1	Statistical comparison of fitting performance and corresponding optimal fitting parameters between proposed MTCM and Brooks-Corey model.....	151
7.1	Inferred Q* values for The Geysers and Salton Sea Geothermal Field Wells.	168

List of Figures

1.1	Hierarchical classification of fracture system in a fracture reservoir.....	2
2.1	Comparison of relative permeability curves from X model, Corey model and viscous coupling model.....	14
2.2	Compendium of previous measurements of relative permeabilities in fractures.....	20
2.3	From Verma [1986]. Comparison of experimental results from steam- water flow in porous media with those of Johnson et al. [1959] and Osaba et al. [1951]	23
2.4	Comparison of steam-water relative permeabilities measured by Satik [1998], Mahiya [1999], O'Connor [2001], and Sanchez and Schechter [1987].....	24
2.5	From Piquemal [1994]. Steam-water relative permeabilities in the unconsolidated porous media at 150°C and the trendlines of the steam- water relative permeabilities at 180°C	25
3.1	Process flow diagram for air-water experiment.....	27
3.2	Photograph of air-water flow through fracture apparatus.....	28
3.3	Schematic diagram and picture of fracture apparatus.....	28
3.4	Homogeneously rough (HR) fracture: (a) two-dimensional rough surface pattern. (b) three-dimensional aperture profile. Z axis is not to scale. (c)	

histogram of the aperture distribution; mean=0.155mm, STD=0.03mm.	
(d) line profile of section <i>AA'</i>	32
3.5 Randomly rough (RR) fracture: (a) three-dimensional aperture distribution. (b) histogram of the aperture distribution; mean=0.24mm, STD=0.05mm. (c) variogram of the aperture distribution; range x ~ 20mm, range y ~25mm (d) line profile of section <i>AA'</i>	33
3.6 Fractional flow ratio detector (FFRD) (a) schematic (b) detected gas and water signal corresponding to different gas and water segments inside FFRD tubing.	36
3.7 The histogram obtained from Figure 3.6.	36
3.8 FFRD calibration (Fluids: water and nitrogen gas; FFRD tubing ID: 1.0mm).	37
3.9 Comparison between the true color image of the flow in the smooth-walled fracture and binary image from the Matlab QDA program used in measuring saturation.	39
3.10 Background image of the RR fracture fully saturated with water. The shadows are generated by light reflection and scattering from the rough surfaces.....	41
3.11 Comparison between the true color image of the flow in the RR fracture and binary image from the Matlab DBTA program used in measuring saturation.	41
3.12 Comparison of the volume of water injected to the RR fracture to the volume of water estimated from the image processing program DBTA.	41
3.13 Data and signal processing flowchart.	43
3.14 Absolute permeability of the smooth-walled fracture (fracture spacer ~130 μ m) at different temperature and fracture pressure.	46

3.15	kA parameter and estimated hydraulic aperture of the HR fracture at different temperature and fracture pressure.....	47
3.16	kA parameter and estimated hydraulic aperture of the RR fracture at different temperature and fracture pressure.....	47
3.17	Steady-state, single-phase pressure drop versus flow rates in the smooth-walled fracture with aperture of 130 μ m. Corresponding Reynolds number is also provided in the secondary x-axis.....	48
3.18	Photographs of flow structures in the smooth-walled fracture. Each set contains four continuous images. Gas is dark, water is light. Flow direction was from left to right.....	51
3.19	Relationship between water saturation (S_w), water fractional flow (f_w) and pressure difference along the fracture in a highly tortuous channel flow.....	52
3.20	Flow structure map for air-water flow in the smooth-walled fracture.....	52
3.21	Sequence of snap-shots of air-water flow behavior in HR fractures.....	54
3.22	Sequence of snap-shots of air-water flow behavior in RR fractures	55
3.23	Flow structure map for air-water flow in the HR fracture.....	56
3.24	Flow structure map for air-water flow in the RR fracture.....	56
3.25	Comprehensive air-water relative permeabilities in the smooth-walled fracture calculated from Equations (2.6) and (2.7).....	58
3.26	Comprehensive air-water relative permeabilities calculated from Equations (2.6) and (2.7) in the HR fracture.....	59
3.27	Comprehensive air-water relative permeabilities calculated from Equations (2.6) and (2.7) in the RR fracture.....	59
3.28	Comparison of average relative permeabilities to prior relative permeability calculated from prior time-average data.....	61

3.29	Comparison of average experimental relative permeability in the smooth-walled fracture with the Corey-curve, X-curve and viscous-coupling models	63
3.30	Nonwetting phase flows in between of wetting phase in an ideal smooth fracture space.	64
3.31	Comparison of average experimental relative permeability in the rough-walled fractures with the Corey-curve and viscous-coupling models.	65
3.32	Plot of average experimental relative permeability in the smooth-walled and rough-walled fractures and their approximate trends.....	65
4.1	From Pruess and Tsang [1990]. Simulated relative permeabilities for the lognormal aperture distribution of (a) short-range isotropic spatial correlation (percolation like behavior; no multiphase flow) and (b) longer-range anisotropic spatial correlation in the flow direction.	69
4.2	A simple model of a straight gas channel in a smooth-walled fracture.	69
4.3	Modified from Nicholl and Glass [1994]. Wetting phase relative permeabilities as function of wetting phase saturation in satiated condition.	71
4.4	Illustration of channel tortuosity algorithm.	72
4.5	Illustration of separating the two-phase flow structures and the major impact parameters in each separated structure considered in the rough-walled TCA for the drainage process.....	74
4.6	A simple superposition method for integrating one-dimensional viscous coupling model to two-dimensional viscous coupling model.....	76
4.7	Effect of water film thickness on air-water relative permeabilities. VCM1D is the one-dimensional viscous coupling model	77

4.8	Representative images and corresponding processed gas-channel and water-channel images extracted from air-water experiment through the smooth-walled fracture	81
4.9	Comparison of representative processed of channel recognition for the smooth and rough fractures and corresponding channel tortuosities evaluated	82
4.10	Relative permeabilities for the smooth-walled fracture from tortuous-channel approach using phase tortuosities obtained from the processing of continuous images and its comparison with the original result: (a) gas phase, (b) water phase.....	83
4.11	Comparison of the experimental relative permeability with the tortuous-channel approach (averaging from Figure 4.10) and viscous-coupling model for the air-water experiment in the smooth-walled fracture.	85
4.12	Relative permeabilities from tortuous-channel approach and its comparison with the experimental result for the RR fracture: (a) all data points (~3000 points), (b) averages of each runs	86
4.13	Relative permeabilities from tortuous-channel approach and its comparison with the experimental result for the HR fracture: (a) all data points (~3000 points), (b) averages of each runs	87
4.14	Reciprocal of average water channel tortuosity versus (a) water saturation and (b) normalized water saturation for smooth and rough fractures.....	89
4.15	Reciprocal of average gas channel tortuosity versus gas saturation for smooth and rough fractures.....	90
4.16	Comparison of the experimental relative permeabilities with tortuous-channel model using Equations (4.13) and (4.14) for the smooth-walled, HR and RR fractures	91

4.17	Using proposed tortuous channel approach (Equation 4.11) and model (Equation 4.13) to interpret flowing-phase relative permeabilities from Nicholl et al. [2000] by setting $S_{wr} = 0.36$	93
4.18	Plot of reciprocal of in-place tortuosities from Nicholl et al. [2000] versus normalized water saturation by setting $S_{wr} = 0.36$	93
4.19	Using proposed tortuous channel model (Equation 4.13) to interpret two sets of water-phase relative permeabilities from the earlier numerical study by Pruess and Tsang [1990]. (S_{wr} was set to be 0.27 and 0.17 respectively)	94
4.20	Reciprocal of phase tortuosities and saturations versus phase rates for the HR fracture with hydraulic aperture $\sim 170\mu\text{m}$ when Q_g/Q_w is fixed to 20: (a) water phase, (b) gas phase.....	96
5.1	Schematic of motion of a homogeneous bubble train containing long air bubbles in a cylindrical capillary tube.....	102
5.2	Schematic of motion of a homogeneous bubble train containing long vapor bubbles in a cylindrical capillary tube.....	109
5.3	Water-phase relative permeability as function of capillary number, Ca^* , in inviscid bubble train model.....	113
5.4	Steam-water relative permeabilities of the inviscid bubble train model: (a) linear plot, (b) logarithmic plot. ($Ca^* = 10 \times 10^{-5}$)	114
5.5	Schematic of a steam bubble transporting through idealized toroidal geometry.....	117
5.6	Schematic of an air bubble transporting through idealized toroidal geometry.....	118
6.1	Process flow diagram and photograph for steam-water experiments.	123
6.2	Schematic diagram of fracture apparatus for steam-water experiments.....	124

6.3	Improved plumbing of the pressure measurement to reduce two-phase problem	127
6.4	Data and signal processing flowchart for steam-water experiments.	129
6.5	Steady-state, gas-phase equivalent pressure drop versus flow rates in the (a) smooth-walled fracture with aperture of 130 μm , (b) HR fracture with aperture of approximately 145 μm . Corresponding Reynolds number is also provided in the secondary x-axis.....	131
6.6	The continuous steam-water flow behavior in smooth-walled fracture. (steam phase is dark, water phase is light, flow is from left to right).....	133
6.7	Sequence of snap-shots of air-water and steam-water flow behavior in smooth-walled, HR and RR fractures around 65% water saturation	136
6.8	Sequence of snap-shots of air-water and steam-water flow behavior in smooth-walled, HR and RR fractures around 40% water saturation	137
6.9	Comprehensive steam-water and air-water relative permeabilities: (a) smooth-walled fracture, (b) HR fracture, (c) RR fracture.	138
6.10	In-place nucleation of immobile steam clusters: (a) HR fracture, (b) RR fracture.	139
6.11	Comparison of average steam-water and air-water relative permeabilities: (a) smooth-walled fracture, (b) HR fracture, (c) RR fracture.	141
6.12	Comparison of average steam-water relative permeabilities in the smooth, HR and RR fractures.	142
6.13	Comparison of average steam-water relative permeability in the rough-walled (HR and RR) fractures with earlier studies of steam-water relative permeability in porous media: (a) all data, (b) data from HR fracture versus Satik's, (c) data from RR fracture versus O'Connor's.....	144

6.14	Comparison of average steam-water relative permeability in the (a) HR, and (b) RR fractures to the Brooks-Corey model	147
6.15	Comparison of average steam-water relative permeability in the smooth- walled fracture to (a) Brooks-Corey model, (b) Brooks-Corey model for the steam phase and Purcell model for the water phase.....	147
6.16	Interpretation of published steam-water relative permeability in porous media using the Brooks-Corey model: (a) data from Satik [1998] measured in Berea sandstone, (b) date from Verma [1986] measured in unconsolidated sand.....	148
6.17	Interpretations of steam-water relative permeabilities using MTCM: (a) smooth-walled fracture data, (b) HR fracture data, (c) RR fracture data, (d) Berea sandstone data from Satik [1998], (e) unconsolidated sand data from Verma [1986].	152
7.1	Q vs. Q_w/Q_s to infer Q^* for the steam-water experiment in smooth- walled fracture.	160
7.2	Comparison of steam-water relative permeabilities from porous media approach and Shinohara's method for the steam-water data from the smooth-walled fracture	161
7.3	Comparison of k_r vs. S_w and k_r vs. $S_{w,f}$ from Shinohara's method for the steam-water data from the smooth-walled fracture.....	162
7.4	The flowing water saturation versus actual (in-place) water saturation for steam-water data from the smooth-walled fracture.....	163
7.5	The flowing water saturation versus actual (in-place) water saturation: (a) experimental results at 104°C ; (b) theoretical results for reservoir conditions (210°C)	164
7.6	Steam and Water Production History of Coleman 4-5, The Geysers Geothermal Field.....	166

7.7	Steam and Water Production History of IID - 9, Salton Sea Geothermal Field.....	166
7.8	Q vs. Qw/Qs to infer Q* for Coleman 4-5, The Geysers Geothermal Field.....	167
7.9	Q vs. Qw/Qs to infer Q* for IID - 9, Salton Sea Geothermal Field.....	167
7.10	Plot of relative permeability curves against flowing water saturation for The Geysers Geothermal Field.....	170
7.11	Plot of relative permeability curves against flowing water saturation for the Salton Sea Geothermal Field.....	170
7.12	Plot of relative permeability curves against water saturation for The Geysers and Salton Sea Geothermal Reservoir Fields.....	171
7.13	Plot of k_{rs} vs k_{rw} for The Geysers and Salton Sea Geothermal Field, with the Corey, X-curves and viscous-coupling model: (a) Cartesian plot, (b) Logarithmic Plot.....	173
7.14	Relative permeability vs. mapped in-place water saturation from the field production data for The Geysers and Salton Sea Geothermal fields, compared to the viscous-coupling model (assuming no residual water saturation).	174
7.15	Relative permeability vs. de-normalized in-place water saturation for the Geysers field: (a) lower bound behavior using reported minimum $S_{wr}=0.3$, compared to the results from rough-walled fractures, (b) upper bound behavior using reported maximum $S_{wr}=0.7$	177

Chapter 1

Introduction

“The importance of fractures can hardly be exaggerated. Most likely man could not live if rocks were not fractured!”

- Ernst Cloos, 1955

Fractures are ubiquitous in the brittle lithosphere in the upper part of earth's crust. They play a critical role in the transport of fluids. Moreover, all major discovered geothermal reservoirs and a considerable number of petroleum reservoirs are in fractured rocks. This restates the importance of studying multiphase flow behavior inside the opened fracture space.

From the engineering point of view, a rock fracture as defined here is simply a complex-shaped cavity filled with fluids or solid minerals. Therefore it is understood to include cracks, joints, and faults. Fractures are formed by a crystallized melt and/or mechanical failure of the rock due to regional or local geological stresses caused by tectonic activity, lithostatic or pore pressure changes and thermal effects. Subsequent mechanical effects are the major cause of the formation of extensive fracture networks in the subsurface. A large-scale fracture network is constructed by many single fractures. Figure 1.1 shows the structural hierarchy of a fractured reservoir.

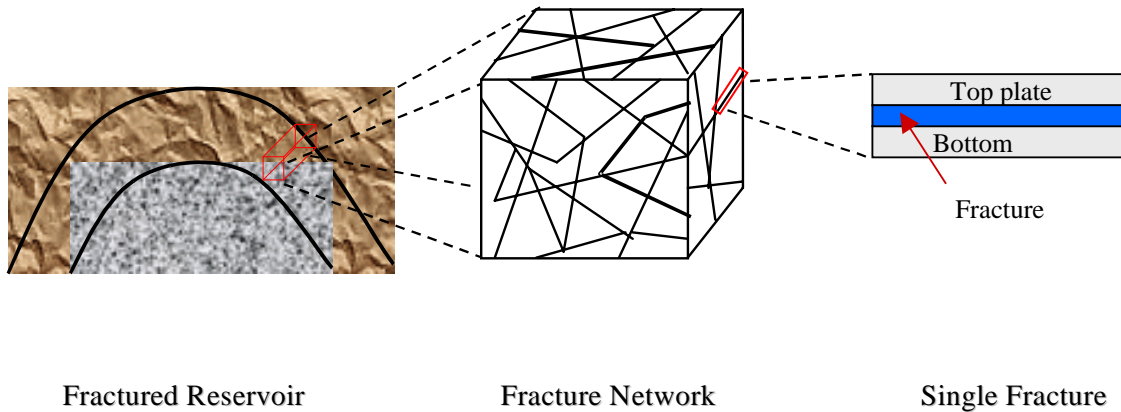


Figure 1.1: Hierarchical classification of fracture system in a fracture reservoir.

Rock fractures normally form high-permeable flow pathways and therefore dominate single- or multiphase fluid transports in fractured porous media in the subsurface. Due to the complexity and unpredictability of large-scale fracture networks in the subsurface, investigations have been performed mostly under simulated conditions by narrowing the scale down to a single, artificial fracture or fracture replica as shown in Figure 1.1.

Several models have been proposed to describe the single-phase hydraulic properties of single fractures [Lomize, 1951; Huitt, 1956; Snow, 1965; Romm, 1966; Louis, 1968; Zhilenkov, 1975; Zimmerman and Bodvarsson, 1996; Meheust and Schmittbuhl, 2001]. For a matrix-fracture system containing parallel set of smooth-walled, planar fractures with unity separation and laminar flow inside them, the average permeability is related to the fracture aperture, b , by the well-studied “*cubic law*” [Snow, 1965; Yih, 1969: Eq. 341]:

$$\bar{k} = \frac{b^3}{12} \quad (1.1)$$

Considering the space in a single smooth-walled, planar fracture, the single fracture permeability is then given by:

$$k_f = \frac{b^2}{12} \quad (1.2)$$

For rough fractures, Lomize [1951] and Louise [1968] studied water flow in several rough fractures by conducting a series of flow experiments. To characterize the surface roughness of fractures, Lomize [1951] created a simplified definition of the surface roughness and found the fracture permeability to be a function of surface roughness. That definition of surface roughness is specific to their simulated fractures and did not account for the spatial correlation of the aperture variation. These historical works inspired subsequent research in fluid flow in fractures. Iwai [1976] studied fluid flow through a single fracture and investigated the validity of the cubic law for fluid flow through a natural fracture considering contact area and roughness of the fracture planes. The cubic law appears to be valid for rough-walled fractures provided the fracture local aperture variation along the flow direction is only minor [Iwai, 1976; Brown, 1987; Thompson and Brown, 1991]. Nuezil and Tracy [1980] performed a numerical study by conceptualizing fractures as a set of parallel openings with different apertures. Their results confirmed the cubic law and showed that the maximum flow occurs through the larger apertures. Witherspoon et al. [1980] validated the cubic law when the rock fractures were open or closed under stress. Their results also indicated that this validation was independent of rock type. The deviations from the ideal parallel plate model only caused an apparent reduction in flow and may be incorporated into the cubic law by a flow modification factor. Recently, numerous efforts were made to study the fracture hydraulic properties incorporating the effects of fracture roughness and imposed stress [Walsh, 1981; Singh, 1997; Ranjith, 2000].

Two-phase or unsaturated flows through fractures are of great importance in several domains such as petroleum recovery, geothermal steam production and environmental engineering. Studies of these issues need not only to consider single-phase flow properties mentioned already, but also to account for the complex interaction between phases. Unfortunately, very few theoretical and experimental studies have been

devoted to establishing the laws governing these flows. In addition, the results presented in the literature often seem to be in contradiction, especially for the relative permeability curves. Therefore, it is admitted that the mechanisms of two-phase flows in fractures are not well understood [Kazemi, 1990]. A detailed review of these studies is provided in following chapters.

Two-phase flow structures (or flow patterns) have long been believed to affect relative permeabilities strongly. Fourar et al. [1993] observed five flow structures in smooth-walled and rough-walled fractures. These structures depend on gas and liquid flow rates. Persoff et al. [1991] found that flow of a phase was characterized by having a localized continuous flow path that undergoes blocking and unblocking by the other phase in the case of rough-walled fracture at small flow rates. Diomampo [2001] also observed localized channel flow undergoing continuous breaking and reforming in the smooth-walled fracture. However, no direct relationship between flow structures and relative permeabilities was derived in these studies. With the advance of flow visualization techniques in laboratories, two-phase flow structures could be observed through transparent analog fractures or fracture replicas. These laboratory investigations suggested that the evolution of water flow channelization (fingering flow) created time-dependent fast moving, spatially preferential flow paths in simulated rough fractures [Nicholl et al., 1992, 1993, 2000; Nicholl and Glass, 1994; Rasmussen and Evans, 1993; Su et al., 1999; Diomampo, 2001]. Nicholl et al. [2000] studied the flowing-phase relative permeability in the presence of an immobile phase. The structure of the flowing phase was evaluated by a term called in-place tortuosity. From both experimental and simulation results, they concluded that the tortuosity is the main factor controlling the flowing phase relative permeability.

Phase transformation effects between liquid and vapor phases are a characteristic of two-phase flows in geothermal reservoirs (steam-water flow) and gas-condensate reservoirs (gas-oil flow). In geothermal reservoirs, the fluids, steam and water, are both derived from the same substance but in different phases. The flow of steam and water is

governed by complex physical phenomena involving mechanical interaction between the two fluids as well as by the thermodynamic effects of boiling heat transfer. This complex interaction has made it difficult to investigate steam-water relative permeability in complex fractured media.

1.1 Problem Statement

Simulations of multiphase flow in fractured reservoirs required knowledge of relative permeability functions. However, as described previously, the relative permeability properties of a fracture are impacted by (1) fracture surface roughness, (2) flow structures, and (3) flow with phase transformation effects. However, the nature of the impact of these factors is poorly understood. In spite of considerable theoretical and experimental efforts during the last two decades for all of these issues, there are still no general models or approaches to describe relative permeability in all types of fractures, either with or without phase transformation effects.

To emphasize the outstanding problems and present the results clearly, this work was divided into two subtopics, namely *conventional* liquid-gas relative permeabilities in fractures and *unconventional* liquid-vapor relative permeabilities in fractures. The word “conventional” means flows of two distinct phases (e.g. air-water or oil-water flow), and “unconventional” means two-phase flow with phase transformation (e.g. steam-water or gas-condensate flow).

1.1.1 Conventional Liquid-Gas Flow in Fractures

Despite the strong impact of relative permeability functions on flow, typical reservoir simulations model multiphase flow in fractures in a highly simplified manner by using linear functions of relative permeability curves, namely the X-model or X-curve [Kazemi and Merrill, 1979; van Golf-Racht, 1982; Thomas et al., 1983; Gilman and Kazemi, 1983]. In the X-model, the wetting phase relative permeabilities equal the wetting

saturations, while nonwetting phase relative permeabilities equal the nonwetting saturations. The reservoir model is then tuned by adjusting other physical or model parameters to agree with the observed production history. This makes the use of these models as forecasting tools limited and unreliable in many cases.

The approach used commonly to describe two-phase flow in a fracture is the porous medium approach using the relative permeability concept, which was developed from multiphase flow in porous media and based on a generalization of the Darcy equation. Numerous models for the relative permeabilities have been suggested based on theoretical, semiempirical and empirical results. Among these, three models have been suggested to approximate the two-phase flow behavior in single fractures from experimental or theoretical investigations: the X-model [Romm, 1966; Pan et al., 1996], the Corey or Brooks-Corey models [Corey, 1986], and the viscous-coupling model [Ehrlich, 1993; Fourar and Lenormand 1998]. As shown later in Figure 2.1, these three models represent three dissimilar relative permeability functions, and therefore they impact the results of reservoir simulation differently.

The experimental results presented in the literature also show different behavior for the relative permeabilities of fractures. Some results are in accordance with the X-model [Romm, 1966; Pan et al., 1996] whereas other results are in accordance with the Corey-model [Diomampo, 2001] or the viscous-coupling model [Fourar and Lenormand 1998]. The geometry and heterogeneity of fracture spaces and the corresponding flow structures have been proposed to be the major factors that control multiphase flow behavior [Pruess and Tsang, 1990; Nicholl et al., 2000]. Despite this, the three models do not take these effects into account.

Presently, the flow mechanism and the characteristic behavior of relative permeability in fractures are still not well determined. Issues such as whether a discontinuous phase can travel in discrete units carried along by another phase or will be trapped as residual saturation as in porous media, are unresolved. The question of phase interference i.e. whether the relative permeability curves follow an X-curve, Corey curve

or some other function, is still unanswered. Most importantly, a general approach to describe two-phase relative permeabilities in fractures, taking into account the surface geometry and flow structure effects, has not been developed.

1.1.2 Unconventional Liquid-Vapor Flow in Fractures

Liquid-vapor flow behavior is different from conventional liquid-gas flow since the former is accompanied by phase transformation effects. The interfacial mass flux enables molecules in one phase to be transported to the other phase or to pass through the other phase without forming connected flow paths. Because fluids are at saturated (boiling) conditions, their thermodynamic properties are extremely unstable. Therefore, the governing flow mechanism for boiling multiphase flow in fractures is still undetermined.

There have been several experimental and theoretical studies conducted for steam-water relative permeabilities [Verma 1986; Sanchez and Schechter 1987; Piquemal 1994; Satik 1998; O'Connor 2001]. These studies were performed in consolidated or unconsolidated porous media. The results of these studies fall generally into two contradictory populations. Some studies suggested that in porous media, the steam-water relative permeability functions behave similarly to the air-water (or nitrogen-water) relative permeability functions [Sanchez and Schechter 1987; Piquemal 1994]. However, another set of studies suggested that steam-water relative permeability functions behave differently from air-water in porous media [Arihara et al. 1976; Counsil 1979; Verma 1986; Satik 1998; Mahiya 1999; O'Connor 2001]. Most of these studies showed that the steam-phase relative permeability is enhanced in comparison with air-phase relative permeability. To the best of our knowledge, no steam-water relative permeability results in fractured media have been reported due to the difficulties of the steam-water experiments and poor knowledge of fracture modeling for multiphase flows. Furthermore, no general models for steam-water relative permeabilities have been proposed yet.

1.2 Outline of the Dissertation

The purposes of this work were: (1) to examine the effects of the flow structures and fracture geometry on relative permeabilities during two-phase flow in single fractures, (2) to model two-phase relative permeabilities in fractures, (3) to gain better understanding of steam-water transport through fractured media and determine the behavior of relative permeability in fractures.

This dissertation is divided into two hierarchical subtopics. After some general overviews and reviews in Chapter 2, Chapters 3 and 4 discuss the conventional air-water flow in different fractures. Then, Chapters 5 to 7 deal mainly with the theoretical and experimental studies of unconventional steam-water flow in different fractures. The whole dissertation is organized as follows:

In Chapter 2, we first present an overview and review of the theoretical and experimental approaches for conventional and unconventional two-phase flow in fractures.

In Chapter 3, we describe the detailed design of the apparatus and the automated measurement techniques, as well as the air-water drainage experimental procedures and results.

In Chapter 4, we discuss the observed flow structures from air-water flow experiments, propose a tortuous-channel approach, as well as study the flow structure effects on relative permeabilities.

In Chapter 5, we move forward to the unconventional steam-water flow by describing theoretical studies of steam-water flow in a capillary.

In Chapter 6, we describe steam-water drainage experiments in the same fractures as in Chapter 3 and discuss the effects of phase transformation and fracture roughness on relative permeabilities. A generalized model for steam-water relative permeabilities in

fractures is proposed based on the modification of the air-water relative permeability model.

In Chapter 7, we scale up the laboratory results to enhance a field-scale method, called the Shinohara method. This method enables us to evaluate steam-water relative permeabilities in a geothermal field.

Finally, in Chapter 8, we outline the main conclusions of this work and recommend future work.

Chapter 2

Relative Permeability in Fractures: Concepts and Reviews

This chapter addresses fundamental theories of this work. We first review the development of the relative permeability concepts, and then we discuss how to treat fractures as connected two-dimensional porous media. Finally, we review several relative permeability models as well as experimental measurements suggested in literature.

2.1 Introduction of Relative Permeability

In 1856, Henry Darcy [1856], the Engineer of the town of Dijon, in Southern France, investigated the flow of water in vertical, homogeneous sand filters connected with the fountains of the city of Dijon. He found a linear relationship between superficial velocity (later called Darcy velocity) and head gradient, which later formed the fundamental equation in the research of fluid flow through porous media, commonly called Darcy's Law:

$$u = -\frac{k}{\mu} \frac{\Delta p}{L} \quad (2.1)$$

where u is the superficial velocity; μ is the dynamic viscosity; Δp is the pressure difference; L is the length; k is the absolute permeability. Though Darcy developed this equation empirically from his sand filter experiments, a century later, Hubbert [1956] derived an identical equation theoretically, except that fluid potential was used instead of the fluid pressure. Darcy's law holds when the flow is laminar; however, when flows become faster and inertial effects become more and more significant, the flow behavior becomes nonlinear; thus, the apparent permeability is no longer constant [Forchheimer, 1901].

The relative permeability concept in two-phase flow was first proposed by Buckingham [1907] from the study of unsaturated flow in soil. He developed a flux law for the transport of water in unsaturated soils:

$$u_w = -K_w \frac{\partial h}{\partial x} \quad (2.2)$$

where u_w is the water superficial velocity; h is the hydraulic head; x is the space coordinate and K_w is the water effective hydraulic conductivity convertible to the later defined relative permeability:

$$K_w = \frac{kk_{rw}\rho_w g}{\mu_w} \quad (2.3)$$

where ρ_w and μ_w are the density and dynamic viscosity of water, respectively; g is the gravity constant and k_{rw} is the water relative permeability. Richards [1931] combined Equation (2.2) together with the mass balance equation and derived the important equation for unsaturated flow in soil science and hydrogeology, commonly called Richards' equation:

$$\frac{\partial \phi S_w}{\partial t} = -\nabla \cdot [K_w \nabla h] \quad (2.4)$$

where ϕ is the porosity, S_w is the water saturation (or water content) and ∇ is the gradient operator. Since these equations were originally derived for the applications of soil sciences, only water phase was considered. The vapor (or gas) phase was assumed immobile, and hence its relative permeability remains zero.

Wyckoff and Botset [1936] were believed to be the first investigators to publish a two-phase relative permeability curve from experiments, and the generalized multiphase Darcy equation was then finally expressed explicitly as:

$$u_\alpha = -\frac{kk_{ra}}{\mu_\alpha}(\nabla p_\alpha - \rho_\alpha g) \quad (2.5)$$

where α = oil, water or gas phase. Equation (2.5) is now commonly used in studying multiphase flow in porous media, especially in petroleum and geothermal engineering as well as in groundwater protection.

2.2 Porous Media Approach

In the last five decades, with the large number of fractured reservoirs exploited, the modeling of multiphase flow through fractures and simulation of fractured reservoirs has become increasingly important. One of the most commonly used approaches to model multiphase flow in fractures is the porous medium approach using Equation (2.5). In the porous media approach, the fracture is treated as a connected two-dimensional porous medium where the pore space occupied by one phase is not available for the flow of the other phase. A phase can move from one position to another only upon establishing a continuous flow path for itself. The competition for pore occupancy is controlled by the capillary pressure if there are no gravity effects. This approach is one of the major frameworks of this work.

For steady-state laminar two-phase flow in a single horizontal fracture without gravity segregation, the generalized Darcy equations in Equation (2.5) can be rewritten in volumetric form. For the water phase:

$$q_w = \frac{kk_{rw}A(p_i - p_o)_w}{\mu_w L} \quad (2.6)$$

To take the compressibility effect of the gas into account, the gas phase equation must be written in the following form [Scheidegger, 1974]:

$$q_g = \frac{kk_{rg}A(p_i^2 - p_o^2)}{2\mu_g L p_o} \quad (2.7)$$

where subscripts w and g stand for water (or liquid) and gas, respectively; p_i and p_o are the pressures at the inlet and the outlet of the fracture; q is the volumetric flow rate; L is the fracture length; k_{rw} and k_{rg} are the relative permeabilities of the water (or liquid) and the gas, respectively. The absolute permeability of a smooth-walled fracture is related to the fracture aperture, b , as described by the cubic law (Equation 1.2):

$$k = \frac{b^2}{12} \quad (2.8)$$

The concept of the relative permeability provides us a means to quantify the relative resistance or interference between phases. For liquid-gas flow, the sum of k_{rw} and k_{rg} indicates the extent of phase interference: the lower the sum of the relative permeabilities below 1, the greater the phase interference. The key point of the generalized Darcy model is the determination of the relative permeabilities, that are generally supposed to be functions only of saturation. When the pressure loss due to the interaction between phases is negligible compared to the pressure loss due to the flow of each fluid, the relative permeabilities can be modeled by the X-curves (see Figure 2.1):

$$k_{rw} = S_w \quad (2.9)$$

$$k_{rg} = S_g \quad (2.10)$$

where S_w and S_g are the water (or liquid) and gas saturation respectively.

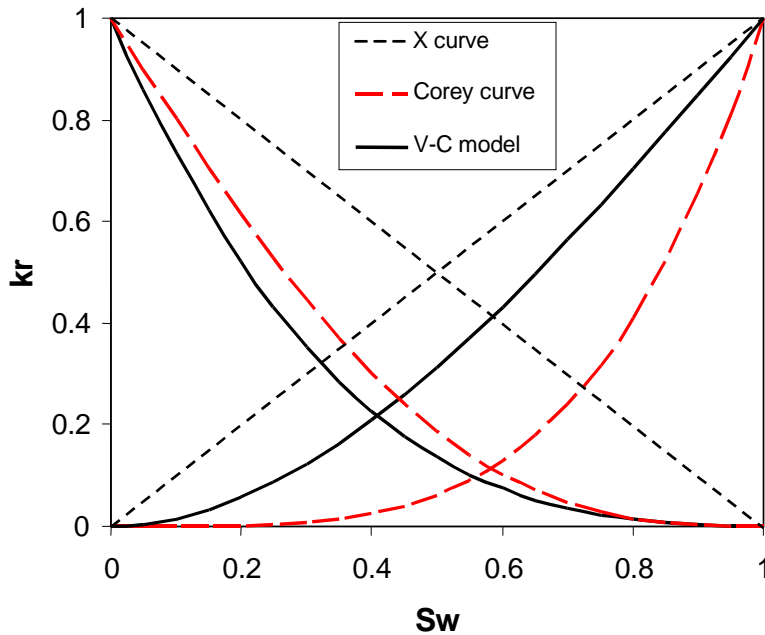


Figure 2.1: Comparison of relative permeability curves from X model, Corey model and viscous coupling model. (No residual water saturations were used in the Corey model)

According to the X-model, the sum of k_{rw} and k_{rg} equals 1, which means the absence of phase interference. Physically this implies that each phase flows in its own path without impeding the flow of the other. In fractures, if each phase flows via perfectly straight channels along the flow direction with negligible capillary pressure and wetting-phase stratified flow (water film flow), then the X-curve model is reasonable. However, for two-phase flows through a real fracture, the surface contact between the two fluids can be important and, consequently, the interference between the two fluids

may be significant. Generally, the fracture flow can be considered either as a limiting case of a flow in a porous medium [Pruess and Tsang, 1990] or as a limiting case of pipe flow [Fourar et al., 1993]

Based on the porous media approach, several numerical studies have been performed [Murphy and Thomson, 1990; Rossen and Kumar 1994; Mendoza and Sudicky, 1991; Pyrak-Nolte et al. 1992]. The main result is that the sum of relative permeabilities is less than 1, and consequently, the X-model is not suitable to describe the relative permeabilities as functions of saturation. However, these studies do not establish theoretical relationships for k_r . The shape of the curves obtained was more similar to the curves obtained in classical porous media, namely the Corey curves [Corey, 1954]:

$$k_{rw} = (S_w^*)^4 \quad (2.11)$$

$$k_{rg} = (1 - S_w^*)^2 [1 - (S_w^*)^2] \quad (2.12)$$

In these equations, S_w^* is the normalized water saturation defined by:

$$S_w^* = \frac{S_w - S_{wr}}{1 - S_{wr} - S_{gr}} \quad (2.13)$$

where subscript r refers to residual saturation. The Corey model represents strong phase-interference in comparison to the X-model (see Figure 2.1).

Several empirical and theoretical models have been proposed to represent the relative permeability in porous and fractured media. In porous media, the Brooks-Corey model has been widely used for modeling two-phase relative permeability and capillary pressure. The Brooks-Corey relative permeability functions are given as:

$$k_{rw} = (S_w^*)^{(2+3\lambda)/\lambda} \quad (2.14)$$

$$k_{rg} = (1 - S_w^*)^2 [1 - (S_w^*)^{(2+\lambda)/\lambda}] \quad (2.15)$$

where λ is the pore size distribution index.

Brooks and Corey [1966] reasoned that media with a wide range of the pore size distribution should have small values of λ . On the other hand, media with a uniform pore size could have λ values close to infinity [Brooks and Corey 1966; Corey 1986]. The value of λ equals 2 for typical porous media, which reduces the Brooks-Corey model to the Corey model (Equations 2.11 and 2.12). In the rough-walled fracture, the behavior of the two-phase flow might be approximated to that in porous media. According to Brooks and Corey's reasoning, the value of λ should approach infinity in the case of fractured media. Therefore, Equations (2.14) and (2.15) were modified with $\lambda \rightarrow \infty$, which leads to the extreme behavior of the Brooks and Corey model for fractures:

$$k_{rw} = (S_w^*)^3 \quad (2.16)$$

$$k_{rg} = (1 - S_w^*)^3 \quad (2.17)$$

Another model for fracture relative permeabilities is to treat flow in fractures as flow in pipes. This is based on the observation that flow structures observed in a fracture show more similarity to the structures observed in a pipe than to those expected for a porous medium [Fourar and Bories, 1995]. These flow structures show strong interference between the two fluids flowing simultaneously. However, the real mechanisms are very difficult to model because the geometry of the interfaces between the fluids is unknown and one of the phases may be discontinuous. Fourar and Lenormand [1998] assumed that the complexity of the real flow can be modeled, as a first approximation, by viscous coupling between the fluids. The fracture is then modeled by two parallel planes with a small aperture. In this model, the two fluids are assumed to flow simultaneously with a planar interface. Fluid w is considered as the wetting fluid and therefore is in contact with the walls, and fluid g (nonwetting) flows in between. The viscous coupling between fluids is derived by integrating Stokes' equation for each

stratum. Identification of the established equations and the generalized Darcy equations leads to:

$$k_{rw} = \frac{S_w^2}{2} (3 - S_w) \quad (2.18)$$

$$k_{rg} = (1 - S_w)^3 + \frac{3}{2} \mu_r S_w (1 - S_w)(2 - S_w) \quad (2.19)$$

where $\mu_r = \mu_g/\mu_w$ is the viscosity ratio. These equations show that the relative permeability of the nonwetting fluid depends on the viscosity ratio μ_r . The relative permeability of the nonwetting phase can be larger than unity when $\mu_r > 1$ (lubrication effects). However, for gas and liquid two-phase flows, $\mu_r \ll 1$ and, consequently, the second term in the right-hand-side of Equation (2.19) is only affected insignificantly.

The comparison of the X-model, Corey model and viscous coupling model is presented in Figure 2.1. From these curves, we see the diversity of relative permeability models in fractures. The range of local aperture variation and high contrast of permeability distribution make it difficult to use these idealized theoretical models to predict relative permeabilities in fractures. To improve the prediction power, it is necessary to start by observing the dynamic flow behavior inside the fracture space through visualization techniques. Through observations, we improve our understanding of the underlying physics and then model relative permeabilities phenomenologically. In the next chapter, we describe such experiments in fractures.

2.3 Reviews of Air-Water Relative Permeabilities

Several experimental studies on two-phase flows in a fracture have been performed. Romm [1966] studied kerosene and water two-phase flow through an artificial fracture by using parallel plates. The surface of each plate was lined with strips of polyethylene or

waxed paper. The strips divided the entire fracture into 10 to 20 narrow parallel bands (2-3 mm width) with alternate wettability.

Persoff et al. [1991] and Persoff and Pruess [1995] also performed experiments on air and water flow through rough-walled fractures using transparent casts of naturally fractured rocks. The study of Persoff et al. [1991] showed strong phase to phase interference similar to that in porous media. In the case of rough-walled fractures at small flow rates, flow of a phase was characterized by having a localized continuous flow path that underwent blocking and unblocking by the other phase.

Diomampo [2001] performed experiments of nitrogen and water flow through smooth-walled artificial fractures. She also observed intermittent phenomenon in her experiments. Furthermore, her results conform mostly to the Corey type of relative permeability curves. This suggests that flow through fractures can be analyzed by treating it as a limiting case of porous media flow and by using the relative permeability approach.

Fourar et al. [1993] and Fourar and Bories [1995] studied air-water two-phase flow in a fracture consisting of two parallel glass plates (1 m x 0.5 m) with an opening equal to 1 mm. The injector consisted of 500 stainless steel tubes of 1 mm outside diameter and 0.66 mm inside diameter. Air and water were injected through alternating capillary tubes to achieve uniform distribution at the inlet. For all experiments, air was injected at a constant pressure and its volumetric flow rate was measured by a rotameter and corrected to the standard pressure. Water was injected by a calibrated pump. At the outlet of the fracture, the gas escaped to the atmosphere and the water was collected. The fracture was initially saturated with water which was injected at a constant flow rate for each experiment. Air injection was then started and increased stepwise. When the steady state was reached for each flow rate, the pressure drop and the saturation were measured. The pressure drop was measured by a transducer and the saturation was measured by using a balance method. Then, the fracture was resaturated with water and the experiment was repeated several times at different liquid flow rates. This study has been extended to

fractures constituted by bricks made of baked clay (30 cm x 14 cm) with different apertures (0.54 mm, 0.40 mm and 0.18 mm).

Results obtained in these various studies are presented in Figure 2.2 in terms of k_{rg} versus k_{rl} . As can be seen from the smooth-walled results in Figure 2.2a, experimental results obtained by Romm [1966] are described well by the X-model, that is the relative permeability of each phase equals its saturation. On the other hand, the relative permeabilities obtained by Fourar and Bories [1995] are rather in accordance with the viscous-coupling model. However, the results obtained by Diomampo [2001] are described well by the Corey model. Lastly, the results of the rough-walled experiments obtained by Persoff and Pruess [1995] show more interaction between phases than the other results (Figure 2.2b). It is obvious that these previous studies show a diversity of behavior of relative permeabilities in fractures. Furthermore, less attention has been paid to study the relationship between flow structures and relative permeabilities. Although the flow structure in the experimental study performed by Romm [1966] is not reported, it is likely that it was a near-straight channel flow due to the fracture configuration (alternate wetting and nonwetting stripes). In this case, the interaction between phases is minimal and, consequently, the results are described by the X-model. The experiments performed by Persoff et al. [1995] showed that the flow is characterized by having a localized continuous flow path that is undergoing blocking and unblocking by the other phase at certain flow ratios. This behavior is related to capillary effects, which are dominant in classical porous media. Consequently, the flow of one phase is strongly impeded by the flow of the other phase. In the experiments performed by Fourar and Bories [1995], several flow structures were observed: bubbles, fingering bubbles, drops and films. It seems that these flows are dominated by viscous forces.

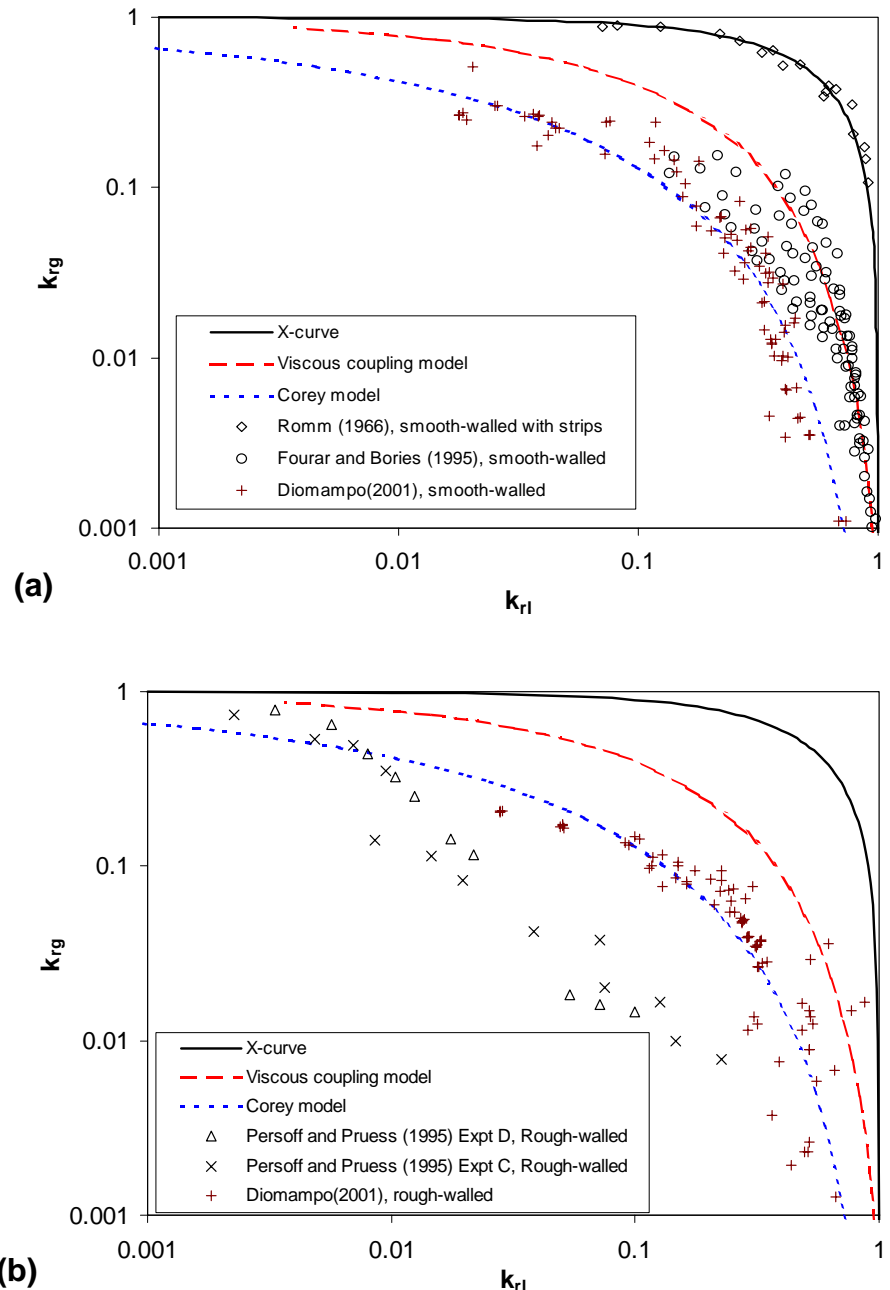


Figure 2.2: Compendium of previous measurements of relative permeabilities in fractures: (a) smooth-walled fractures, (b) rough-walled fractures. (Romm [1966] results from kerosene-water flow, the rest were air-water flow).

2.4 Reviews of Steam-Water Relative Permeabilities

The phase transformation effects are a distinct feature of liquid-vapor flows in geothermal reservoirs (steam-water flow) and gas-condensate reservoirs (gas-oil flow). In the forecasting of geothermal reservoir performance, reservoir engineers assume that steam-water flow behavior complies with generalized Darcy's equations given by Equations (2.6) and (2.7). Hence, obtaining the representative relative permeability functions becomes a critical issue in geothermal reservoir engineering. Regardless of this importance, no successful models or consistent measurements of steam-water relative permeabilities are available to represent the behavior of actual geothermal reservoirs. Because of this, the steam-water relative permeabilities used in the mathematical modeling of the geothermal reservoirs have been chosen arbitrarily [Faust and Mercer, 1979; Pruess et al., 1982].

In geothermal reservoirs, steam and water are transported mainly through fractured media. Despite this fact, most steam-water flow studies have been done in porous media, which is less representative of the real geothermal reservoir behavior. Table 2.1 summarizes 27 years of work in determining steam-water relative permeabilities from 1974 to 2001. Except for some field studies, all of these measurements were done in laboratory-scale consolidated or unconsolidated porous media. Despite the advance of measurement techniques and the number of these studies, some results have been in contradiction and no rigorous theoretical models have been specifically suggested to describe these results.

Some of the earliest attempts to measure the steam-water relative permeability in porous media were made by Miller [1951], Arihara et al. [1976], Chen [1978] and Council [1979]. However, these results have been deemed to be less reliable due to the limitations of measurement techniques at this early stage; for example, their saturation measurements were either absent or inferred from capacitance probes. Later, Verma [1986] improved the saturation measurement by using the gamma-ray densitometer in his

steam-water experiment in an artificial sand pack. The measured steam-water relative permeabilities were compared with experimental results obtained by other investigators [Johnson et al., 1959 and Osoba et al., 1951] for conventional two-phase, two-component flows, as presented in Figure 2.3. Verma's results revealed strong enhancement of the steam-phase relative permeability and he remarked that the phase transformation effects led to more efficient transport of the steam phase and reduced the pressure drop across the flow channels. Two mechanisms attributed to the enhancement of the steam-phase relative permeability were suggested: (1) phase transformation in converging-diverging flow channels with hydrophilic walls can cause an enhancement of steam phase relative permeabilities; and (2) phase transformation along the interface of a stagnant phase and the other phase flowing around it controls the irreducible phase saturation of the stagnant phase [Verma, 1986].

Table 2.1: Previous experiments relevant to steam-water relative permeabilities, 1974–2001. [after Horne et al., 2000]

Reference	Year	Experiment type	Saturation technique	Core type
O'Connor	2001	Steam-water	CT scanner	Berea sandstone
Mahiya	1999	Steam-water	CT scanner	Berea sandstone
Satik	1998	Steam-water	CT scanner	Berea sandstone
Ambusso	1996	Steam-water	CT scanner	Berea sandstone
Piquemal	1994	Steam-water	Gamma ray	Unconsolidated sand
Closmann and Vinegar	1988	Steam-water-oil	CT scanner	Natural core
Sanchez and Schechter	1987	Steam-water	Tracer	Unconsolidated sand
Verma and Pruess	1986	Steam-water	Gamma ray	Unconsolidated sand
Monsalve et al.	1984	Surfactant-steam-water	Tracer	Berea sandstone
Counsil and Ramey	1979	Steam-water	Capacitance probe	Consolidated synthetic
Horne and Ramey	1978	Steam-water	Production history	Field study
Chen et al.	1978	Steam-water	Capacitance probe	Consolidated synthetic
Grant	1977	Steam-water	Production history	Field study
Trimble and Menzie	1975	Steam-water-oil	Did not measure	Berea sandstone
Arihara	1974	Steam-water	Did not measure	Consolidated core

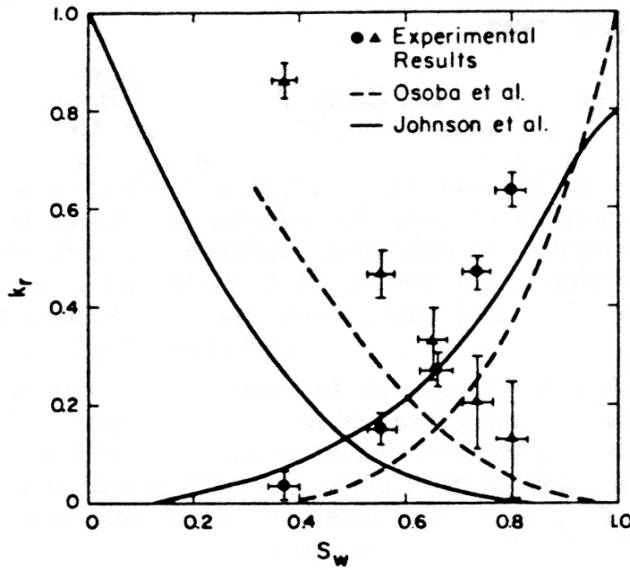


Figure 2.3: From Verma [1986]. Comparison of experimental results from steam-water flow in porous media with those of Johnson et al. [1959] for oil-water and Osoba et al. [1951] for oil-gas. The steam phase relative permeabilities are higher than nonwetting phase relative permeabilities obtained by other investigators.

In the last decade, with the advance of tomographic technology, X-ray CT scanners have been used to determine the saturation distribution for steam-water flow in porous media, by Satik [1998], Mahiya [1999] and O'Connor [2001]. Horne et al. [2000] summarized Satik's and Mahiya's results and compared them with air-water flow. Both results agreed qualitatively that the steam-phase relative permeability is higher than that of the air phase, which is consistent with Verma's results. However, Sanchez and Schechter [1987] and Piquemal [1994] presented contradictory findings. Sanchez and Schechter estimated the average water saturation through an entire core of unconsolidated porous medium and ignored the spatial variations in saturation. Their results showed that the steam-water relative permeabilities behaved similarly to those of the air-water flow. Piquemal [1994] conducted steam-water flow experiments at 180°C in an unconsolidated material packed in a tube 25 cm long and with an internal radius of 5cm. During the experiment, pressure and temperature were measured at four points along the core holder 5cm apart. The results also suggested that steam-water flows are

similar to those of air and water. The experimental results from these investigators are shown in Figures 2.4 and 2.5.

These previous studies show a diversity of observations of steam-water relative permeabilities in porous media. Issues such as whether the phase transformation enhances steam-phase permeabilities, and how the surface roughness of fractures affects relative permeabilities remain unresolved. One of the main objectives of our research was to contribute to the resolution of these issues.

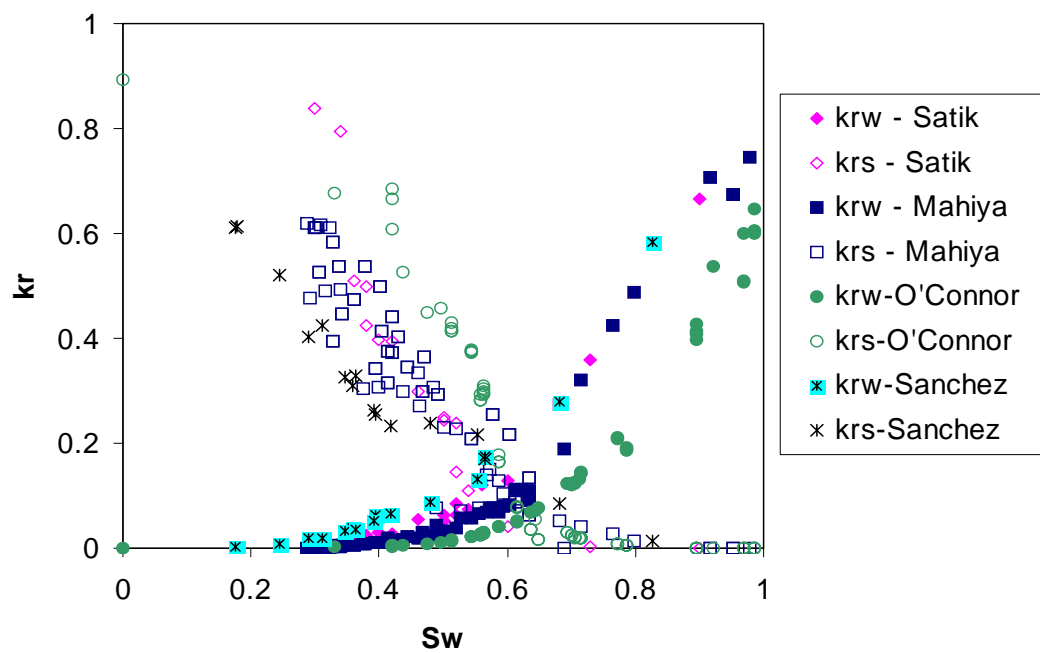


Figure 2.4: Comparison of steam-water relative permeabilities measured by Satik [1998], Mahiya [1999], O'Connor [2001], and Sanchez and Schechter [1987]. See Table 2.1 for detailed experimental description.

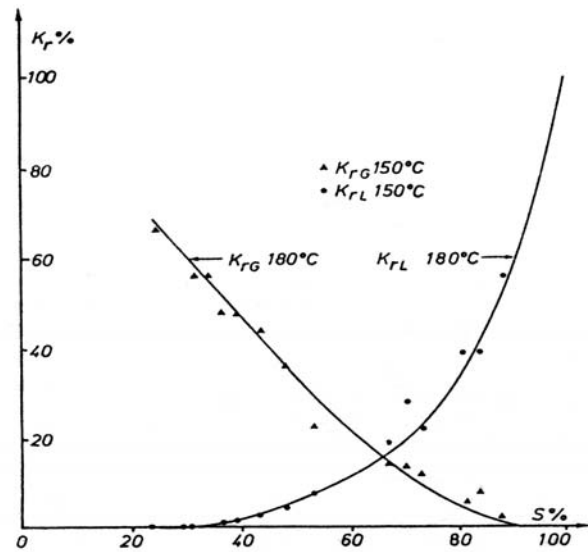


Figure 2.5: From Piquemal [1994]. Steam-water relative permeabilities in the unconsolidated porous media at $150^\circ C$ (solid symbols) and the trendlines of the steam-water relative permeabilities at $180^\circ C$ (solid lines).

Chapter 3

Experimental Study of Air-Water Flow in Fractures

This chapter describes the experimental work of air-water flow in smooth-walled, homogeneously rough-walled (HR) and randomly rough-walled (RR) fractures. These three specially designed fractures represent three distinct surface geometries and heterogeneities. Two-phase flow structures and relative permeability behavior are studied and discussed for these three cases. The chapter is organized as follows. In Sections 1 and 2, we describe the experimental apparatus, measurement techniques and experimental procedures. In Section 3, we describe the observed flow structures and calculated relative permeabilities. In Section 4, we summarize this chapter.

The experimental apparatus built for this work and the experimental procedure are presented in the next section.

3.1 Experimental Apparatus and Measurements

Cocurrent air-water drainage experiments were conducted at 24°C. The term “*drainage*” means that gas intrudes into fracture spaces that are filled with either flowing or static liquid. The fluids were pure nitrogen and deionized water. The experimental system is

illustrated in Figure 3.1, that shows the fluid supply, the fracture apparatus, data acquisition system, and digital image recording. A photograph of the whole system is shown in Figure 3.2. The water injection was controlled by a meter pump (Dynamax, SD-200, rate: 0.1-200 ml/min). Gas injection was controlled through a flow regulator (Brooks Instrument, Flow Controller Model 0151E), which was connected to a gas meter (Brooks Instrument, Flow Meter model 5850E, max. rate: 200 SCCM; standard cubic centimeters per minute). All measurements were electronic and digitized by using a high-speed data acquisition system (DAQ; National Instrument, SCSI-1000 with PCI 6023E A/D board) and digital video recording system (Sony Digital-8 560X with Pinnacle Studio DV IEEE 1394 image capture card). The details of each important component in the system, measuring techniques and experimental procedure are presented in the following sections.

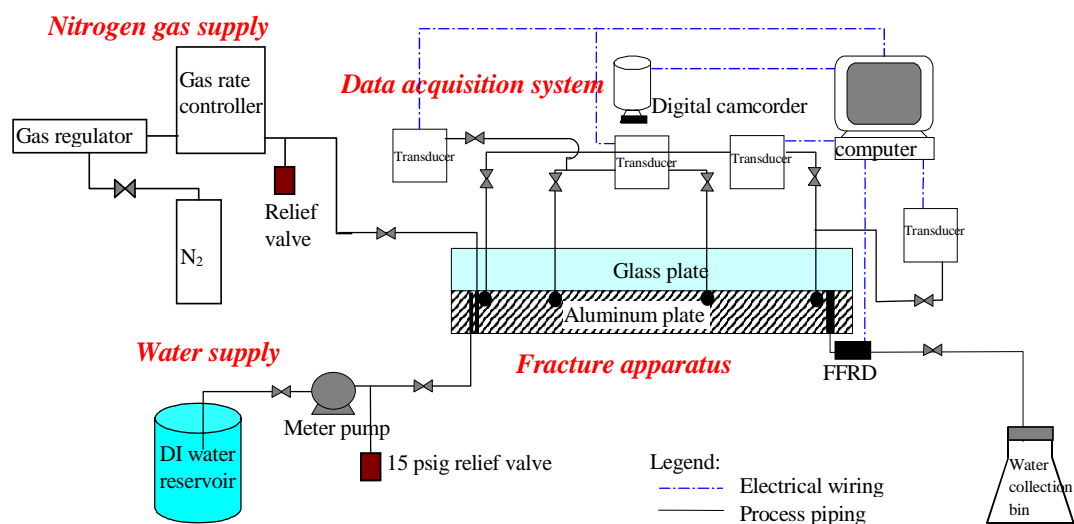


Figure 3.1: Process flow diagram for air-water experiment.

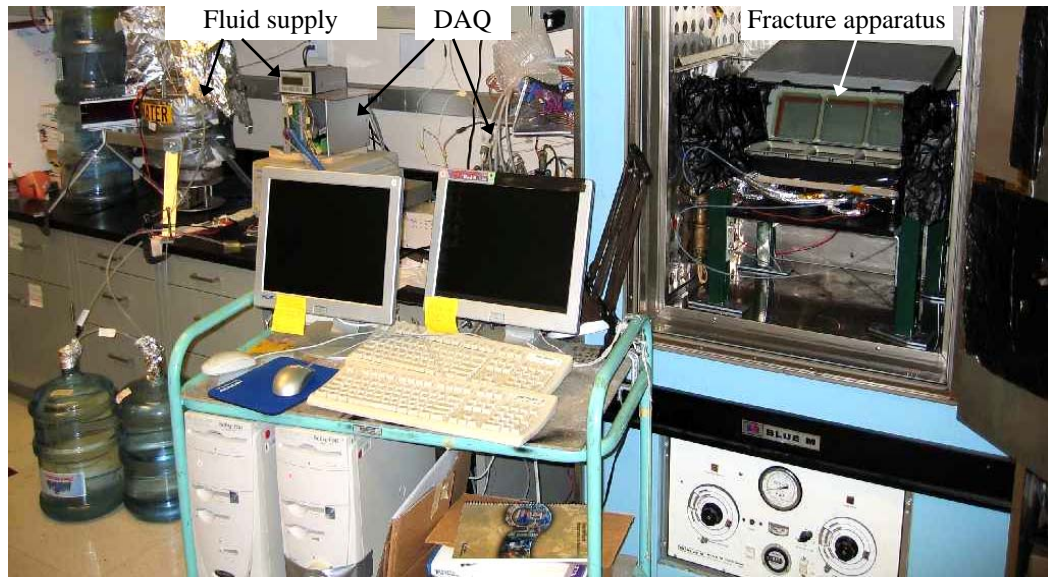


Figure 3.2: Photograph of air-water flow through fracture apparatus.

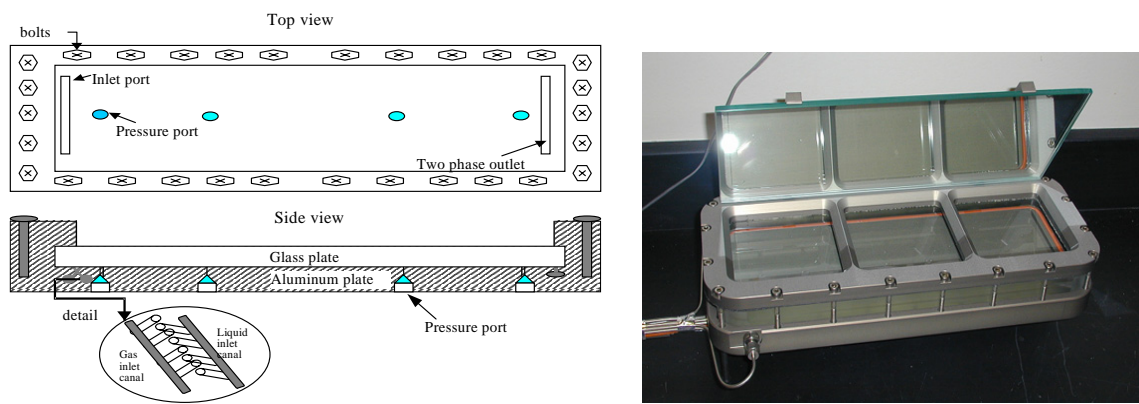


Figure 3.3: Schematic diagram and picture of fracture apparatus.

3.1.1 Fracture Apparatus Description

The fracture apparatus was modified from the original design of Diomampo [2001]. The fracture was created by mounting a smooth or rough glass plate on top of an aluminum

plate, confined by a metal frame bolted to the bottom plate. Table 3.1 shows the contact angle range of the material forming our fractures (silica glass and aluminum metal) measured by earlier investigators [Anderson and Gasp, 1997; CAMTEL, 2000]. Though these ranges are wide, both top and bottom surface can still be categorized as water-wet material. The frame was designed to hold the seal and to avoid deformation of the glass due to system pressure. Several windows and a mirror attached to the frame allow the flow visualization (see Figure 3.3). The fluids enter the fracture through two separate canals containing a total of 123 capillary ports (diameter 0.51mm) which align on the surface alternately (see the schematic diagram in Figure 3.3). These capillary ports were used to deliver the fluids to the fracture surface evenly. The surface of the fracture apparatus was designed such that there is an available 30.48cm by 10.16cm (12inch by 4inch) space for flow. Throughout the flow area, four pressure ports with a diameter of 0.51mm were drilled throughout the flow area to minimize surface discontinuity. The two-phase fluid exits through a single outlet. The apparatus was designed to be of sufficient length that end effects only affect a small part of the flow window – experimental observations have confirmed this to be true.

Table 3.1: Reported contact angle of aluminum and silica glass.

Material	Static contact angle range (degree)
Aluminum	50~60
Silica Glass	0~20

The fractures for the experiments were made by transparent silica glass with dimensions around 35cm (L) x 15cm (W). Three fractures with distinct surface roughness, smooth, randomly rough (RR) and homogeneously rough (HR) fractures,

were used in the steady-state air-water cocurrent drainage experiments to represent three distinct surface geometries and heterogeneities.

For the smooth-walled experiment, a plain glass slab was used as the top plate. The aperture of the fracture was set by installing the stainless steel shims with thickness 130 μm as the fracture spacer. For the rough-walled experiment, two specially designed, rough-walled glass plates were used as the top plate. These two rough glass plates were placed above the aluminum bottom plate with thin silicon shims or gasket sealant (thickness < 100 μm) in between. An optical surface profilometer (OGP; Optical Gaging Product, SmartScope Avant ZIP video measuring system) was used to determine the surface profile of the HR surface. As shown in Figure 3.4, the HR surface has a repeatable wedge-shaped pattern with around 160 μm maximum local vertical variation and around 90 μm mean vertical variation. Since the HR fracture was formed by mounting the HR surface and a smooth aluminum plate with a tiny silicon shim in between, there is an additional aperture (b_{open}) formed by the silicon shim besides the contacting aperture b_c (i.e. the aperture form by contacting two surfaces). To evaluate b_{open} , the hydraulic aperture b_h from the cubic law (described later in Section 3.3.1) was used as the mean aperture of the HR fracture. Earlier studies have showed that the deviation of the mean aperture from the hydraulic aperture is insignificant for open fractures with small correlation length or large ratio of the mean separation between the surfaces to the standard deviation of the aperture distribution, b_m/σ_b [Witherspoon et al., 1980; Brown 1987]. Therefore, the cubic law appears to be valid for rough-walled fractures provided the fracture local aperture variation along the flow direction is only minor [Iwai, 1976; Brown, 1987; Thompson and Brown, 1991]. After applying $b_h = 150\mu\text{m}$, Figure 3.4b shows the three-dimensional aperture distribution of the HR fracture, and Figure 3.4d shows a line profile in the aperture field. As indicated, the b_{open} is roughly 60 μm .

The RR fracture has a randomly distributed hill-shaped pattern with around 350 μm maximum vertical variation. The hydraulic aperture at 24°C is around 240 μm , which

is described later in Section 3.3.1. The surface profile of the RR glass was measured by a Leitz PMM 12106 CMM Stylus Machine ($20\mu\text{m}$ resolution, $\sim 2\mu\text{m}$ precision). After applying the hydraulic aperture as mean aperture, the aperture profile, histogram and variogram (γ) of the RR fracture are shown in Figure 3.5. The standarized sill (i.e. $\gamma = 1.0$) indicates no spatial correlations in the direction specified. Both x-direction and y-direction variograms jump to 0.8 in less than 5mm distance, which may indicate that the RR aperature has only weak spatial correlations when the lag (i.e. horizontal separation distance) is more than 5mm. Therefore, we roughly defined the short correlation length as 5mm for both directions. If long range correlation is considered, as can be seen in Figure 3.5c, the long range correlation length in the x direction ($L_{c,x}$) is about 20mm, whereas y direction ($L_{c,y}$) is 25mm. This is also 15 times smaller than the fracture flow length (300mm). The line profile in Figure 3.5d indicates that the b_c is around $150\mu\text{m}$, while the b_{open} caused by the fracture boundary sealant is roughly $90\mu\text{m}$.

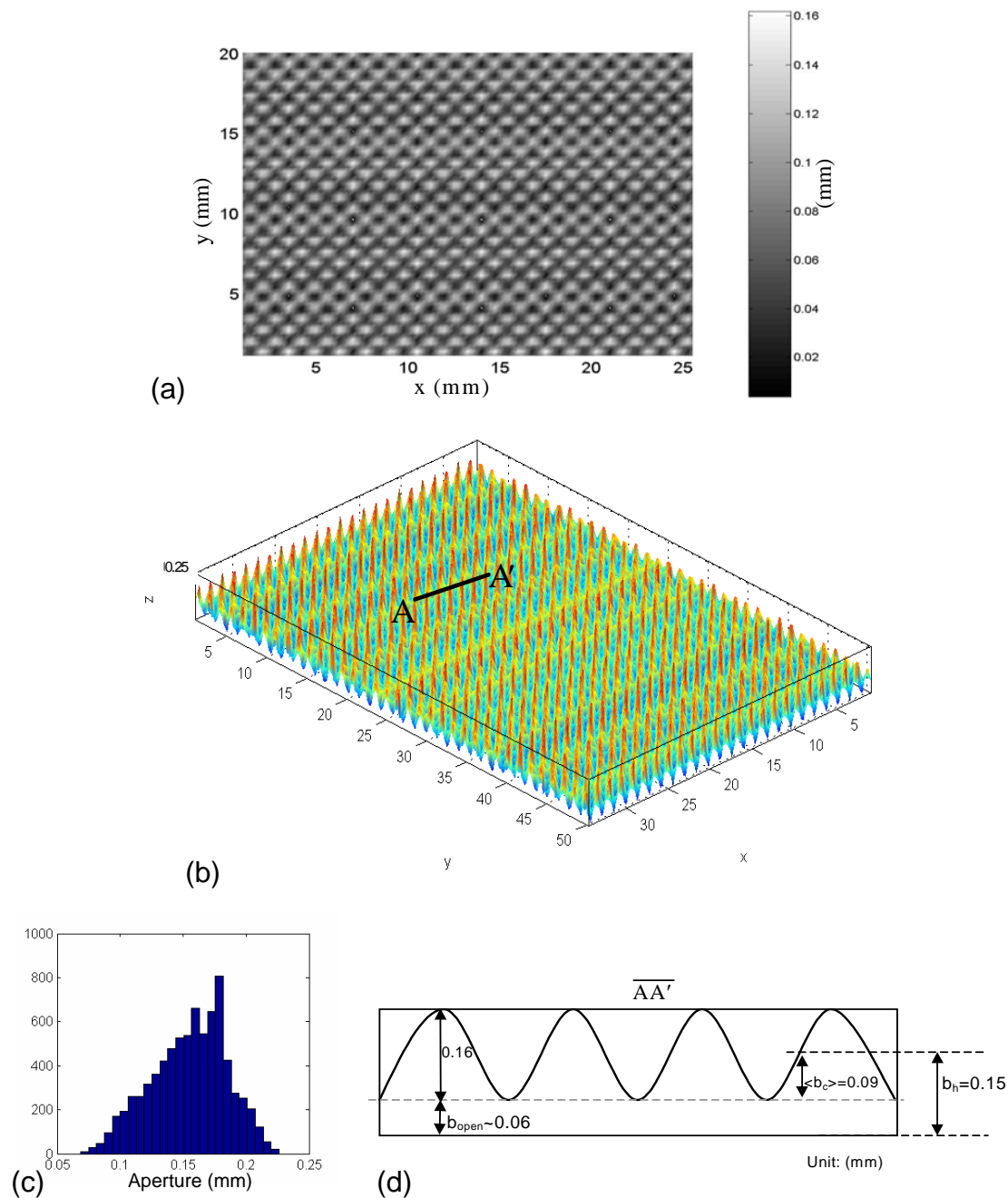


Figure 3.4: Homogeneously rough (HR) fracture: (a) two-dimensional rough surface pattern. (b) three-dimensional aperture profile. Z axis is not to scale. (c) histogram of the aperture distribution; mean=0.155mm, STD=0.03mm. (d) line profile of section AA'.

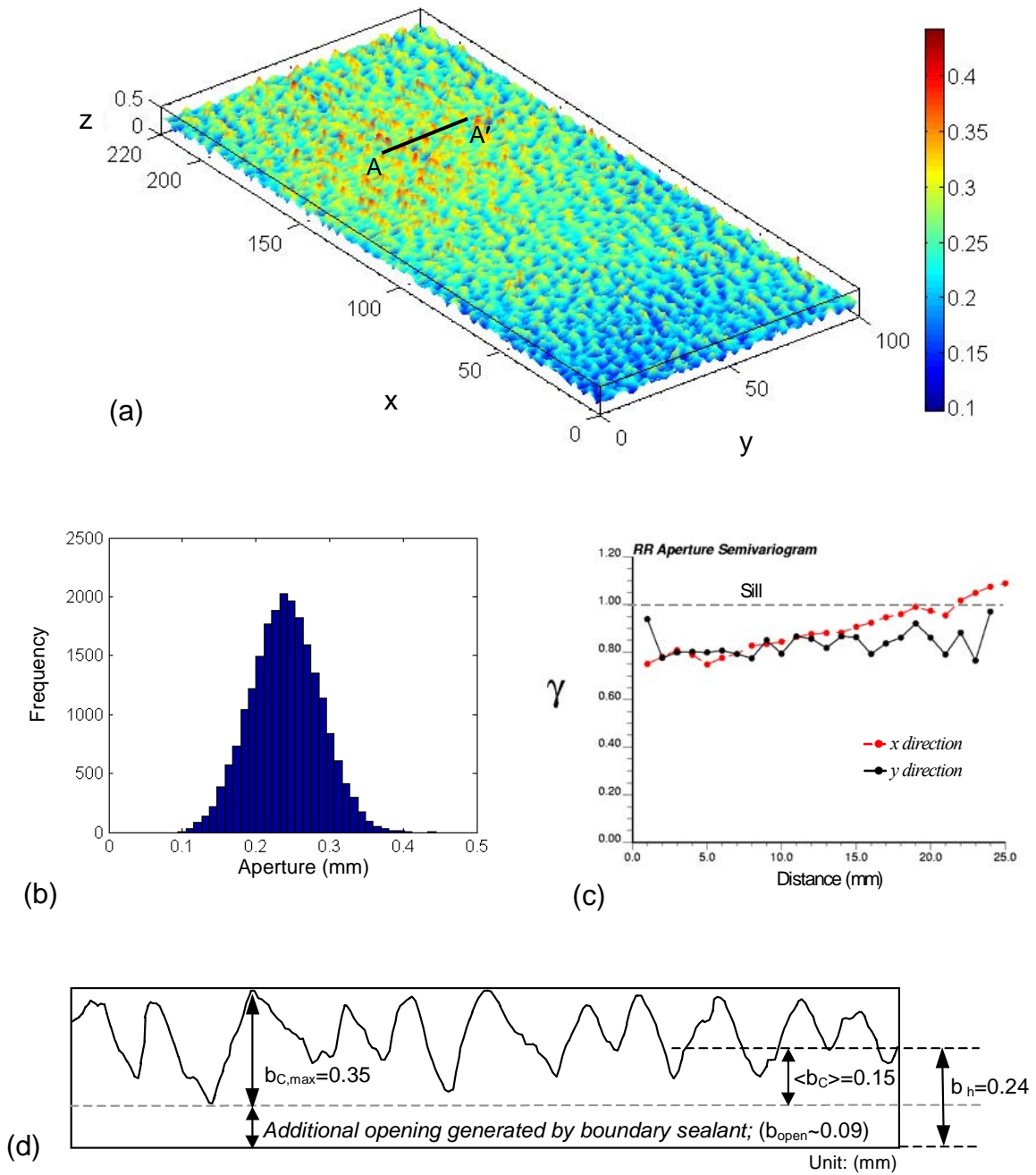


Figure 3.5: Randomly rough (RR) fracture: (a) three-dimensional aperture distribution. (b) histogram of the aperture distribution; mean=0.24mm, STD=0.05mm. (c) variogram of the aperture distribution; range $x \sim 20\text{mm}$, range $y \sim 25\text{mm}$ (d) line profile of section AA', where $b_{c,max}$ denotes maximum vertical variation of the fracture surface.

3.1.2 Pressure Measurements

Capillary end effect was an issue because of its influence on the pressure measurement. To minimize this, four pressure ports were drilled along the fractures for both whole-range and intermediate pressure difference measurements. The inlet, outlet and intermediate absolute pressure along the length of the fracture was also acquired for calculation of gas relative permeabilities and determination of thermodynamic properties. Low-range differential transducers were used to measure the pressure difference through the fracture, as well as the intermediate pressure and the two-phase outlet pressure. Two liquid-filled differential transducers (Validyne Transducer, model DP-15, range 0-2 psig) were attached to four pressure ports inside the fracture to measure the pressure difference through the fracture. Another transducer (Validyne Transducer, model DP-15, range 0-5 psig) was attached to the middle point of the fracture. The fourth transducer (Validyne Transducer, model DP-15, range 0-5 psig) was attached to the two-phase outlet of the fracture apparatus. These transducers send electrical signals to the data acquisition system, which was monitored using the LabView® programmable virtual instrument software. The complete measurement configuration in the fracture apparatus is shown in Figure 3.1.

3.1.3 Flow Rates Measurements

Aside from the known input rates, a fractional flow ratio detector (FFRD) was designed and constructed as shown in Figure 3.6a to obtain the instantaneous flow rates. The FFRD was used to measure the outlet gas and water fractional flows, f_g and f_w .

$$f_g = \frac{q_{out,g}}{q_{out,t}} \quad \text{and} \quad f_w = \frac{q_{out,w}}{q_{out,t}} \quad (3.1)$$

$$q_{out,t} = q_{out,w} + q_{out,g} \quad (3.2)$$

where $q_{out,g}$ is the outlet gas flow rate, $q_{out,w}$ is the outlet water flow rate, and $q_{out,t}$ is the outlet total flow rate.

The principle of the FFRD is that different phases present different refractive indices. A phototransistor (NTE 3038, NPN-Si, Visible) was installed inside the FFRD, producing different voltages when sensing different strengths of light. The water phase produces a higher voltage when flowing through the FFRD as shown in Figure 3.6b. After the gas and water responses are obtained from the FFRD, the statistical histogram is plotted and the gas and water phase flow ratios are obtained by determining the threshold of the histogram. This is shown in Figure 3.7 and Table 3.2. Once f_g and f_w are obtained at steady-state condition, it is easy to calculate $q_{out,g}$ in Equation (3.1) by assuming that water flow rate remains constant from inlet to outlet of the fracture. This assumption can hold if the wetting phase, water, flows in a continuous channel, and the water viscosity is much larger than the nonwetting phase. The calibration of the FFRD demonstrated a good linearity between measurement and actual values (Figure 3.8). As can be seen from Figure 3.8, at both high and low water flow rates the FFRD shows high accuracy in measuring fractional flow at different nitrogen flow rates. Even when the nitrogen flow rate is much higher than the water flow rate, the FFRD can recognize the fractional flow ratio over a period of several seconds. Therefore, the FFRD technology should be appropriate to calculate gas and water outlet flow rates. This technology was also used for determining steam and water rates in the later steam-water experiments in this work.

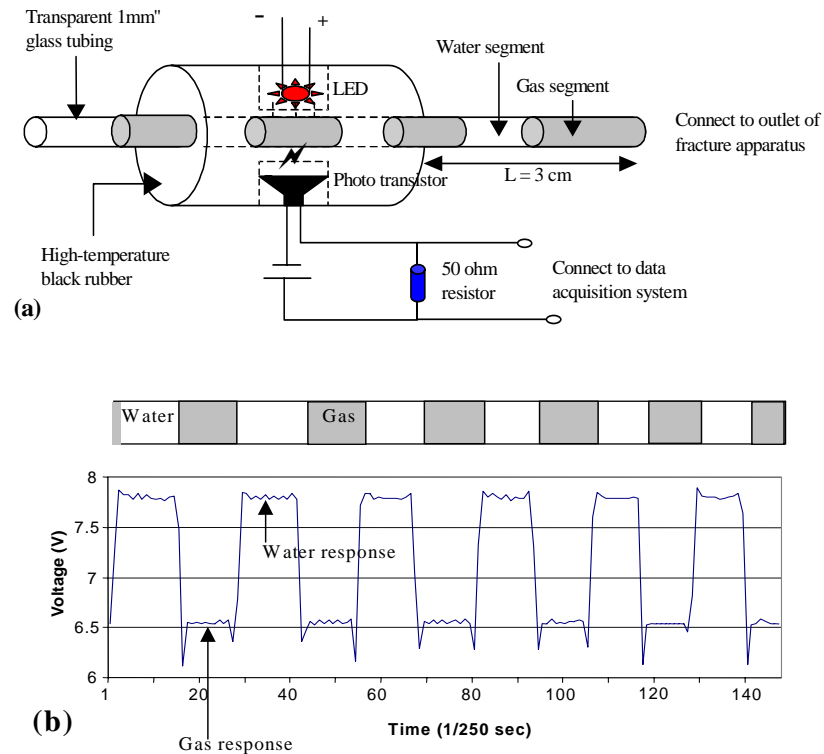


Figure 3.6: Fractional flow ratio detector (FFRD) (a) schematic (b) detected gas and water signal corresponding to different gas and water segments inside FFRD tubing.

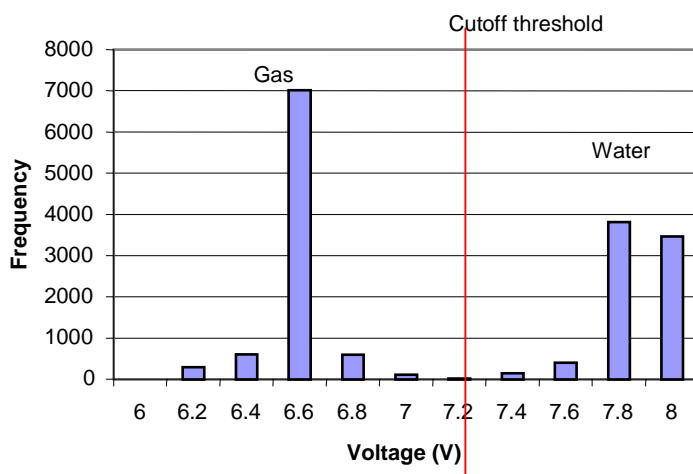


Figure 3.7: The histogram obtained from Figure 3.6.

Table 3.2: The analysis results of gas and water fractional flows from Figure 3.7.

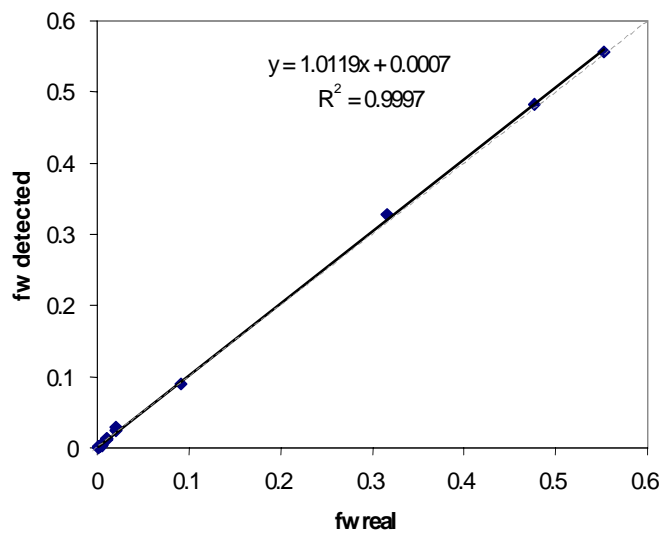
Volt.	Frequency	Discrimination
6.2	287	Gas
6.4	603	Gas
6.6	7021	Gas
6.8	600	Gas
7	110	Gas
7.2	20	Threshold
7.4	146	Water
7.6	400	Water
7.8	3810	Water
8	3462	Water
More	0	

→

Gas total	8631
Water total	7828
Grand total	16459

↓

Fractional flow	
f_g	0.5243939
f_w	0.4756061

**Figure 3.8:** FFRD calibration (Fluids: water and nitrogen gas; FFRD tubing ID: 1.0mm).

3.1.4 Saturation Measurements

Instantaneous saturation measurement has long been a major challenge in multiphase flow experiments. The transparent top glass enables us to visualize and videotape the two-phase flow scenes in real time. Still images were then extracted with less than one-second frequency from the digital video recorded during the experiments. These images were synchronized with the logged data through the time read from the LCD monitor. The top image in Figure 3.9 shows a typical video image taken from the experiments. The photographs were processed in a computer program that does quadratic discriminant analysis (QDA) or divided binary threshold analysis (DBTA) to group the pixels of the picture into three groups: the water phase, gas phase and the frame, based on color differences. Finally, saturation is computed as total pixels of the liquid group over the sum of the gas and liquid groups.

Several earlier studies [Pan et al. 1996, Persoff and Pruess, 1995; Diomampo 2001] used similar techniques for the saturation measurement or flow visualization; however due to the transparent and colorless characteristic of both fluids, they all dyed the liquid phase to enhance the color differences. Dyeing the water may alter the physical and thermodynamic properties, which discouraged us from using this procedure. To obtain distinct color differences between gas and water, a carefully designed lighting system was placed at the rear of the fracture. The light beams pass through the transparent top wall of the fracture (the glass plate) horizontally, which makes the fluids stereoscopic and darkens the gas phase. Earlier study [Pan et al., 1996] noted that the source of errors in this technique is the quality of the photographs and the water film adsorbed on the surfaces of the plates with the latter being of minimal effect. Good quality photographs are the ones with clear distinction between the gas and liquid phase. Good lighting is necessary so that the colors in the image come out clearly. The lighting should also be positioned in a way that it does not produce shadow on the flow area, as the program will mistakenly take the shadow as gas phase even if there is liquid.

For the smooth-walled fracture, the QDA program was used to recognize each phase and reconstruct the binary images. The program utilizes neural network techniques to discriminate each phase based on the variance of color intensity. Figure 3.9b is a binary image produced by the QDA program from the original color photograph of two-phase flow in the smooth-walled fracture. Better accuracy has been achieved compared to the results from the dyeing approach.

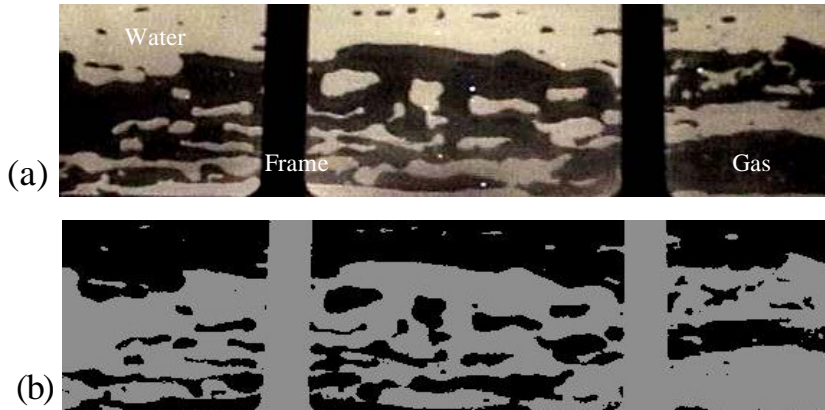


Figure 3.9: Comparison between the true color image of the flow in the smooth-walled fracture and binary image from the Matlab QDA program used in measuring saturation.

For the rough-walled fractures, however, the QDA program could not reach acceptable accuracy, because the shadows generated by light reflection and scattering from the rough surfaces were inevitable. Figure 3.10 shows the light intensity field in the water-filled RR fracture. Though the intensity of the shadows is not significant, it can produce 10% absolute difference of S_w according to our sensitivity tests. To resolve this problem, we created another DBTA computer program for rough-walled fractures image processing. This program first does the background correction by compensating the intensity of the targeting image according to the water-filled background image. Then it divides the targeting images to several subregions each of which has similar background intensity. The binary conversion was achieved by assigning binary thresholds for each subregion based on the histogram analysis of the light intensity analysis similar to the

technique used by Nicholl and Glass [1994]. Figure 3.11 compares the processed binary image to the original true-color image. After the background compensation and sub-region division, the binary transformation of Figure 3.11a shows reasonable quality. Sensitivity tests show that the S_w determined has less than 3% absolute error.

As shown in Figure 3.5d, the top surface of the RR fracture has irregular roughness. Even though its variograms show weak spatial connectivity, the gas and water might compete to find the larger aperture area. Therefore, the feasibility of using this two-dimensional image processing technique to infer the three-dimensional phase volume is unsure. The saturation is defined purely by the ratio of phase area to total area. The implicit assumptions are that both areas share the same hydraulic aperture and each pixel in the image is occupied by only one phase. Considering that water only occupies one of the correlation areas formed by short-range correlation lengths ($L_{c,x} = L_{c,y} = 5\text{mm}$) and long-range correlation lengths ($L_{c,x} = 20\text{mm}$, $L_{c,y} = 25\text{mm}$), the corresponding estimated saturations (volumetric ratio) using area ratio are 0.001 and 0.016, respectively. This may indicate that less accurate volumetric ratio is calculated for a single-phase (water) cluster whose occupied area to the total area is less than 0.016, provided its aspect ratio is close to 1. Since the evidence of the unity aspect ratio is weak, a constant volume injection test was conducted to examine the accuracy of using area ratios to represent volumetric ratios (saturation) in the RR fracture. Water with fixed volume was injected from the middle of the RR fracture. The estimated volume was obtained by multiplying the corresponding area ratios output from DBTA program by the hydraulic aperture of the whole fracture. The comparison of the estimated volume to the injected volume is shown in Figure 3.12. This test was done within 55% water saturation because water broke through two ends of the fracture when $S_w > 55\%$. Nevertheless, the estimated volumes have good agreement with the actual volumes. This validates the application of the image processing method for S_w calculation to the RR fracture.



Figure 3.10: Background image of the RR fracture fully saturated with water. The shadows are generated by light reflection and scattering from the rough surfaces.

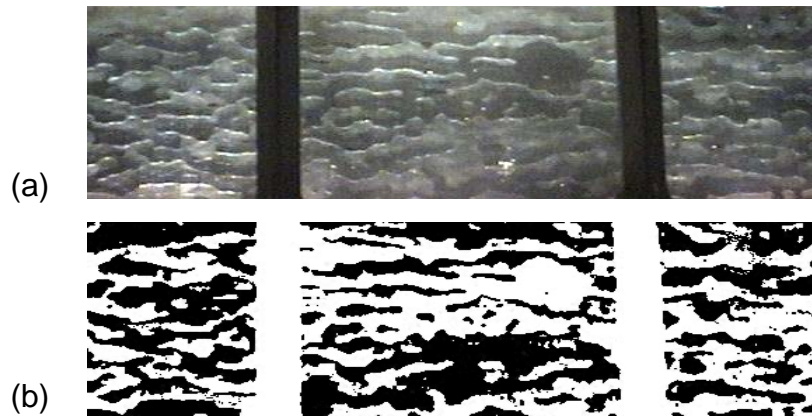


Figure 3.11: Comparison between the true color image of the flow in the RR fracture and binary image from the Matlab DBTA program used in measuring saturation.

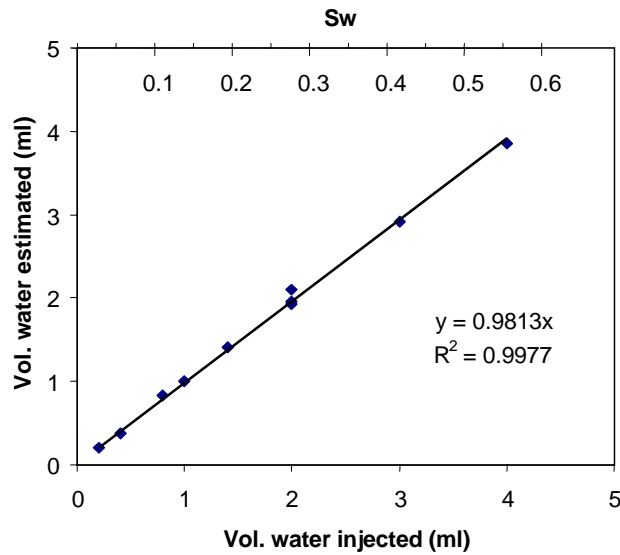


Figure 3.12: Comparison of the volume of water injected to the RR fracture to the volume of water estimated from the image processing program DBTA.

3.2 Experimental Procedure and Data Processing

First, single-phase water flow experiments were conducted at room temperature and high temperature to characterize the hydraulic properties of the fractures. After that, the air-water flow experiments were conducted in a drainage process.

The fractures were fully saturated with deionized water initially. The drainage process was controlled by adjusting water and gas injection rates to decrease the water saturation. First, the water rate was kept constant while increasing gas rate to decrease the water saturation in the fracture until the water saturation was no longer sensitive to the increase of the gas rates. Then, the water rate was decreased further and the previous procedure was repeated. To avoid the dissolution of the gas phase and evaporation of the water phase, the water was equilibrated with air and the air was saturated with water-vapor. During each designated input rate of gas and water, the data were acquired when a stable or repeatable flow structure had been reached. After finishing one run (one pair of prescribed water and gas rates), the flow structures were destroyed by rapidly flushing water through the fractures, and then another run was commenced.

According to air-water experiments reported by earlier studies [Persoff and Pruess, 1995; Diomampo, 2001], the fracture flow experiments are unsteady by nature. While input rates of water and gas were fixed, considerable pressure fluctuations accompanied by saturation changes occurred, which made flow rates through the fractures vary. Traditional time-average data processing was deemed to be infeasible and unrepresentative since every datum fluctuation may indicate a corresponding fluctuation of flow structure and saturation. To overcome these issues, all instantaneous data were acquired in a period less than or equal to one second. In addition, instantaneous outlet rates of gas were also measured by the FFRD device for the relative permeability calculation and flow rate comparison. Digital video was taken in each run when the flow reached steady state or repeated similar fluctuating behaviors. The continuous images of each run were extracted from the video every 0.33 seconds. These hundreds of images in

each run were then input into the computer programs for the saturation calculation, flow structure recognition and characterization of the stability of the two-phase flow. The data acquisition task requires frequent gathering of instantaneous and synchronized pressure, flow rate and saturation values. Instantaneous gathering of data was accomplished by the use of the high-speed data acquisition system and digital video camcorder. Video shots were taken of the pressure, time and saturation data displayed all at the same time. Pressure data and related time were displayed by the LCD monitor connected to the computer, which also ran the data acquisition system. The methodology used to integrate all the data and signals and then calculate the gas-water relative permeability is illustrated in the flow chart in Figure 3.13.

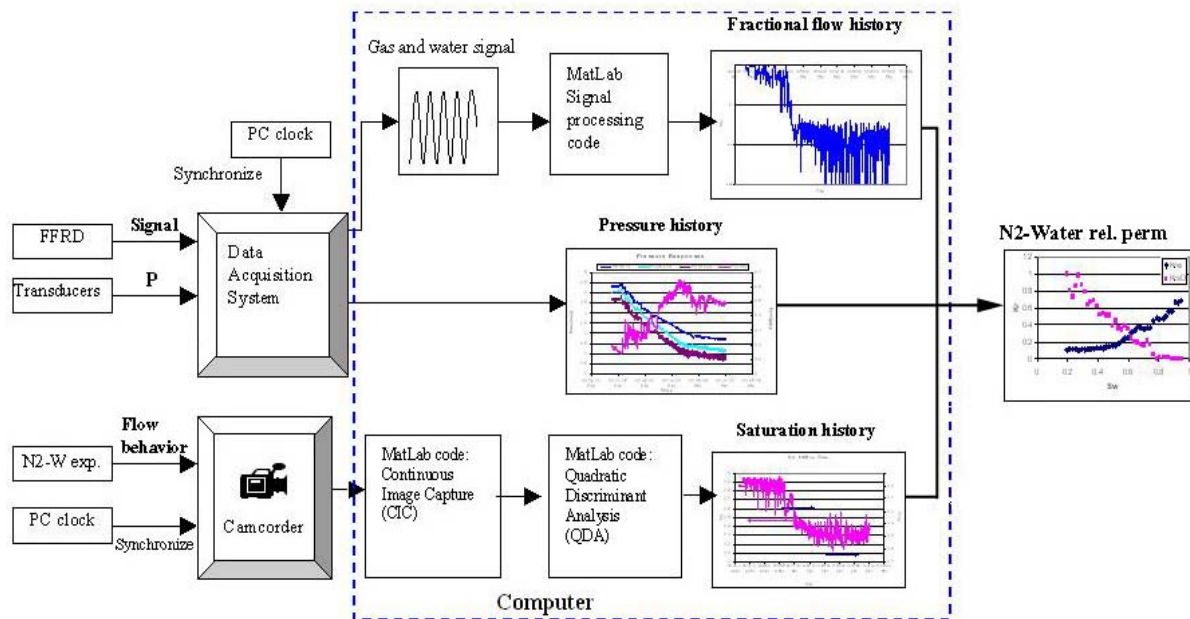


Figure 3.13: Data and signal processing flowchart.

3.3 Experimental Results

We first present the hydraulic properties of the fractures, and then describe flow structures observed during the experiment and the relative permeabilities calculated at one-second frequency in each run as well as their averaged values. Finally, we interpret the relative permeabilities using models from earlier studies.

3.3.1 Hydraulic Properties of the Fractures

Before the two-phase measurements, single-phase flow experiments at 24°C and 90°C were conducted to obtain the absolute permeabilities or the product of absolute permeability and cross-sectional area, namely the kA parameter. The parameter kA was used in the subsequent calculations for the rough-walled fracture since the cross-section area and the aperture of the rough fracture are not constant. Therefore, it is practical to use the combined kA parameter for the relative permeability calculation from Equations (2.6) and (2.7) in the case of the rough-walled fracture. The 90°C values of k and kA were used to calculate steam-water relative permeabilities (which were actually conducted at 104°C) in Chapter 6 later, because it was difficult to maintain purely single-phase flow when the fracture temperature exceeded 90°C. Figure 3.14 shows the measured absolute permeability of the smooth-walled fracture at the two temperatures and different fracture pressures. The measured absolute permeability of the smooth-walled fracture is around 1510 darcies ($1.51 \times 10^{-9} \text{ m}^2$) at 24°C and 1400 darcies ($1.40 \times 10^{-9} \text{ m}^2$) at 90°C when the fracture pressure is less than 3 psig. The corresponding apertures estimated from the cubic law range from 127 to 137 μm which are consistent with the fracture spacer installed (130 μm). Additionally, the fracture deformation due to the increase of the fracture pressure is small enough to assume constant absolute permeability throughout the smooth-walled experiments.

For the rough-walled fractures, thin silicon rings and gasket sealant were used as the fracture spacer because the stainless steel shims could not seal against leaks due to the surface roughness. Though the kA parameter was used to replace the absolute permeability, the corresponding hydraulic aperture could still be estimated by combining the cubic law and Darcy's law:

$$b_h = \sqrt[3]{\frac{12\mu qL}{w\Delta P}} \quad (3.3)$$

where, b_h is the hydraulic aperture of the fracture, and w is the fracture width.

Figures 3.15 and 3.16 show the kA parameter and estimated hydraulic aperture versus the fracture pressure of the HR and RR fractures at 24°C and 90°C. Although our target was to keep the hydraulic aperture of the rough-walled fracture as close as possible to the aperture of the smooth-walled fracture, slight fracture dilation occurred as pressure increased due to the flexibility of the silicon ring. This fracture dilation phenomenon is significant in the high-temperature case, because the silicon spacer became more compliant and more sensitive to the stress or pressure applied. The RR fracture at 90°C has the highest dilation effect. However, good linearity was observed between the hydraulic aperture and pressure. Therefore, further kA parameter correction functions with respect to the fracture pressure were used for the rough-walled relative permeability calculation. The correlation functions are shown in Figures 3.15 and 3.16.

The generalized Darcy's equations in Equations (2.6) and (2.7) assume that flow in fractures is laminar and that inertia effect is negligible. To confirm the validity of applying these equations in our cases, we examined single-phase pressure drop versus flow rates in the fractures studied. Figure 3.17a demonstrates the linear relationship between pressure drop and water volumetric rates used in this study, which indicates that inertia contribution of water flow is negligible. Regarding the gas phase, the linear relationship between the equivalent pressure drop $(p_i^2 - p_o^2)/2p_o$ from Equation (2.7) and

gas volumetric rates in Figure 3.17b indicates that the gas inertia effect is also negligible. The dimensionless Reynolds numbers in the fracture is defined as:

$$N_{Re} = \frac{\rho u d}{\mu} \quad (3.4)$$

where u and μ are the superficial velocity and dynamic viscosity, respectively; d is the hydraulic diameter or characteristic length. For fractures with small aperture, $d=2b_h$. The maximum volumetric flow rates in the air-water experiments were 15 ml/min for water phase and 200 ml/min for gas phase. As shown in Figure 3.17, the maximum Reynolds numbers for both cases were less than 5. The results from rough-walled fractures also confirm that inertia contributions within the flow rate range were insignificant.

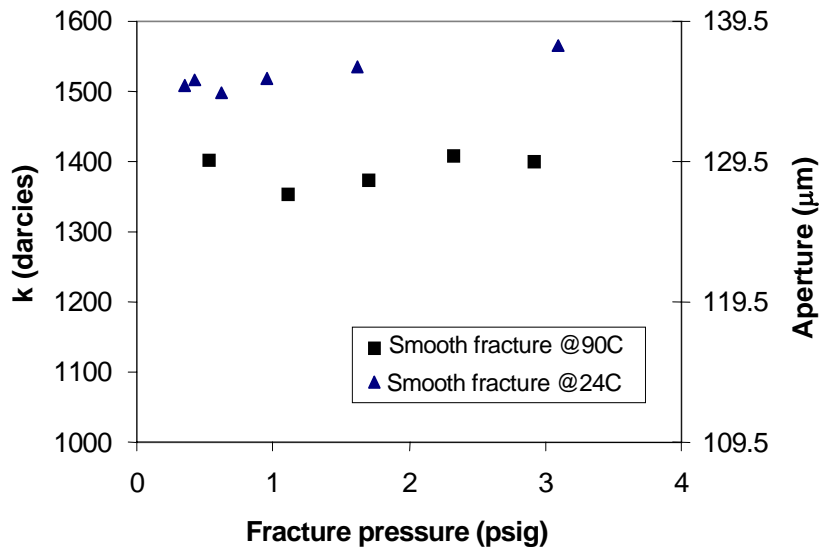


Figure 3.14: Absolute permeability of the smooth-walled fracture (fracture spacer $\sim 130\mu\text{m}$) at different temperature and fracture pressure.

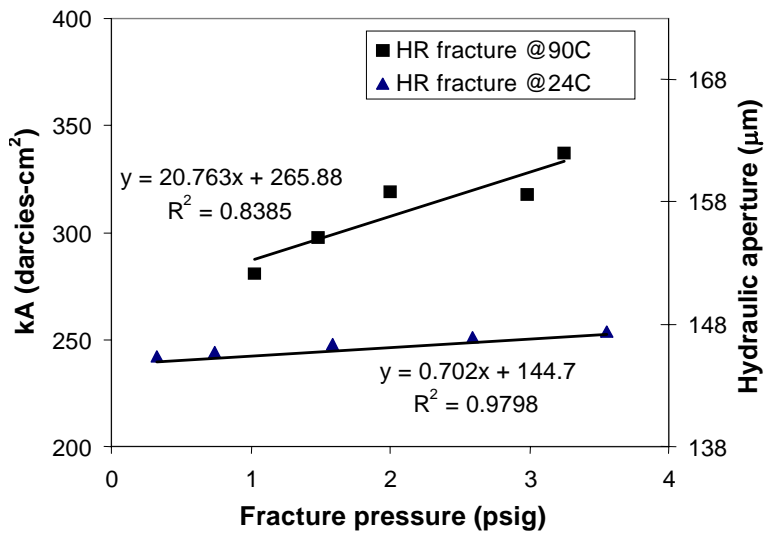


Figure 3.15: kA parameter and estimated hydraulic aperture of the HR fracture at different temperature and fracture pressure.

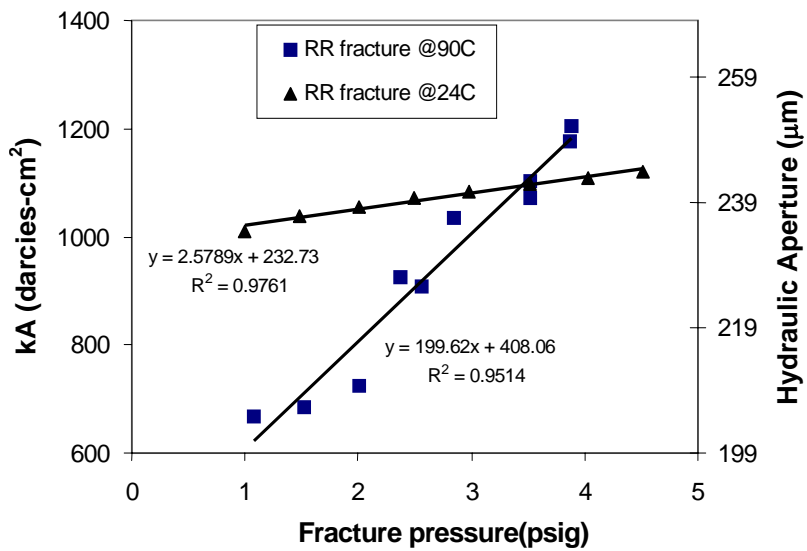


Figure 3.16: kA parameter and estimated hydraulic aperture of the RR fracture at different temperature and fracture pressure.

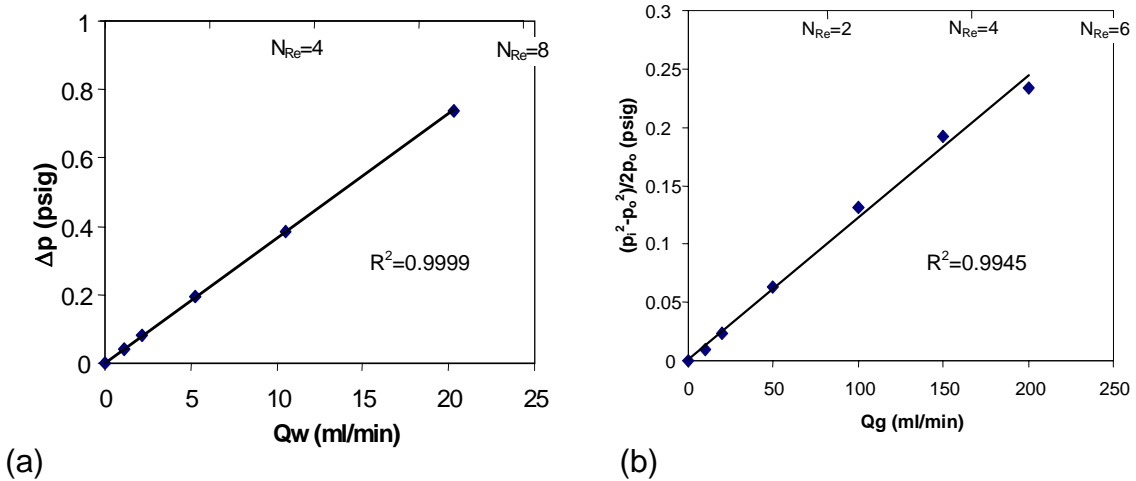


Figure 3.17: Steady-state, single-phase pressure drop versus flow rates in the smooth-walled fracture with aperture of $130\mu\text{m}$: (a) water flow, (b) nitrogen flow; where y axis is equivalent gas pressure drop used in Equation (2.7). Corresponding Reynolds number is also provided in the secondary x-axis.

3.3.2 Description of Flow Structures

The use of a transparent glass plate allows us to observe and videotape the two-phase flow structures. The recorded digital video was then transformed to a series of snapshots with the frequency of 3 images/sec (0.33 seconds period) for the smooth-walled case and 1 image/sec for the rough-walled fractures. More than 3000 still images were extracted from the digital video and used for the flow structure characterization and saturation calculation. Several flow structures depending on the flow rates were observed. Generally, when the water saturation decreases, one observes successively bubbles, slugs or intermittent channels and channels.

I. Flow structures in smooth-walled experiment

The bubble flow regime was observed only in the smooth-walled fracture at extremely high values of the water saturation. Due to the small fracture aperture ($130\mu\text{m}$), large gas bubbles propagate either in bullet-like or ellipse-like forms with greater longitudinal length (Figure 3.18a). As the gas flow rate increases or water flow rate decreases, gas

moves in narrow slugs and flows discontinuously when the gas rate is still relatively low as shown in Figure 3.18b. The higher pressure difference occurs mostly when a slug tries to break through the water region. Once the slug reaches the outlet of the fracture, the pressure difference decreases. This type of slug movement was seen frequently for high values of S_w . With the appearance of bubbles and slugs, the two-phase flow is fairly unstable. When the longitudinal size of slugs increases as the gas rate increases, the moving slugs tend to form stable gas channels and reach a steady condition. However, the steadiness collapses either because water breaks the thinnest throat of the short-lived channel or because of the insufficient gas supply. This causes continuous fluctuations in the saturation, fractional flow and pressure difference.

As the gas rate increases further, the short-lived channel becomes more stable. The gas channel meanders through the fracture with branches and junctions because the viscous force is insufficient to break through intermediate water islands. We define this kind of channel as a tortuous channel as shown in Figure 3.18c. The lifetime of these channels seems to depend on the complexity and meander of their structure. Some tortuous channels might exist just for a few seconds, whereas others exist for long periods. The water saturation, fractional flow, and pressure difference histories plotted in Figure 3.19 were obtained from a tortuous-channel-dominated run. Clearly, even though constant gas and water rates were injected into the fracture, the saturation fluctuates in the fracture and the instantaneous fractional flow sensed from the FFRD follows this saturation fluctuation as shown in the top plot of Figure 3.19. The corresponding pressure response was also recorded as shown in the bottom plot of Figure 3.19. Most of the peaks in these two plots are due to the collapse, reconstruction and reconfiguration of channels, and some intrusions from other minor flow structures (bubbles and slugs). It is also observed that the more tortuous the channel, the larger the pressure difference along the fracture for the same water saturation.

On the other hand, straighter channels were observed more frequently in high gas saturation and gas fractional flow situations shown in Figure 3.18d. In this situation,

almost all of the gas flows solely in a fairly straight channel, while most of the water flows above and below the gas path. Except for a small amount of immobile water inside the central gas channel, the gas path is more uniform and less tortuous in comparison with the tortuous channel flow. Three major factors may affect the morphology of gas channels. These factors are the gas fractional flow (viscous force), gas-water viscosity ratio (viscous force) and the interfacial tension (capillary force). Therefore for the same saturation, flows with the viscosity ratio closer to one or smaller interfacial tension have straighter channels.

Figure 3.20 shows a flow structure map for the experiment. The corresponding S_w is also provided in this figure. It is easy to see that the channel flow spans most of the S_w range and major bubble and gas slug flows only exist in high S_w situations. The shadowed areas in the flow maps indicate transitional flow which means the flow structure is a combination of the two neighboring structures. The transition between slug flow and channel flow is defined as unstable channel flow. In this region, some large fingering slugs were able to bridge the two ends of the fracture. However, the bridged slug collapsed in a short time due to its unstable structure, water intrusion and the insufficient gas supply. The flow structure map is similar to the flow map presented by Fourar and Bories [1995] for a glass fracture.



Figure 3.18: Photographs of flow structures in the smooth-walled fracture. Each set contains four continuous images. Gas is dark, water is light. Flow direction was from left to right.

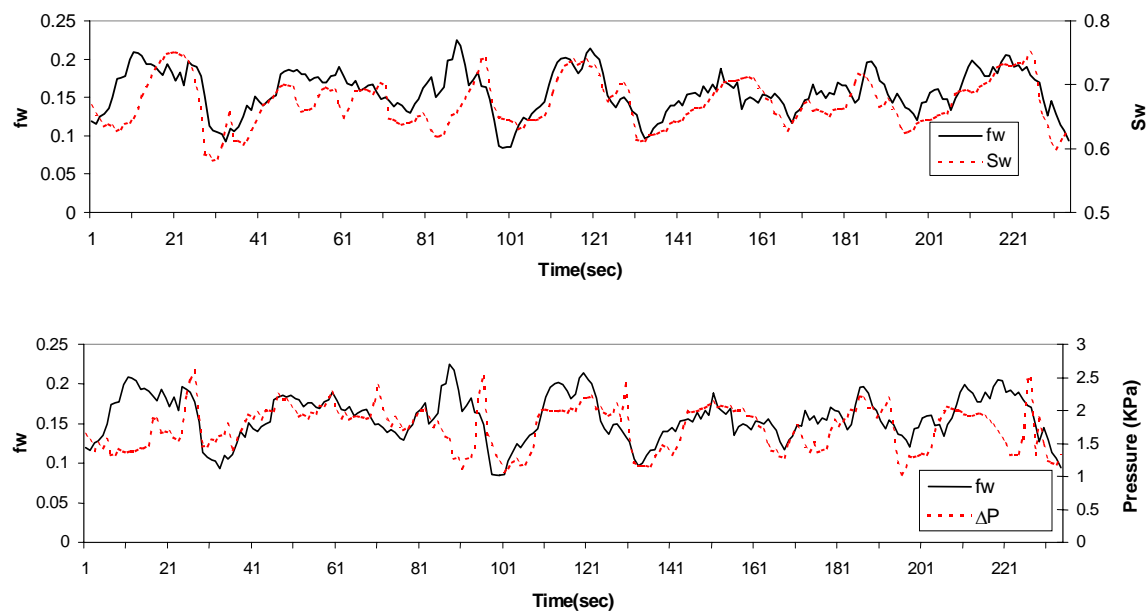


Figure 3.19: Relationship between water saturation (S_w), water fractional flow (f_w) and pressure difference along the fracture in a highly tortuous channel flow.

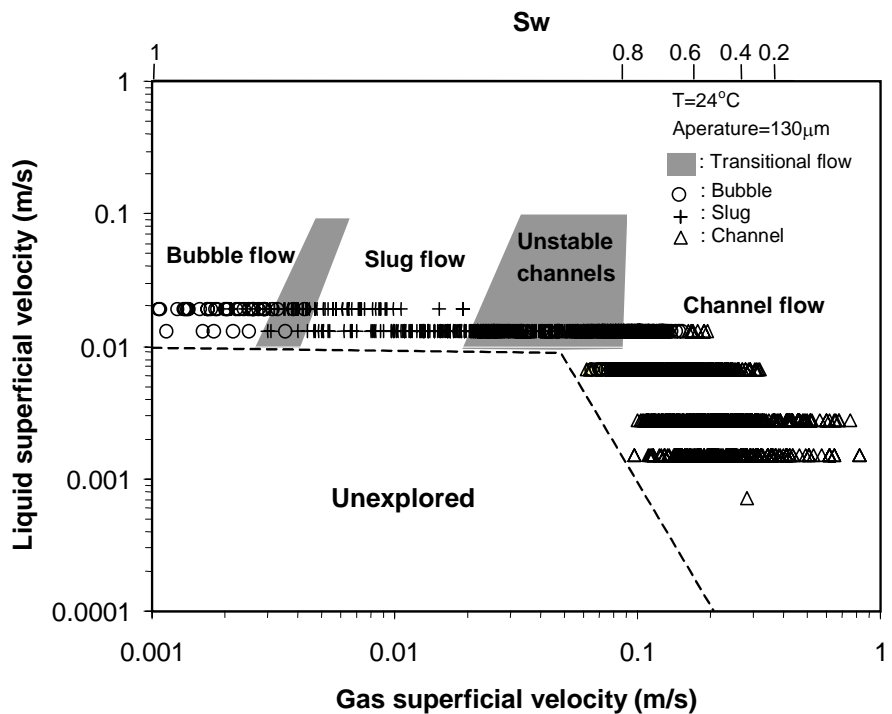


Figure 3.20: Flow structure map for air-water flow in the smooth-walled fracture.

II. Flow structures in rough-walled experiments

Figures 3.21 and 3.22 summarize several typical flow structures observed during air-water experiments in HR and RR fractures, respectively. Each set of photographs contains a sequence of four snapshots 1 second apart. The water saturation in the three sets of snap-shots of these two figures is approximately 0.85, 0.65 and 0.4. The flow is from left to right. Gas phase is dark, and liquid phase is light. Generally, air-water flow forms relatively stable structures in rough-walled fractures in comparison to the smooth-walled cases for similar S_w . The flow structures in the rough-walled fracture always behave in a more scattered, chaotic and tortuous manner, because the aperture variation tends to trap phases and increase capillary effects. Most of the trapped phase, especially the gas phase, become stationary and contributes to the immobile phase saturations.

No bubble and slug flows were observed in either rough-walled cases. Instead, intermittent gas flow behavior occurred in both HR and RR fractures at high values of S_w because some preferential flow pathways formed by the geometric configuration or entrapped gas phase, as shown in Figures 3.21a and 3.22a. This intermittent phenomenon was also observed by Su et al. [1999] who conducted liquid infiltration experiments on a transparent replica of a natural, rough-walled rock fracture. As the gas rate increases, the gas intermittent channel flow evolves into tortuous channel flow (Figures 3.21b and 3.22b). However, the gas channels in the HR case are more aggregate than the RR case in which the gas channels are multibranched. Part of these pathways are believed to correspond to relatively big aperture regions with better connectivity. This different behavior was clearer when both cases approach the end point of the water saturation (Figures 3.21c and 3.22c), where considerable amounts of immobile phases were entrapped.

Figures 3.23 and 3.24 show flow structure maps for the experiments in the HR and RR fractures. The corresponding approximate S_w is also provided in both figures. Unlike bubble and slug flows in the smooth-walled fracture, the intermittent flow occurs

in rough-walled fractures at high S_w . After short transition regions, the channel flow spans most of the S_w range similar to smooth-walled case.



Figure 3.21: Sequence of snap-shots of air-water flow behavior in HR fractures. The flow is from left to right. Gas phase is dark, liquid phase is light. Frame interval is one second.

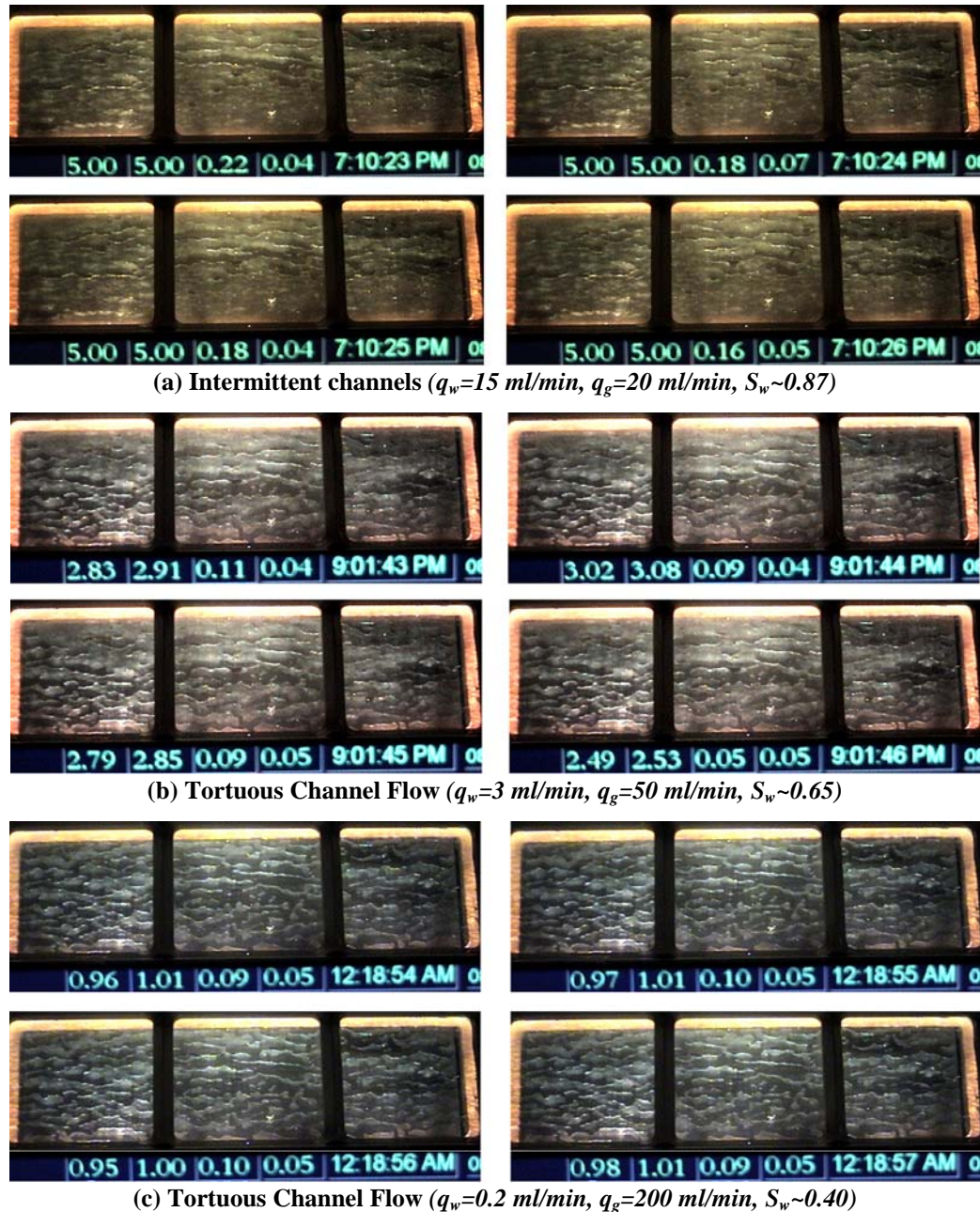


Figure 3.22: Sequence of snap-shots of air-water flow behavior in RR fractures. The flow is from left to right. Gas phase is dark, liquid phase is light. Frame interval is one second.

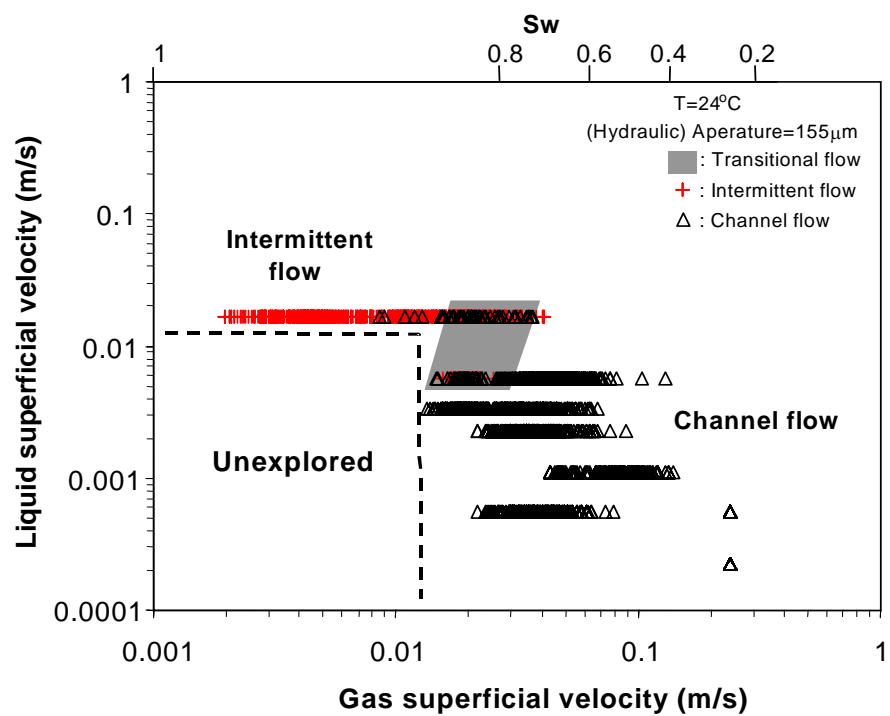


Figure 3.23: Flow structure map for air-water flow in the HR fracture.

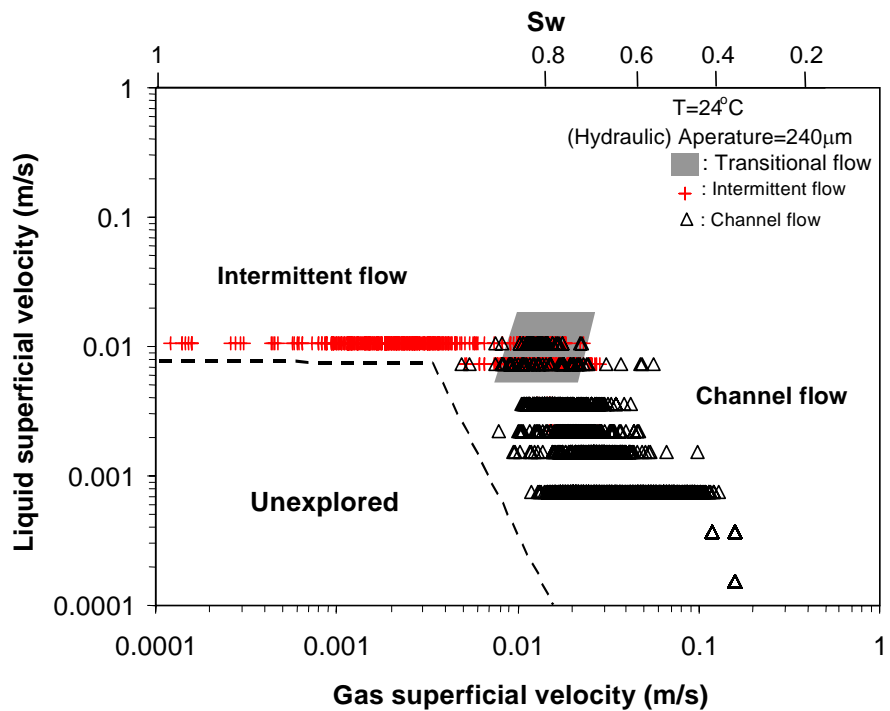


Figure 3.24: Flow structure map for air-water flow in the RR fracture.

3.3.3 Calculations of High-Resolution Relative Permeabilities

As mentioned previously, the automated high-speed data acquisition system and digital video processing enabled us to acquire the pressure, temperature, flow rates and saturation data with less than one-second frequency. The comprehensive, high-resolution relative permeabilities were calculated based on these acquired data using Equations (2.6) and (2.7) as well as the analysis procedure illustrated in Figure 3.13. Figures 3.25 to 3.27 show the comprehensive collection of air-water relative permeabilities in the smooth-walled, HR and RR fractures. Comprehensive water relative permeabilities are scattered at high water saturation owing to the slug or intermittent-channel flows and unstable-channel flows in the gas phase as shown in part a of Figures 3.18, 3.21 and 3.22.

Comparing these three provided high-resolution relative permeabilities, we found readily that the scattering decreases in the order of increasing fracture roughness (from smooth to HR to RR fractures), because of the increase of flow stability discussed previously. In the smooth-walled fracture, the vertically scattered effect observed with the gas-phase relative permeability at extremely low S_w may be associated with either the pressure fluctuation due to the moving water slugs or the difficulty in sensing the instantaneous f_w from the FFRD at low f_w . Judging from the magnitude of the scattered points associated with the corresponding flow structures provided in Figures 3.20, 3.23 and 3.24, the bubble and slug flows have highest scattering, meaning high uncertainty of measured relative permeabilities. This also reveals that the applicabilities of generalized Darcy's equations and relative permeability concepts in bubble and slug flow regimes may be questionable, despite the narrow S_w span dominated by these two types of flow. However, both regimes had no major appearance in the rough-walled fractures studied. Instead, the less unstable, intermittent flow appears at extremely high S_w . As S_w increases further, the intermittent behavior was collapsed to stable channels. This might be closer to air-water flow in natural rock fractures. Comparing water phase results with gas phase results in these three fractures, the water phase relative permeabilities always behave in a more scattered fashion than the gas phase data. This may result from two reasons. First, the unstable flows occur at a rather high S_w range that is associated with large k_{rw} and correspondingly

to small k_{rg} ; therefore, the scattering was magnified by the larger k_{rw} . Secondly, even though the dense and viscous water phase flows continuously and inertly in most S_w ranges, the instantaneous water rate was believed to vary over a small magnitude for fixed inlet water rates. Therefore, the assumption of constant water rates in the FFRD algorithm mentioned in Section 3.1.3 may generate some errors contributing to the scattering in k_{rw} .

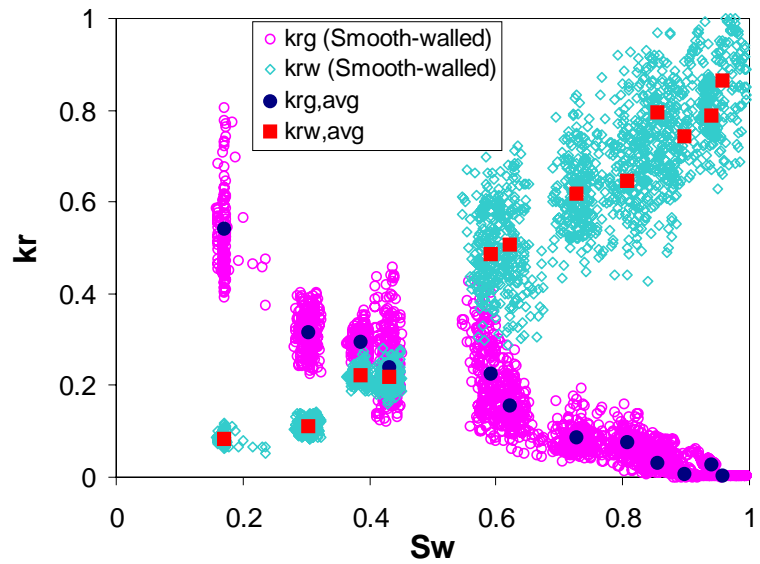


Figure 3.25: Comprehensive air-water relative permeabilities in the smooth-walled fracture calculated from Equations (2.6) and (2.7). Solid symbols are average values of each run.

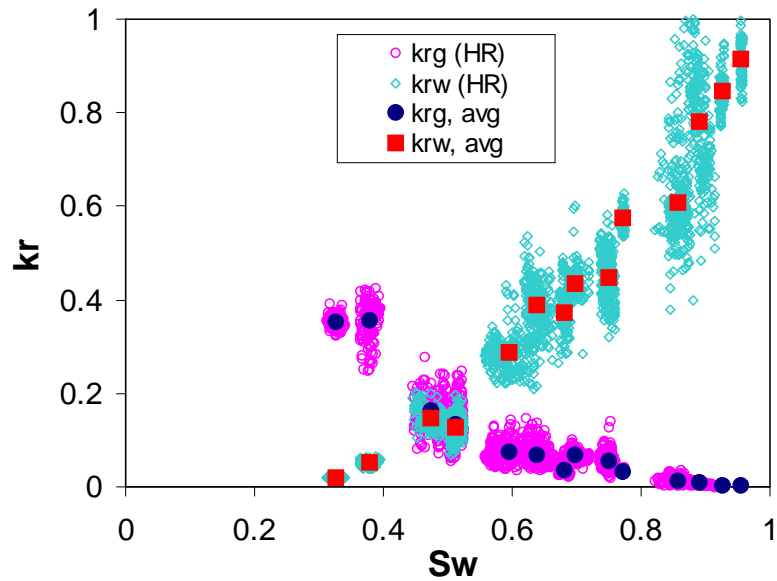


Figure 3.26: Comprehensive air-water relative permeabilities calculated from Equations (2.6) and (2.7) in the HR fracture. Solid symbols are average values of each run.

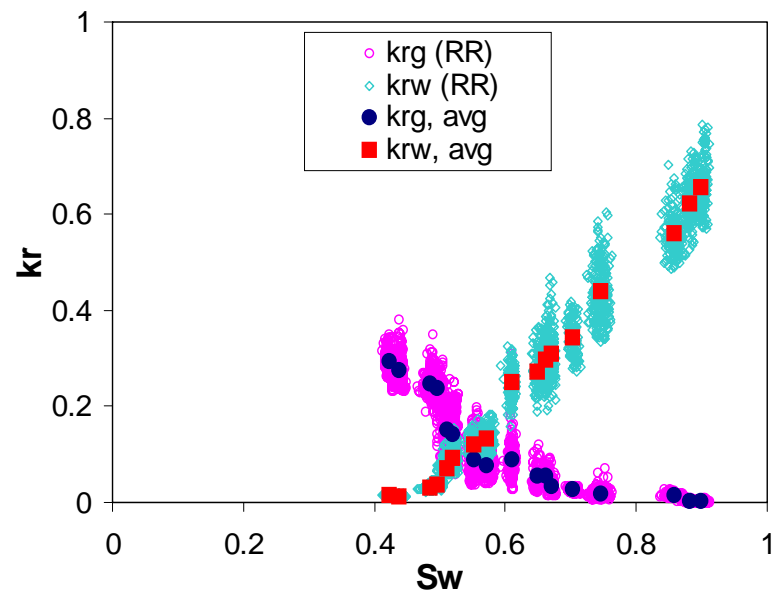


Figure 3.27: Comprehensive air-water relative permeabilities calculated from Equations (2.6) and (2.7) in the RR fracture. Solid symbols are average values of each run.

3.3.4 Average Relative Permeabilities: Prior versus Posterior

The comprehensive, high-resolution relative permeabilities allow us to access the experimental uncertainty of unsaturated flow in fractures. To our knowledge, earlier experimental investigations did not account for the effects of the unsteady nature or experimental accuracy on the corresponding relative permeabilities. Either time-average data of pressure, flow rates or saturation were used [Persoff and Pruess, 1995; Fourar et al., 1993; Fourar and Bories, 1995] or claimed representative instantaneous data were picked from whole experimental period [Diomampo, 2001] in order to calculate the relative permeabilities. In contrast to the time-averaged data, the representation of picked instantaneous data is weak and challengeable. As can be illustrated in Figures 3.25 to 3.27, significantly overestimated or underestimated air-water relative permeabilities will be obtained, if the picked data were to represent points around the upper or lower limit of the provided high-resolution relative permeabilities.

Here, we defined relative permeability values calculated from using prior time-average pressure, flow rates and saturation data as *prior* relative permeabilities, and relative permeability values obtained from averaging high-resolution relative permeabilities as *average* relative permeabilities. To examine the influence of using these two averaging techniques, Figure 3.28 compares the prior relative permeabilities with the average relative permeabilities of the smooth-walled, HR and RR fractures. The former carries no information about uncertainty and can only applied to steady-state conditions, whereas the latter enables us to calculate the standard deviation error bars of relative permeability and saturation. As shown in Figure 3.28, no significant discrepancies between these two average techniques were found in these three fractures. When the local aperture variation increases from smooth-walled fracture to HR fracture and then to RR fracture, the match of the prior results to the average results becomes better. This is due to the increase of the stability of flow structures and the subsequent decrease of the data fluctuation as shown in Figures 3.25 to 3.27. The detailed interpretation of average results is presented next with respect to surface roughness.

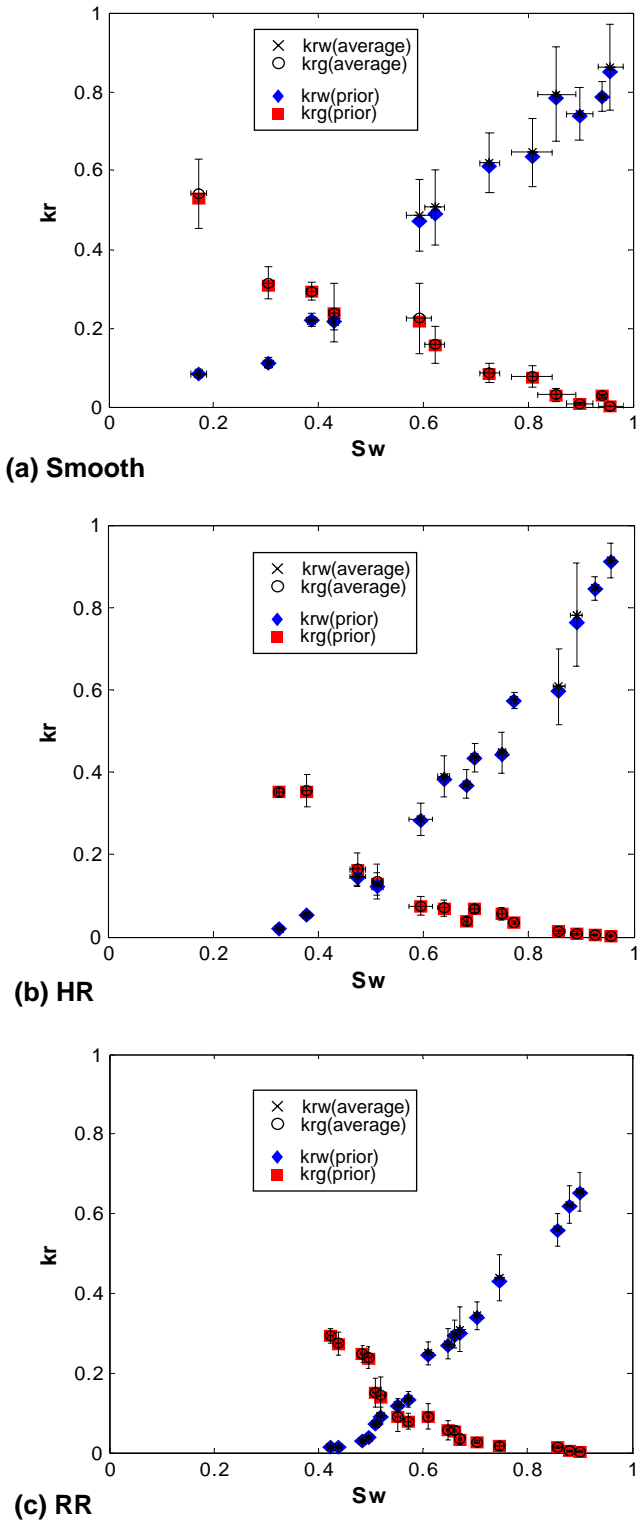


Figure 3.28: Comparison of average relative permeabilities to prior relative permeability calculated from prior time-average data: (a) smooth-walled fracture, (b) HR fracture, (c) RR fracture. The error bars mean \pm standard deviation of kr and S_w .

3.3.5 Relative Permeabilities Interpretation

I. Smooth-walled fracture

The averaged values of the relative permeabilities and the saturation with their standard deviation error bars for each pair of liquid and gas flow rates are presented in Figure 3.29. Also plotted in this figure are the curves of the X-model (Equations 2.9 and 2.10), the optimal Corey-model (Equations 2.11 and 2.12) with $S_{wr} = 0$ and $S_{gr} = 0$, and the viscous-coupling model (Equations 2.18 and 2.19). It appears that the X-model does not fit the experimental data. Although gas-phase experimental values are closer to the Corey curve, water-phase values are much higher than the water-phase Corey curve. Therefore, neither the Corey curve nor the X-curve can fit the experimental result. On the other hand, the viscous-coupling model is in good agreement with experimental results, especially for the water-phase. For the gas phase, the viscous-coupling model shows acceptable fitting, but it seems to be less accurate at high water saturation. The photographs in Figure 3.18 provide some clue about this less accurate result. At high values of S_w , most of the water channels extend from longitudinal boundaries of the fracture space and flow straighter and more continuously. On the other hand, the active gas flows as fingering slugs and channels with amorphous shapes. These changing shapes generate the corresponding pressure, saturation and flow rate changes as illustrated in Figure 3.19. The relative permeability may be affected by these changes that are not considered by the previous models (X, Corey and viscous-coupling).

One interesting feature of this relative permeability behavior is that the cross point of the water and gas curves stays slightly less than 0.5 water saturation. As one might know from traditional porous media analysis, the cross point of relative permeability curves should be located at a S_w value greater than 0.5 for a water-wet solid [Willhite, 1986]. Table 3.1 shows that both top and bottom surface of the fractures investigated can be categorized as water-wet material. This might contradict the rule of thumb from porous media. We considered this discrepancy as one exception occurring in smooth fractures. For a perfectly smooth fracture placed horizontally with negligible

gravity and buoyancy effects, ideally (but may be not practically), the wetting phase contacts the top and bottom fracture surfaces, while nonwetting phase flows in between (see Figure 3.30). The relative permeabilities can be derived by integrating Stokes' equation for each stratum, which conforms to the viscous-coupling behavior. The detailed derivation of the viscous-coupling model can be found in Ehrlich [1993]. For air-water flow in a smooth-walled fracture, our measured relative permeabilities also show similar behavior to the theoretical viscous-coupling model whose relative permeability cross point is located at a S_w value of 0.42. This may explain the deviation of the relative permeability behavior in the smooth-walled fracture from that in traditional porous media.

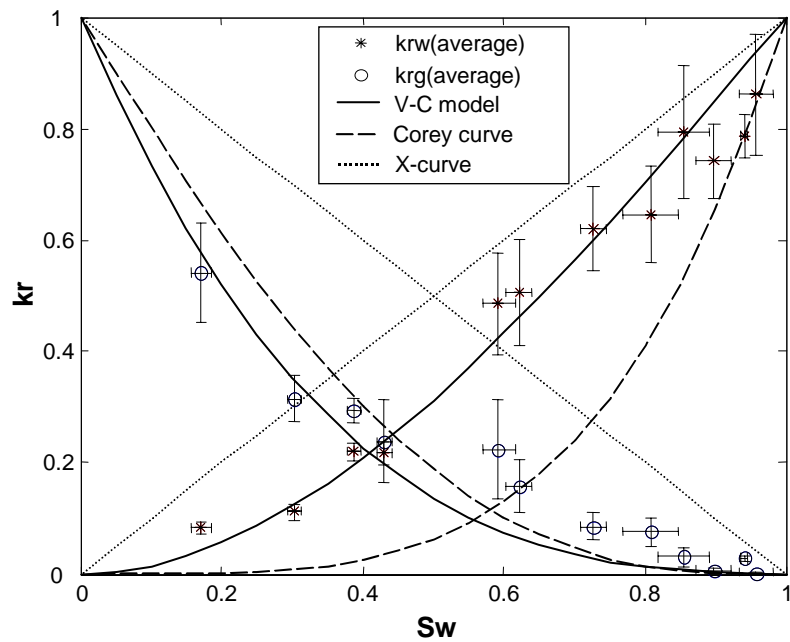


Figure 3.29: Comparison of average experimental relative permeability in the smooth-walled fracture with the Corey-curve, X-curve and viscous-coupling models. The error bars mean \pm standard deviation of kr and Sw .

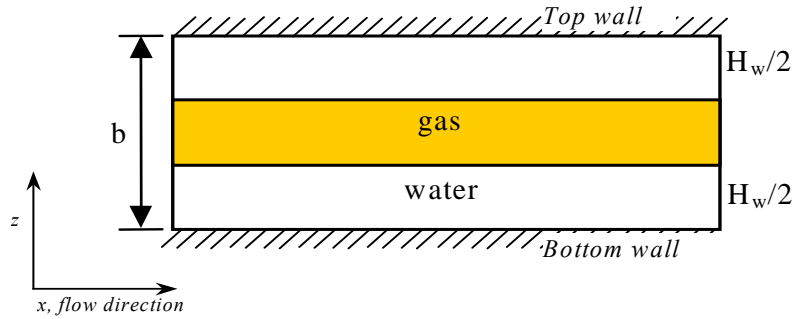


Figure 3.30: Nonwetting phase flows in between of wetting phase in an ideal smooth fracture space.

II. Rough-walled fractures

Figure 3.31 compares the average experimental relative permeability in the HR and RR fractures with the Corey-curve and viscous coupling model. Unlike the smooth-walled case, none of these models can describe both water and gas relative permeabilities satisfactorily. Even though the optimal residual water saturation was used in the Corey model, it still failed to describe the experimental results. On the other hand, the viscous coupling model models fractures as two parallel planes with a small aperture. The two fluids are flowing simultaneously and the interface is assumed to be planar. The wetting fluid is in contact with the walls, and the nonwetting fluid flows in between. The viscous coupling between fluids is derived by integrating Stokes' equation for each stratum. Therefore, it is impossible to consider the residual water saturation in this model. Nevertheless, a considerable residual water saturation (~0.25 for HR case and ~0.39 for RR case) was found during the experiments.

Figure 3.32 shows the average experimental relative permeability in all these three fractures. The gas phase relative permeabilities seem to have less effect due to the fracture roughness, whereas the water phase relative permeabilities demonstrate more phase interference and more residual water saturation when the heterogeneity and roughness of the fracture increase. Furthermore, as pointed out from Figures 3.18, 3.21, and 3.22, the surface roughness and heterogeneity have strong effects on the two-phase

flow structures, which were deemed to affect the relative permeabilities. These inspired the work of a flow-structure model for the relative permeabilities in fractures, described in the next chapter.

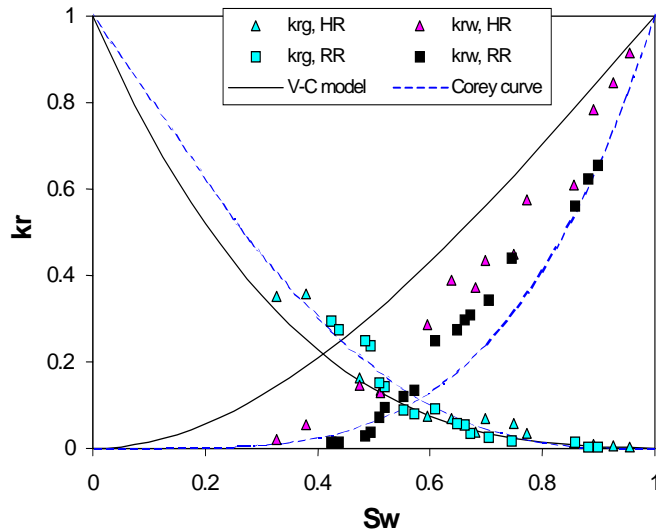


Figure 3.31: Comparison of average experimental relative permeability in the rough-walled fractures with the Corey-curve and viscous-coupling models.

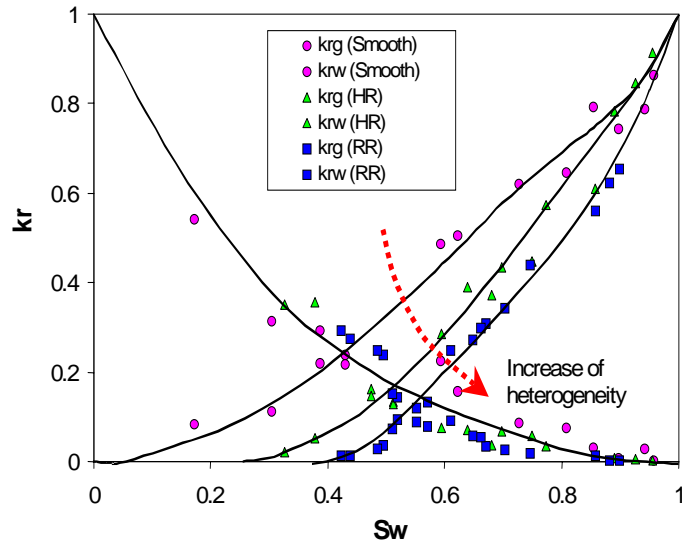


Figure 3.32: Plot of average experimental relative permeability in the smooth-walled and rough-walled fractures and their approximate trends.

3.4 Chapter Summary

In this chapter, we described an experimental apparatus that was built to capture the unstable nature of the fractures and display the flow structures under different flow configurations in real time. Three fractures with distinct roughness, smooth, homogeneously rough and randomly rough, were studied for two-phase flow structures and relative permeabilities. Different flow configurations were visualized from the three fractures investigated: bubbles, slugs or intermittent flow and channels. The channel flow was observed to be the major flow structure in the fractures investigated.

Experimental results of pressure drop, flow rates, and saturation were interpreted by using the relative permeability concept, and the air-water relative permeability obtained from experiment show deviation from models suggested by earlier studies. Although of the three models considered the theoretical viscous-coupling model provides the best estimate of the air-water relative permeabilities in the smooth-walled fracture, this model performs poorly in representing the relative permeabilities from rough-walled fractures. Moreover, the viscous coupling model does not take into account the real flow structures and hence is a poor physical representation of the actual flow behavior occurring in the fracture space. Based on these discoveries, a new approach accounting for the effects of flow structures was developed, as described in the next chapter.

Chapter 4

A Flow-Structure Model for Two-Phase Relative Permeabilities in Fractures

In this chapter, we describe a new approach that was developed to describe the two-phase relative permeability behavior in the smooth-walled and rough-walled fractures based on the two-phase flow structures. This approach lumps the microscale physical mechanism (viscous and capillary forces) into an apparent observable parameter, *channel tortuosity*, which was found to dominate the reduction of the relative permeabilities from the values that would be expected based on the X-curve. The artificial fractures used in Chapter 3, smooth-walled, homogeneously rough-walled (HR) and randomly rough-walled (RR) fractures, were studied to represent distinct surface geometry and heterogeneity. The experimental results from Chapter 3 were used to verify this model.

4.1 Motivation

The diversity and variability of the geometry of a single, natural fracture and the complexity of the two-phase interaction and interference have made it difficult to reach a unique and accurate model to describe the two-phase flow behavior by means of the relative permeability concept. Pruess and Tsang [1990] used a conceptual and numerical model to solve for relative permeabilities on a 20x20 grid representing rough fractures.

The void space of real rough-walled fractures was conceptualized as two log-normal aperture distributions with short-range isotropic spatial correlation and longer-range anisotropic spatial correlation in the flow direction. Pruess and Tsang modeled the fractures as a two-dimensional heterogeneous porous medium and assumed that grid block occupancy was dependent only on the capillary pressure of the block. The phase occupancy and permeability were derived by assuming a parallel-plate model for small subregions in the fracture plane. The numerical results of these two cases are shown in Figure 4.1. For short-range correlation almost no multiphase flow occurred since the nonwetting phase relative permeabilities remain zero when the nonwetting phase saturation is smaller than 84%. For longer-range anisotropic spatial correlation in the flow direction, the two-phase flow regime increases. Although their nonwetting phase relative permeabilities and those from earlier experimental studies are less alike, the wetting phase relative permeabilities did follow a conventional pattern and could be approximated as a power law function of saturation (Corey-like).

With the development of the visualization and surface measurement techniques, it has become possible to observe multiphase flow behavior dynamically and to quantify the geometrical heterogeneity in fracture space [Nicholl and Glass, 1994; Pan et al., 1996; Persoff and Pruss, 1995; Su et al. 1999]. In Chapter 3, Figures 3.20 to 3.24 show that the channel flow was the dominant flow structure in the experiments of this work. We might expect at first that these flows would be described by the X-model; however they behave considerably differently from the conceptual configuration that underlies the X-model. This is explained by characterizing the morphology of phase channels and quantifying the magnitude of the “tortuosity” in this flow structure. A new approach is discussed here to include the tortuosity created by the phases.

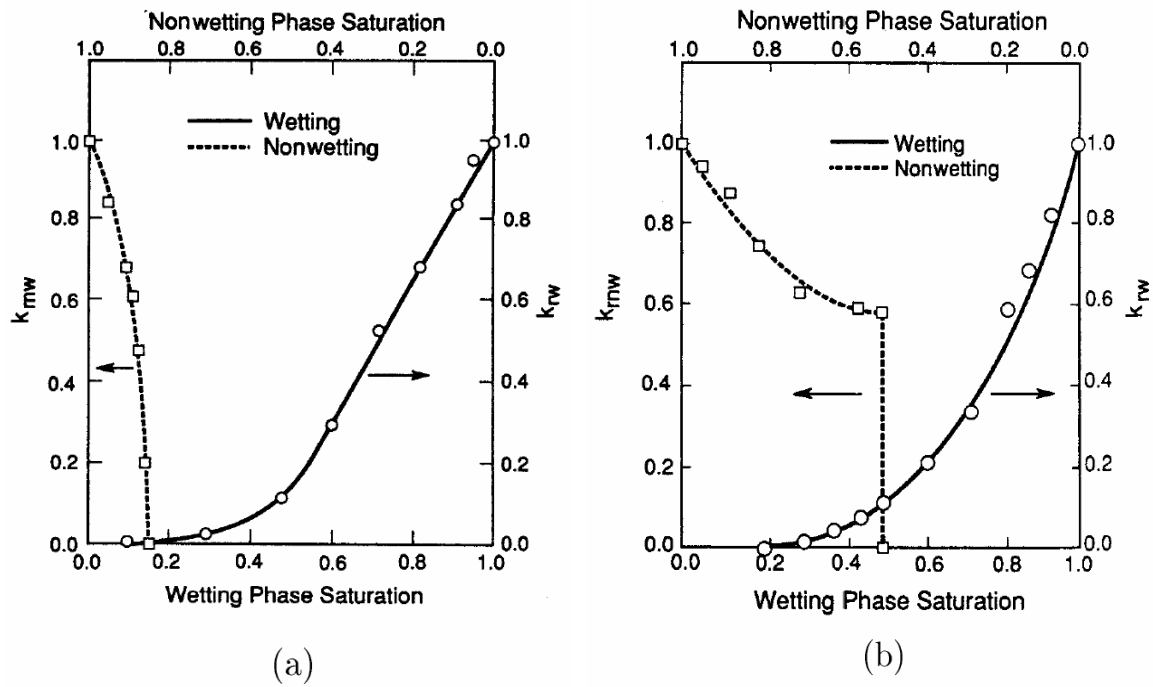


Figure 4.1: From Pruess and Tsang [1990]. Simulated relative permeabilities for the lognormal aperture distribution of (a) short-range isotropic spatial correlation (percolation like behavior; no multiphase flow) and (b) longer-range anisotropic spatial correlation in the flow direction.

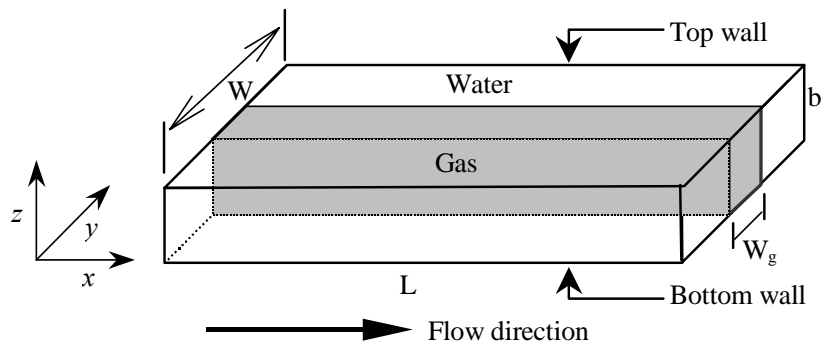


Figure 4.2: A simple model of a straight gas channel in a smooth-walled fracture.

Considering a simplified fracture space with a dimension of L (length) \times W (width) \times b (aperture) as shown in Figure 4.2, the fluids, water and gas, form ideal and straight channels through the fracture. From fundamentals of multiphase flow, the X-curve behavior is derived readily from Darcy's law and the cubic law by assuming negligible capillary pressure, gas slippage, inertia effect and wetting-phase stratified flow.

Consequently, a straight phase-channel in a smooth-walled fracture will yield the X-curve relative permeability as shown by Romm [1966]. However, as shown in this study, the actual flow structures in fractures seldom reach the ideal straight channel even though the fracture is smooth-walled. Most of the flow structures are either fingering or tortuous channels instead, and the relative permeability obtained from our experiments shows a deviation from the X-curve as presented earlier in Figures 3.29 and 3.31. As a result, a physical, tortuous-channel approach is required to modify the X-curve and take into account the channel tortuosity.

Nicholl et al. [2000] studied the effect of the immobile phase on the flowing-phase relative permeability in the satiated condition ($S_w = S_{wr}$) and developed a conceptual model for flowing-phase relative permeability by using the effective medium approach suggested by Zimmerman and Bodvarsson [1996]. In the conceptual model of Nicholl et al. [2000], an in-place tortuosity induced by the immobile phase was used as a correction term to decrease the effective hydraulic gradient. The flowing-phase (water) relative permeability is then obtained as:

$$k_{rw} = S_w \tau_{ip} \underbrace{\left[\frac{\langle b_f \rangle^2}{\langle b \rangle^2} \right]}_A \left[\left(1 + \frac{9\sigma_b^2}{\langle b \rangle^2} \right)^{1/2} \left(1 + \frac{9\sigma_{bf}^2}{\langle b_f \rangle^2} \right)^{-1/2} \right] \quad (4.1)$$

where k_{rw} and S_w are the wetting-phase (water) relative permeability and saturation respectively, $\langle b \rangle$ and σ_b^2 are the mean and variance of the aperture field, the subscript (f)

refers to parameters for the region occupied by the flowing phase, and τ_{ip} (range from 0 to 1) is the in-place tortuosity. From the definition of Nicholl et al., the smaller the value of τ_{ip} , the more tortuous the flowing phase structure behaves. The data used were from experiments conducted in the satiated condition [Nicholl and Glass, 1994]. Nonwetting (air) phase remained entrapped. Nonwetting phase relative permeability was therefore always zero. The wetting phase relative permeability is shown in Figure 4.3. From the experimental data, Nicholl et al. [2000] concluded that the in-place tortuosity is the dominant factor controlling the flowing phase relative permeability. However, the in-place tortuosity could not be measured in their study. Instead, in-place tortuosity was estimated independently by further simulating flow on the measured phase geometries under some simplified assumptions. In the next section, we will suggest a simple method to evaluate the tortuosity induced by phases and develop a new approach, called the Tortuous Channel approach (TCA), to describe two-phase relative permeabilities in fractures.

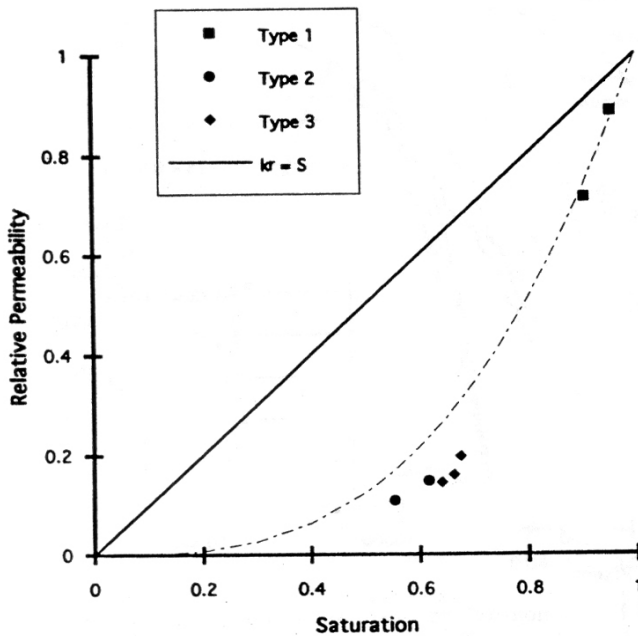


Figure 4.3: Modified from Nicholl and Glass [1994]. Wetting phase relative permeabilities as function of wetting phase saturation in satiated condition.

4.2 Model Description

The concept of the tortuous-channel approach (TCA) is based on the relationship between the fluid tortuosity and the relative permeability. As the channel flow observed in our study is tortuous (Figures 3.21 and 3.22), we define a tortuosity coefficient for the channel flow, τ_c , to characterize its morphology. The definition of this apparent parameter is based on the area of the channel and the smallest bounding rectangle that covers the whole channel for a specific phase. As shown in Figure 4.4, the binary images processed from continuous true-color images were input into another image-processing program, which allows recognition and separation of the different flow structures. Then, the channel area, A_c (unit: pixel²), length and width of the smallest bounding box, L_x and L_y (unit: pixel), were computed. The channel tortuosities for gas and water are then defined as:

$$\tau_{c,g} = \left(\frac{L_x L_y}{A_c} \right)_g \quad \text{and} \quad \tau_{c,w} = \left(\frac{L_x L_y}{A_c} \right)_w \quad (4.2)$$

For multiple channels, volume-weighted averaging was used to calculate average τ_c . The coefficient τ_c for each phase varies between 1 and ∞ . This coefficient is related to the interfacial area and, consequently, allows quantifying the shear stress at the interface between the two fluids.

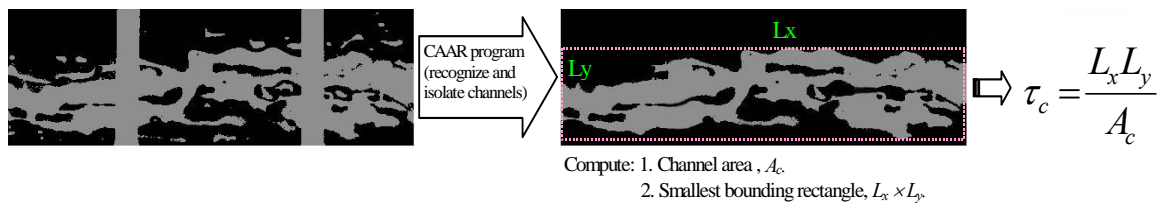


Figure 4.4: Illustration of channel tortuosity algorithm.

It is worth noting that because of the different definitions of the tortuosity, the variables $\tau_{c,w}$ in Equation (4.2) and τ_{ip} in Equation (4.1) should be close to reciprocal. Therefore, for smooth-walled fractures ($\langle b \rangle = \langle b_f \rangle$ and $\sigma_b^2 = \sigma_{bf}^2$), and Equation (4.1) can be simplified to:

$$k_{rw} = \frac{S_w}{\tau_{c,w}} \quad (4.3)$$

Using the same analog, the gas relative permeability can be expressed by:

$$k_{rg} = \frac{S_g}{\tau_{c,g}} \quad (4.4)$$

This relationship implies that the channel tortuosity is directly proportional to the deviation from X-curve behavior. In the case where each phase flows in the form of homogeneous strata (no dispersed phase), $\tau_{cw} = 1$ and $\tau_{cg} = 1$ and Equations (4.3) and (4.4) reduce to the X-model.

For the drainage relative permeabilities in rough-walled fractures, a major factor that was not considered in Equations (4.3) and (4.4) was the residual water, which was observed to be negligible in the smooth-walled case. The significant capillary force due to local aperture field variation can entrap considerable amounts of water phase, and ultimately some of it will contribute to the residual water saturation (S_{wr}). To this end, a more rigorous approach by separating different phase structures was developed. Figure 4.5 illustrates the principle and concepts of this rough-walled tortuous channel approach. The two-phase flow structures were separated into three major parts, namely the flowing channels, the entrapped phases and the water film flowing along the fracture surfaces. During the steady-state drainage process, the first two parts were fully or partially included in the channel tortuosity terms, except for the considerable immobile and residual water phase. In analogy to earlier studies of relative permeability modeling in porous media [Corey, 1954; Brooks and Corey, 1966; van Genuchten, 1980], the

immobile and residual phases were taken into account by normalizing the water saturation. For the drainage process, the normalized water saturation is:

$$S_w^* = \frac{S_w - S_{wr}}{1 - S_{wr}} \quad (4.5)$$

where subscript (r) refers to residual saturation.

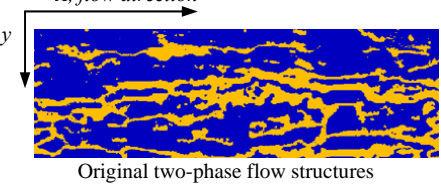
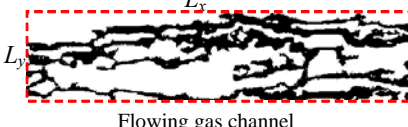
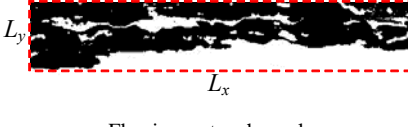
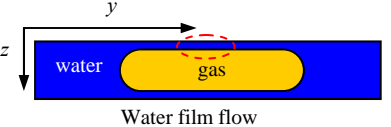
	Separated structures (in dark color)	Major impact	Included terms
	 Flowing gas channel	<ul style="list-style-type: none"> • Gas rates • Gas tortuosity 	$\tau_{c,g}$
	Entrapped gas phase	<ul style="list-style-type: none"> • Water tortuosity 	$\tau_{c,w}$
	Flowing water channel	<ul style="list-style-type: none"> • Water rates • Water tortuosity 	$\tau_{c,w}$
	Entrapped water phase	<ul style="list-style-type: none"> • Gas tortuosity • Immobile water saturation 	$\tau_{c,g}$ S_{wr}
	Water film flow	<ul style="list-style-type: none"> • Gas rates • Water rates 	F_m

Figure 4.5: Illustration of separating the two-phase flow structures and the major impact parameters in each separated structure considered in the rough-walled TCA for the drainage process.

Regarding the water film flow along the fracture surfaces, an extended two-dimensional viscous coupling model was used to evaluate the effect of film thickness on relative permeabilities. The one-dimensional viscous coupling model obtained by integrating Stoke's equations under a parallel-plate assumption was described previously in Equations (2.18) and (2.19). Because the one-dimensional viscous coupling model has poor representation of the real two-phase flow behaviors in fractures, the simplified but more practical geometrical consideration of the drainage process in an ideal fracture space is shown in Figure 4.6. The gas channel was initially assumed to be in a round-ended rectangular column with constant column height ($b-H_w$), which is close to but always smaller than the fracture aperture, b . The relative permeability was computed by using either the superposition or integration of the one-dimensional solution in each vertical slice as shown in Figure 4.6. After the gas channel reaches the fracture boundaries (Stage 2), the gas phase starts to expand vertically and the corresponding relative permeability approximately follows one-dimensional viscous coupling in Stage 3.

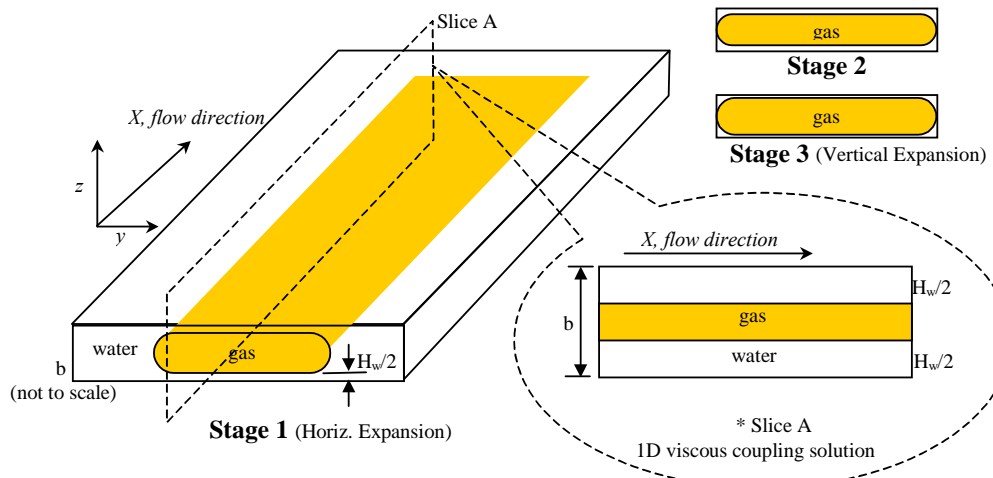


Figure 4.6: A simple superposition method for integrating one-dimensional viscous coupling model to two-dimensional viscous coupling model. The water film thickness, H_w , was assumed being constant during stage 1 and 2. After Stage 2, the H_w starts decreasing and the corresponding relative permeabilities approximately follows one-dimensional viscous coupling. (b and H_w are not to scale)

By setting different values of the water film ratio, H_w/b , and assuming the fracture width was much larger than its aperture, the effect of water film thickness on air-water relative permeabilities is shown in Figure 4.7. The water film ratio affects the relative permeabilities almost linearly because the scale of the fracture aperture is relatively small. In addition, the effect on gas-phase relative permeabilities is stronger than on the water phase. Consequently, film flow correctors, F_{mw} and F_{mg} , were suggested as corrections to the relative permeabilities to account for the water film flow. Combining all factors in Figure 4.5, the modified TCA for describing the relative permeabilities of smooth or rough fractures can be written in the following form:

$$k_{rw} = \frac{S_w^*}{\tau_{c,w}} F_{mw} \quad (4.6)$$

$$k_{rg} = \frac{S_g}{\tau_{c,g}} F_{mg} \quad (4.7)$$

Comparing Equation (4.6) to Equation (4.1) and examining the definition of the channel tortuosities, we can see that part A in Equation (4.1) has inherently contributed to the coefficients of $\tau_{c,w}$, and S_w^* .

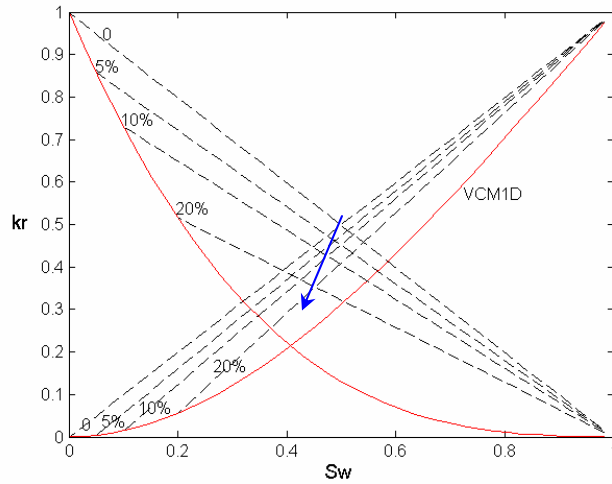


Figure 4.7: Effect of water film thickness on air-water relative permeabilities. VCM1D is the one-dimensional viscous coupling model. The percentage means the water film ratio (H_w/b).

Generally, the water film on partially saturated rock fracture surfaces is attributed to adsorptive forces on flat surfaces of minerals or by capillary effects within the surface roughness. The matric potential is the major parameter that controls the thickness of the film. By considering the fracture-matrix interaction in fractured porous media, Tokunaga and Wan [1997] measured average surface film thickness ranging from 2 to 70 μm . On the other hand, Rossen and Kumar [1994] suggested that wetting film flow in natural fractures only provides a small amount of conductivity, and therefore its effects on relative permeability is insignificant. Moreover, for a single fracture with an impermeable matrix as in our cases, earlier studies indicated that the water film ratio was less than 1% [Romm, 1966; Pan et al., 1996] for smooth-walled fractures. However, this ratio may increase for the rough-walled fractures since surface roughness and pits on the surface increase capillary and absorption forces. To the best of our knowledge, no practical methods exist to estimate the H_w in accordance with different surface geometry for a single fracture with impermeable surfaces.

Nevertheless, Bretherton [1961] analyzed the motion of long bubbles and computed the thickness of the liquid film between the bubble and the capillary wall (h_∞) theoretically. For a very long bubble, Bretherton found that h_∞ depends on the dimensionless capillary number of the liquid phase (Ca) when $Ca \leq 10^{-2}$:

$$\frac{h_\infty}{R} = 0.643(3Ca)^{2/3} \quad (4.8)$$

where Ca is defined by

$$Ca = \frac{\mu_w u_w}{\sigma} \quad (4.9)$$

Here R is the radius of the capillary tube, σ is the interfacial tension between the bubble and the suspending liquid. Later study has proved that Equation (4.8) applies for bubbles with infinite length down to bubbles with volumes as small as $0.95(4\pi/3)R^3$ [Olbricht, 1996]. Therefore, we can use Equation (4.8) to evaluate the order of the magnitude of the film ratio in current study. Wong et al. [1995a] extended the circular capillaries to polygonal capillaries with different aspect ratios. In parallel-plate fractures, the analytical solutions from Wong et al. [1995a] suggested that Equation (4.8) can be written approximately as:

$$\frac{H_w}{b} = 0.643(3Ca)^{2/3} \quad (4.10)$$

From the flow map of the smooth-walled fracture in Figure 3.20, the order of magnitude of u_w in the experiments of current study ranges from 0.02 to 0.001 m/sec; thus Ca is from 2.78×10^{-4} to 1.39×10^{-5} . Substituting this into Equation (4.10), the H_w/b is from 5.7×10^{-3} to 7.73×10^{-4} , which has insignificant effect on the relative permeability as shown in Figure 4.7. However, the film ratio may increase for the rough-walled fractures.

Judging from this theoretical evaluation and from the studies by Romm [1966] and Rossen and Kumar [1994], the water film ratio should be small and F_m should be close to one for the fractures considered in this work. Following this result, Equations (4.6) and (4.7) may be further simplified to:

$$k_{rw} = \frac{S_w^*}{\tau_{c,w}} \quad (4.11)$$

$$k_{rg} = \frac{S_g}{\tau_{c,g}} \quad (4.12)$$

In these simple equations, only two measurable parameters are needed. The residual saturation is obtained readily in the laboratory; however, the channel tortuosity has to be obtained by the aid of tomography or visualization techniques during two-phase flow experiments, unless some correlation between channel tortuosities and fracture geometry can be developed to predict the channel tortuosity. To this end, experimental results in Chapter 3 were used to explore this issue and verify as well as to generalize this approach.

4.3 Channel Tortuosity in Fractures

First, thousands of continuous images extracted from the video of the experiments in Chapter 3 with a period less than or equal to 1 second were analyzed, and the tortuosities of gas and water were deduced for the channel flow configuration. Illustrations of these calculations are presented in Figure 4.8, which shows images extracted from the smooth-walled experiments. It appears that water channels are less tortuous than gas channels. This may be due to the fact that the water-viscosity is higher than the gas-viscosity, and that water channels tend to adhere to longitudinal boundaries of the fracture, while gas channels flow in between.

The computer code “*CAAR*” (Channels Aspect and Area Recognition) was written to recognize phase channels and compute corresponding tortuosity automatically for images from air-water experiment through the smooth-walled, HR and RR fractures. Figure 4.9 shows several representative images extracted from these three experiments as well as the smooth-walled images. Snapshots in each row in Figure 4.9 have similar water saturation but are from different types of fractures. Clearly, the channel tortuosity increases when the heterogeneity of the fracture surface increases. The phase channels in RR fracture are always the most tortuous among these three cases. In general, for a specific fracture, the channel tortuosity of one phase has a countertrend to the saturation of that phase. In other words, the water (gas) channel tortuosity increases when the water (gas) saturation decreases. With increasing surface heterogeneity, the nested behavior of flow structures was increasingly apparent. Even though the flow structures were destroyed before changing the input rates, the gas phase had some stationary preferential pathways in the rough fractures, particularly in the RR fracture. When the gas saturation increased further, the gas channels expanded from these base pathways or branched from them. This behavior may demonstrate the likely flow structure evolution in natural fractures.

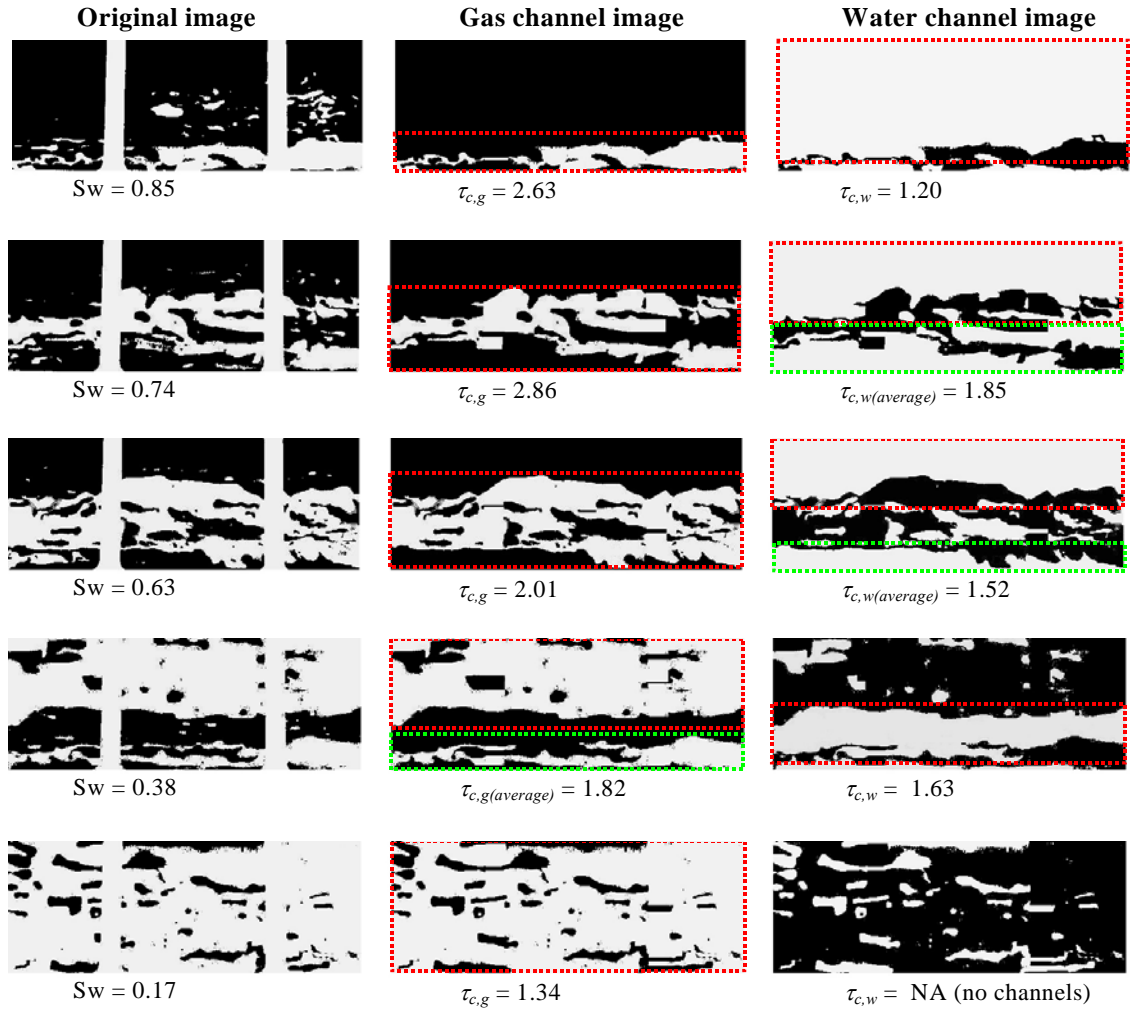


Figure 4.8: Representative images and corresponding processed gas-channel and water-channel images extracted from air-water experiment through the smooth-walled fracture. (In the original images, gas is white and water is black; in the phase channel images, the phase interested is in white. Rectangles indicate the bounding boxes of the phase channels.)

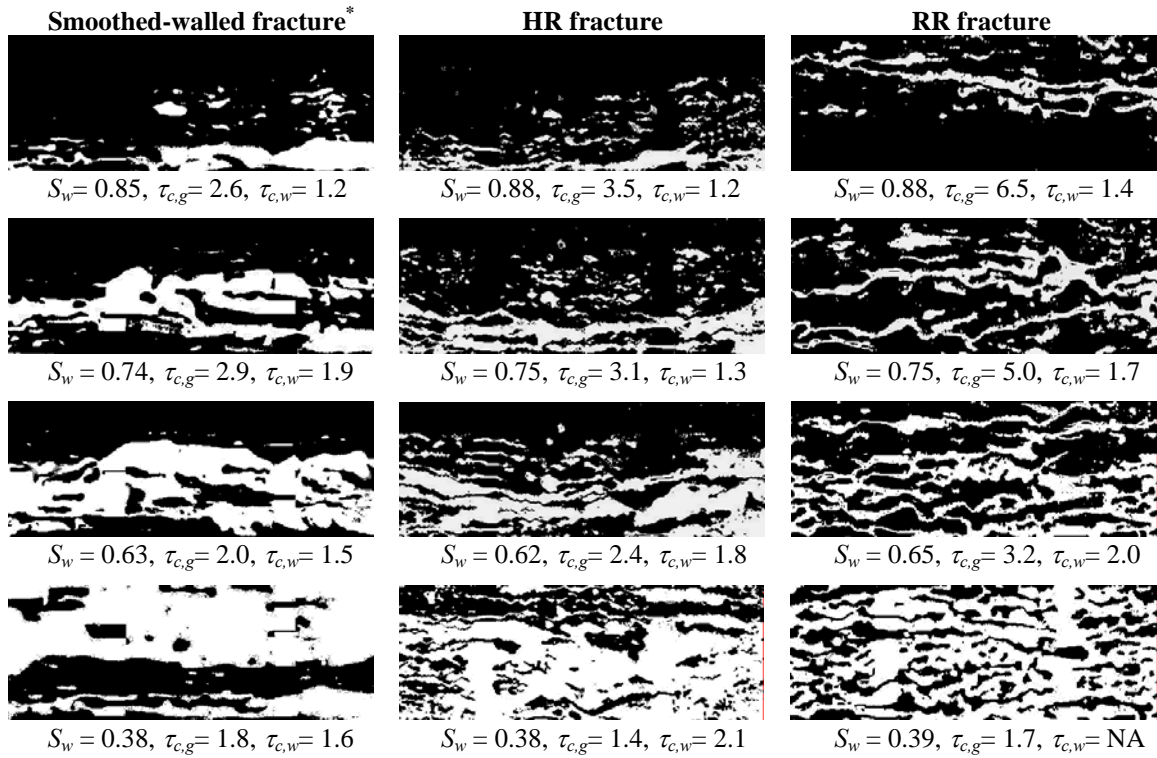


Figure 4.9: Comparison of representative processed of channel recognition for the smooth and rough fractures and corresponding channel tortuosities evaluated (Gas phase is white and water is black).

4.4 Reproduction of Relative Permeabilities

After analyzing thousands of images, the channel tortuosities of each phase were evaluated, and then the relative permeabilities were computed using the proposed approach in Equations (4.11) and (4.12).

I. Relative permeability in smooth-walled fracture

By deducing both water and gas tortuosities from the air-water flow images in the smooth-walled fracture, the comprehensive water-phase and gas-phase relative permeabilities obtained from Equations (4.11) and (4.12) are shown in Figure 4.10. The original experimental results (Figure 3.25) are also provided in this figure. The results from the tortuous-channel approach show good reproduction of the experimental results in both water and gas phases. Thus, the tortuous-channel approach leads to low scatter in comparison with the experimental relative permeabilities. This is because some unstable phenomena, bubbles and slugs, were excluded and there are almost no sources of measurement errors in the tortuous-channel approach, except for the image processing errors.

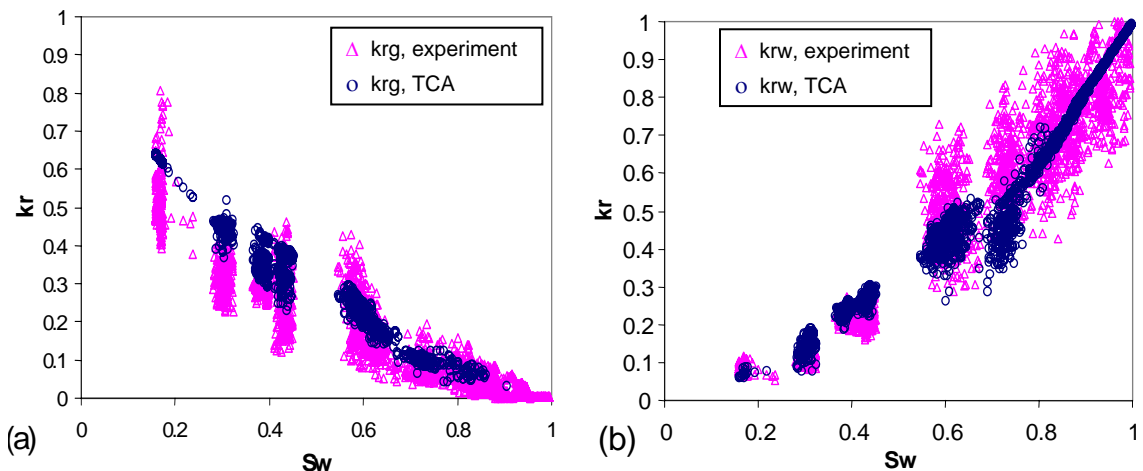


Figure 4.10: Relative permeabilities for the smooth-walled fracture from tortuous-channel approach using phase tortuosities obtained from the processing of continuous images and its comparison with the original result: (a) gas phase, (b) water phase.

The mean tortuosity of gas and water channels was then computed by averaging all tortuosities in each run. Table 4.1 presents the mean channel tortuosity in each run for the experiments as well as the relative permeabilities from the experiment and the suggested approach. From Table 4.1, it is evident that the greater the phase saturation, the less tortuously those phase channels exhibit. The relative permeabilities calculated by using the average tortuosity in Table 4.1 and Equations (4.11) and (4.12) are presented in Figure 4.11 (the square and diamond symbols). They are in a good agreement with average experimental relative permeabilities for both gas and water phases. Aside from generally matching performance, the tortuous-channel approach not only approximates the experimental result but also closely reproduces some experimental points, especially the portion where the viscous-coupling model performs poorly.

Table 4.1: Averages of tortuous-channel parameter obtained from CAAR image processing program and the relative permeability values for the tortuous-channel approach and experiment.

Saturation		Average channel tortuosities		Experiment results		Tortuous-channel approach	
S_w	S_g	$\tau_{c,g}$	$\tau_{c,w}$	$krg_{,expe}$	$krw_{,expe}$	$krg_{,T-C}$	$krw_{,T-C}$
0.957	0.043	NA*	1.038	0.002	0.863	NA	0.922
0.941	0.059	NA	1.065	0.028	0.788	NA	0.884
0.897	0.103	2.476	1.098	0.007	0.743	0.041	0.817
0.854	0.146	2.600	1.143	0.030	0.794	0.056	0.747
0.807	0.193	2.771	1.246	0.077	0.646	0.069	0.648
0.726	0.274	2.797	1.610	0.086	0.619	0.098	0.451
0.622	0.378	2.033	1.434	0.158	0.506	0.186	0.434
0.592	0.408	1.699	1.437	0.225	0.487	0.240	0.412
0.430	0.570	1.702	1.540	0.239	0.217	0.335	0.279
0.387	0.613	1.746	1.639	0.294	0.221	0.351	0.236
0.304	0.696	1.583	2.051	0.315	0.112	0.440	0.148
0.171	0.829	1.337	2.464	0.541	0.083	0.620	0.069

*: No channel detected.

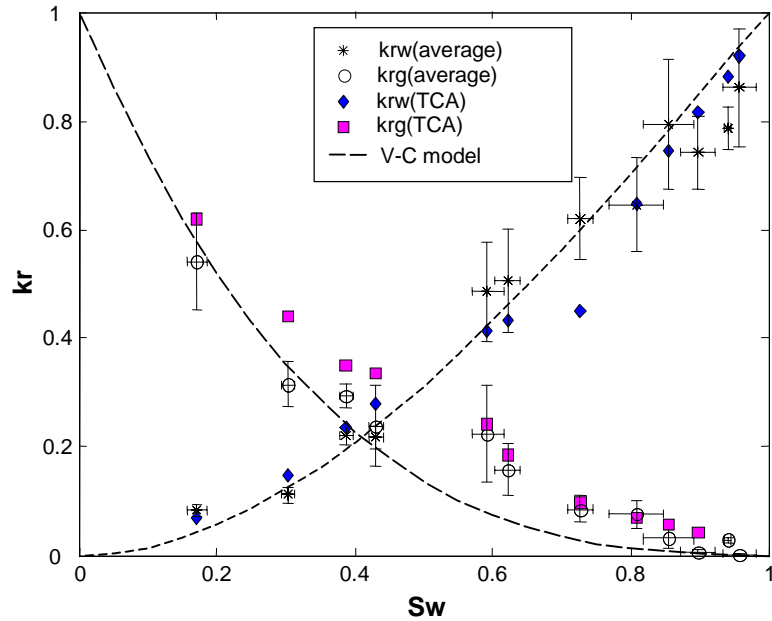


Figure 4.11: Comparison of the experimental relative permeability with the tortuous-channel approach (averaging from Figure 4.10) and viscous-coupling model for the air-water experiment in the smooth-walled fracture.

II. Relative permeability in rough-walled fractures

Figures 4.12 and 4.13 compare the relative permeabilities computed from TCA to the reference experimental relative permeabilities from the generalized Darcy equations for the RR and FR fractures respectively. Due to the unstable nature of the flow, the experimental relative permeabilities are scattered. For the RR fracture, the result from TCA fits the experimental result with good accuracy. The gas-phase relative permeabilities seem to be overestimated slightly. Close agreement was also obtained in the HR fracture case. However, the gas-phase values from TCA were larger than the experimental result. The overestimation in gas-phase relative permeability may be attributed to the water film flow effect as demonstrated in the previous section (but neglected in the current study), or the experimental and image processing errors. The major source of the image processing errors was from the recognition of the channel connectivity, particularly for the rough-walled fractures. Because of the local aperture

variation, some phase channels were connected via thin threads that were too narrow to be recognized in the images in a few cases. This led to the less accurate calculation of tortuosity.

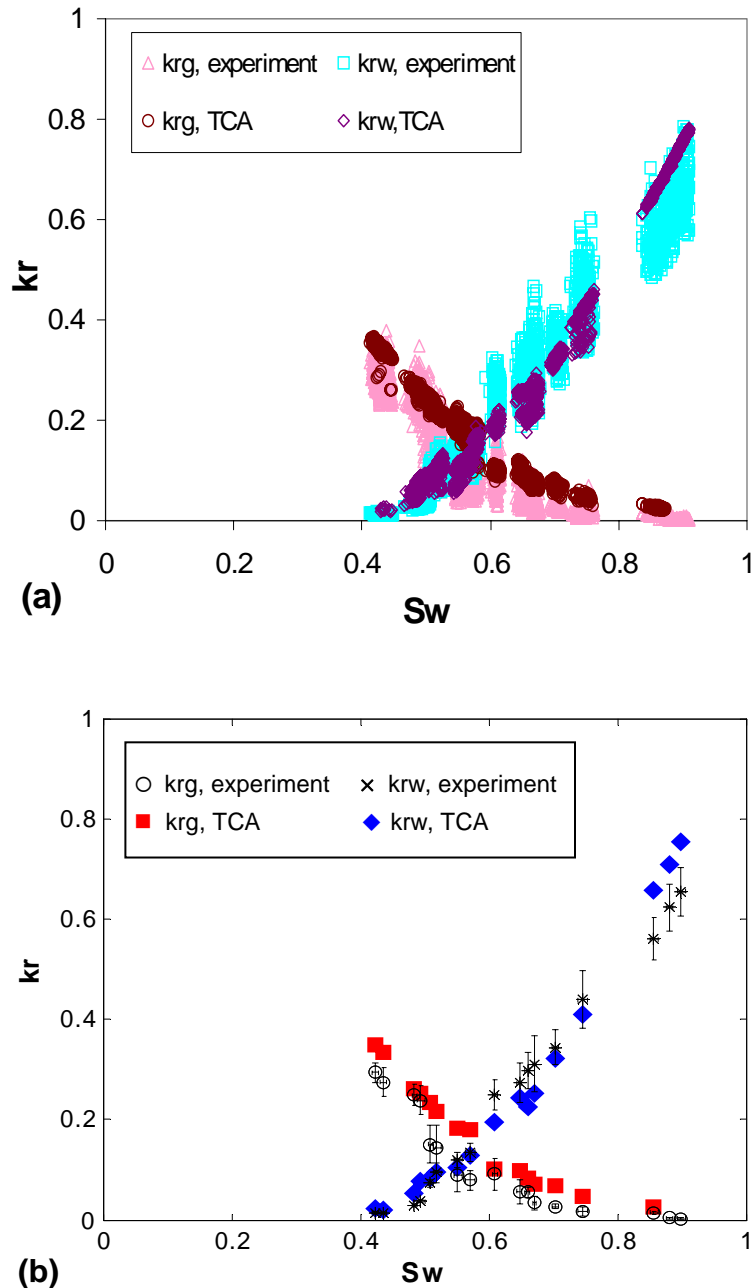


Figure 4.12: Relative permeabilities from tortuous-channel approach and its comparison with the experimental result for the RR fracture: (a) all data points (~3000 points), (b) averages of each runs in (a) with standard errorbars of k_r and S_w .

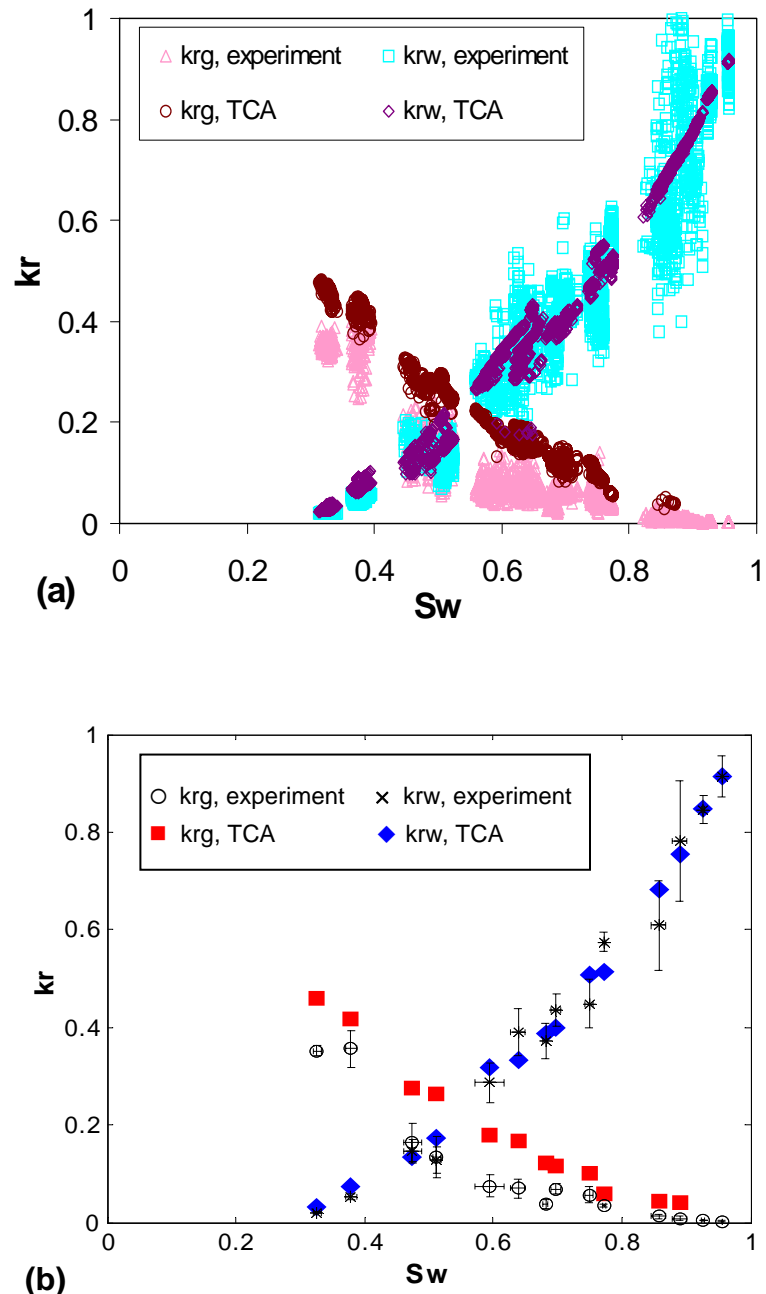


Figure 4.13: Relative permeabilities from tortuous-channel approach and its comparison with the experimental result for the HR fracture: (a) all data points (~ 3000 points), (b) averages of each runs in (a) with standard errorbars of k_r and S_w .

4.5 Tortuosity Modeling

The evolution of phase channels shown in Figure 4.9 may reveal the correlation between the channel tortuosity and the surface geometry and heterogeneity of fractures. Earlier studies also suggested that relative permeabilities in fractures are sensitive to the nature and range of spatial correlation between apertures [Pruess and Tsang, 1990]. Combining the rough-walled results with smooth-walled results, Figure 4.14a shows the reciprocal of average water-phase tortuosity versus water saturation for all of the fractures studied. A straight channel has a value of reciprocal of tortuosity equal to 1.

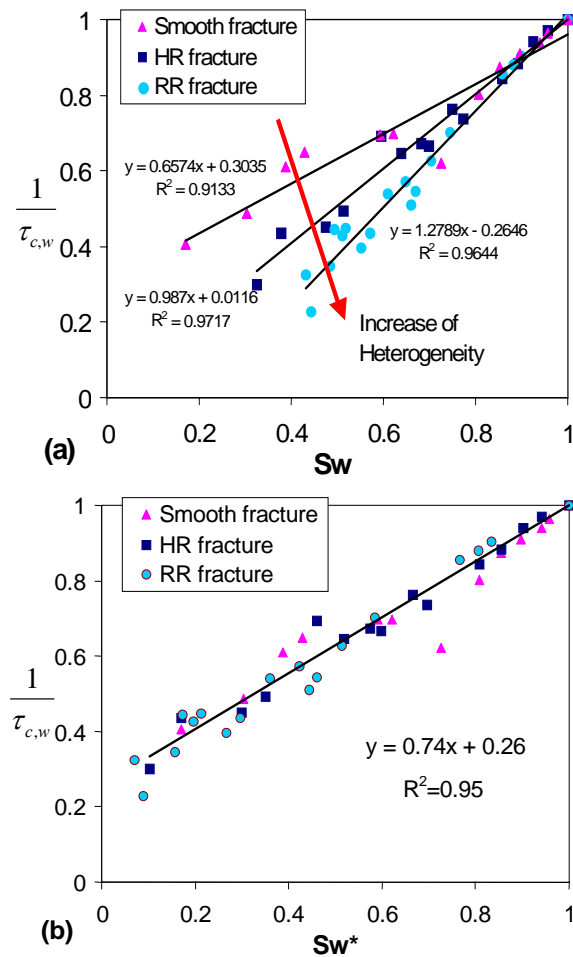


Figure 4.14: Reciprocal of average water channel tortuosity versus (a) water saturation and (b) normalized water saturation for smooth and rough fractures.

As can be seen in Figure 4.14a, acceptable linear trends can be found in these three cases, while their slopes increase when the heterogeneity of the fracture surfaces increases. Interestingly, these data seem to collapse to a single linear trendline when plotted in normalized water saturation as shown in Figure 4.14b. On the other hand, the average gas channel tortuosities show similar trends in the smooth and the HR fractures while the RR fracture results demonstrate a slightly more tortuous trend as shown in Figure 4.15. However, most of the deviated points in Figure 4.15 were close to the end point of the gas saturation, which has a less significant inference on the Equations (4.11)

and (4.12). All of these gas-phase tortuosities can be expressed approximately in a second-order relationship with respect to gas saturation.

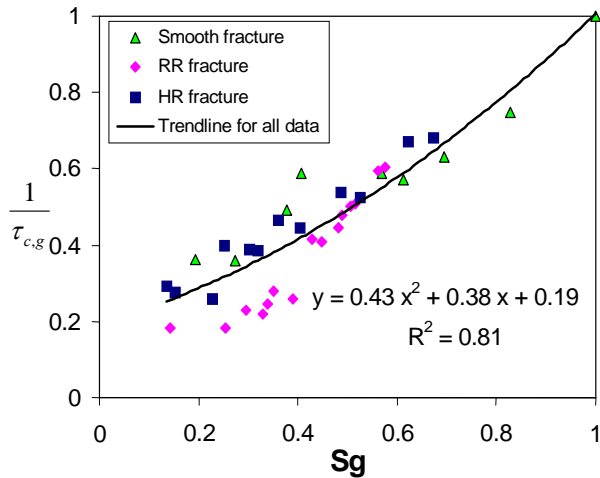


Figure 4.15: Reciprocal of average gas channel tortuosity versus gas saturation for smooth and rough fractures.

Generalizing from these three specific types of fractures, preliminary and empirical correlation equations between the channel tortuosity and saturation can be obtained as shown in Figures 4.14b and 4.15. Substituting these equations into Equations (4.11) and (4.12), the tortuous channel model (TCM) for the three fractures we studied is then obtained as:

$$k_{rw} = 0.74S_w^{*2} + 0.26S_w^* \quad (4.13)$$

$$k_{rg} = 0.43S_g^3 + 0.38S_g^2 + 0.19S_g \quad (4.14)$$

Plotting this model against the experimental results is shown in Figure 4.16. Close agreement was obtained between this tortuous channel model and the experimental measurements. Using measured values of residual water saturation S_{wr} from the experiments of the rough fractures, this model can describe the water-phase relative

permeabilities of all three fracture types with good accuracy, accounting for the residual phase. The gas-phase curve generalized from all gas-phase tortuosities seems to overestimate k_{rg} slightly compared to the experimental result; nevertheless the model curve can still capture the trend of the experimental data.

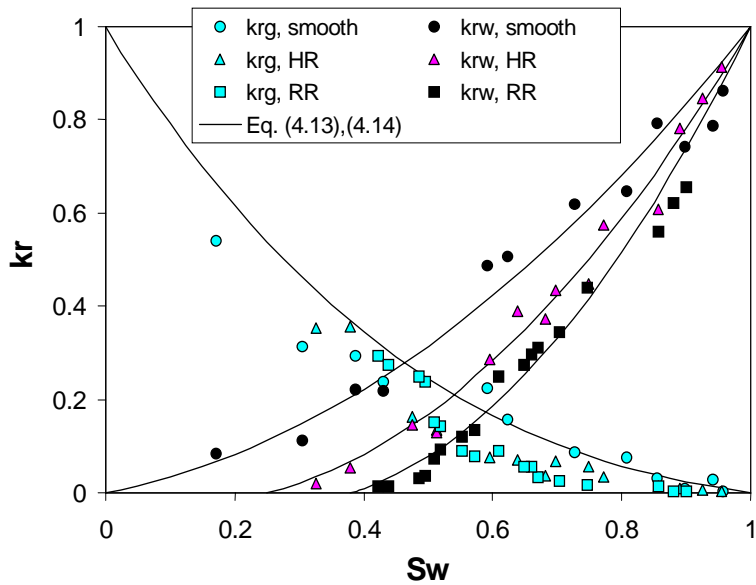


Figure 4.16: Comparison of the experimental relative permeabilities with tortuous-channel model using Equations (4.13) and (4.14) for the smooth-walled, HR and RR fractures. The S_{wr} for HR and RR fractures is 0.25 and 0.39 respectively determined from the experiments.

4.6 Applicability and Limitations

It is admitted that two-phase flow in natural fractures is complex, and there are essential difficulties in developing a unique model to predict two-phase flow behaviors and relative permeabilities in these rock fractures due to the variability and unpredictability of fracture aperture heterogeneity. The TCM is definitely not a universal model to encompass these poorly understood issues. Instead, it is a first step towards relating

complex fluid and geometry interactions (viscous forces, capillary forces, saturations etc.) to macroscopic hydraulic outcomes under some simplifications. Therefore, the power of using TCM to predict unsaturated relative permeabilities in general fractures is not emphasized here. However, several papers using comparable techniques or under similar simplifications can serve to evaluate the proposed TCM. In addition, the dependency of flow structures, characterized by channel tortuosity, on flow rates (velocities) and some suggestions of future extension are other important issues to address.

4.6.1 Fitting Results from Earlier Studies

Nicholl and Glass [1994] conducted experiments to measure flowing-phase (water phase) relative permeabilities in the presence of entrapped gas phase in a homogeneous, isotropic fracture. The corresponding in-place tortuosities were inferred from simulated flow rates using measured phase geometries [Nicholl et al., 2000]. Although their experiments were conducted in satiated condition (water was the only flowing phase) and the final residual water saturation was not reported, Equation (4.11) or (4.13) still shows an acceptable fit to Nicholl et al.'s flowing relative permeabilities by using their simulated tortuosities or the tortuosity model generalized from this study and setting a reasonable value for S_{wr} (0.36), as illustrated in Figure 4.17. In addition, most of the correlated simulated tortuosities seem to follow the linear trendline suggested in this study (Figure 4.18). Pruess and Tsang [1990] predicted fracture relative permeabilities from numerical simulation of conceptual and heterogeneous fracture geometries as presented in Figure 4.1. The phase occupancy and permeability were derived by assuming a parallel-plate model for small subregions in the fracture plane. Although only qualitative applications were suggested and the nonwetting phase relative permeabilities were deemed to be less physical in their simulated results, the wetting-phase relative permeabilities did follow a conventional pattern. As shown in Figure 4.19, these numerical results can be interpreted by the proposed tortuous channel model by setting a reasonable value for S_{wr} .

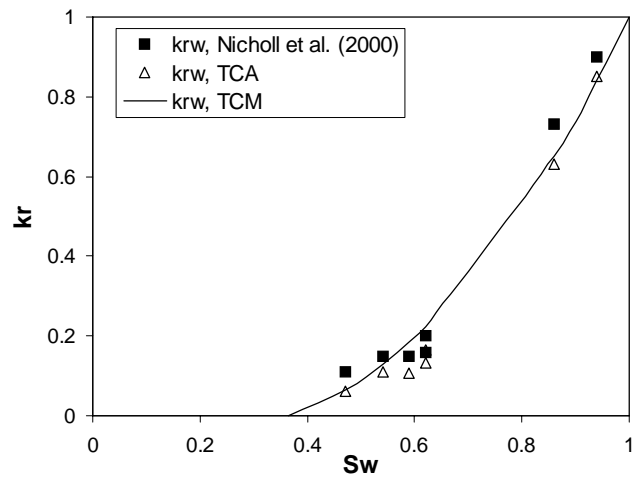


Figure 4.17: Using proposed tortuous channel approach (Equation 4.11) and model (Equation 4.13) to interpret flowing-phase relative permeabilities from Nicholl et al. [2000] by setting $S_{wr} = 0.36$.

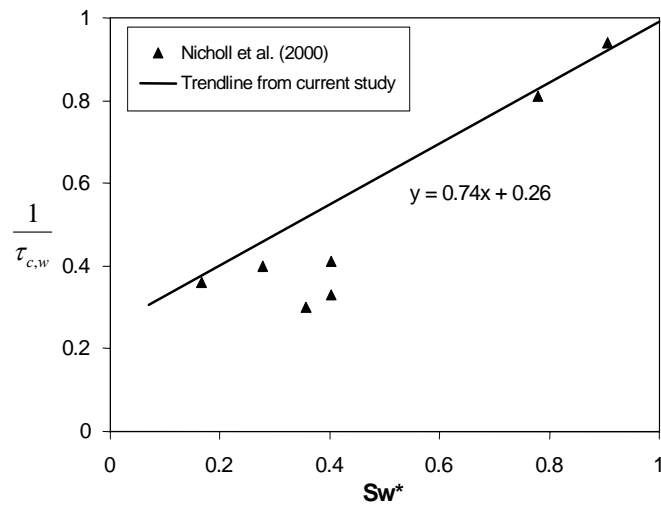


Figure 4.18: Plot of reciprocal of in-place tortuosities from Nicholl et al. [2000] versus normalized water saturation by setting $S_{wr} = 0.36$.

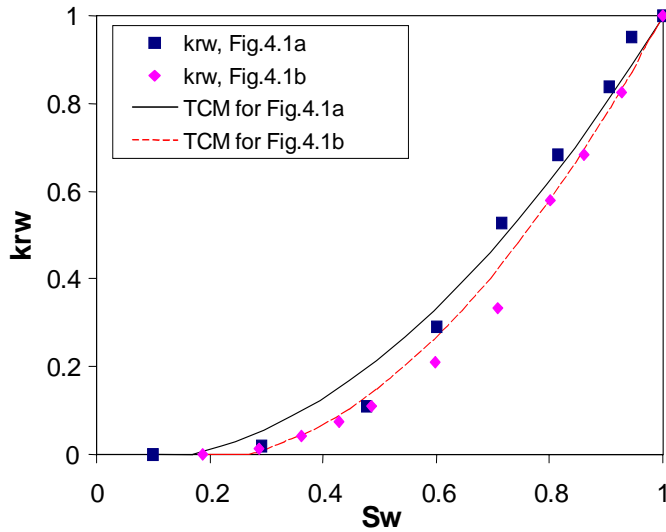


Figure 4.19: Using proposed tortuous channel model (Equation 4.13) to interpret two sets of water-phase relative permeabilities from the earlier numerical study by Pruess and Tsang [1990]. (S_{wr} was set to be 0.27 and 0.17 respectively)

4.6.2 Effects of Flow Rates on Flow Structures

Some investigations have shown that flow rates (velocities) may influence flow structures and hence alter relative permeabilities for certain experimental scales and high fluid velocities [Fourar et al. 1993; Fourar and Lenormand, 1998; 2001]. Although the experiments in Chapter 3 were designed carefully to avoid the rate dependency by choosing smaller flow rates ($Q_w=0.5$ to 15 ml/min; $Q_g=2$ to 200 S.cm³/min), it was difficult to examine the rate dependency on flow structure simply by visualization. Furthermore, different saturations were generated by changing ratios of water and gas rates in our experiments; therefore, saturation and flow rates were coupled. It is inappropriate to consider each of these two coupled parameters solely from the experimental results.

The relationship between saturation and channel tortuosity was developed in the previous sections. However, whether these tortuosity evolutions also affected by flow

rates remains questionable. Although we found that the rate effects were unclear from experimental observation in all three fractures, a separate investigation on this dependency was carried out in the HR fracture for air-water flow. In this supplementary investigation, the HR fracture was rebolted with hydraulic aperture ($\sim 170\mu\text{m}$) slightly different to the aperture studied in Chapter 3. The rest of the apparatus and techniques remained the same as described in Chapter 3. To isolate the dependency among rate ratios, absolute rates and saturations, a fixed ratio of rates ($Q_g/Q_w=20$) was specified, while the absolute values of gas and water rates varied. The channel tortuosity and saturation of each phase corresponding to each pair of absolute rates were calculated. These results are shown in Figure 4.20 for water phase and gas phase separately. No significant increase or decrease of saturation or tortuosity versus phase rates were observed under the specified rate ratio. Even though saturations fluctuated within a 0.1 range, the channel tortuosities in both phases appear to follow this trend of fluctuation. This may reveal that the effects of flow rates on flow structures are insignificant, and the channel tortuosity is mainly related to the saturation for the rate ranges and fractures studied. Therefore, we considered the flow structures and relative permeabilities to depend solely on saturations in our study. For conditions of higher flow rates and short fracture length with long correlation distance of local aperture distributions, however, the flow rates may dominate the flow structure and hence change the shape of relative permeability curves. Nevertheless, it is noteworthy that the validity of TCA is independent of flow rates, provided that they affect flow structures and relative permeabilities considerably. The key role of TCA is to link the flow structures to resultant relative permeabilities. Even though the flow structures were dominated significantly by high flow rates (velocities) under some circumstances, the TCA still relates these structures to the rate-dependent relative permeabilities correctly. However, the component of rate effects may need to be incorporated into TCM under this circumstance. After the satisfaction of this preliminary step towards relating complex fluid and geometry interactions to macroscopic hydraulic outcomes, the issues discussed above may serve as good topics for the future extensions to move toward relative permeability predictions.

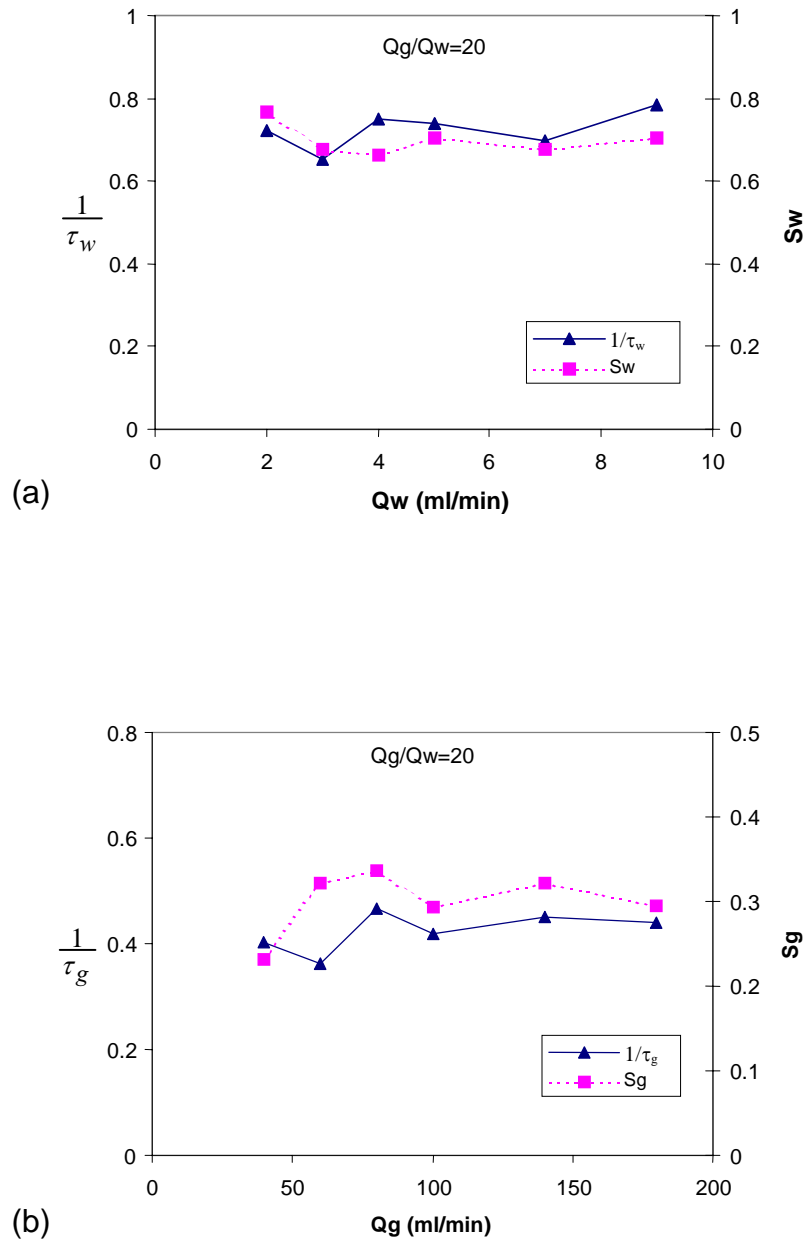


Figure 4.20: Reciprocal of phase tortuosities and saturations versus phase rates for the HR fracture with hydraulic aperture $\sim 170 \mu\text{m}$ when Q_g/Q_w is fixed to 20: (a) water phase, (b) gas phase.

4.6.3 Suggestions

Although some successful descriptions of relative permeabilities in rough-walled fractures using the proposed tortuous channel approach and model were achieved, it is very important to emphasize the limitations. At this moment, the method of evaluating the coefficient of tortuosity and the feasibility of using the tortuous-channel approach were only validated in specific artificial fractures made of silica glass. To account for the complex connectivity and flow structures in full-scale naturally-fractured media, the algorithm to evaluate tortuosity τ_c and the methodology to characterize the flow-based heterogeneity may have to be developed further. Characterizing the flow-based heterogeneity of the fractures is believed to be the major challenge of the future application. The tortuous-channel model (Equations 4.13 and 4.14) was developed from current results empirically. The characteristics of heterogeneity in natural fractures are certainly much more complex and variable. Therefore more studies of the relationship between tortuosity and fracture geometry may be needed to gain rigorous models for predicting fracture relative permeabilities accurately. If such work can be achieved, perhaps the relative permeabilities of natural fractures can be predicted simply by measuring S_{wr} and the geometry of the fracture surface or by using tomographic technology to determine channel tortuosity.

4.7 Chapter Summary

This study has demonstrated the possibility of using a flow-structure model to predict the corresponding relative permeabilities in rough-walled fractures. The proposed approach can represent the experimental data from current and earlier studies with good agreement. By studying three fractures with different surface roughness, we found that the magnitude of the flow channel tortuosity increases when the heterogeneity of fracture surface increases. Generalizing from all the channel tortuosities measured in these three fractures, we suggested an empirical, tortuous channel model. Although there are not many reliable

measurements of two-phase relative permeabilities in fractures from earlier studies to which our model can be compared, the water-phase function in the suggested model has been in accordance with some earlier experimental and numerical results.

Chapter 5

Theoretical Study of Phase Transformation Effects on Steam-Water Relative Permeabilities

In this chapter, we extend the work from conventional two-phase flow (air-water flow) to the unconventional two-phase flow (steam-water flow) by considering phase transformation effects. Phase transformation affects multiphase flow in geothermal and gas-condensate reservoirs due to the same substance occurring in different phases. These effects change the phase behavior and the flow characteristics. This chapter specifically focuses on theoretical study of effects of phase transformation on liquid-vapor relative permeabilities, while the next chapter focuses on the experimental study of steam-water flow.

The goal of this study was to model the effects of phase transformation on steam-water relative permeabilities and to explain the behavior of enhanced steam-phase relative permeabilities. The inviscid bubble train model based on the Bretherton theory was used and coupled with the relative permeability concepts. The phase transformation effects were evaluated by introducing the interfacial mass flux based on the carry-away and precipitation processes of vapor molecules. The chapter is organized as follows. After the introduction, we first derive conventional, noncondensable gas-water relative

permeability. Steam-water relative permeability functions with phase transformations are then introduced by using the kinetic theory of gas. After that, a toroidal pore throat is used to demonstrate qualitatively the transport differences between steam-water flow and noncondensable gas-water flow. Finally, we summarize this study.

5.1 Introduction

Boiling phenomena occur in geothermal reservoirs when the reservoir pressure is equal or less than the saturated pressure at the reservoir temperature. Boiling generates unconventional two-phase flow because of phase transformations, which affect multiphase flow in geothermal reservoirs due to the same substance occurring in different phases. Phase transformation effects also change the phase behavior and the flow characteristics [Horne et al., 2000].

In geothermal reservoir simulations, it has long been debated whether these effects influence the relative permeability functions significantly [Verma, 1986; Horne et al., 2000; Chen et al., 2004; Schechter and Schechter, 1987; Piquemal, 1994]. Several studies suggested that in porous media, the steam-water relative permeability curves behave similarly to the air-water relative permeability curves [Schechter and Schechter, 1987; Piquemal, 1994]. However, another set of studies suggested that steam-water relative permeability curves in porous media behave differently from air-water curves [Verma, 1986; Satik, 1998; Horne et al., 2000]. These studies showed that the steam-phase relative permeability is enhanced in comparison to the air-phase relative permeability. Among these studies, none were conducted theoretically considering the saturated, superheated and subcooling thermodynamics as well as interfacial mass flux, except for the study done by Verma [1986], where he conducted theoretical and numerical studies of the phase transformation effects on steam-water flow in porous media. In an idealized toroidal geometry, Verma [1986] concluded that the phase transformation phenomenon results in a lower pressure drop across the flow channel and

can lead to enhancement of steam phase relative permeabilities in high conductivity media. However, direct theoretical or numerical investigation of how the phase transformation effects influence relative permeabilities was not conducted.

One uncomplicated method to study the steam-liquid transport theoretically is to consider it as the motion and interactions of discrete bubble trains (or droplet trains) in capillary tubes. These bubble train models were generally used to study pore network models for gas-water or foam-water flow behaviors [Foulser et al., 1991; Babchin and Yuan, 1997; Stark and Manga, 2000]. Hunt and Manga [2003] studied the effects of noncondensable gas bubbles on the hydraulic conductivity using Bretherton's theory and suggested a capillary-number-dependant liquid relative permeability function. However, the gas (bubble) relative permeability function was absent. Furthermore, none of these earlier studies have conducted an evaluation of the effects of phase transformation on the steam bubbles flow in this simple geometry.

This study may be deemed a preliminary evaluation of the effects of phase transformation on steam-water (vapor-water) flow behavior in terms of the relative permeability concept by using the theory of the moving of bubble trains in cylindrical capillary tubes. Several complicated interfacial physical chemistry and thin film effects were ignored at this stage. To avoid confusion, the terms “*air*” or “*noncondensable gas*” are used to refer to the gas phase in multiphase flow without phase transformations, while terms “*steam*” or “*vapor*” are used to refer to the gas phase in multiphase flow with phase transformations.

5.2 Inviscid Bubble Train Model

5.2.1 Model Description

The inviscid bubble train model considers the gas phase inside the bubble as an inviscid fluid which does not obey a linear pressure-velocity relation. This is generally referred to

as Bretherton bubble behavior [Bretherton, 1961]. When an inviscid long bubble is inserted into the cylindrical capillary in which a Newtonian liquid is flowing, the pressure-velocity relation becomes nonlinear due to several mechanisms active around the bubble, which include the drag of the bubble, the film lubrication as well as the pushing force exerted by the liquid [Wong et al., 1995a, 1995b; Ratulowski and Chang, 1989]. Hunt and Manga [2003] studied the effects of bubbles on the hydraulic conductivity using Bretherton's theory and suggested a capillary-number-dependant liquid relative permeability function. However, the gas relative permeability was claimed to be meaningless and thus was absent in their study, as the gas phase is not continuous.

Though the gas phase is discontinuous at the instantaneous scale, it may be considered as continuous on average at the macroscopic scale if the gas phase is in the form of a homogeneous bubble train. To embed relative permeability concepts and couple phase transformation effects in these models, the consideration of gas viscosity and interfacial mass flux due to phase transitions becomes critical. In this section, we first modify the theoretical derivation from the study of Hunt and Manga [2003] and then study the phase transformation effects on the relative permeability functions obtained by introducing the concept of the interfacial mass flux in a steam-water system.

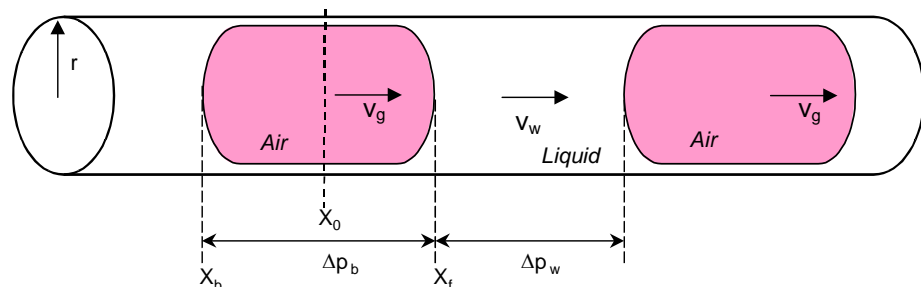


Figure 5.1: Schematic of motion of a homogeneous bubble train containing long air bubbles in a cylindrical capillary tube.

Considering the motion of long bubbles in Figure 5.1, for small Reynolds number, Bretherton [1961] used a matched-asymptotics method in deriving the motion of long bubbles in a circular capillary. The relationship between average bubble velocity and liquid velocity is suggested as:

$$v_g = \frac{v_w}{1 - \omega} \quad (5.1)$$

where v_g and v_w are bubble and liquid velocities respectively, and:

$$\omega = 1.29(3Ca)^{2/3} \quad \text{and} \quad Ca = \frac{\mu_w v_g}{\sigma} \quad (5.2)$$

where σ is the interfacial tension, Ca is the capillary number, and μ_w is the water dynamic viscosity.

As shown in Equation (5.1), the relationship between the average bubble velocity and liquid velocity is nonlinear, and the average bubble velocity exceeds the average liquid velocity by a factor of ω . For small Reynolds number and slow moving fluids, the coefficient ω is very small for noncondensable gas bubbles. Bretherton's study showed that the pressure drop across a bubble (Δp_b) and the liquid film between the bubble and tube wall (h_∞) also scales as $Ca^{2/3}$ for a sufficient small Ca . This pressure drop can be expressed as:

$$\Delta p_b = 3.58 \frac{\sigma}{r} (3Ca)^{2/3} \quad (5.3)$$

where r is the radius of the capillary tube.

The total pressure drop across the tube and the length of the tube are:

$$\Delta p_t = \sum \Delta p_w + \sum \Delta p_b \quad (5.4)$$

$$L_t = \sum L_w + \sum L_b \quad (5.5)$$

The saturation is defined as the length ratios:

$$S_w = \frac{\sum L_w}{L_t} \quad \text{and} \quad S_g = \frac{\sum L_b}{L_t} \quad (5.6)$$

For a long and homogeneous bubble train shown in Figure 5.1, every bubble has an identical volume, V_b ; therefore, the total volume of gas (vapor) in the bubble train can be expressed as:

$$N_b V_b = \pi r^2 \sum L_b = \pi r^2 L_t S_g \quad (5.7)$$

and the number of bubbles can be written as:

$$N_b = \frac{\pi r^2 L_t S_g}{V_b} \quad (5.8)$$

where N_b is the number of bubbles in the bubble train. The total pressure drop of bubbles throughout the tube is then:

$$\sum \Delta p_b = N_b \frac{3.58\sigma}{r} (3Ca)^{2/3} \quad (5.9)$$

Applying the relationship in Equation (5.1), Equation (5.9) can be rewritten as:

$$\sum \Delta p_b = N_b \frac{7.45(\frac{\sigma}{r})(\frac{\mu_w q_w}{\sigma \pi r^2})^{2/3}}{(1-\omega)^{2/3}} \quad (5.10)$$

Since the liquid phase is a continuous Newtonian fluid, the Poiseuille equation can be used to calculate the total liquid pressure drop. For a steady-state, continuous flow, the water rate can be expressed as:

$$q_{w,p} = \frac{\pi r^4}{8\mu_w} \frac{\Sigma \Delta p_w}{\Sigma L_w} \quad (5.11)$$

As one can imagine, the flow of bubble train is in quasisteady state (or pulsed steady state) in the instantaneous sense. There are alternative single-phase instantaneous flows passing through a specific cross section. To apply two-phase generalized Darcy's equations and account for the alternative flow, the void (gas) portion has to be excluded from the flowing water phase. Therefore, the (average) water flow rate was obtained by multiplying Equation (5.11) by water saturation:

$$q_w = S_w q_{w,p} \quad (5.12)$$

From Equations (5.11) and (5.12), the total liquid pressure drop is:

$$\sum \Delta p_w = \frac{8\mu_w \sum L_w}{\pi r^4} q_{w,p} = \frac{8\mu_w \sum L_w}{S_w \pi r^4} q_w \quad (5.13)$$

To impose the relative permeability concept into this model, the total pressure drop throughout the capillary has to be related to the generalized Darcy equations. Since Darcy's equations are based on steady-state, laminar flow, the average flow rates have to be used as Darcy rates in the case studied in order to represent the macroscopic and generalized behavior. For incompressible fluids, two-phase Darcy's equations are given as:

$$q_w = \frac{k k_{rw} A}{\mu_w} \frac{\Delta p_t}{L_t} \quad (5.14)$$

$$q_g = \frac{kk_{rg}A}{\mu_g} \frac{\Delta p_t}{L_t} \quad (5.15)$$

For a cylindrical tube:

$$k = \frac{r^2}{8} \quad \text{and} \quad A = \pi r^2 \quad (5.16)$$

The bubble and the liquid velocities are related to the Darcy velocities by dividing the latter by saturations:

$$v_w = \frac{u_w}{S_w} = \frac{q_w}{AS_w} = \frac{kk_{rw}}{S_w \mu_w} \frac{\Delta p_t}{L_t} \quad (5.17)$$

$$v_g = \frac{u_g}{S_g} = \frac{q_g}{AS_g} = \frac{kk_{rg}}{S_g \mu_g} \frac{\Delta p_t}{L_t} \quad (5.18)$$

Thus, the ratio of the liquid velocity to the bubble velocity is:

$$\frac{v_w}{v_g} = \frac{S_g k_{rw} \mu_g}{S_w k_{rg} \mu_w} \quad (5.19)$$

Considering the water phase, we eliminated the total pressure term by relating it to the (average) water rate. From Equations (5.14) and (5.16) the total pressure drop can be expressed as:

$$\Delta p_t = \frac{8\mu_w L_t}{\pi r^4 k_{rw}} q_w \quad (5.20)$$

Substituting Equations (5.10), (5.13) and (5.20) into Equation (5.4), yields:

$$\frac{8\mu_w L_t}{\pi r^4 k_{rw}} q_w = \frac{8\mu_w \sum L_w}{S_w \pi r^4} q_w + N_b \frac{7.45(\frac{\sigma}{r})(\frac{\mu_w q_w}{\sigma \pi r^2})^{2/3}}{(1-\omega)^{2/3}} \quad (5.21)$$

Reducing and solving Equation (5.21) for k_{rw} , we obtain:

$$k_{rw} = \frac{1}{1 + 0.931 \frac{\pi r^3 (1 - S_w)}{V_b} \frac{Ca^{-1/3}}{(1 - \omega)^{2/3}}} \quad (5.22)$$

To evaluate the gas-phase relative permeability function and impose the generalized Darcy equations, the gas viscosity still has to be applied even though the gas phase is considered inviscid for Bretherton's derivations. As the relationship between average bubble velocity and liquid velocity is nonlinear, we used the velocity ratio method to evaluate the gas-phase relative permeabilities with and without the effects of phase transformation. For the gas-water flow without phase transformation effects, combining Equations (5.19) and (5.1), we obtain:

$$\frac{v_w}{v_g} = \frac{S_g k_{rw} \mu_g}{S_w k_{rg} \mu_w} = 1 - \omega \quad (5.23)$$

Therefore:

$$k_{rg} = \frac{(1 - S_w) \mu_g}{S_w \mu_w (1 - \omega)} k_{rw} \quad (5.24)$$

Substituting Equation (5.22) into Equation (5.24), the noncondensable gas relative permeability is then:

$$k_{rg} = \frac{\left[\frac{(1-S_w)\mu_g}{S_w\mu_w(1-\omega)} \right]}{1 + 0.931 \frac{\pi r^3 (1-S_w) Ca^{-1/3}}{V_b (1-\omega)^{2/3}}} \quad (5.25)$$

Equations (5.22) and (5.25) are used as the base relative permeability functions for conventional gas-water flow without phase transformations.

5.2.2 Interfacial Flux for Vapor Bubbles in a Capillary

For vapor-liquid flow in a cylindrical tube in isothermal equilibrium, the phase transformations enhance the flow of vapor bubbles due to vaporization-condensation effects. Here, flow of a vapor bubble train in a capillary tube is used to evaluate the interfacial mass flux and the movement of interface. The bubble train is assumed homogeneous with identical bubbles and spacing. As shown in Figure 5.2, due to the pressure drop across the bubble, vaporization occurs at the leading interface of the bubble, while condensation occurs on the trailing interface of the bubble as the system is at isothermal conditions. This vaporization-condensation phenomenon not only makes the liquid molecular transport through the vapor bubble via vaporization-then-condensation, but also enhances the bubble velocity because of the extra displacement of the bubble contributed by the vaporization-condensation effects. To quantify the magnitude of these effects, the following assumptions were adopted in this model:

1. System is in isothermal conditions; $T(\text{liquid}) = T(\text{vapor}) = T(\text{tube wall}) = \text{constant}$.
2. Pressure distribution inside the bubble is uniform and under saturated conditions; $p_v = p_{sat}(T_v) = \text{constant}$.
3. Flat interface occurs at $x = x_0$; therefore, $p_v = p_l(x=x_0)$.
4. The bubble is long enough that the curvature of the front and end caps of the bubble can be ignored for the interfacial mass flux calculation. In other words, the bubble is considered as cylindrical shape in calculating the interfacial mass flux.

5. The thin film between the bubble and the tube wall is small and the phase transformations within it are small and do not affect the longitudinal interfacial mass flux in the previous assumption.

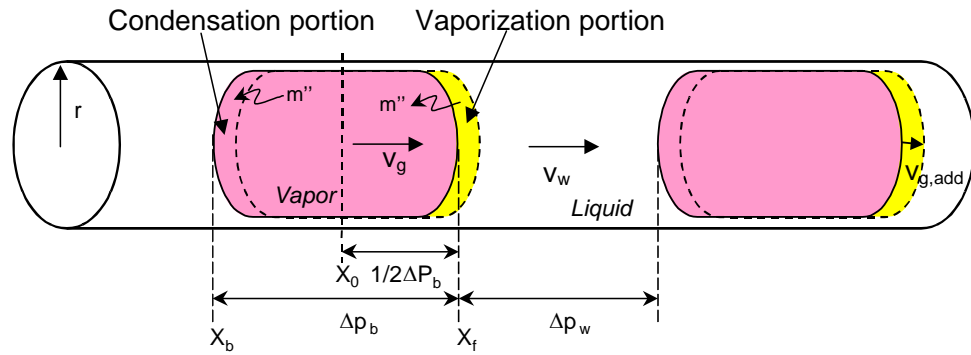


Figure 5.2: Schematic of motion of a homogeneous bubble train containing long vapor bubbles in a cylindrical capillary tube.

Considering a single saturated vapor bubble surrounded by moving liquid, x_0 is the center position of the bubble, x_f and x_b are the front and back ends of the bubble, and m'' is the interfacial mass flux due to vaporization or condensation. Due to the pressure difference (Δp_b) across the bubble, vaporization takes place in the front cap and causes the inward mass flux, while condensation takes place in the back cap and causes the outward mass flux as shown in Figure 5.2. Under equilibrium, these two interfacial mass flux are equal but different in sign resulting in an extra average velocity ($v_{g,add}$) of the bubble besides the original average velocity in Equation (5.1). The interfacial mass flux was calculated from the kinetic theory of vapor molecules [Silver and Simpson, 1961]:

$$m'' = \left[\frac{2\hat{\sigma}}{(2 - \hat{\sigma})} \right] \left[\frac{\bar{M}}{2\pi\bar{R}} \right]^{1/2} \left(\frac{p_v}{T_v^{1/2}} - \frac{p_l}{T_l^{1/2}} \right) \quad (5.26)$$

where $\hat{\sigma}$ is the accommodation coefficient ($\hat{\sigma} = 0.4$ is employed [Fujikawa and Maerefat, 1990]) and \bar{M} is the molecular weight. \bar{R} is the gas constant. This equation has also been referred to as the Hertz-Knudsen-Langmuir formula or Kucherov-Rikenglaz equation in the Soviet literature [Carey, 1992; Kucherov and Rikenglaz, 1960; Akhatov et al., 2001].

Considering the assumptions listed above and the leading (right) cap of the bubble where the vaporization is prevailing, the pressure difference between the liquid phase and vapor phase can be expressed as:

$$p_v - p_l = p_l(x=0) - p_l(x=x_f) = \frac{1}{2} \Delta p_b \quad (5.27)$$

The mass flux passing through the leading interface (at $x=x_f$) becomes:

$$m'' = \left[\frac{2\hat{\sigma}}{(2 - \hat{\sigma})} \right] \left[\frac{\bar{M}}{2\pi\bar{R}} \right]^{1/2} \left(\frac{0.5\Delta p_b}{T^{1/2}} \right) \quad (5.28)$$

The extra velocity due to phase transformation effects is then obtained by dividing Equation (5.28) by the liquid density:

$$v_{g,add} = \left[\frac{2\hat{\sigma}}{(2 - \hat{\sigma})} \right] \left[\frac{\bar{M}}{2\pi\bar{R}} \right]^{1/2} \left(\frac{0.5\Delta p_b}{\rho_w T^{1/2}} \right) \quad (5.29)$$

To incorporate the extra bubble velocity in Equation (5.29) and evaluate the effects of phase transformation on liquid-vapor relative permeabilities, we may introduce:

$$\varepsilon = \frac{v_w}{v_g + v_{g,add}} = \frac{S_g k_{rw} \mu_g}{S_w k_{rg} \mu_w} \quad (5.30)$$

where $v_{g,add}$ is obtained from Equation (5.29) in which Δp_b is calculated from Equation (5.3). The liquid-phase relative permeability remains unchanged, as the net mass flux due to vaporization and condensation does not affect the net movement of the liquid phase. By using the velocity ratio method illustrated previously, the enhanced vapor-phase relative permeability is then given by:

$$k_{rg} = \frac{\left[\frac{(1-S_w)\mu_g}{S_w\mu_w\varepsilon} \right]}{\left[1 + 0.931 \frac{\pi r^3 (1-S_w) Ca^{-1/3}}{V_b (1-\omega)^{2/3}} \right]} \quad (5.31)$$

5.2.3 Modeling Results

In this section, we compare the relative permeabilities with and without phase transformation effects using the inviscid bubble train model. As can be seen in Equations (5.22) and (5.25), the relative permeability functions are not unique and hence depend on the capillary number. To evaluate these functions, we first solved the nonlinear bubble velocity according to the specified liquid velocity and then calculated ω , Ca and Δp_b . Unlike in a Newtonian fluid, the Δp_b does not depend on the bubble length, but depends on the Ca , σ and r as shown in Equation (5.3). To calculate the enhancement of the steam relative permeabilities, the capillary radius (r) was adjusted to generate different values of Δp_b . The parameters used for calculating the steam-water relative permeabilities are illustrated in Table 5.1.

By using Equation (5.22) and Table 5.1, the water-phase relative permeabilities, k_{rw} , is shown in Figure 5.3 for different capillary number, Ca^* defined as:

$$Ca^* = \frac{\mu_w v_w}{\sigma} \quad (5.32)$$

For slow and constant average water velocity, most of the k_{rw} curve follows the typical behavior. However, k_{rw} cannot approach zero as it moves close to the end point ($S_w=0$), which shows an unphysical asymptotic. In addition, relative permeabilities increase with the increase of Ca^* ; however the unphysical artifact also increases. This can be attributed to the neglecting of the gas viscosity, challenges of the slow moving assumptions as well as some hypothesis in calculating Δp_b . Moreover, Bretherton's theory was developed at low Reynolds number, low capillary number and for long bubbles [Bretherton, 1961; Olbricht, 1996] and it performs poorly as these restrictions become weaker. This may demonstrate the inconsistency and incompatibility of applying the "inviscid" Bretherton theory to the "viscous-dominant" generalized Darcy equations, because this inviscid model is controlled by the capillary number referenced to the average fluid velocity and the single bubble volume (or length).

Despite this fact, we can still evaluate the effects of the phase transformation qualitatively if the Ca^* is kept small. By using Equations (5.22), (5.25) and (5.31), Figure 5.4 shows liquid-vapor relative permeabilities of the inviscid bubble train model with and without phase transformation effects. The bubble pressure drop was adjusted to 1, 2 and 10 psig in evaluating the phase transformation effects. Figure 5.4a shows the linear plot of relative permeability curves in this inviscid model and Figure 5.4b is the logarithmic plot of them. The enhancement of the steam-phase relative permeabilities due to phase transformation effects is less evident in the linear plot because the values of the base k_{rg} are very small over most of the S_w range. However the logarithmic plot in Figure 5.4b shows the enhancement of the steam phase mobility more clearly in the three cases. In the aspect of the phase transformation effects, the larger the bubble pressure drop, the more enhanced the steam relative permeabilities behave. However, the magnitude of the enhancement in this model is not very significant because of the extremely small values

in most of the base k_{rg} curve due to the two-ordered viscosity difference between liquid and vapor phases flowing in such a simple geometry.

Table 5.1: Fluid properties and parameters used in the inviscid bubble train model.

Temperature; T ($^{\circ}\text{C}$)	104
Water density; ρ_w (kg/m^3)	955.44
Water viscosity μ_w (cp)	0.2703
Steam viscosity μ_g (cp)	0.0124
Interfacial tension; σ (N/m)	0.0580
Accommodation coef.; $\hat{\sigma}$	0.4
Molecular weight, \bar{M} (kg/kmole)	18
Gas constant; \bar{R} ($\text{J}/\text{kmole-K}$)	8314.4
Single bubble volume; V_b	$1.5 \times \left(\frac{4}{3}\pi r^3\right)$
Water velocity; v_w (m/s)	0.01

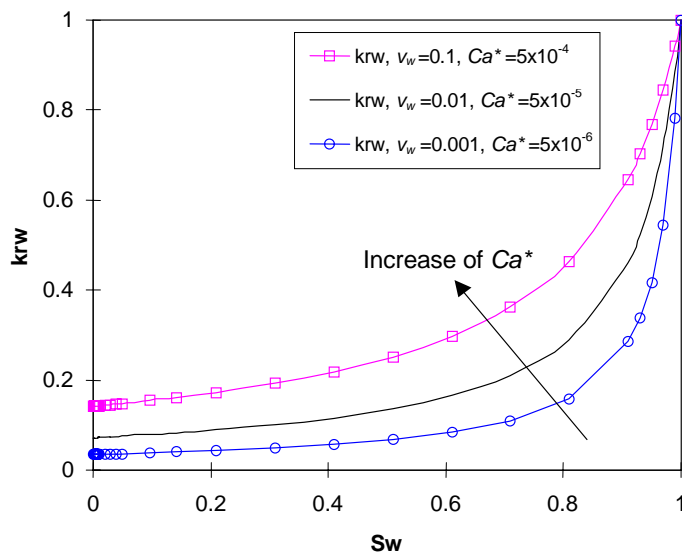


Figure 5.3: Water-phase relative permeability as function of capillary number, Ca^* , in inviscid bubble train model.

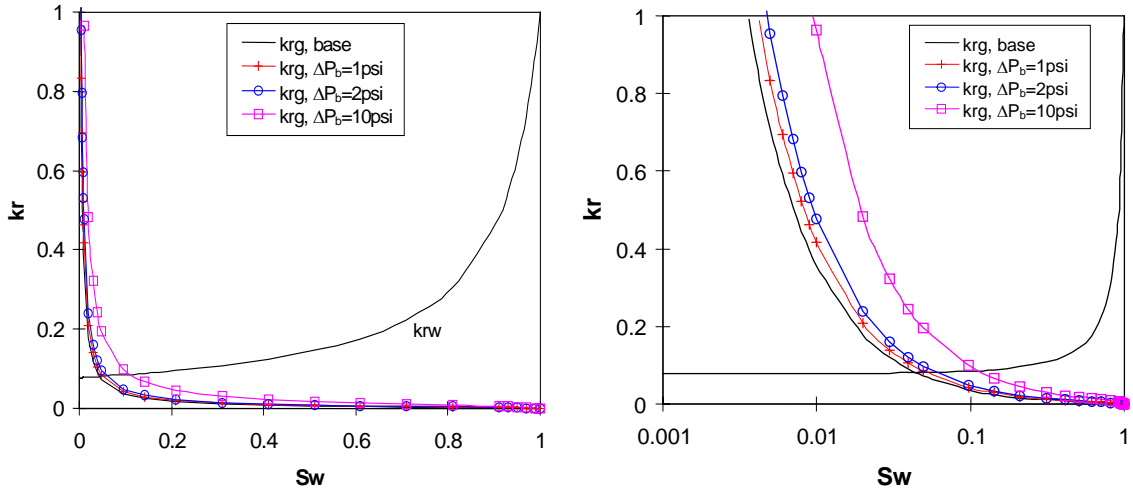


Figure 5.4: Steam-water relative permeabilities of the inviscid bubble train model: (a) linear plot, (b) logarithmic plot. ($Ca^* = 10 \times 10^{-5}$)

5.3 Discussion

In this study we have suggested a simplified model to evaluate the effects of the phase transformation on steam-water relative permeabilities. The interfacial mass flux in steam-water saturated or close-to-saturated condition is a difficult issue which has not been fully understood, because it involves saturated thermodynamics, unstable phase behaviors, thermal-capillary behaviors and other physical chemistry problems. The interfacial mass flux equation based on the kinetic theory of gas was employed in this study.

Comparing these theoretical results to earlier studies discussed in Section 2.4, the theoretical results show qualitative consistency with conclusions drawn by most earlier investigators, that is the steam-phase relative permeability is enhanced in comparison with the air-phase relative permeability [Arihara et al. 1976; Counsil 1979; Verma 1986; Satik 1998; Mahiya 1999; O'Connor 2001]. The shapes of curves from theory and measurement show significant discrepancy, as is to be expected. Hence, quantitative

interpretations using the suggested models are not suggested currently for several reasons. First of all, the cylindrical capillary is inherently different geometrically from the fractures used in the experiments. Regarding the corresponding flow structures, as discussed previously, the observed flow structures of steam-water flow in the fractures are complex combinations of bubbles, slugs and unstable channels. These complex structures certainly generate different curves of relative permeability from those considering only bubble flow. Moreover, the ignored capillary pressure and gravity (buoyancy) effects as well as the assumptions used in the models may be important factors in the situation of the smooth-fracture and rough-fracture experiments.

For the steam-water flow in the rough-walled fractures, the local aperture variation may also enhance steam flow. The aperture variation is assumed to be represented by an idealized toroidal geometry as shown in Figures 5.5 and 5.6, which illustrate the intrinsic difference between steam-water transport and air-water transport through a toroidal throat. For the steam-water transport, after the bubbles contact the solid body, unlike the conventional metamorphic transport in the air-water case, the steam bubble may perform a more efficient transport behavior, called substitution transport. As shown in Figure 5.5b and 5.5c, after arriving at the upstream throat entry, the steam bubble first blocks the entry and causes the downstream water pressure, $p_{w,d}$, to approach zero if surface film flow is negligible. The bulk steam bubble in the upstream is condensing due to the small increase of the upstream water pressure, $p_{w,u}$. The heat released due to condensation then transports though the contacted solid bodies via conduction. This extra energy and lowering downstream pressure generate steam nucleation behavior near the downstream exit due to the change of the thermodynamic properties. As this process continues, the steam bubble condensing in the upstream entry eventually disappears, and an equal-volume steam bubble generated in the downstream exit departs. On the other hand, the major behavior occurring in the air-water transport through the throat is the bubble metamorphic transport controlled by the mechanism of capillary allowance as shown in Figure 5.6. If we define the minimum condensing

pressure to initiate the condensation in the prevailing temperature as p_{cond} and the pressure drop across the throat as:

$$\Delta p_{throat} = p_{w,u} - p_{w,d} \quad (5.33)$$

The maximum capillary pressure through the throat is:

$$P_{C,M} = \frac{2\sigma}{r_t} \quad (5.34)$$

The condition needed to create the substitution transport of the steam bubble is

$$p_{w,u} > p_{cond} \quad (5.35)$$

On the other hand, the condition needed to create the metamorphic transport of the air bubble is:

$$\Delta p_{throat} > P_{C,M} \quad (5.36)$$

Generally speaking, Condition (5.35) is easier to reach than Condition (5.36) if the throat is small. In steam-water equilibrium conditions, only a slight increment of the pressure can condense the steam phase before the steam bubble passes through the throat, whereas the capillary pressure in air-water flow resisting the air bubble in the throat may be much larger due to the small throat radius, r_t . Even though a whole fracture space constituted by many toroidal throats is considered, these two conditions compete for preferential transport in the steam-water flow; whereas, only Condition (5.36) can possibly occur in the air-water flow. Therefore, steam-phase transport is more efficient than the air-phase transport for similar pressure and temperature conditions, which enhances the steam phase relative permeabilities.

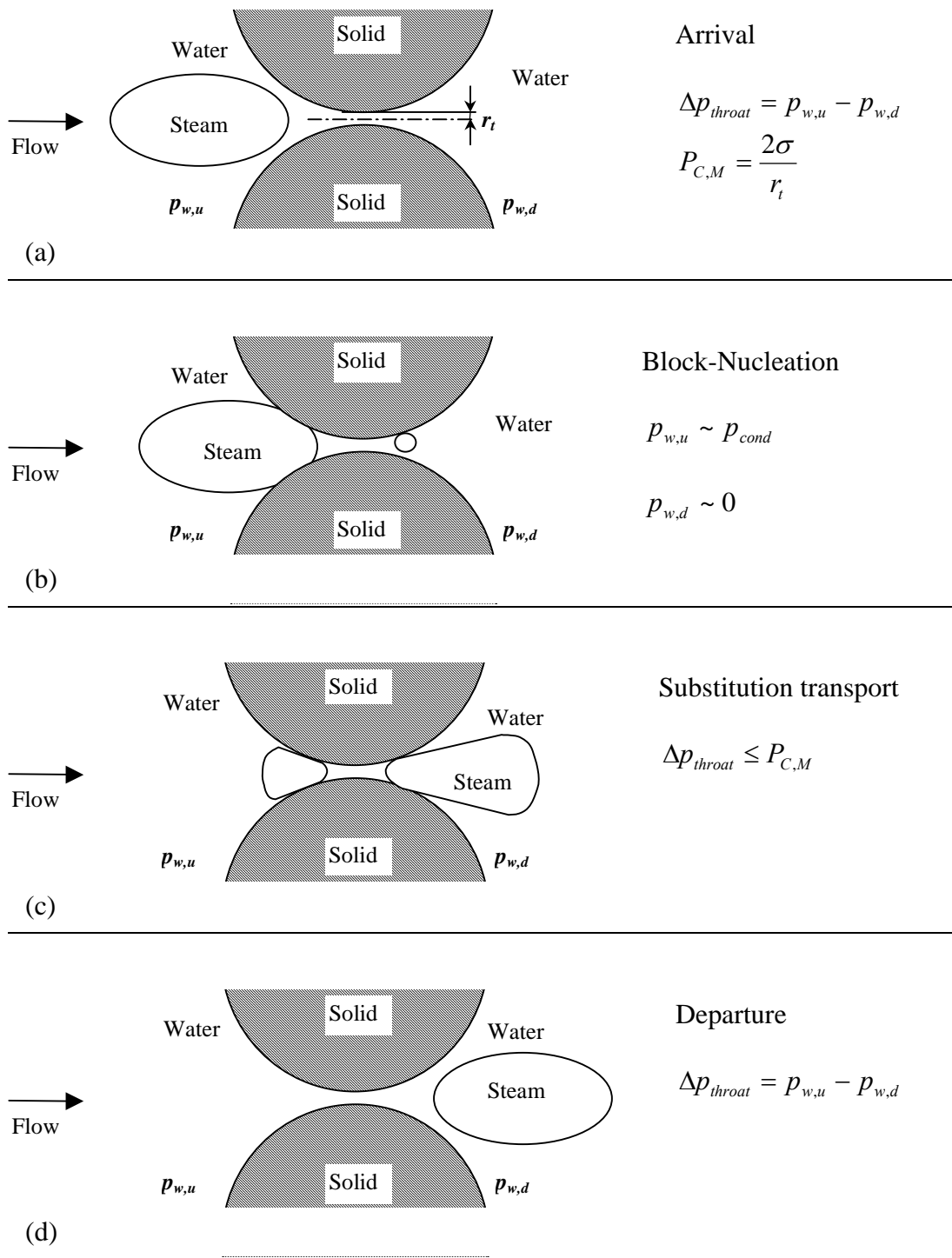


Figure 5.5: Schematic of a steam bubble transporting through idealized toroidal geometry.

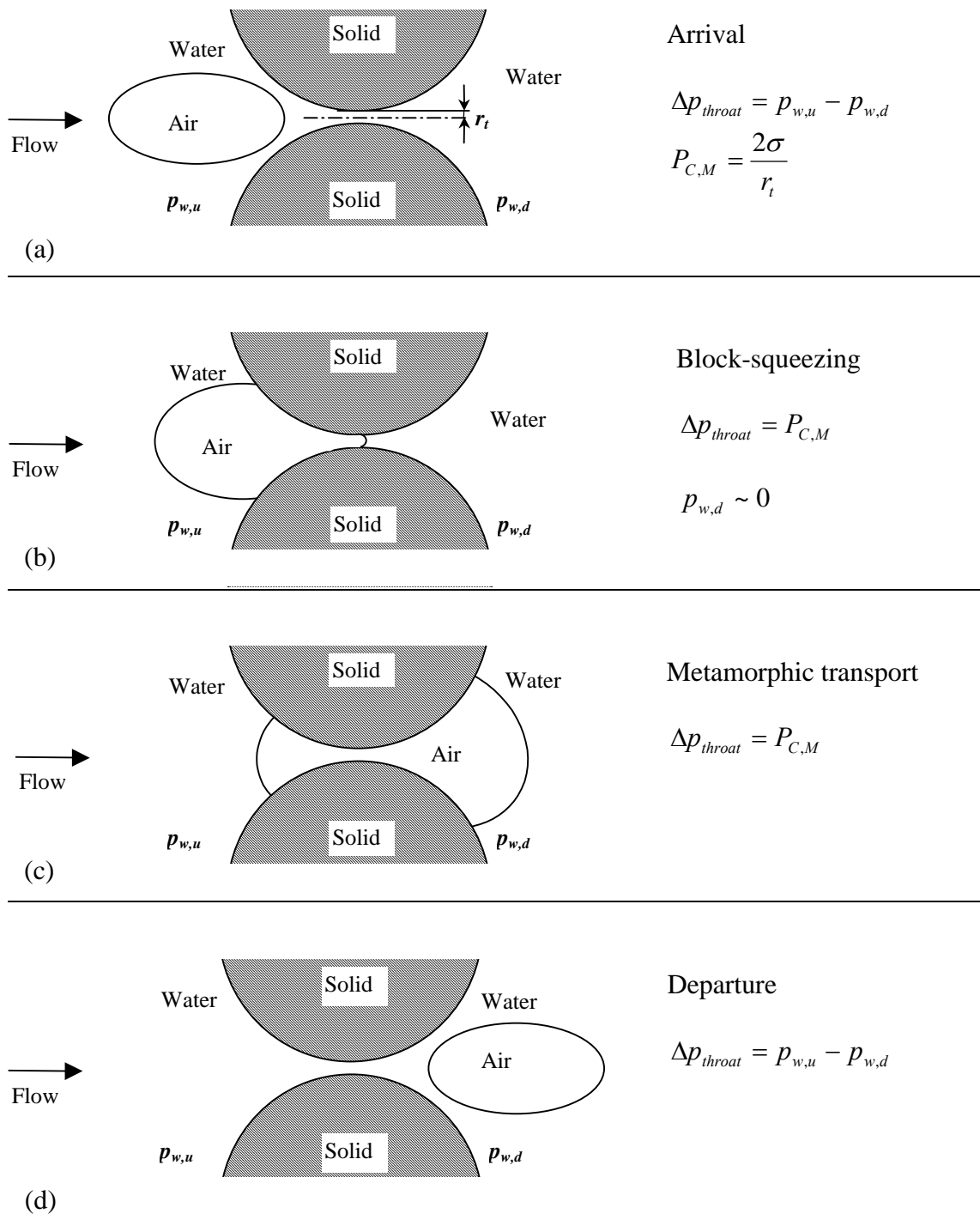


Figure 5.6: Schematic of an air bubble transporting through idealized torroidal geometry.

Verma [1986] studied the effects of phase transformation on effective permeability of channel flows of steam and water through a toroidal throat using semianalytic solution of the balance equations and entropy generation equations. The dimensionless enhancement coefficient due to phase transformations is defined as:

$$En = \frac{(T_{in} - T_{out})_0 - (T_{in} - T_{out})_{PT}}{(T_{in} - T_{out})_0} \times 100 \quad (5.37)$$

where T_{in} and T_{out} are the temperatures at the inlet face and outlet face of the toroidal throat, respectively. Subscript (PT) denotes the solution with phase transformation, while subscript (0) denotes the solution without phase transformation. Through his analytic study, Verma found that the degree of constriction of the toroidal geometry has a significant effect on effective permeability enhancement. In the aspect of the advection efficiency, Verma also concluded that the phase transformation phenomenon results in a lower pressure drop across the flow channel and can lead to enhancement of steam phase relative permeabilities in high conductivity media. Although no direct influence on relative permeabilities were discussed by Verma [1986], his results are in accordance with the observation in the current study, which is that “steam or vapor flows in a more efficient way than noncondensable gas.”

5.4 Chapter Summary

In this study, the interfacial mass flux equation based on the kinetic theory of gas was used to evaluate the effects of phase transformation on vapor bubble transport. Based on earlier studies, a bubble train model was utilized to derive the relative permeability functions accounting for the phase transformation effects. The suggested inviscid bubble train model provided a successful qualitative explanation of some earlier experimental measurements. The shapes of the relative permeability curves from calculation and from earlier measurements were not alike owing to the geometry and flow structure difference as well as the neglect of some physics in the simplified models.

Aside from the bubble train model, a simulated torroidal geometry model was used to demonstrate the enhanced efficiency of steam bubble transport. The thermodynamically controlled substitution transport of steam bubbles is more efficient than the conventional capillarity-controlled metamorphic transport of air bubbles. This is another factor contributing to the enhancement of steam-phase relative permeabilities.

Despite the qualitative consistency with most earlier studies in this preliminary investigation, more rigorous assumptions and theoretical studies are suggested to model and compare the results obtained from these experiments. In addition, no steam-water relative permeability results in fractured media have been reported, to the best of our knowledge, due to the difficulties of the steam-water experiments and poor knowledge of fracture modeling for multiphase flows. Besides this theoretical study, we believe laboratory investigations of steam-water relative permeabilities in fractures can provide more detail insight of the physics and more practical engineering applications. Therefore, in the next chapter, we describe the results of steam-water flow experiments in fractures and discuss the effects of phase transformation and fracture roughness on steam-water relative permeabilities.

Chapter 6

Experimental Study of Steam-Water Flow in Fractures

In this chapter, we describe the steam-water flow experiments in fractures and compare the flow behavior and relative permeabilities difference between two-phase flow with and without phase transformation effects in smooth-walled and rough-walled fractures. The experimental system described in Chapter 3 was modified and improved in order to be operated at high temperature. Two-phase flow experiments with phase transformation effects (steam-water flow) were conducted. The porous medium approach was used to calculate two-phase relative permeabilities. These results are compared with the conventional air-water relative permeabilities measured in Chapter 3. The flow behavior and relative permeabilities difference between two-phase flow with and without phase transformation effects in smooth-walled and rough-walled fractures are discussed.

This chapter is structured as follows: we first describe the improvement of the apparatus and the automated measurement techniques, as well as the experimental procedures. Next, we report the experimental results, present the flow behavior images, and discuss the effects of phase transformation and fracture roughness on relative permeabilities. Finally, we compare our results with earlier studies and suggest a model for steam-water relative permeabilities.

6.1 Apparatus, Measurements and Procedure

The experimental system was modified from the air-water experiments described in Chapter 3. Identical fractures (smooth-walled, HR and RR fractures) were used. However, the steam-water flow experiment is more complex than an air-water experiment because the former has to be performed at high temperature, and there is a fundamental difficulty in measuring how much of the fluid flows as steam and how much as liquid. To this end, the whole system was designed to be conducted at an isothermal condition by installing the fracture apparatus inside an air bath, which maintained a constant temperature. All measurements were electronic and digitized by using a high-speed data-acquisition system and digital video recording system, as mentioned in Chapter 3. The whole experiment system is illustrated in Figure 6.1, which shows the deaerated water supply, the fracture apparatus (inside the air bath), data acquisition system, and digital image recording. The fracture descriptions and saturation measurement method remain the same as the air-water experiments in Chapter 3. Only the modified experimental methodology, components and procedure are discussed in this section. As shown in Figure 6.2, throughout the flow area, needle-sized temperature ports with the diameter of 0.02 inch were drilled to minimize surface discontinuity. Fourteen T-type thermocouples were installed in these temperature ports to measure the temperature distribution throughout the fracture during the steam-water experiments.

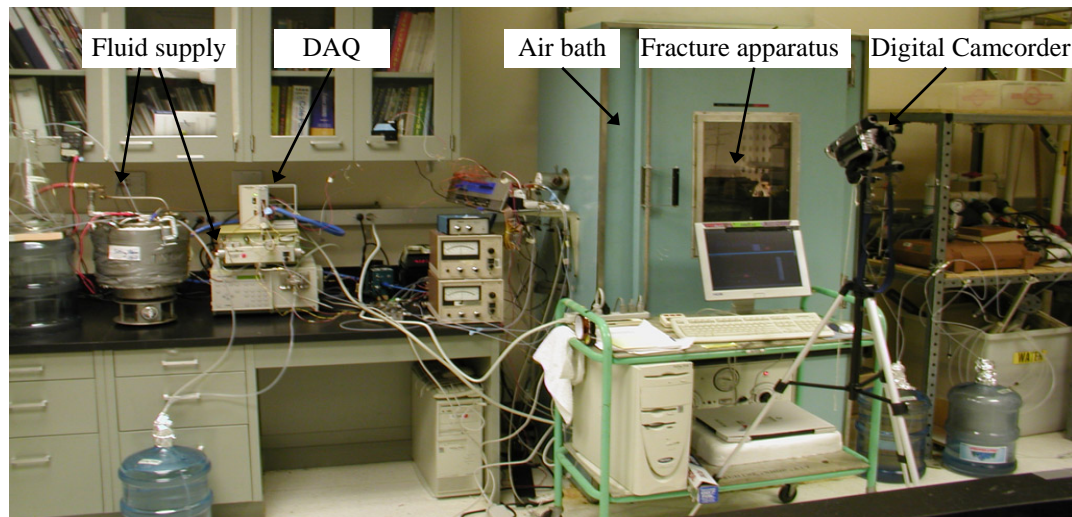
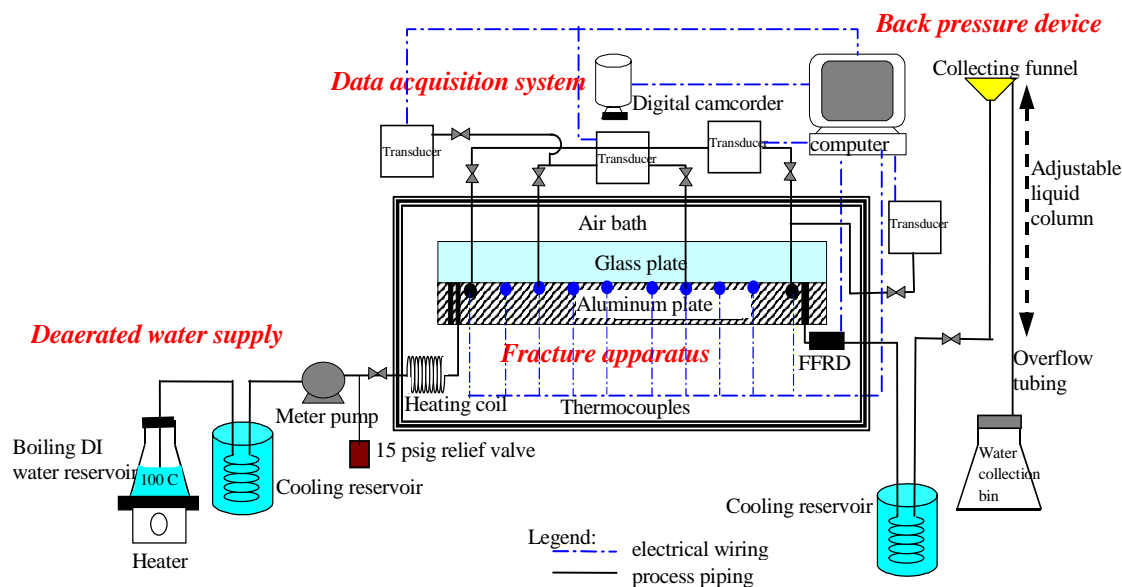


Figure 6.1: Process flow diagram and photograph for steam-water experiments.

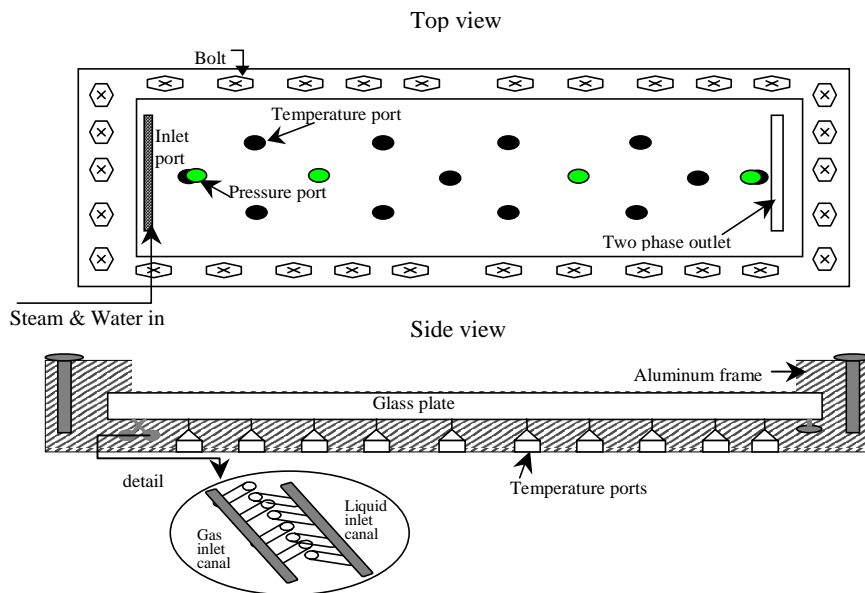


Figure 6.2: Schematic diagram of fracture apparatus for steam-water experiments.

6.1.1 Steam and Water Rates Measurements

One of the main challenges of the steam-water flow experiment was to measure the steam and water flow rates, since phase transition occurs when steam and water flow through the fracture. Therefore using flow meters to measure the rate of each phase becomes inappropriate, because it is always impossible to separate steam from water without any mass loss or gain. Therefore the FFRD technique described in Chapter 3 was used for this task. In order to minimize the heat loss, the FFRD device was installed as close to the outlet of the fracture as possible (about 1 inch distance). To catch the fast and unsteady steam and water segments in the outlet tubing, the FFRD was connected to the high-speed data acquisition system with 250Hz sampling frequency.

Once the steam and water responses were obtained from the FFRD, the statistical histogram was plotted, and then the steam and water phase flow ratios were obtained by

determining the threshold of the histogram. The outlet steam and water fractional flows, f_s and f_w , are defined as:

$$f_s = \frac{q_{out,s}}{q_{out,t}} \quad (6.1)$$

$$f_w = \frac{q_{out,w}}{q_{out,t}} \quad (6.2)$$

where $q_{out,s}$ is the output steam flow rate. As f_s and f_w are obtained, it is easy to evaluate $q_{out,s}$ and $q_{out,w}$ by using mass balance if a short-term steady condition is reached. The mass balance equation is:

$$m_{in} = q_{out,t}(f_w \rho_w + f_s \rho_s) \quad (6.3)$$

Substituting Equation (6.3) into Equations (6.1) and (6.2), the end-point steam and water flow rates are then given by:

$$q_{out,w} = f_w \frac{m_{in}}{f_w \rho_w + f_s \rho_s} \quad (6.4)$$

$$q_{out,s} = f_s \frac{m_{in}}{f_w \rho_w + f_s \rho_s} \quad (6.5)$$

The end-point steam quality is:

$$X_o = \frac{\rho_s q_{out,s}}{m_{in}} \quad (6.6)$$

where, m_{in} stands for the input mass, ρ is the density.

The flow rates obtained are end-point flow rates, which may differ from the representative rates due to the pressure and temperature change along the fracture.

Therefore, a further calculation is needed to obtain the center-point flow rates. Since the experiments were conducted under near-adiabatic conditions, and the temperature variations across the fracture (30 cm in length) recorded during the steam-water experiments were less than 0.5°C, the heat loss across the fracture was negligible. Using mass and energy balances with flat interface thermodynamics assumption, the steam quality (X) in the flow at any position would be given by:

$$X_x = \frac{L_{To}}{L_{Tx}} X_o + \frac{h_{Lo} - h_{Lx}}{L_{Tx}} \quad (6.7)$$

where L_T is the latent heat of vaporization at the prevailing temperature and pressure, and h_L refers to the liquid specific enthalpy, subscripts o and x denote the end-point and section x considered, respectively. The center-point steam quality was used to calculate the center-point flow rates of steam and water.

Though the FFRD method has demonstrated successful measurement as found in Chapter 3, it is necessary to discuss its limitations found during testing. The limitation of the FFRD method is that if the flow is in an extremely unsteady state, some mixed phase response will occur in the FFRD, and the calculated flow rates will become less accurate. However, if the flow is in a quasisteady state (i.e. the steam or water flow rate changes at a fairly slow rate), rates obtained by this method should approximate the real flow rates except for a short delay of the phase response. The experiments were conducted in a sequence of constant pressure steps to minimize the rapid, unstable flow.

6.1.2 Pressure Measurements

Pressure transducers were identical to those used in Chapter 3, but connected in a different arrangement. An important issue that affects the pressure measurement is phase transformation inside the pressure tubing. Since steam-water experiments were conducted at a temperature at the boiling point of water, the water-filled pressure tubing connected to the pressure transducers had a tendency to boil. This means both liquid water and

vapor coexist inside the pressure tubing. Insensitive and erratic pressure response was obtained due to the different compressibility in water and gas and the solubility of gas. To resolve this, additional outer cooling tubing was added to cool the pressure tubing to minimize this two-phase phenomenon. This cooling jacket quenches the tubing and maintains the content inside the inner tubing in the liquid phase (water). The plumbing of the pressure measurement is shown in Figure 6.3.

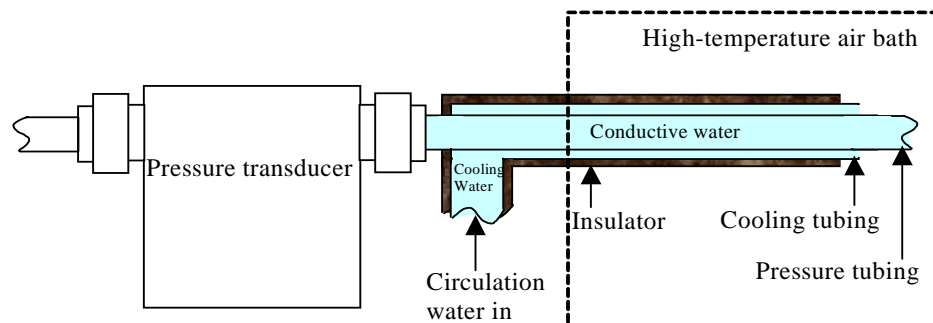


Figure 6.3: Improved plumbing of the pressure measurement to reduce two-phase problem.

6.1.3 Experimental Procedure

First, single-phase water flow experiments were conducted at 90°C to characterize the hydraulic properties of the fractures. These results can be found in Section 3.3.1 and Figures 3.14, to 3.16. After that, the steam-water flow experiments were conducted at 104°C in a drainage process.

From steam-water experiments conducted by earlier investigators, there are two methods available to produce steam-water flow inside the fracture. One method is by injecting steam and water separately into the apparatus [Counsil and Ramey, 1979; Satik 1998; O'Connor 2001]. The steam would be produced using a steam generator inside the air bath to boil steam from deaerated water. The other method is by injecting only

deareated water into the apparatus, after which the steam phase is produced by adjusting either pressure or temperature in the fracture to make the water boil [Piquemal, 1994]. Since the steam quality from a steam generator is hard to control, the heat loss from the steam generator to the fracture apparatus is hard to determine, and there is a significant phase transformation at the moment when the injected steam and water meet in the inlet port, the latter method was used in this experiment. First, the air bath was heated to 104°C, and then the fracture was fully saturated with water using a vacuum pump. Next, water was injected using a metered pump (Dynamax, SD-200, rates: 0.1-200 ml/min) which controlled the rate of injection. The water used in the experiment needs to be deareated almost completely. To reach this quality, distilled water was evacuated using a vacuum pump for 2 hours, and then the water was boiled to achieve a low dissolved-gas condition. The deareated water entered the air bath and then passed through a 6-feet long metal heating coil to reach the air bath temperature and produce two-phase conditions. A physical back-pressure device was connected to the outlet of the apparatus to constrain the pressure inside the fracture as shown in Figure 6.1. At the beginning of the experiment, the fracture pressure was set to be larger than the saturated pressure of water at air bath temperature, and then the fracture pressure was decreased in steps to generate two-phase conditions and increase the magnitude of the steam saturation. Within each pressure step, the two-phase flow data and video were not acquired until a repeatable flow structure and saturation variation were reached. This reduced the instability of the flow and hence decreased the experimental errors.

The high-speed data acquisition system gathered instantaneous pressure, temperature and flow rate. Instantaneous gathering of saturation data was accomplished by the use of the digital video camcorder and automatic image processing technique with faster than one-second frequency. The methodology and work flow used to integrate all the data and signals and then calculate relative permeabilities is illustrated in the flow chart in Figure 6.4.

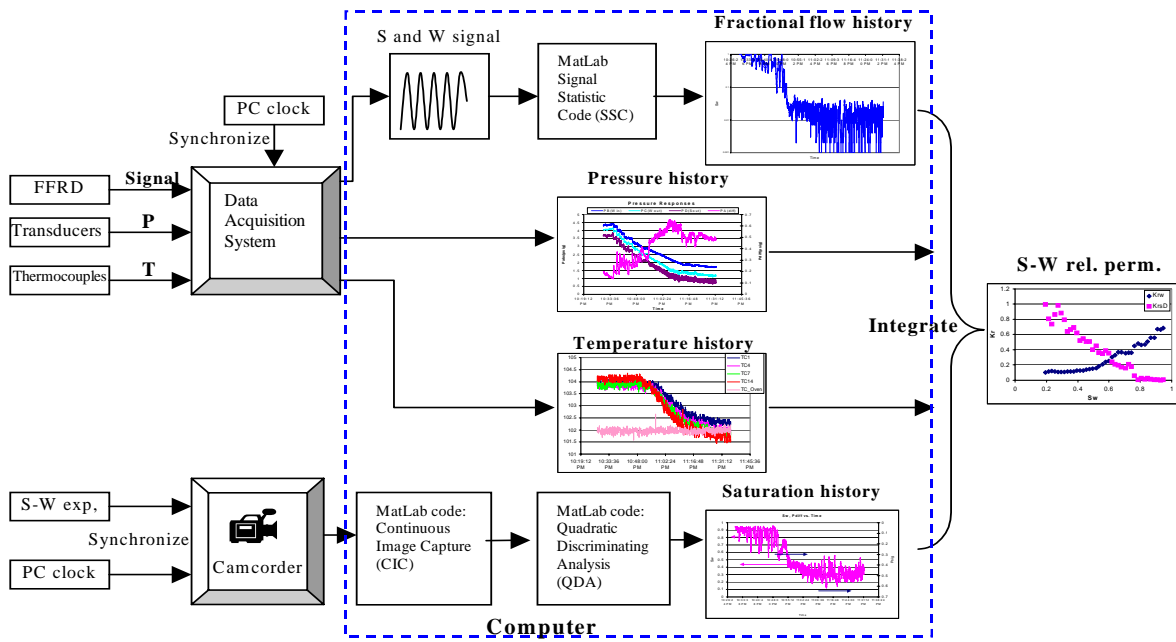


Figure 6.4: Data and signal processing flowchart for steam-water experiments.

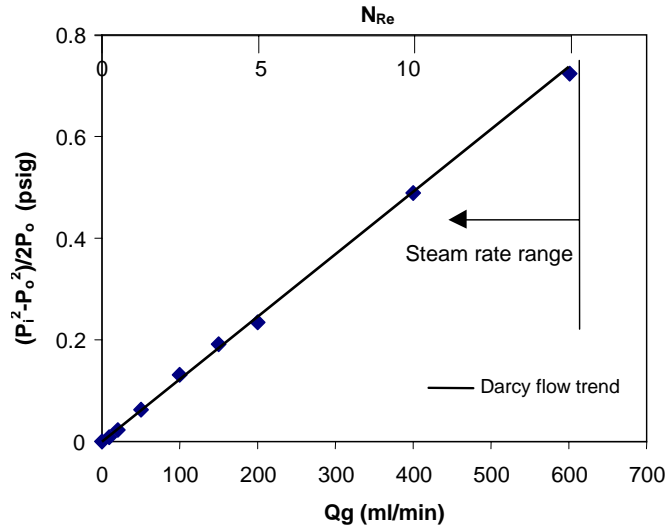
6.2 Results and Discussion

In this section, we present and compare the results from the smooth-walled, homogeneously rough-walled (HR) and randomly rough-walled (RR) fractures. The results of these three fractures from air-water experiments in Chapter 3 are used to compare with the steam-water results.

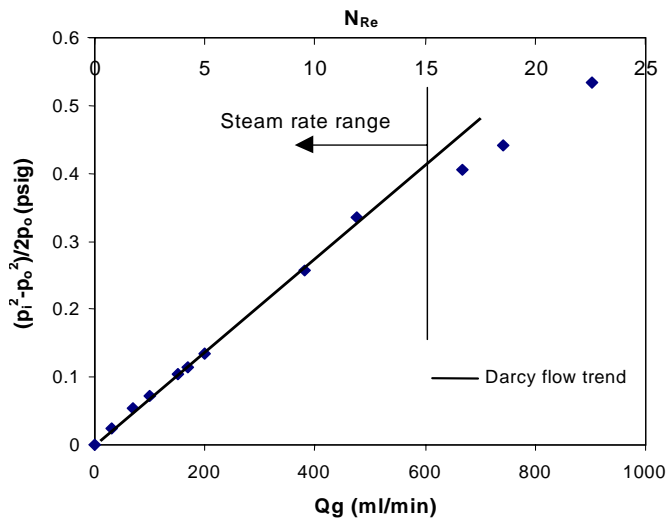
6.2.1 Effects of Non-Darcy Flow

Equations (2.6) and (2.7) assume that flow is laminar with negligible inertia effect, which means that pressure gradient or equivalent pressure gradient increase linearly with flow rates. As we illustrated in Figure 3.17, the air-water flow obeys Darcy behavior with Reynolds number less than 5. Earlier studies suggested that inertia forces contributed an additional term to the drag force that is quadratic in velocity when Reynolds number is greater than unity [Oseen, 1910; Kovscek et al., 1995]. Flow with significant inertia effects is commonly called non-Darcy flow [Forchheimer, 1901; Barree and Conway, 2003; Olson et al., 2003]. If the inertia effects are significant, a second-order velocity term is added to modified Darcy's equation. In our air-water studies, however, these effects appear to be insignificant for the flow in the three fractures studied. In the steam-water experiments, steam was produced by vaporizing the injected water. Though the maximum water rates used are less than 5 ml/min, the maximum steam rates (which can be calculated from the FFRD or estimated from the ideal gas law) are approximately 600 ml/min. As shown in Figure 6.5, the maximum steam rates in the smooth-walled and HR fractures stay close to the Darcy flow trend, although slightly non-Darcy flow occurs in the HR fracture around the end points of steam-phase relative permeability. The non-Darcy flow inspection for the RR fracture is unavailable due to damage of the rough surface before the inspection. Since the three cases have similar maximum steam rate and Reynolds number, we assumed the inertia effects for steam-water flow in the RR fracture were also insignificant. Therefore, we consider that Equations (2.6) and (2.7) are

appropriate in the steam-water studies conducted, and the gas inertia effects is insignificant, hence can be negligible.



(a) Smooth fracture



(b) HR fracture

Figure 6.5: Steady-state, gas-phase equivalent pressure drop versus flow rates in the (a) smooth-walled fracture with aperture of $130\mu\text{m}$, (b) HR fracture with aperture of approximately $145\mu\text{m}$. Corresponding Reynolds number is also provided in the secondary x-axis.

6.2.2 Flow Structures and Relative Permeabilities

The steady-state steam-water flow experiments were conducted at around 104°C. The continuous snapshots of the steam-water flow behavior in the smooth-walled fracture in different water saturation are shown in Figure 6.6. Each set of photographs contains a sequence of four snapshots 1 second apart. The flow regime under high water saturation conditions behaved similarly to the air-water case. As can be seen in the top photograph set in Figure 6.6, the steam phase flows in fast moving slugs; however, the shape of slugs is more amorphous than that in the air-water case. As the water saturation decreased further, the steam-water flow behavior became different from that of the air-water case under intermediate and low water saturations. As illustrated in the middle and bottom photograph sets in Figure 6.6, the steam can flow via slugs, bubbles, and channels. On the other hand, the water flows via water slugs, water bubbles, and water channels. Even under the low water saturation conditions, the steam-water flow is still unstable and no stable channels were formed. The steam phase and water phase can flow together in several different forms. This two-phase cocurrent flow situation was rarely seen in the air-water case.

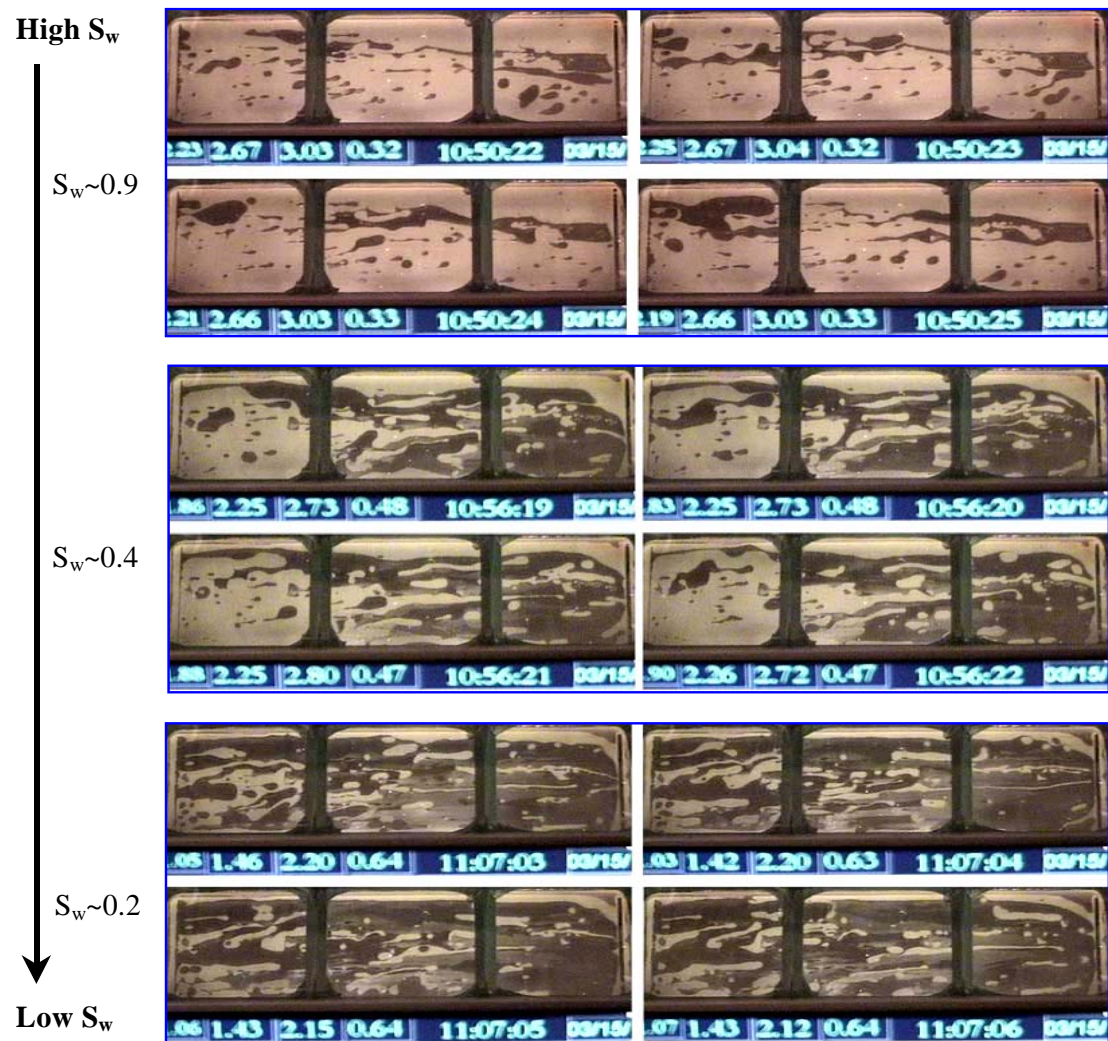


Figure 6.6: The continuous steam-water flow behavior in smooth-walled fracture. (steam phase is dark, water phase is light, flow is from left to right).

To compare the flow structure difference between the steam-water and air-water cases, Figures 6.7 and 6.8 summarize several typical flow structures observed during air-water and steam-water experiments in the smooth-walled, HR and RR fractures. The photographs in Figure 6.7 have water saturation close to 65%; whereas those in Figure 6.8 have water saturation close to 40%. The flow is from left to right. Gas phase is dark, and liquid phase is light. Generally, air-water flow forms relatively stable aggregate structures in comparison to the steam-water cases in these three fractures. The flow structures in the rough-walled fractures always behave in a more scattered and tortuous manner in comparison with the smooth-walled case. The aperture variation in the HR and RR fractures tend to entrap phases and increase capillary effects. Most of the entrapped gas phase contributes to the immobile phase saturation. On the other hand, some entrapped water phase becomes residual water ultimately.

In air-water flow, the air phase forms fairly stable channels (Figures 6.7a, 6.7c and 6.7e, Figures 6.8a, 6.8c and 6.8e), although those in the HR and RR fractures are multibranched and tortuous, especially in the RR fracture. On the other hand, almost no stable channels were found in steam-water cases. As can be seen in Figure 6.7b, the steam phase flows as fast moving slugs at $S_w \sim 65\%$ in the smooth-walled fracture. The shape of the slugs is amorphous. As S_w decreases further, the steam can flow via slugs, bubbles, and channels, whereas the water flows via water slugs, water bubbles, and water channels (Figure 6.8b). This unusual behavior was rarely seen in the air-water case. Considering the effect of fracture roughness, the mobile and immobile steam and water phases distributed more evenly through the flow area in the rough-walled fractures than in the smooth-walled fracture. This can be attributed to the capillary trapping mechanism and the in-place nucleation of immobile steam clusters throughout the fracture space.

At high S_w , these immobile, nucleated steam clusters result in a significant interference to water flow. These scattered clusters have larger surface area than air channels at the same S_w , hence generate larger resistance against water flow. Despite the fact that all of these experiments were conducted in the drainage process, and steam was

generated from the heating coil and then injected to the fractures accompanied by water, some in-site generation of immobile, nucleated steam clusters was still inevitable. These nucleated steam clusters would also form in real fractures and fractured rocks. According to thermodynamics and surface chemistry studies, the cavities and protrusions on the rough surface are favored locations for the formation of nucleated bubbles [Carey, 1992; Benjamin and Balakrishnan, 1997; Mann et al., 2001; Qi et al., 2004]. Since the rough glass used in this study was either homogeneously or randomly textured, the trapping and nucleation mechanism occurred more evenly (or randomly), as can be seen from the processed grayscale images in Figure 6.10. This nucleation of the vapor phase through the fracture occurring when the liquid approaches its saturated condition is one of the distinct characteristics of steam-water flow. However, at lower S_w (Figure 6.8d and 6.8f), most of these immobile steam clusters merge to flowing steam channels; therefore, the lowering effect on k_{rw} becomes weaker. Instead, the phase change prevails as shown in Figure 6.8d and 6.8f (indicated in white circles).

As mentioned previously, the automated high-speed data acquisition system and digital video processing enabled us to acquire the pressure, temperature, flow rates and saturation data with less than one-second frequency. The comprehensive, high-resolution relative permeabilities were calculated based on these acquired data using Equations (2.6) and (2.7). Figure 6.9 compares the comprehensive collection of steam-water relative permeabilities with air-water relative permeabilities in these three fractures. In the next section, we interpret the influences of these observed phenomena on steam-water relative permeabilities with respect to phase transformation effects (steam vs. air) and surface roughness (smooth-walled fracture vs. rough-walled fracture).

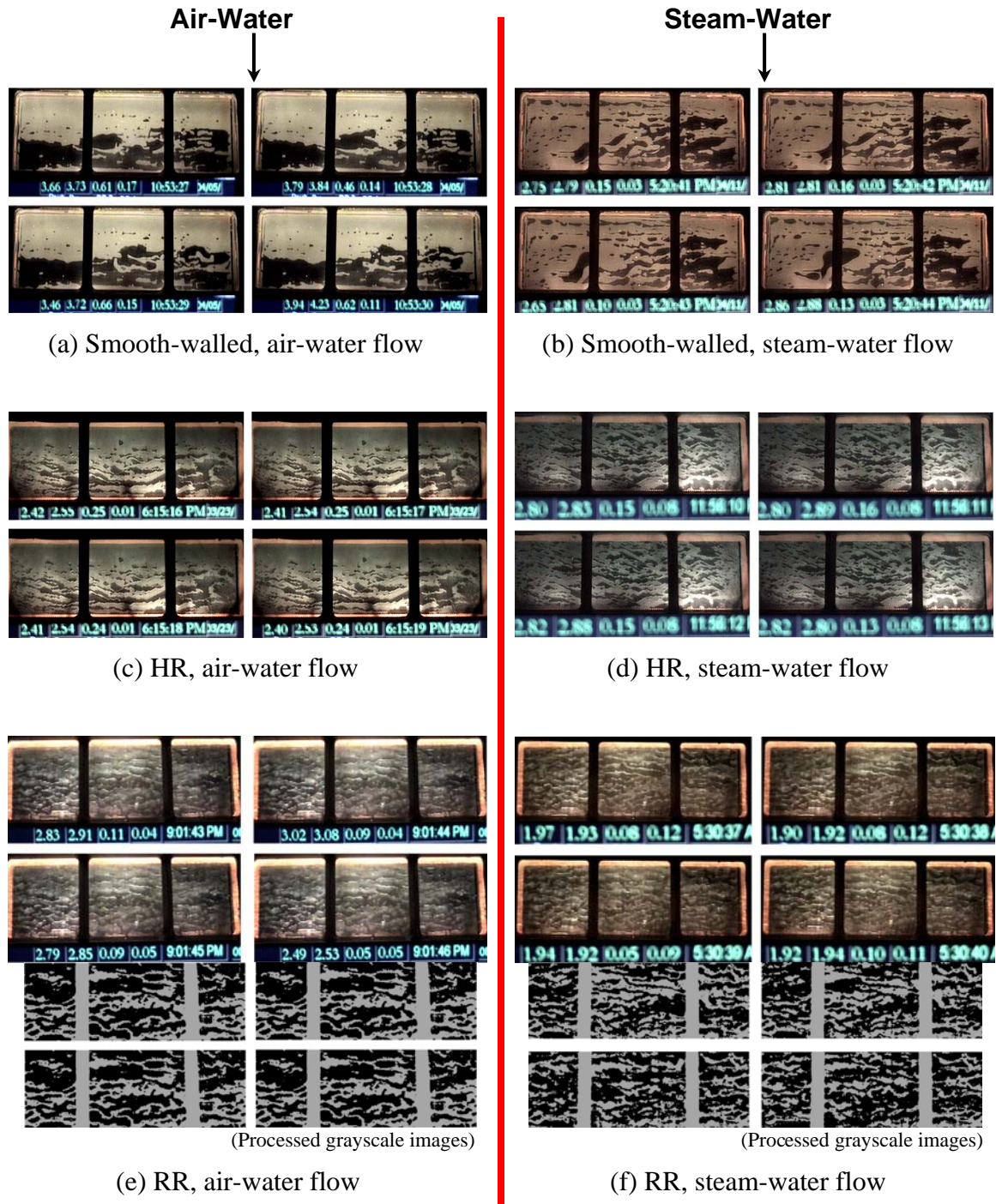


Figure 6.7: Sequence of snap-shots of air-water and steam-water flow behavior in smooth-walled, HR and RR fractures around 65% water saturation. The flow is from left to right. Gas phase is dark, liquid phase is light. Frame interval is one second. RR grayscale images are provided to enhance visualization.

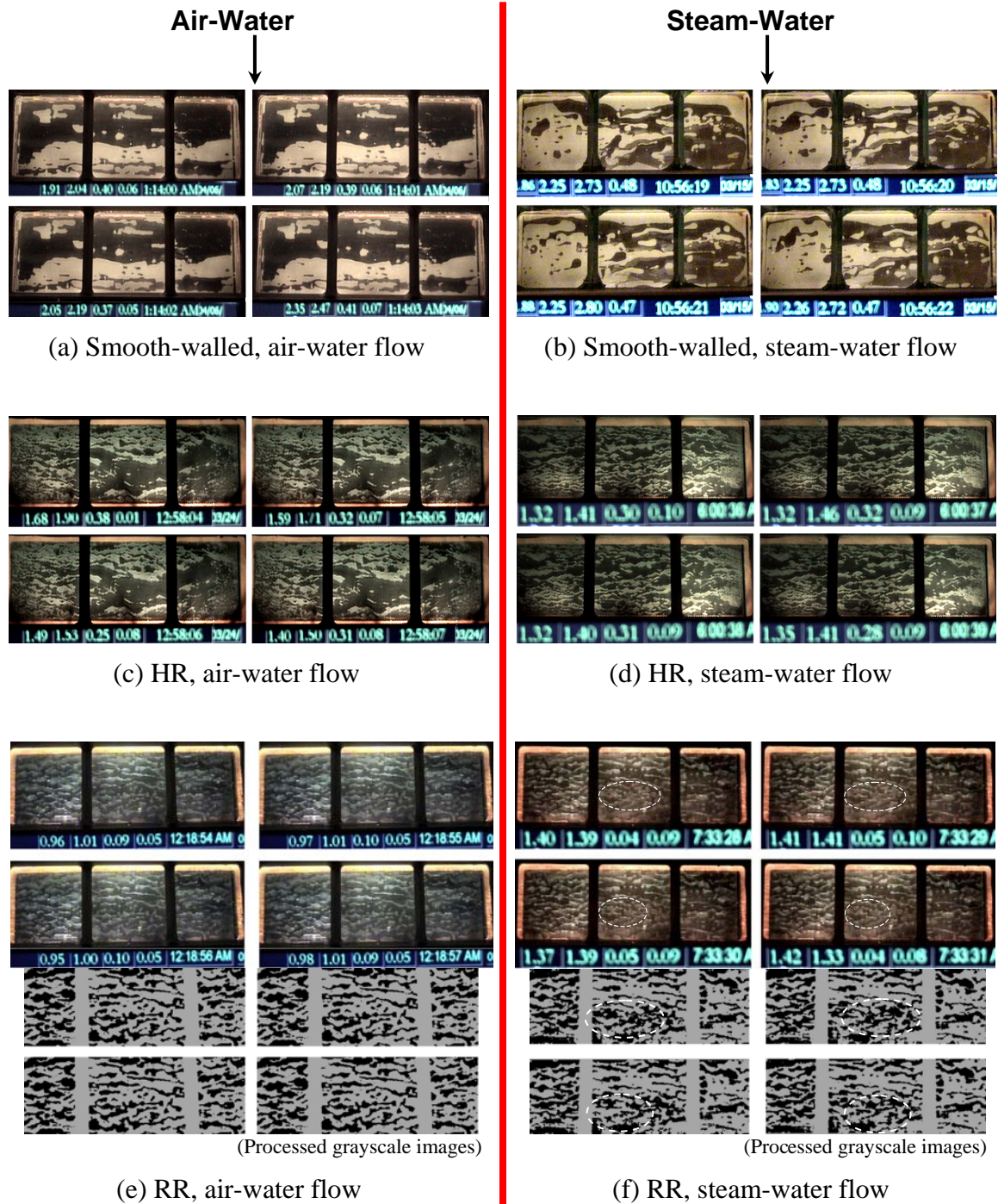


Figure 6.8: Sequence of snap-shots of air-water and steam-water flow behavior in smooth-walled, HR and RR fractures around 40% water saturation. Frame interval is one second. RR grayscale images are provided to enhance visualization.

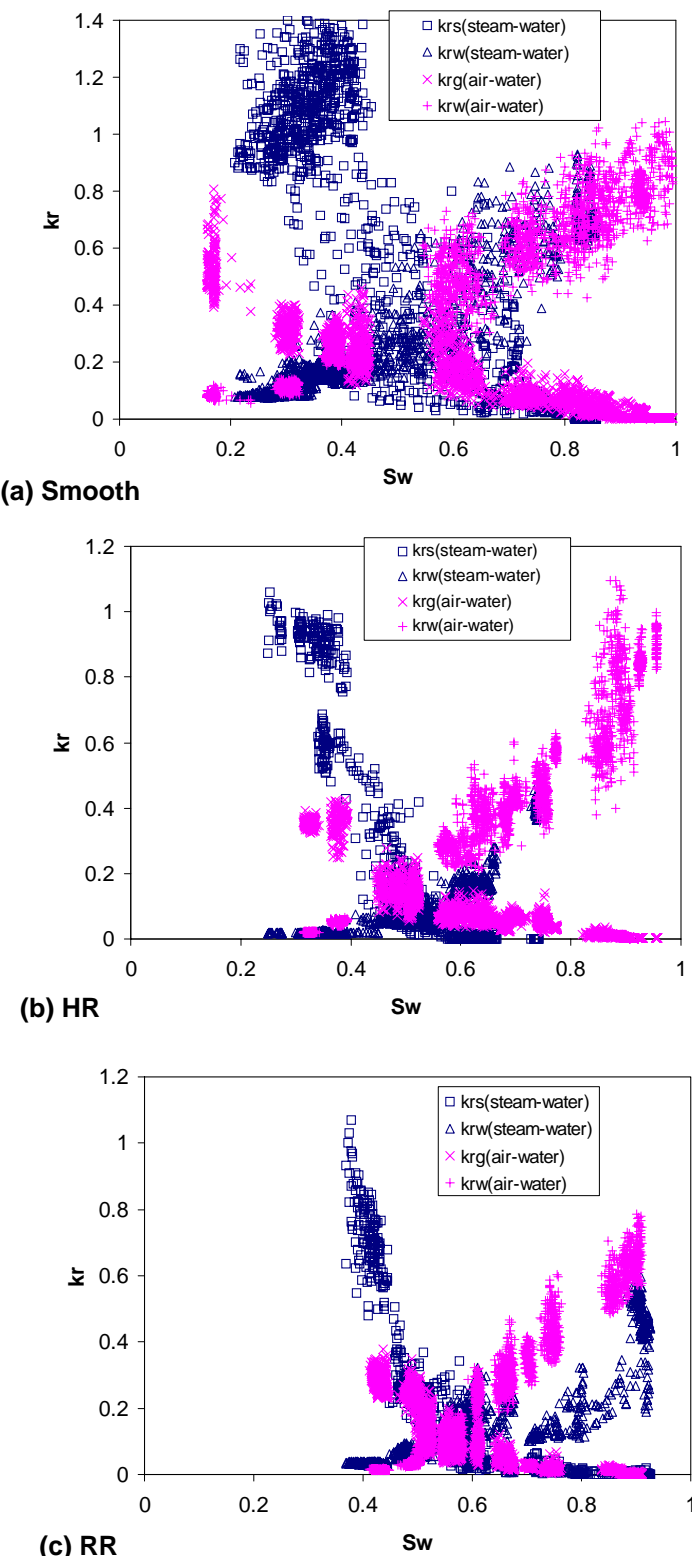


Figure 6.9: Comprehensive steam-water and air-water relative permeabilities: (a) smooth-walled fracture, (b) HR fracture, (c) RR fracture.

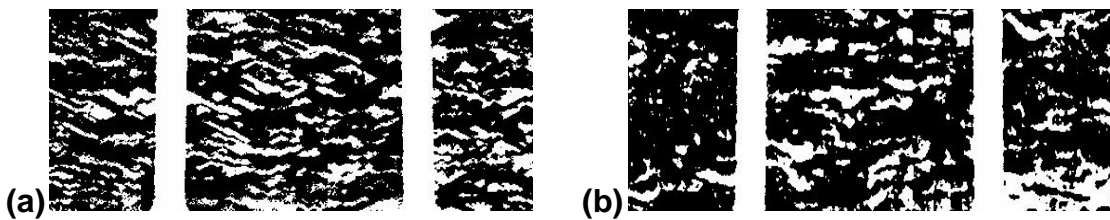


Figure 6.10: In-place nucleation of immobile steam clusters: (a) HR fracture, (b) RR fracture.

6.2.3 Effects of Phase Transformation

To gain better visual recognition, a window averaging technique was applied to the high-resolution results shown in Figure 6.9. Two repeated experiments were conducted for the steam-water flow in the HR fracture to demonstrate the repeatability and assure the quality control. Figure 6.11 compares the average relative permeabilities between steam-water and air-water cases in the three fractures studied. The curves on both plots show the approximate trends of the data.

In the smooth-walled fracture (Figure 6.11a), the liquid curves have similar trends, but the gas curves behave very differently. The steam curve shows a much more mobile character than the air curve, which can be seen from the higher relative permeability values in the steam curve.

In the rough-walled fractures (Figure 6.11b and 6.11c), steam-water relative permeabilities are subject to the in-place nucleated steam clusters as described in the previous section. These immobile saturations are characterized as the “immobile, nucleated steam saturation” (S_{gn}). The S_{gn} in the smooth-walled fracture is not clear; however, the S_{gn} is about 0.3 in the rough-walled results (Figure 6.11b and 6.11c), because the rough surfaces enhance the capillary trapping mechanism and facilitate in-place nucleation of steam clusters. Clearly shown in the steam-water cases in Figure 6.11b and 6.11c, within S_{gn} the k_{rw} curves are much lower than those curves in the air-

water cases since the nucleated steam clusters increase the resistance to the water flow. On the other hand, k_{rs} remains approximately zero within S_{gn} because there is almost no flowing steam. However, once $S_w < I - S_{gn}$, the k_{rs} curves increase to unity rapidly and surpass the k_{rg} curves, which shows consistency with the smooth-walled case. The phenomenon of enhanced steam mobility was also observed from the digital images. Under similar water flow rates and saturations, steam slugs tend to move faster than air slugs, which may reveal the effect of the phase transformation. This is qualitatively in accordance with our theoretical results in Chapter 5.

Some earlier studies proposed that the phase transformation effects lead the vapor phase to advance more efficiently and reduce the pressure drop across the flow channels, thus increasing steam permeability [Verma, 1986]. Our theoretical study in the previous chapter also confirms this. These effects were also observed and attributed to the condensation-vaporization effects with flux “short-circuiting” at liquid islands in unsaturated soils (Walker et al. 1981). However, no published theoretical or numerical results have confirmed these effects to our knowledge. Despite this, the enhancement of steam-phase relative permeability shows consistency with many of the experimental measurements in porous media, including those done by Arihara et al. [1976], Verma [1986], Satik [1998], Mahiya [1999] and O’Connor [2001].

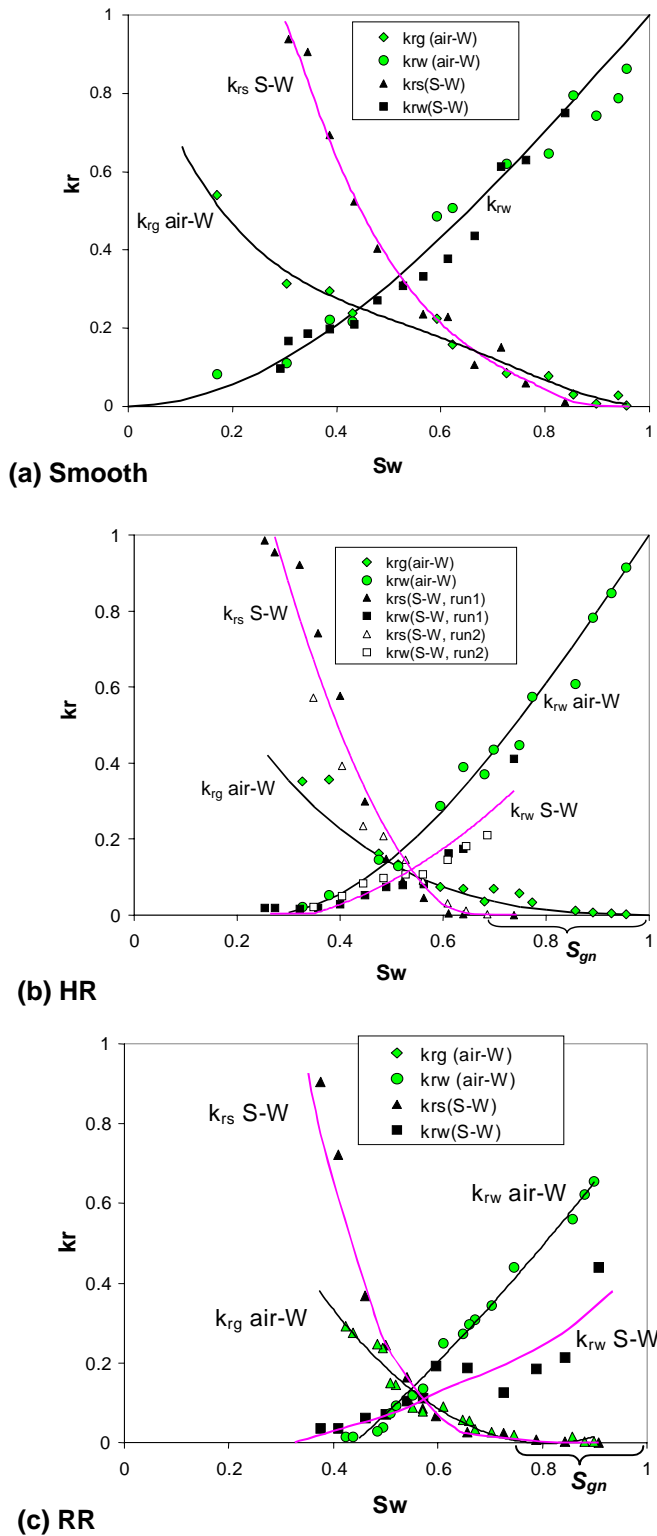


Figure 6.11: Comparison of average steam-water and air-water relative permeabilities:
(a) smooth-walled fracture, (b) HR fracture, (c) RR fracture.

6.2.4 Effects of Surface Roughness

To evaluate the effect of the surface roughness, Figure 6.11 was replotted for the steam-water relative permeabilities with different fracture roughness. Figure 6.12 compares the steam-water relative permeabilities among the smooth-walled, HR and RR fractures. The effects of surface roughness in k_{rw} curves are similar to the air-water case shown in Chapter 4 (Figure 4.16), but the magnitude of the differences seems to increase. From Figure 6.12, the rougher the fracture is, the more resistance to the water phase and the lower the k_{rw} curves. On the other hand, the k_{rs} curves exhibit an interesting feature. The k_{rs} curves become steeper as k_{rw} curves becomes lower, although the difference between the k_{rs} curves in HR fracture and that in RR fracture is not obvious. Moreover, the nucleated steam saturation S_{gn} increases in the rough-walled case due to more extensive in-place nucleation and subsequent trapping on the rough surface.

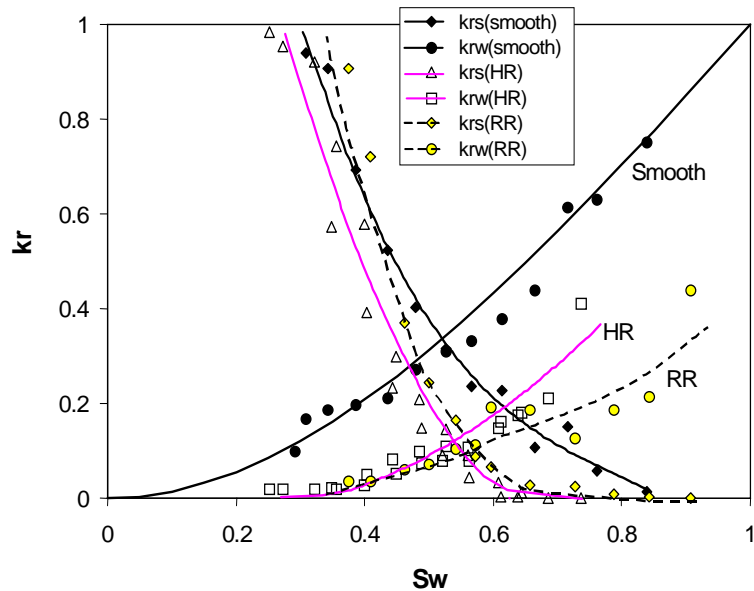


Figure 6.12: Comparison of average steam-water relative permeabilities in the smooth, HR and RR fractures.

6.3 Comparison with Earlier Results from Porous Media

Since there are no experimental studies of steam-water flow in fractures reported, to the best of our knowledge, a preliminary comparison of the steam-water results in the rough-walled fracture with earlier studies in porous media was made.

As shown in Figure 6.13a, the results from the rough-walled fractures conform to most of the porous media results. The steam-water relative permeabilities from the HR and RR fracture behave similarly to Satik's [1998] and O'Connor's [2001] results, respectively (see more detailed plots in Figure 6.13b and 6.13c). The steam-phase behaviors among these four cases are nearly identical. The large flat portion in k_{rs} (indicated in elliptic regions) may reveal that immobile, nucleated clusters also occur in Satik's and O'Connor's experiments. After this portion, k_{rs} data increase rapidly to one; therefore, conform to the enhanced k_{rs} suggested by earlier investigators [Verma 1986]. These results imply that steam-water relative permeabilities in rough fractures may share similar mechanisms to those in consolidated porous media, especially for the steam-phase curves.

On the other hand, the steam-phase result from Sanchez and Schechter [1987] shows less enhancement and a lower trend. Sanchez and Schechter asserted that there is no distinct difference between the steam-water and air-water relative permeabilities in unconsolidated porous media and suggested that the steam permeability may be represented accurately by air permeability under conditions of two-phase flow. This contradicts our results from the rough-walled fracture and most earlier results from porous media [Verma, 1986; Satik, 1998; Mahiya, 1999; O'Connor, 2001].

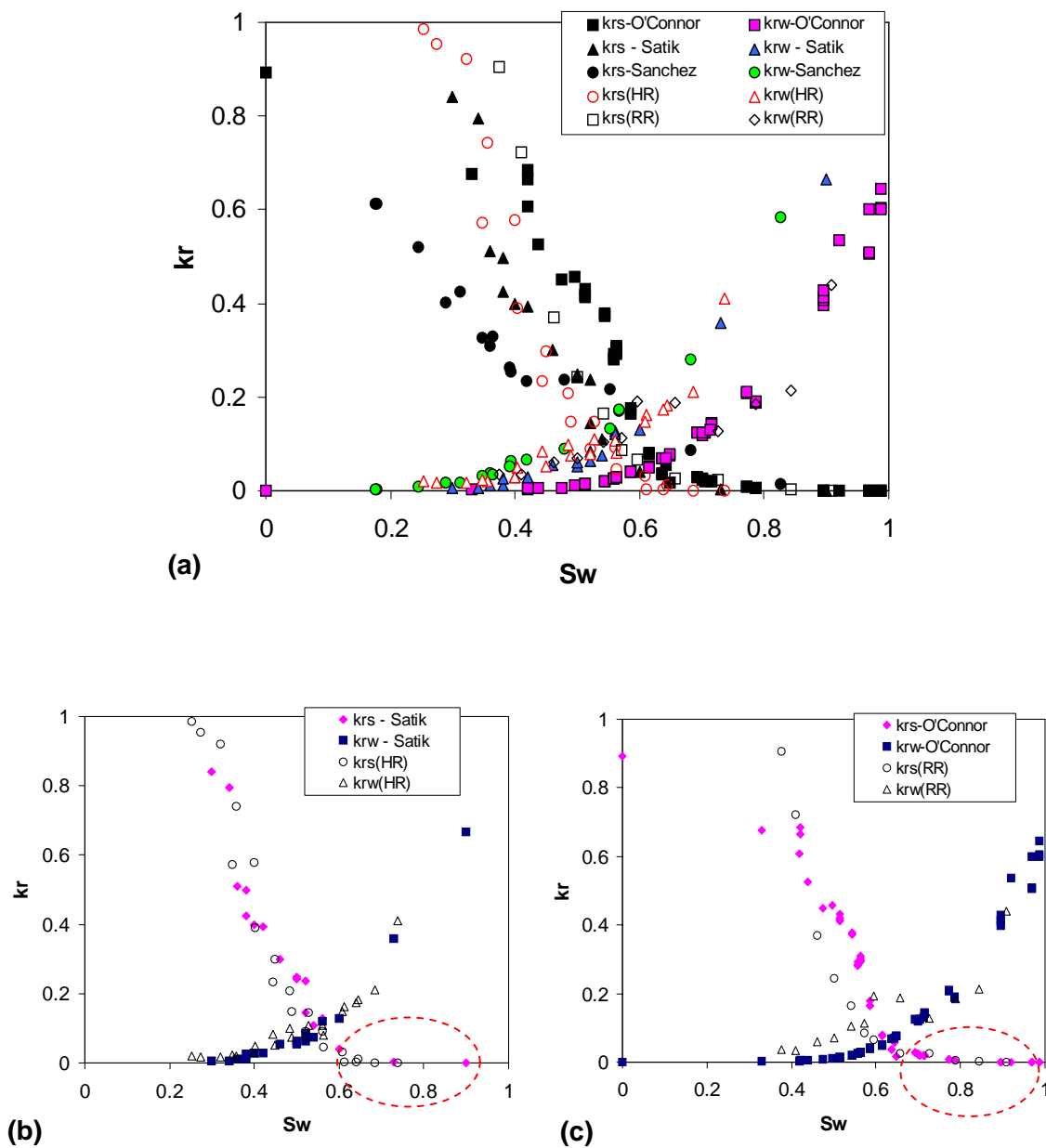


Figure 6.13: Comparison of average steam-water relative permeability in the rough-walled (HR and RR) fractures with earlier studies of steam-water relative permeability in porous media: (a) all data, (b) data from HR fracture versus Satik's, (c) data from RR fracture versus O'Connor's.

6.4 Relative Permeability Interpretations Using Known Models

As discussed in Section 2.2, three potential models for interpreting two-phase relative permeabilities in fractures are the X-model (Equations 2.9 and 2.10), Brooks-Corey fracture model (Equations 2.16 and 2.17) and Viscous Coupling model (Equations 2.18 and 2.19). The Tortuous Channel approach developed in Chapter 4 could not be applied in the steam-water case directly. As can be seen in Figure 6.6, the unstable steam and water flow via bubbles and slugs, instead of as connected channels which are the major element in the tortuous channel approach.

Since no models for steam-water relative permeabilities in fractures have been proposed, a qualitative comparison of these data with the existing traditional models can aid to explore the behavior of steam-water relative permeabilities further. The Brooks-Corey model was reported to describe steam-water relative permeabilities in porous media (Berea sandstone) with acceptable agreement [Satik, 1998]. As shown in Figure 6.14, the Brooks-Corey model from Equations (2.16) and (2.17) can describe the measured steam-water relative permeabilities in the HR and RR fractures acceptably by using residual saturations of $S_{wr}=0.25$, $S_{gr}=0.15$ for HR case and $S_{wr}=0.25$, $S_{gr}=0$ for RR case, whereas other models, the linear X-model and viscous-coupling models, cannot. However, when S_w is within the range of the nucleated saturation S_{gn} , the Brooks-Corey model performs worse in fitting both k_{rs} and k_{rw} (indicated via rectangular regions on the graphs), particularly for the RR fracture.

On the other hand, the Brooks-Corey model could not describe the steam-water relative permeabilities in the smooth-walled fracture satisfactorily. As shown in Figure 6.15a, the values of the water-phase relative permeability predicted are much smaller than the experimental results. Li and Horne [2002] obtained similar behavior in their steam-water relative permeabilities in a core of Berea sandstone and suggested that for the steam-water flow in porous media, the steam-phase relative permeabilities could be

represented by the Brooks-Corey model, whereas the water-phase relative permeabilities were represented better by the Purcell model. The Purcell model is given as:

$$k_{rw} = (S_w^*)^{(2+\lambda)/\lambda} \quad (6.8)$$

As $\lambda \rightarrow \infty$ for the fracture case, Equation (6.8) is reduced to the normalized linear curve:

$$k_{rw} = S_w^* \quad (6.9)$$

Figure 6.15b shows a comparison of the steam-water relative permeabilities in the smooth-walled fracture to the Brooks-Corey model (Equation 2.17) for the steam phase and the Purcell model (Equation 6.9) for the water phase. As can be seen, this combined model describes the smooth-walled results satisfactorily, which shows inconsistency with the interpretation of the results from the rough-walled fracture. The smooth-walled fracture was believed to be the most dissimilar from the porous media because it has almost no aperture variation. The applicability of using this combined porous media model to a smooth fracture is questionable. Furthermore, no other studies have confirmed this model in describing other data from porous media.

Figure 6.16 shows the fitting results of Satik's Berea sandstone data and Verma's sand pack data using the Brooks-Corey model. The Brooks-Corey model can describe Satik's data satisfactorily. However, in order to obtain the best fit, the pore size distribution index (λ) has to approach infinity, which is believed to be less representative for conventional porous media ($\lambda \sim 2$). Moreover, data from unconsolidated sand reported by Verma [1986] could not be fitted by the Brooks-Corey model at all. Figure 6.16 illustrates these fitting results. From the Brooks-Corey interpretations of the data in current fractured media and those published data from porous media, we doubt the feasibility of using it to predict the steam-water relative permeabilities in geothermal reservoirs. In addition, the previously-mentioned in-place nucleated steam cluster phenomenon seems to control the relative permeabilities in

some way. The proposed TCM in Chapter 4 also reveals a generalized behavior of conventional relative permeabilities in the fractures. In the next section, we incorporate these two considerations and proposed a modified TCM for steam-water relative permeabilities based on the magnitude of nucleated steam clusters.

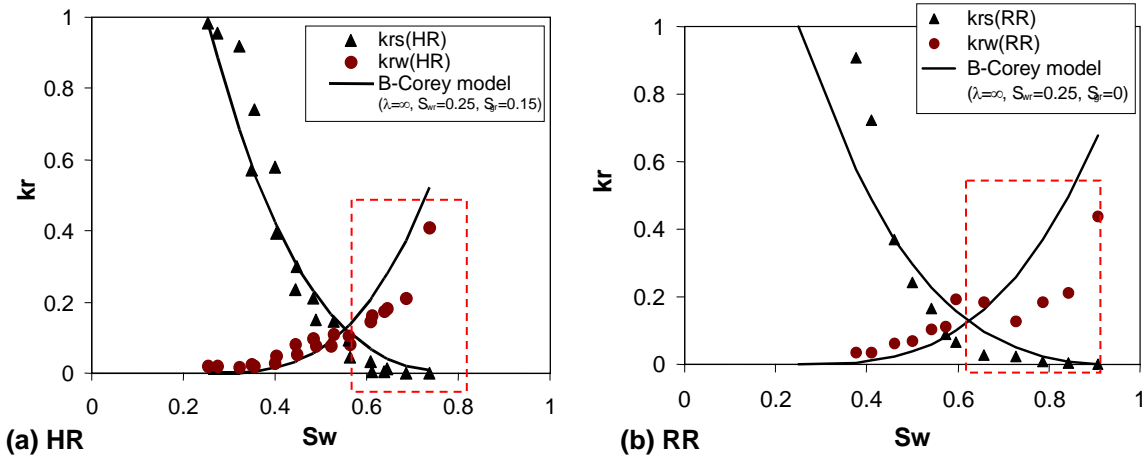


Figure 6.14: Comparison of average steam-water relative permeability in the (a) HR, and (b) RR fractures to the Brooks-Corey model.

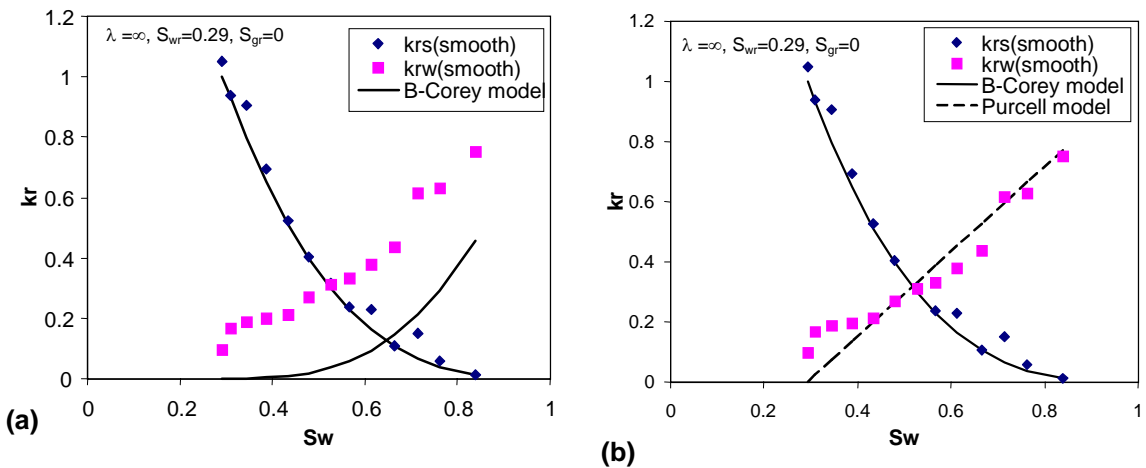


Figure 6.15: Comparison of average steam-water relative permeability in the smooth-walled fracture to (a) Brooks-Corey model, (b) Brooks-Corey model for the steam phase and Purcell model for the water phase.

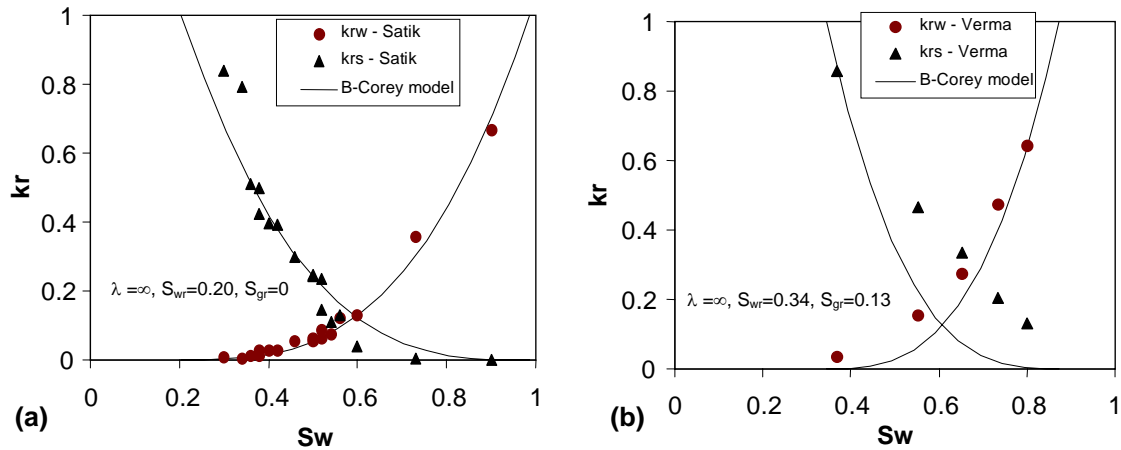


Figure 6.16: Interpretation of published steam-water relative permeability in porous media using the Brooks-Corey model: (a) data from Satik [1998] measured in Berea sandstone, (b) date from Verma [1986] measured in unconsolidated sand.

6.5 Modeling Steam-Water Relative Permeability Using Modified Tortuous Channel Model (MTCM)

As stated, no theoretical models have been reported to predict the steam-water relative permeability in fractures, owing to the complexity of modeling the phase transformation effects and including the thermodynamic and surface chemical properties of both steam and water. Although a preliminary theoretical concept of steam-water relative permeabilities has been built in Chapter 5, efforts are still needed to extend it in modeling practical steam-water flow in complex geometries such as porous and fractured media. Nevertheless, the information obtained during flow visualization may aid us to study the steam-water behavior phenomenologically.

The air-water relative permeabilities in the fractures has been modeled successfully using the proposed Tortuous-Channel approach (TCA) based on characterizing connected flowing channels as discussed in Chapter 4. Generalizing from the tortuosity analysis in the three fractures studied, we proposed an empirical Tortuous-Channel model (TCM) to predict the air-water relative permeabilities in fractures. The TCM is given as:

$$k_{rw} = 0.74S_w^{*2} + 0.26S_w^* \quad (6.10)$$

$$k_{rg} = 0.43S_g^3 + 0.38S_g^2 + 0.19S_g \quad (6.11)$$

where S_w^* is normalized water saturation defined as

$$S_w^* = \frac{S_w - S_{wr}}{1 - S_{wr}} \quad (6.12)$$

In the steam-water case, we found that some parts of “instantaneous” steam flow signatures in rough-walled fractures are similar to the air flow signatures under similar S_w , aside from the unstable flow behavior and nucleated steam clusters. Some of these signatures are revealed in comparing Figure 6.7e with 6.7f and Figures 6.8e with Figures 6.8f. Therefore, we may use the TCM as the base functions for deriving the steam-water relative permeabilities.

As can be seen in Figure 6.11a, the k_{rw} curve in the steam-water case is almost identical to that in the air-water case for the smooth-walled fracture. However, when fracture surface roughness and heterogeneity increase, as those in rough-walled case, the k_{rw} curves in steam-water case are lower than those in the air-water cases. We proposed that this lowering behavior is due to the in-place nucleation of immobile steam clusters which can be quantified by using the immobile nucleated steam saturation S_{gn} as discussed in Section 6.2.3. On the other hand, the k_{rs} curves start the sharp increase at $S_w=1-S_{gn}$ and then reach unity ($k_{rs}\sim 1$) at $S_w=S_{wr}$. This is also observed in other published data obtained in porous media (see Figure 6.13). Therefore, the S_{gn} is

considered not only as a reduction factor in lowering k_{rw} curve but as a turning point in enhancing k_{rs} curves in comparison with the air-water cases. To describe steam-water relative permeabilities correctly, the unique parameter of S_{gn} has to be considered. Therefore, we proposed a modified Tortuous-Channel model (MTCM) for modeling steam-water relative permeabilities in fractures by including the parameter of S_{gn} . The MTCM modifying Equations (6.10) and (6.11) by adding a reduction factor to the k_{rw} function and accounting for the immobile nucleated steam saturation S_{gn} in the k_{rs} function is expressed as:

$$k_{rw} = (1 - S_{gn})(0.74S_w^{*2} + 0.26S_w^*) \quad (6.13)$$

$$k_{rs} = 0.43S_g^{*3} + 0.38S_g^{*2} + 0.19S_g^* \quad (6.14)$$

where S_g^* is normalized gas saturation defined as:

$$S_g^* = \frac{1 - S_w - S_{gn}}{1 - S_{wr} - S_{gn}} \quad (6.15)$$

Comparing Equation (6.13) to Equation (6.10), the first term in Equation (6.13) serves as a reduction factor for lowering k_{rw} curves due to the immobile steam clusters. Equation (6.14) has the same form as Equation (6.11), except for the newly defined normalized gas saturation. The definition of the normalized gas saturation incorporated the parameter of S_{gn} ; hence, the k_{rs} function in Equation (6.14) starts at $S_w=1-S_{gn}$ and increases to unity at $S_w=S_{wr}$. These prescriptions are consistent with the general behavior of our observation and measurements.

Subsequently, the proposed MTCM were used to describe the steam-water relative permeabilities from smooth, HR and RR fractures (current study), as well as consolidated Berea sandstone [Satik, 1998] and unconsolidated sand [Verma 1986]. The fitting results are shown in Figure 6.17. Comparing these results to the Brooks-Corey model in Figures 6.14 to 6.16, the MCTM interprets all these data in good agreement not only for those that could be described by the Brooks-Corey model, but also for those in

which the Brooks-Corey model failed (data from smooth-walled fracture and Verma's unconsolidated sand). Table 6.1 summarizes the fitting performance of the MTCM and Brooks-Corey model by means of the mean absolute errors (MAE). The optimal fitting parameters were also provided. As shown in Equations (6.13) to (6.15), the MTCM only needs two parameters (S_{wr} and S_{gn}) to fully describe the steam-water relative permeabilities in the cases studied, while the Brooks-Corey model needs three parameters and still cannot describe those data successfully. Judging from the mean absolute error (MAE) between these two models, the MTCM fits most of these data much better than the Brooks-Corey model. Hence, the MTCM may have better modeling power for steam-water relative permeabilities for both porous and fractured media, based on the data available currently.

It is important to address the power of prediction by using MTCM. One important issue of predicting the steam-water relative permeabilities in the future is the determination of S_{gn} . Table 6.1 and Figure 6.13 reveal that the S_{gn} is around 0.3 for the rough-walled fracture and the Berea sandstone core studied. However, the data of unconsolidated sand provided by Verma [1986] indicated negligible in-place nucleation effects ($S_{gn}=0$), which we thought only occurs in a perfectly smooth-walled fracture since the nucleated bubbles is deemed to be trapped much easier in a pore-throat configuration formed by sand grains.

Table 6.1: Statistical comparison of fitting performance and corresponding optimal fitting parameters between proposed MTCM and Brooks-Corey model.

Media types	Brooks-Corey model				MTCM		
	<i>MAE</i>	S_{wr}	S_{gr}	λ	<i>MAE</i>	S_{wr}	S_{gn}
<i>Smooth fracture</i>	3.38	0.29	0	∞	2.24	0.20	0
<i>HR fracture</i>	2.05	0.25	0.15	∞	1.80	0.25	0.31
<i>RR fracture</i>	2.14	0.25	0	∞	1.04	0.36	0.32
<i>Berea Sandstone</i> (Satik, 1998)	1.05	0.20	0	∞	1.32	0.26	0.31
<i>Unconsolidated sand</i> (Verma, 1986)	1.09	0.34	0.13	∞	0.40	0.33	0

MAE: mean absolute error = $mean(|k_{r,exp} - k_{r,model}|)$

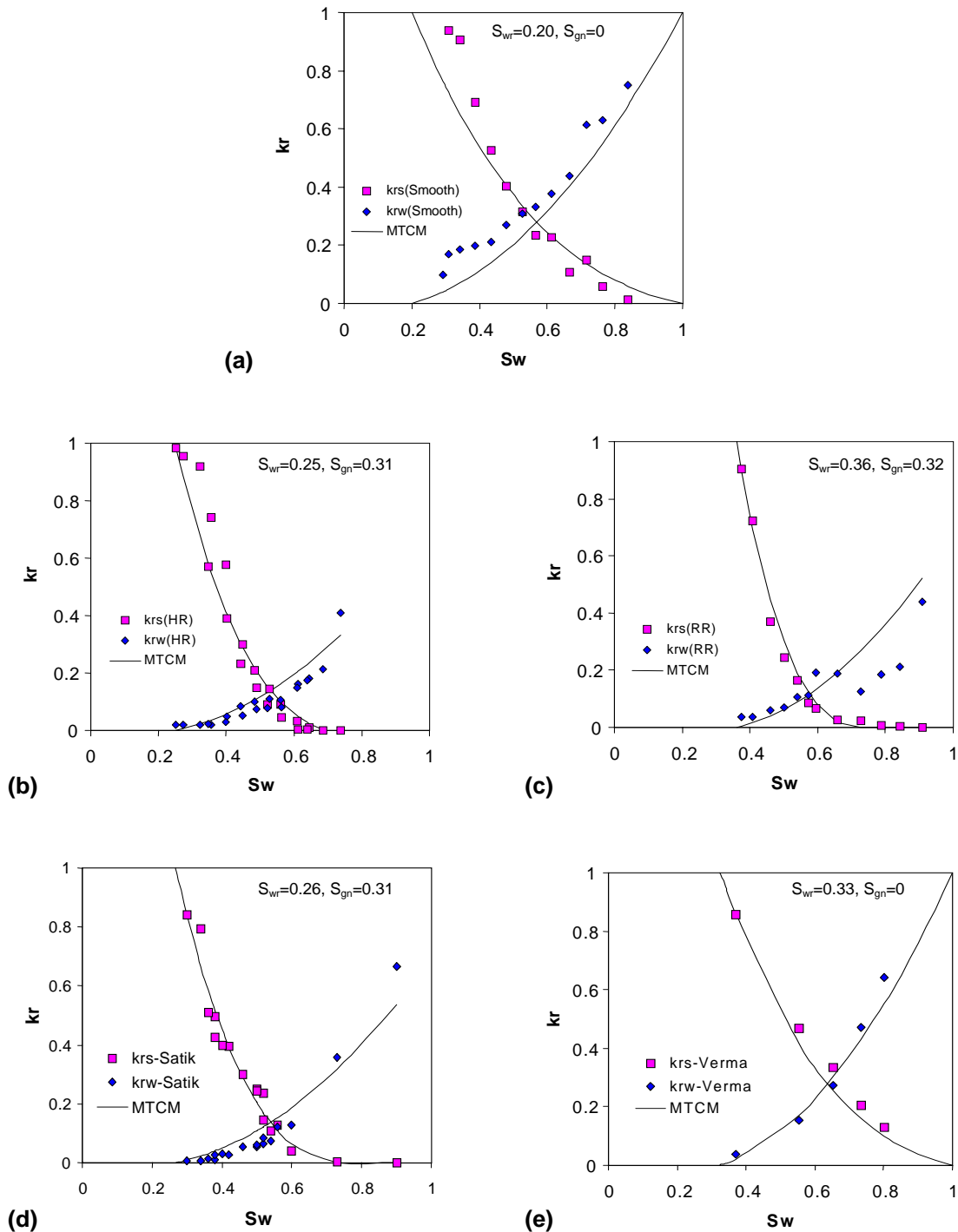


Figure 6.17: Interpretations of steam-water relative permeabilities using MTCM: (a) smooth-walled fracture data, (b) HR fracture data, (c) RR fracture data, (d) Berea sandstone data from Satik [1998], (e) unconsolidated sand data from Verma [1986].

6.6 Chapter Summary

The steam-water flow behavior in fractures is different from that of air-water flow. In the smooth-walled fracture, steam and water can flow in multiple patterns (bubbles, slugs and channels) simultaneously and both phases can flow concurrently; however, they never form stable flow structures. Contrarily, air and water have the tendency to form their own flow paths and block each other. Due to the capillary trapping mechanism, more immobile phase was found in the rough-walled case, as expected.

Extensive steam nucleation on the rough-walled surfaces was observed from the flow video. This effect generates the nucleated steam clusters, which is a distinct characteristic of the steam-water flow. Most of these nucleated steam clusters are trapped as immobile phase on the rough surface at high water saturation. This contributes to the steam phase saturation and increases the resistance against water flow. Based on the results from the three fractures studied, steam-water relative permeabilities are different from air-water relative permeabilities. Water phase curves in the steam-water cases are lower than those in the air-water cases due to the additional resistance contributed by the nucleated steam saturation S_{gn} . Steam-phase curves show less phase interference in comparison to the air-phase curves, which can be attributed to the effects of phase transformation referred to in Chapter 5. This enhanced steam permeability shows consistency with most earlier studies in porous media as well as our theoretical study in the previous chapter. By modifying the Brooks-Corey relative permeability functions to expressions for fractured media ($\lambda \rightarrow \infty$), the steam-water relative permeability in the HR and RR fracture seems to be represented acceptably by such expressions; however the smooth-walled result and some published results could not. Therefore, using Brooks-Corey type curves to model steam-water relative permeabilities as suggested in earlier studies in both fractured and porous media is questionable.

In this study, we defined the immobile, nucleated steam saturation (S_{gn}) as an additional parameter controlling the behavior of steam-water relative permeability, based

on analyzing the relationship between the visualized flow behavior and the corresponding relative permeabilities. The S_{gn} is considered not only as a reduction factor for water phase but also as a turning point in enhancing the steam phase mobility in comparison with the air-water cases. After incorporating the S_{gn} in the previously developed TCM for air-water flow, the proposed MTCM can describe not only the steam-water relative permeabilities from smooth, HR and RR fractures studied currently, but also the earlier results from consolidated Berea sandstone [Satik, 1998] and unconsolidated sand [Verma 1986].

Chapter 7

Verification and Improvement of a Field-Scale (Shinohara) Method

As is well known in earth sciences, the outcome of any physical interaction among wetting fluid, nonwetting fluid and rock in geologically complex fractured media depends highly on the length scales studied. Therefore, knowledge of the field-scale relative permeabilities of steam and water provide more direct and accurate information in estimating the performance of a geothermal field and its capacity for further exploitation.

In this chapter, we first use the experimental data from the previous chapter to verify and calibrate a field-scale method in inferring steam-water relative permeabilities from production data, called Shinohara method [Shinohara, 1978]. After that, actual production data from two active geothermal fields, The Geysers and Salton Sea, in California are used to calculate the relative permeabilities of steam and water. This provides better understanding of the fluid flow interactions in actual geothermal reservoirs.

**Special acknowledgment goes to former graduate student Jericho Reyes for analyzing field production data and contributing to part of this chapter. Some of this work was described in Reyes, Chen, Li and Horne (2004).*

7.1 Background

There have been numerous attempts to characterize the steam and water relative permeability curves both experimentally and theoretically. The main difficulty of direct measurement has been the phase changes that occur during steam and water multiphase flow. Current research on steam-water relative permeability in fractures (Chapter 5 and 6) gives us some insight on the characteristics of the interaction of these two phases.

In the previous chapters, we developed a method to compare steam- and air-water transport through single fractures. The main finding was that steam-water flow behavior in fractures is different from air-water flow. The laboratory-scale production data, saturations and relative permeabilities we acquired are used as verification data sets in this chapter. Aside from these laboratory data, field-scale data were obtained from the DOGGR database, which has been made available publicly by the California Division of Oil, Gas and Geothermal Resources. The database contains production histories of, among others, The Geysers and Salton Sea geothermal wells. The data include temperature, pressure, and steam and water production rates. These parameters were used in this study. The Geysers Geothermal Field, a vapor-dominated reservoir field, is located in Northern California about 130 km north of San Francisco. The Salton Sea Geothermal Field, a liquid-dominated reservoir field, is located in Imperial County in Southern California.

7.2 Method

Based on an earlier method due to Grant (1977), Shinohara (1978) described a method to estimate the steam and water relative permeabilities in geothermal reservoirs using field data, and applied this method to production data from the Wairakei geothermal field in New Zealand. This method is simple and useful, in that it only needs the production flow

rate history and the temperature of the reservoir, as well as the ability to evaluate each well separately. Some of the assumptions of this method are:

1. The pressure gradient is constant for a reasonable time in each well.
2. The product of permeability and flowing area is constant in each well.
3. Fluid flow follows Darcy's law.
4. Flow to the well is predominantly horizontal.

Under these assumptions, the steam-water flow in a geothermal reservoir follows Darcy's law:

$$Q_w = \rho_w \frac{k}{\mu_w} k_{rw} A p' \quad (7.1)$$

$$Q_s = \rho_s \frac{k}{\mu_s} k_{rs} A p' \quad (7.2)$$

where Q is the mass flow rate, ρ is the density, μ is the dynamic viscosity, k_r is the relative permeability, k is the absolute permeability of the geothermal rock, A is the cross sectional area of flow, and p' is the pressure gradient. The subscript (w) and (s) refer to water and steam respectively.

Dividing Equation (7.1) by Equation (7.2) gives us:

$$\frac{Q_w}{Q_s} = \frac{\nu_s}{\nu_w} \frac{k_{rw}}{k_{rs}} \quad (7.3)$$

where ν is the kinematic viscosity. Taking the sum of Equations (7.1) and (7.2) gives us:

$$Q = Q_w + Q_s = \left(\rho_w \frac{k_{rw}}{\mu_w} + \rho_s \frac{k_{rs}}{\mu_s} \right) k A p' = \left(\frac{k_{rs}}{\nu_s} \right) \left[1 + \left(\frac{Q_w}{Q_s} \right) \right] k A p' \quad (7.4)$$

where Q is the total of mass production rate of steam and water.

If we assume kAp' is constant in each well, then Equation (7.4) shows that a plot of Q vs Q_w/Q_s would be almost linear when Q_w/Q_s is small, and we can find the value of kAp' from either the intercept or the gradient of the line on the graph. This intercept, where $Q_w/Q_s = 0$, becomes Q^* , where:

$$Q^* = \frac{1}{v_s} kAp' \quad (7.5)$$

Because $k_{rs} = 1$ at $Q_w = 0$, then, substituting Equation (7.5) into Equations (7.1) and (7.2),

$$k_{rw} = \left(\frac{v_w}{v_s} \right) \left(\frac{Q_w}{Q^*} \right) \quad (7.6)$$

$$k_{rs} = \frac{Q_s}{Q^*} \quad (7.7)$$

Therefore knowing Q^* , we can calculate k_{rs} and k_{rw} by also knowing Q_w , Q_s , v_s , and v_w . Unfortunately, the actual in-place water saturation cannot be inferred merely from the production data in actual geothermal reservoirs. To estimate water saturation using the production data only, the volumetric ratios can be used to infer the reservoir water saturation in the absence of residual saturation and for homogeneous flow of both phases. This estimated water saturation is called the *flowing* water saturation in geothermal engineering, and can be calculated from:

$$S_{w,f} = \frac{(1-X)v_w}{(1-X)v_w + Xv_s} = \left(1 + \frac{1}{\mu_r} \frac{k_{rs}}{k_{rw}} \right)^{-1} \quad (7.8)$$

Hence, the relative permeability ratio can be expressed as

$$\frac{k_{rs}}{k_{rw}} = \mu_r \left(\frac{1 - S_{w,f}}{S_{w,f}} \right) \quad (7.9)$$

where X is the mass fraction of steam and ν_w and ν_s is the specific volume of water and steam, respectively. By definition, this flowing saturation is identical to the *fractional flow* in the previous chapters. It must be understood that the flowing saturation is different from the actual in-place (*static*) saturation in a geothermal reservoir. This also reveals the main limitation of the Shinohara method; *the field production data carry no information about in-place saturation*. To overcome this problem, some representative correlation functions of in-place water saturation against flowing water saturation is needed. To avoid confusion, unless term “*flowing*” is used, the saturation used in this chapter denotes conventional in-place saturation (or static saturation). Note that the flowing saturation S_{wf} is equivalent to the fractional flow f_w described in Chapter 3.

In the next sections, we first present a verification of Shinohara’s method by applying it to the laboratory data from Chapter 6 in which the steam-water relative permeabilities were already known. Then, we apply this method to field data from The Geysers and Salton Sea geothermal fields and study possible correlation between flowing water saturations and in-place water saturations in these two fields.

7.3 Laboratory Verification

To confirm Shinohara’s method and examine the relationship between the flowing saturation and the actual in-place saturation, data from laboratory experiments conducted in Chapter 6 were used. The “production” data were obtained from the steam-water flow experiments in the smooth-walled fracture. As mentioned previously, the FFRD (fractional flow ratio detector) device and the temperature distribution along the fractures were used to calculate both steam and water production rates. Flow visualization and image processing techniques were used to determine the water saturation (in-place), and differential pressure transducers were used to measure the pressure drop through the artificial reservoir (a single fracture). We used this "production data" from the laboratory

to estimate relative permeabilities using Shinohara's method, and compared the results with those from the standard porous media approach provided in Chapter 6.

Since the pressure gradient in the laboratory scale experiment was not constant, we scaled the data to a constant pressure gradient prior to the calculations. Figure 7.1 shows the Q vs. Q_w/Q_s plot in the experiment. The y-intercept indicates the value of Q^* in Equation (7.5) is 0.0032 g/sec in this case. The steam-water relative permeabilities calculated from Shinohara's method (Equations 7.6 and 7.7) were compared with those from the porous media approach (Equations 7.1 and 7.2). A close agreement of relative permeability values from these two methods is shown in Figure 7.2. The steam-phase and water-phase values show less than 5% relative error between the two methods.

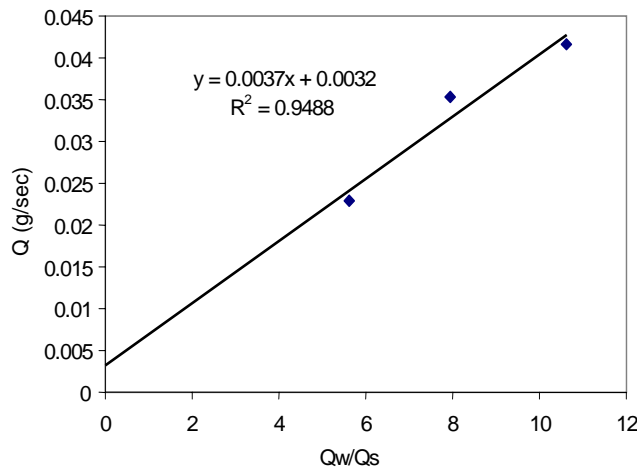


Figure 7.1: Q vs. Q_w/Q_s to infer Q^* for the steam-water experiment in smooth-walled fracture.

The relationship between flowing and in-place water saturations was examined by comparing the actual (in-place) water saturation measured in the experiment with the flowing water saturation calculated from Equation (7.8). From Figures 7.3 and 7.4, it is evident that the flowing water saturation is significantly less than the actual water saturation. As a result, the shape of relative permeability curves was compressed

leftward. The relationship between the two saturations can be expressed by a logarithmic trend as shown in Figure 7.4.

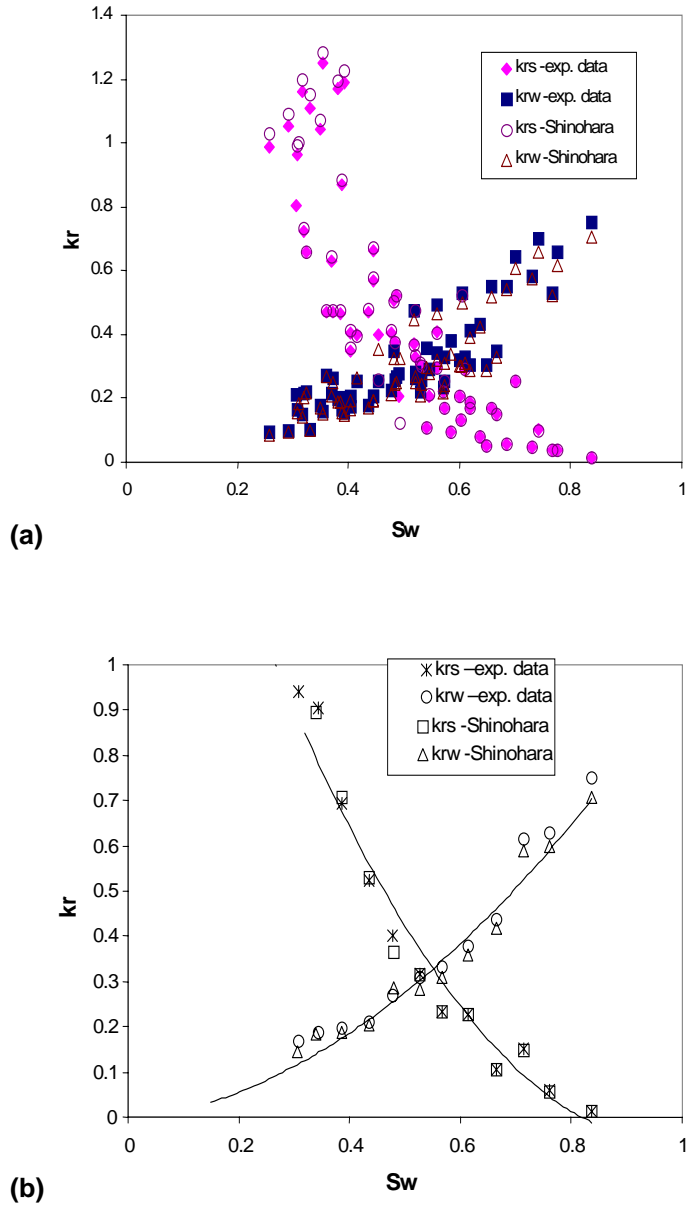


Figure 7.2: Comparison of steam-water relative permeabilities from porous media approach and Shinohara's method for the steam-water data from the smooth-walled fracture: (a) generalized from five experimental runs; (b) averaged values.

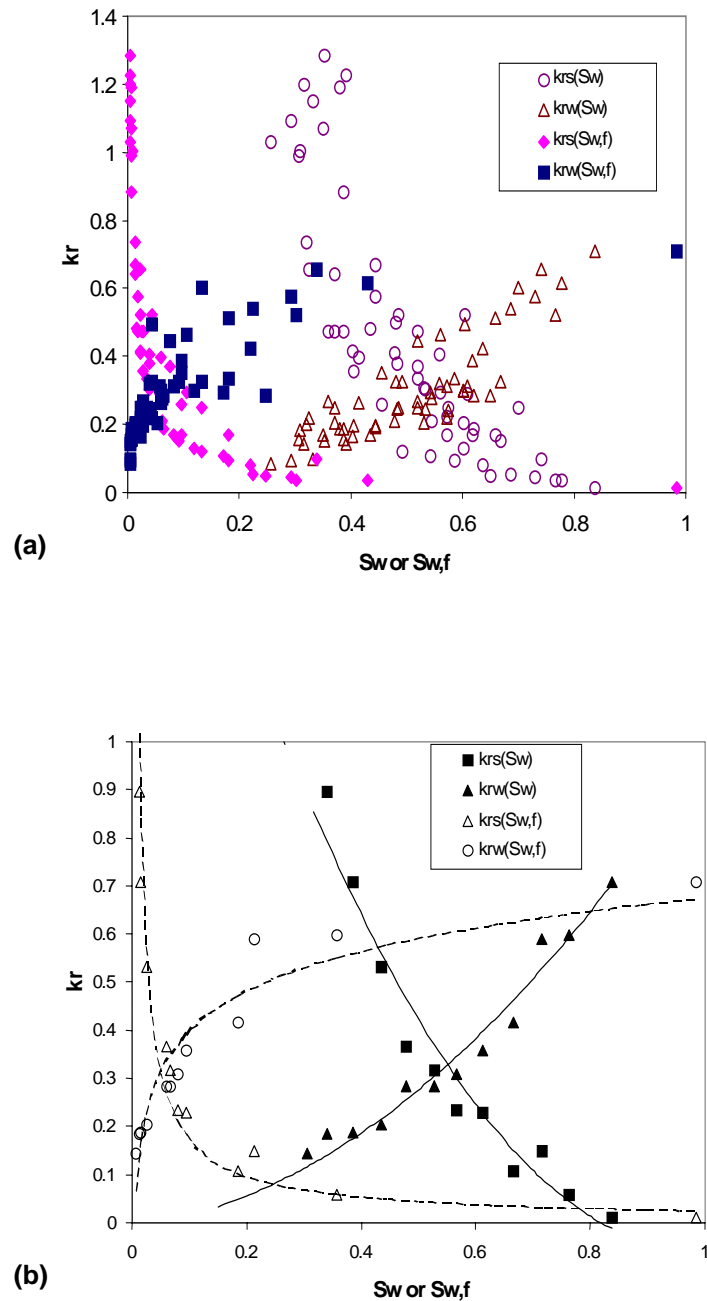


Figure 7.3: Comparison of kr vs. S_w and kr vs. $S_{w,f}$ from Shinohara's method for the steam-water data from the smooth-walled fracture: (a) generalized from five experimental runs; (b) averaged values.

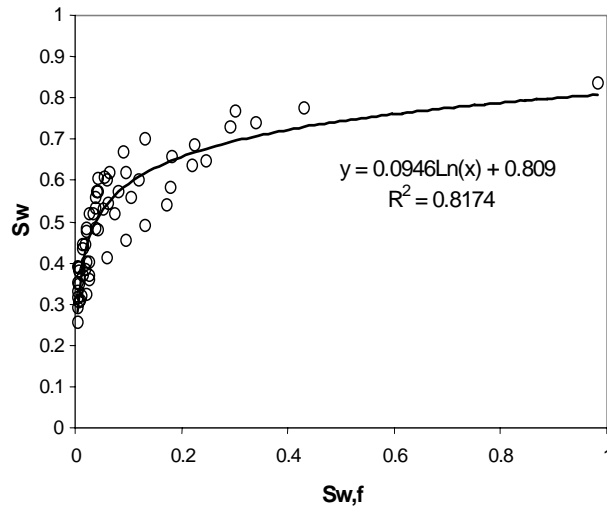


Figure 7.4: The flowing water saturation versus actual (in-place) water saturation for steam-water data from the smooth-walled fracture.

From Figures 7.2 and 7.3, Shinohara's method can be seen to obtain accurate relative permeabilities if the reservoir pressure gradient is close to constant. However, the flowing saturation values inferred from Equation (7.8) are a significant underestimate of the in-place saturation. The difference between the two saturations is due to the velocity differences between steam and water phases, to the effects of immobile phases, and to the phase transformation effects. Therefore, we cannot simply use the flowing saturation to substitute for the real reservoir saturation. Figure 7.5 provides possible mapping equations to relate the flowing and the actual water saturations for the laboratory scale measurements in the three fractures studied (Figure a) and theoretical outcomes from X-curve, Corey curve and viscous-coupling model (Figure b). As shown in these curves, each experimental result or theoretical outcome offers a dissimilar correlation function between S_w and $S_{w,f}$. Therefore, it is crucial to choose a representative mapping equation in converting field-scale relative permeabilities. In the next section, we describe the application of Shinohara's method to the production data from The Geysers and Salton Sea geothermal fields. Comparison with theoretical models and data from laboratory

investigations also reveals the relationship between the flowing saturation and the actual (in-place) saturation.

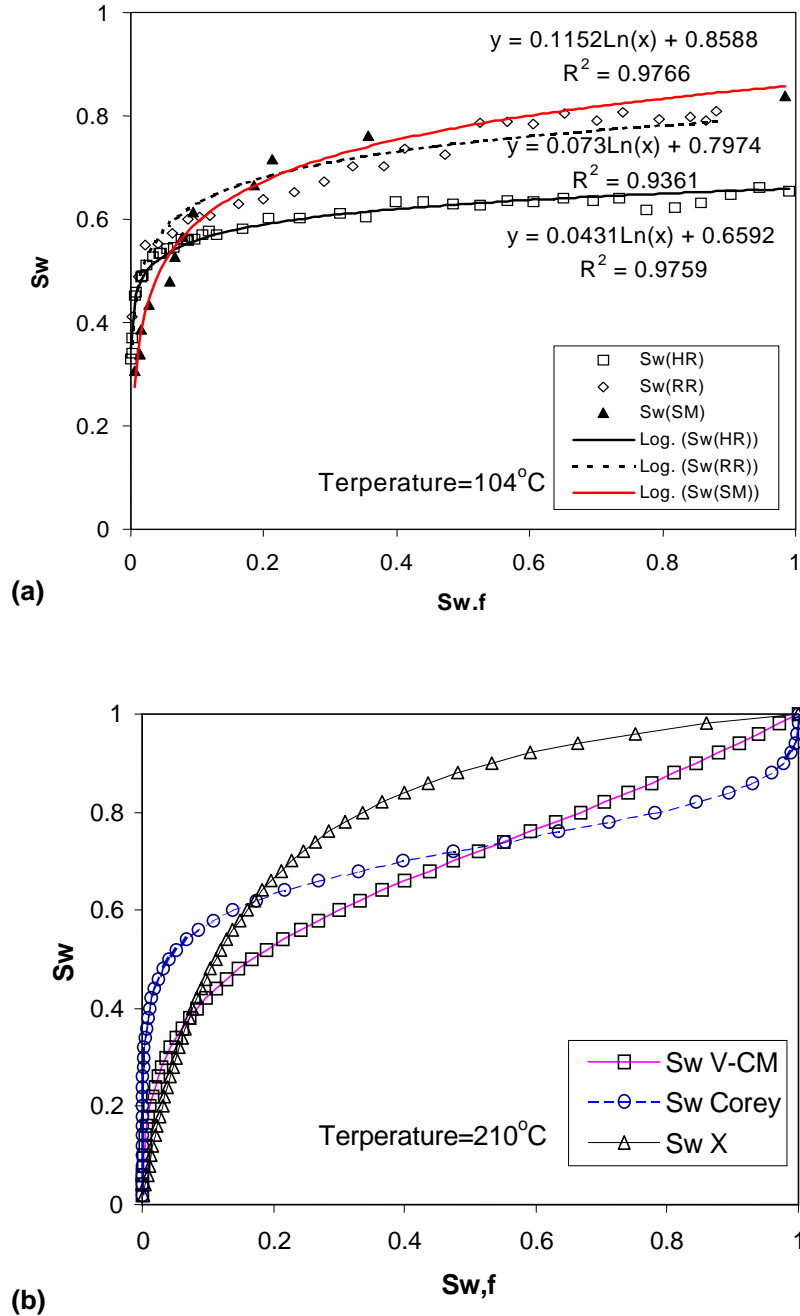


Figure 7.5: The flowing water saturation versus actual (in-place) water saturation: (a) experimental results at 104°C; (b) theoretical results for reservoir conditions (210°C).

7.4 Reservoir Applications

The production data in The Geysers and Salton Sea geothermal fields include temperature, pressure and steam and water production rates. Generally, reservoirs in The Geysers have temperature ranging from 180 to 230°C, while reservoirs in Salton Sea have temperature ranging from 200 to 240°C. In choosing the wells to be used in this study, a number of issues had to be addressed. First, for the vapor-dominated reservoir, we had to find data from wells that had both steam and water production. Of the 503 wells made available to us from The Geysers, only 25 produced water. Nine wells were ultimately used, as these wells had a sufficient number of readings for the calculation. Also, the first assumption of Shinohara's method tells us that it is necessary to choose a time period over which we can assume a constant pressure gradient. Since production data are usually intermittent in nature and often have periodic fluctuations, we had to find data sets that had significant stable periods. Of the 128 wells documented in the database that belong to the Salton Sea field operated by CalEnergy, we used six wells for our liquid-dominated case.

Figures 7.6 and 7.7 are examples of steam and water production histories from Coleman 4-5, a Geysers well, and IDD – 9, a well from the Salton Sea geothermal field. Well IDD-9 (Figure 7.7) from Salton Sea had zero production for much of its history. We chose an interval that we can assume to have a roughly constant pressure gradient. For this work we chose an interval from mid-1990 to late-1992. Choosing the time interval for the vapor-dominated well is much easier. We tried to omit extreme readings from our analysis, therefore the spike seen in 1986-1987 was not chosen as part of the range. For this work, we used a data interval from mid-1987 to 1989. Figures 7.8 and 7.9 show the Q vs Q_w/Q_s graphs for Coleman 5-5 and IDD – 9, respectively. The value of Q^* is inferred from the y-intercept value from the linear fit to the graph. Table 7.1 shows the Q^* inferred from all the wells used in the study.

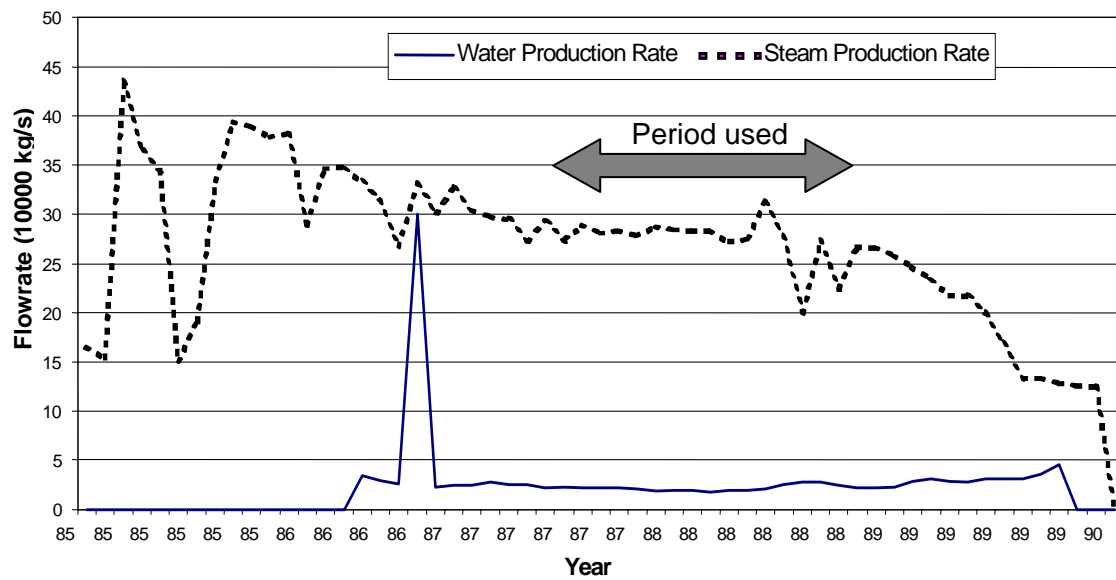


Figure 7.6: Steam and Water Production History of Coleman 4-5, The Geysers Geothermal Field.

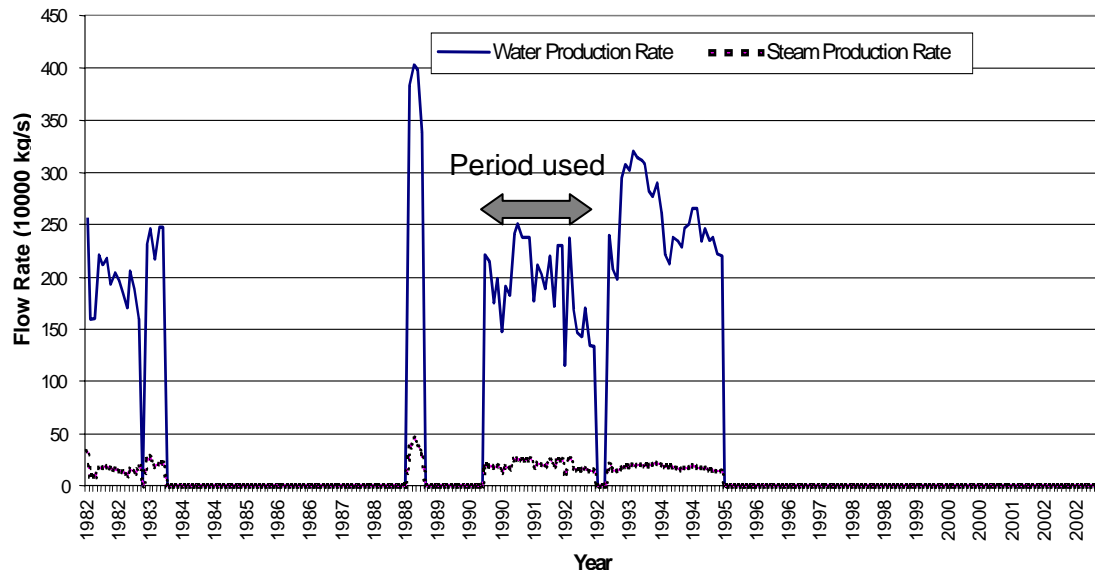


Figure 7.7: Steam and Water Production History of IID - 9, Salton Sea Geothermal Field.

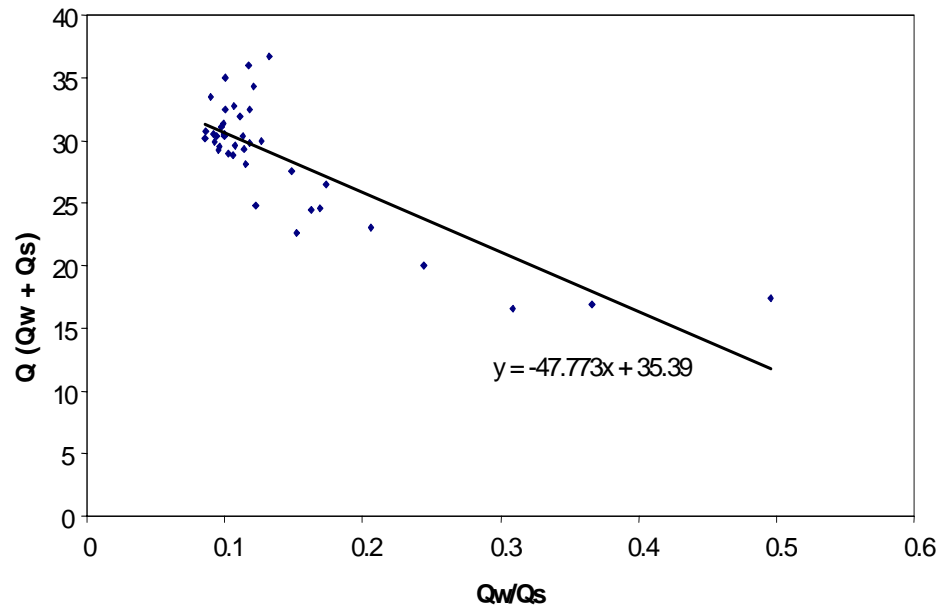


Figure 7.8: Q vs. Q_w/Q_s to infer Q^* for Coleman 4-5, The Geysers Geothermal Field.

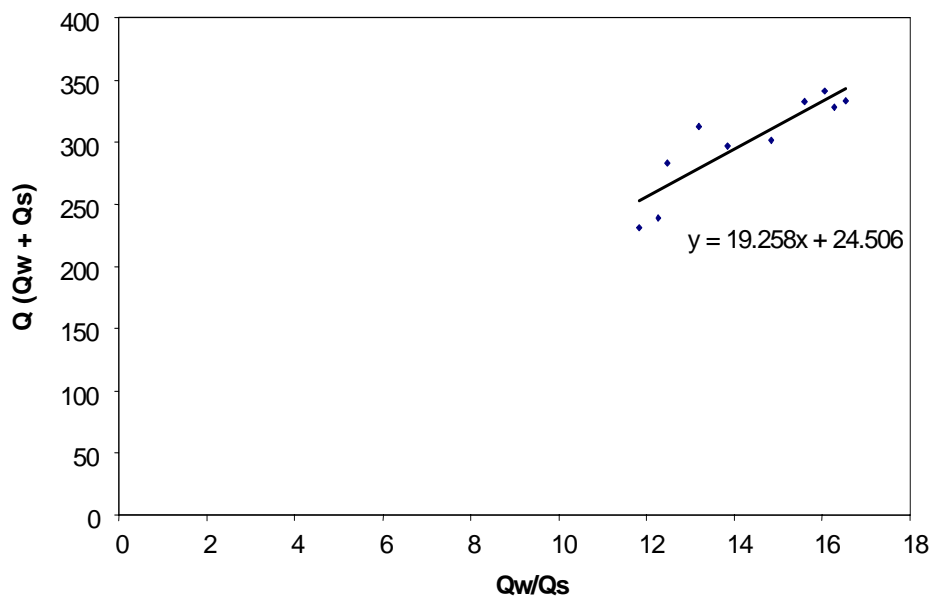


Figure 7.9: Q vs. Q_w/Q_s to infer Q^* for IID - 9, Salton Sea Geothermal Field.

Table 7.1: Inferred Q^* values for The Geysers and Salton Sea Geothermal Field Wells.

Geysers Wells	Q^*	Salton Sea Wells	Q^*
Coleman 4-5	35.39	IID – 9	100
Coleman 5-5	35.649	Sinclair 20	75
Coleman 3-5	24.186	Vonderahe 1	437.56
Francisco 2-5	24.182	Sinclair 10	298.62
Coleman 1A-5	24.09	Elmore 100	200
Thorne 6	33.59	Sinclair 11	256.5
Thorne 1	17.384		
Francisco 5-5	23.52		
CA-5636 6.8E-20	27.868		

If we compare the Q^* values between The Geysers wells and the Salton Sea wells, we can see that The Geysers' Q^* values are smaller than those from the Salton Sea. Also, The Geysers' Q^* values are close to each other. This is an extension of the second assumption made by Shinohara in developing his method. Not only is kAp' constant in a well, wells that are near each other or belong to the same geothermal field also have similar kAp' values. Since the wells in a certain geothermal field mainly have the same k values, and to a certain extent, A and p' , then our inferred values are consistent with each other. The Salton Sea wells have a wider range of values of Q^* , but are generally of the same magnitude and larger than those in The Geysers. To evaluate the kinematic viscosities and mass production rates of the steam and water correctly, we must infer the bottomhole conditions, as these reflect the true flowing conditions of the well. We made temperature corrections based on the documented depths of the wells.

After these procedures, Equations (7.6) and (7.7) were used to calculate the relative permeabilities of steam and water. Figures 7.10 and 7.11 show us plots of relative permeability with water saturation for The Geysers and Salton Sea geothermal wells, respectively. Note that these graphs are plotted against the flowing saturation, $S_{w,f}$ as defined by Equation (7.8) because the actual (in-place) water saturation was not

available. The flowing saturation excludes the immobile water and steam fractions and assumes no-slip and homogeneous flow. Figure 7.10 shows The Geysers relative permeability plot. Because The Geysers is a vapor-dominated reservoir, we expected the low water saturation values. Figure 7.11, the Salton Sea examples, shows us a larger range for flowing water saturation, with a maximum at around 0.25. It is also found that even if water mass production rate is greater, the steam saturation values still dominate in a liquid-dominated reservoir.

We may see the general trend of the relative permeability curves by plotting both well samples together. From Figure 7.12, the relative permeability values for the vapor-dominated and liquid-dominated samples appear only partially consistent with each other. For the relative permeability of steam, The Geysers calculation exhibits a sharp drop in k_{rs} at small values of $S_{w,f}$. A plateau of values approaching $S_{w,f} = 0.1$ are, however, formed by the Salton Sea data cluster. For the water phase data, a more constant and stable rise can be seen as the water saturation increases. The steepness of the rise for both sets of well samples is consistent. The water saturation in these figures might appear to be much smaller than the traditional behavior of relative permeability curves, but this is only because of the use of flowing saturation based on Equation (7.8), rather than the true in-place saturation. This phenomenon conforms to the laboratory investigation in Figure 7.3. Relative permeability functions without respect to in-place water saturation are not useful in reservoir simulations for performance estimation, because most simulators assume relative permeabilities depend on in-place saturation only and curves of k_r versus S_w are the standard form to input these simulators. To this end, a likely mapping between flowing and in-place water saturations is required.

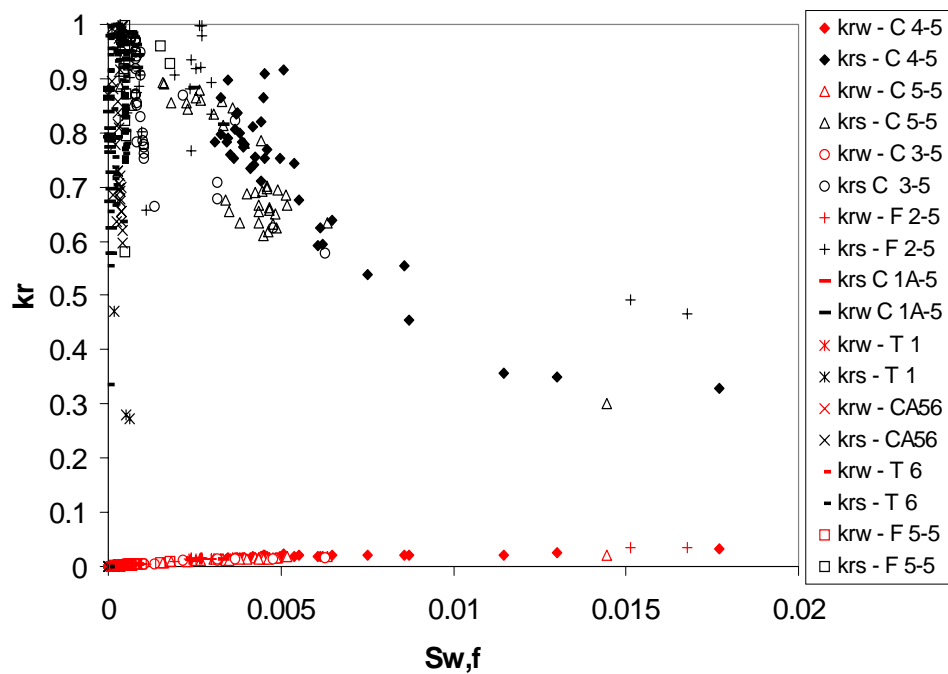


Figure 7.10: Plot of relative permeability curves against flowing water saturation for The Geysers Geothermal Field.

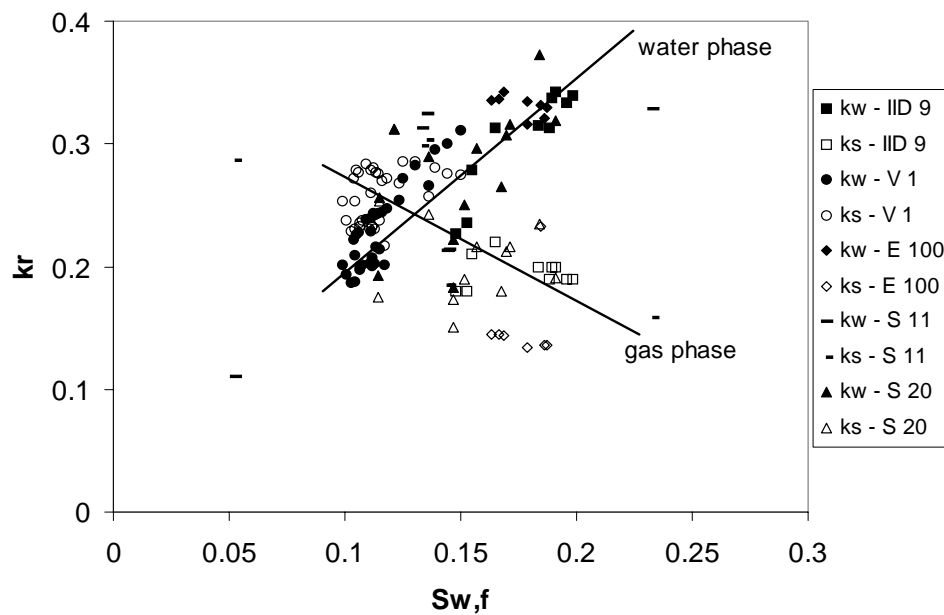


Figure 7.11: Plot of relative permeability curves against flowing water saturation for the Salton Sea Geothermal Field.

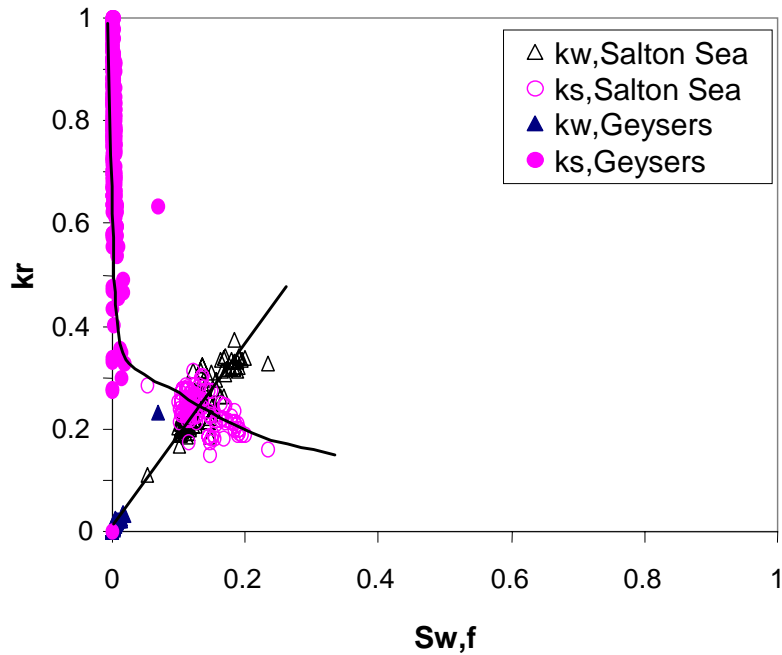


Figure 7.12: Plot of relative permeability curves against water saturation for The Geysers and Salton Sea Geothermal Reservoir Fields.

To compare the estimated relative permeability values with the experimental results in Chapter 6 as well as the three most commonly assumed models of relative permeabilities in fractures, we plotted the computed k_{rw} and k_{rs} values with these laboratory measurements and model curves in Figure 7.13. The top graph shows linear Cartesian plot, while the bottom graph shows the logarithmic plot to demonstrate the trend of small values. We see from both graphs that the calculated values for both The Geysers and Salton Sea wells lie between the X- and Corey-curves. Considering The Geysers data only, we found they agree with the viscous-coupling model and some near-end points of the homogeneously rough-walled (HR) and randomly rough-walled (RR) fractures. On the other hand, most data from Salton Sea conform to the viscous-coupling model. Supposing that both fields share similar hydrogeological, fluid and thermodynamic properties, the joint relative permeabilities of both fields appear to match the viscous-coupling-like behavior most. Hence, the $S_{w,f}$ from field data should be similar to those calculated from

viscous-coupling model since both cases have similar k_{rs}/k_{rw} in the right hand side of Equation (7.8).

Assuming that residual gas and water saturations in both fields are negligible at this point, the viscous-coupling curve in Figure 7.5b is reasonable in serving as a correlation function to transform the flowing water saturation to the in-place water saturation. Substituting its relative permeability functions in Equations (2.18) and (2.19) into Equation (7.9), we obtain

$$\frac{(1 - S_w)^3 + \frac{3}{2} \mu_r S_w (1 - S_w)(2 - S_w)}{\frac{S_w^2}{2} (3 - S_w)} = \frac{(1 - S_{w,f})\mu_r}{S_{w,f}} \quad (7.10)$$

Since $S_{w,f}$ is known from the production data, Equation (7.10) can be written in a cubic form which was solved numerically for $S_{w,f}$. After converting the (flowing) water saturation values estimated from both The Geysers and Salton Sea production data, Figure 7.14 shows the relative permeability values against the inferred (in-place) water saturation. The dashed lines are the trends for the viscous-coupling model in reservoir conditions. The relative permeabilities previously spanning from 0 to 0.23 (flowing) water saturation now range from 0 to 0.5 (in-place) water saturation after applying the viscous-coupling correlation. As expected, the relative permeability curves follows the viscous-coupling model and hence show a more conventional relative permeability behavior. Nevertheless, a steep decreasing trend from unity still can be seen from k_{rs} in The Geyser cluster, which is consistent with the laboratory investigation for HR and RR fractures (Chapter 6).

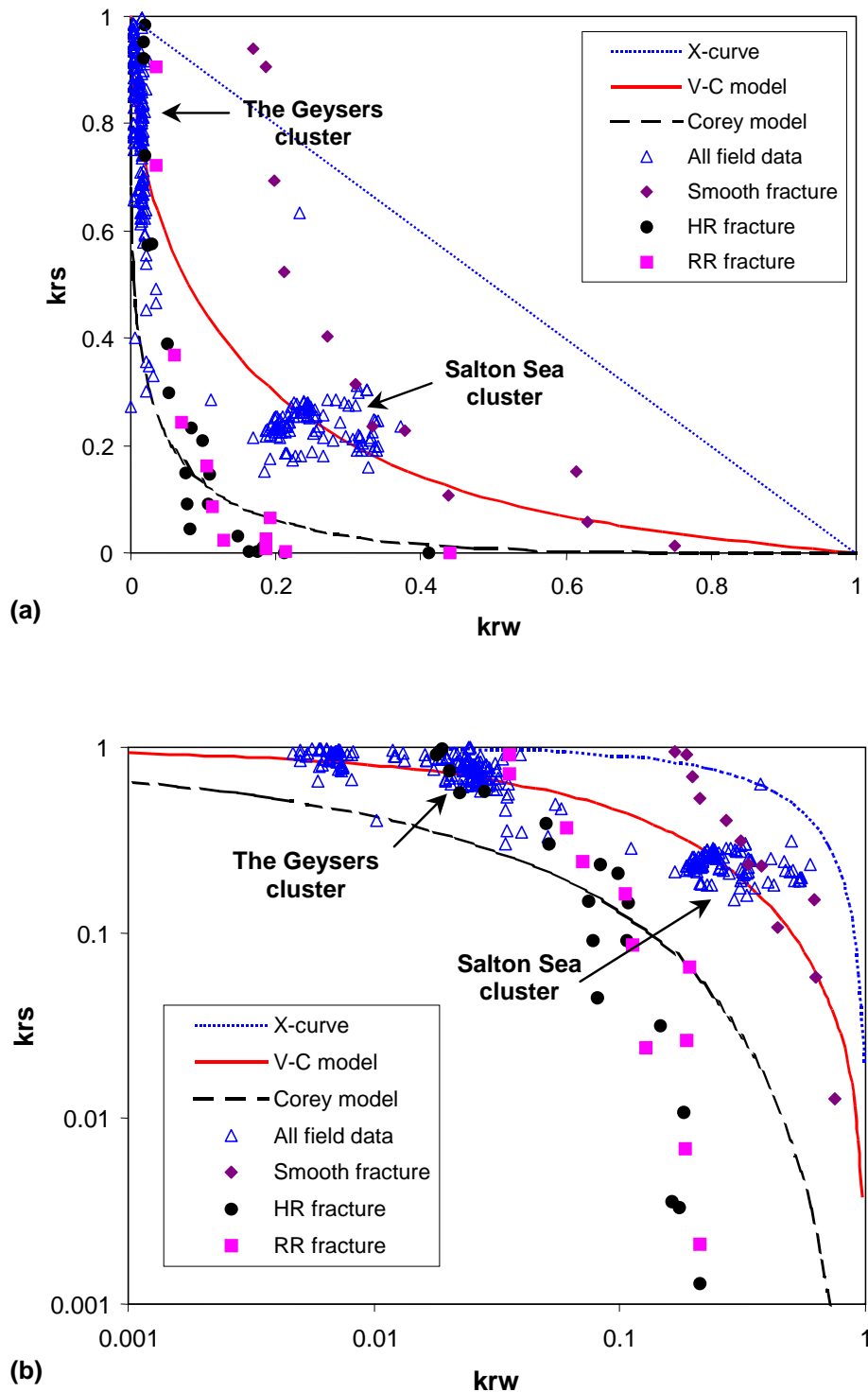


Figure 7.13: Plot of k_{rs} vs k_{rw} for The Geysers and Salton Sea Geothermal Field, with the Corey, X-curves and viscous-coupling model: (a) Cartesian plot, (b) Logarithmic Plot.

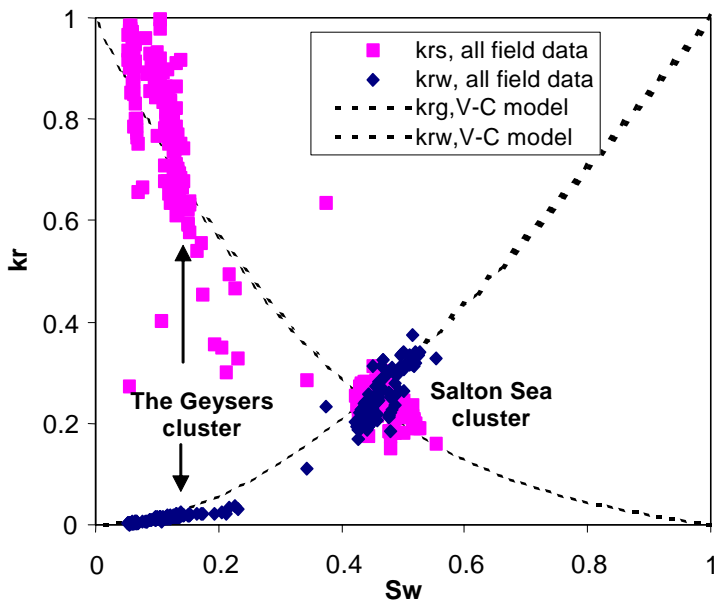


Figure 7.14: Relative permeability vs. mapped in-place water saturation from the field production data for The Geysers and Salton Sea Geothermal fields, compared to the viscous-coupling model (assuming no residual water saturation).

7.5 Discussion

The relative permeability cross plots in Figure 7.13 show that most Geysers data cluster lies on end points of results from the rough-walled (HR and RR) fractures though the range of k_{rw} is fairly short, whereas the Salton Sea data do not follow the rough-walled trends at all. This might indicate that reservoirs in the Salton Sea field have different geological structures, such as transport media and heterogeneity; therefore, these two fields may have different types of relative permeability curves. These may explain why the estimates from the field production data are dissimilar to the values measured from the single fracture experiments in Chapter 6. Conservatively, the direct comparison among this joined result and other experimental or theoretical results may not be applicable, unless: 1) future geological interpretation, field investigations or laboratory

analyses confirm that both fields share similar geological properties and have similar residual saturations and 2) more representative data are available.

Although limited field studies have been reported regarding the Salton Sea geothermal field, numerous studies have been done in The Geysers geothermal field in estimating reservoir geological and hydraulic properties. The assumption of negligible residual saturations is not practical in The Geysers field. Earlier studies have suggested some methods in estimating in-place water saturation based on production histories [Grant et al. 1982; Belen and Horne, 2000]. A study applying these methods to 177 wells in The Geysers field was conducted by Reyes et al. [2003]. Their results show that The Geysers field had in-place water saturation ranging from 0.3 to 0.7 during the period when production data were acquired. Since The Geysers field is a vapor-dominated reservoir, and steam mass rates are much larger than water production rates as can be seen in Figure 7.6, the in-place water saturations there may more or less approach to residual water saturation. Hence, we can consider that significant residual water saturations exist in The Geysers field. Consequently, the saturation calculated from Equation (7.10) is actually normalized water saturation, identical to Equation (2.13), rather than actual saturation. To denormalize the water saturation, information regarding residual water and steam saturations is needed. We may use the upper and lower limits to evaluate upper and lower bounds of relative permeabilities in the Geysers field, assuming reservoirs have liquid-filled initial condition ($S_{gr}=0$). In such conditions, Equation (2.13) can be written as the denormalized form:

$$S_w = S_{wr} + S_w^*(1 - S_{wr}) \quad (7.11)$$

The S_w^* were obtained from Equation (7.10). Figure 7.15a shows the lower bound relative permeability against denormalized in-place water saturation for the Geysers field using the reported minimum residual water saturation of 0.3 [Reyes et al., 2003]. The relative permeabilities from HR and RR fractures in Chapter 6 also provided, because the laboratory investigation for both fractures also conform to similar residual water

saturation. Good agreement was discovered between The Geysers estimates and laboratory data. Particularly, both show the steep decreasing trend from unity for steam phase relative permeabilities. This trend has been characterized as one of the unique features in steam-water relative permeabilities as discussed in Chapter 6. The upper bound behavior using the reported maximum residual water saturation of 0.7 [Reyes et al., 2003], however, reveals less conventional relative permeabilities (Figure 7.15b). The study conducted by Reyes [2003] indicates that those wells having high in-place water saturations may be influenced by the surface water reinjection.

Lastly, several issues contributing to the uncertainty of this study need to be addressed here. First, the effects of wellbore liquid hold-up and phase transformation on production rates may be significant, but are not included here. Secondly, the fracture and matrix interaction was not included in the single fracture experiments. The surface morphology, the complexity of natural fracture network, and the wettability difference of the materials were not considered in the smooth-walled and rough-walled fracture models of Chapter 6. Lastly, the scale difference between laboratory and field may be important too. All these issues may outline future extensions of this subject.

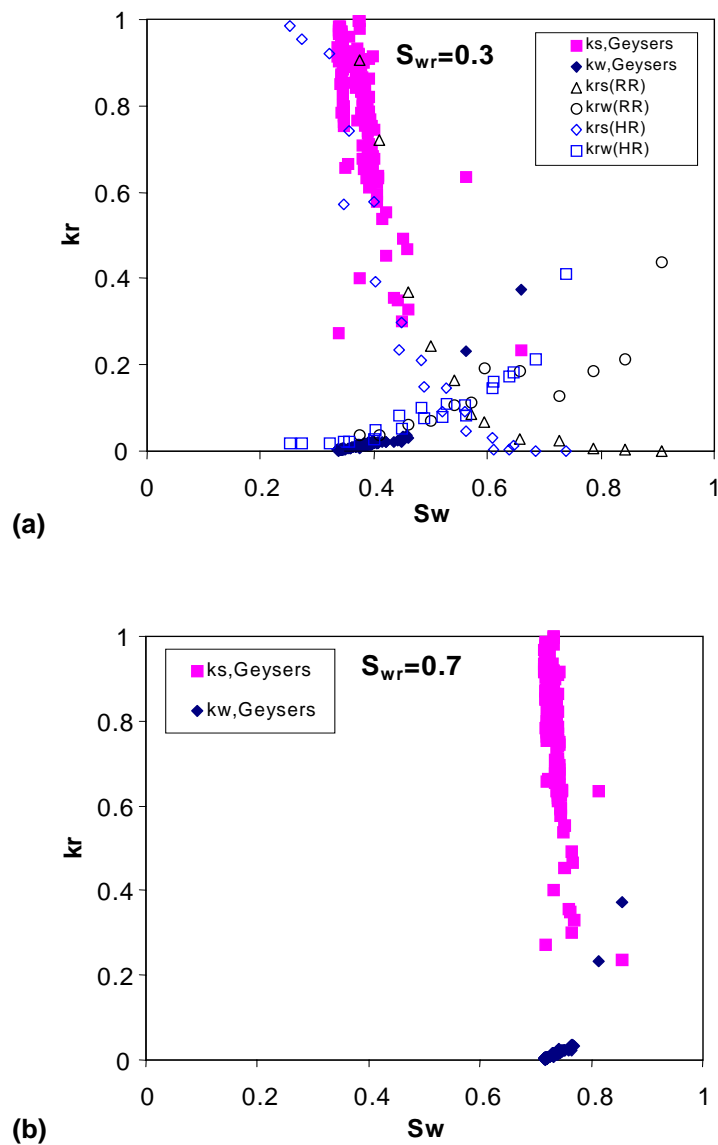


Figure 7.15: Relative permeability vs. de-normalized in-place water saturation for the Geysers field: (a) lower bound behavior using reported minimum $S_{wr}=0.3$, compared to the results from rough-walled fractures, (b) upper bound behavior using reported maximum $S_{wr}=0.7$.

7.6 Chapter Remarks

1. We can infer the steam and water relative permeabilities from field measurements of the production flow rate history and bottomhole temperature. Comparison with laboratory data demonstrated that this method could estimate the values of relative permeability reasonably.
2. The estimated values of relative permeability in The Geysers and the Salton Sea geothermal fields lie between the X-curve and the Corey curve and conform mostly to the viscous-coupling model. After applying the viscous-coupling correlation, the k_r versus S_w curves from field data show a more conventional appearance.
3. After denormalizing water saturations using reported minimum and maximum residual water saturations, the lower and upper bounds of relative permeabilities in The Geysers geothermal field were obtained. The lower bound result shows good agreement with our laboratory investigation results of rough-walled fractures.
4. To estimate relative permeabilities more accurately from field production data, more representative production data as well as more accurate information about residual saturations is needed.

Chapter 8

Conclusions and Future Work

This research has explored the fundamental physics of liquid-gas (unsaturated) flow in single fractures by means of visualization techniques and physical modeling. The results provide important information on the interaction of unsaturated fluids and with the surrounding solid surface. Based on this knowledge, we examined the effects of flow structures and fracture geometry on the relative permeabilities, modeled two-phase relative permeabilities in fractures, and understood better how phase transformations affect steam-water transport through fractures.

8.1 Conclusions

In this work, three fractures with distinct surface roughness types, namely smooth-walled, randomly rough-walled and homogeneously rough-walled fractures, were used in the steady-state liquid-gas cocurrent drainage experiments to represent three distinct surface geometries and heterogeneities. Using a high-speed data acquisition system, real-time visualization of the flow dynamics and automated digital image processing technology, the experimental apparatus was able to characterize the unstable nature of the flow and assess the experimental uncertainty.

Through air-water flow experiments, different flow configurations were visualized. There are bubbles, slugs and channels in the smooth-walled fracture and intermittent channels and stable channels in the rough-walled fractures. Experimental results of pressure drop, flow rates, and saturation were interpreted by using the relative permeability concept and compared to three models from the literature: the X-model, the Corey-model and the viscous-coupling model. Although the theoretical viscous-coupling model shows good agreement with the air-water relative permeabilities in the smooth-walled fracture, this model performs poorly in describing the relative permeabilities from rough-walled fractures. What is more, from the flow visualization, the actual air-water flow behavior occurring in the fracture space is completely different from the fundamental framework of the viscous coupling model which does not take into account the actual horizontal flow structures.

By introducing the tortuous-channel concept, we showed that the relative permeability behavior in fractures is controlled by the flow paths formed by the phases. A method to evaluate the mutual tortuosities induced by the blocking phase, namely the *channel tortuosity*, was proposed from observations of the flow structure images. With verification from laboratory experiments and visualizations, the proposed tortuous-channel approach reproduced both original and average relative permeability measurements in all fractures studied. Though smooth-walled fractures have poor representation of natural rock fractures, relative permeability functions deduced by the proposed tortuous-channel model may provide an upper bound of the air-water relative permeability at room temperature for simulations of fractured reservoirs, due to their smooth surfaces, negligible capillary effects and absence of fracture-matrix interaction.

By studying three fractures with different surface roughness, we found that the magnitude of the flow channel tortuosity increases when the heterogeneity of fracture surface increases (changing from smooth to homogeneously rough and then to randomly rough). This could be attributed to the heterogeneity of local capillary gap. Major physical signatures of this mechanism are the appearance and distribution of entrapped

phases which enhances channel tortuosities and alters saturations. The relationship between these two outcomes in the three types of fractures studied could be correlated by converting the residual saturations into normalized saturations. After applying mathematical expressions of phase tortuosity coefficients, a more general tortuous-channel model was proposed to describe two-phase relative permeabilities in both smooth and rough fractures.

After the success in studying conventional air-water flow in single fractures, we advanced to the second part of this research by studying unconventional steam-water flow in single fractures. The modeling study of steam-water relative permeabilities is a major challenge of the geothermal reservoir engineering. Since 1951 when the first steam-water relative permeability was presented experimentally by Miller [1951], no rigorous theoretical model has been provided to model or explain the steam-water flow behavior in spite of the considerable published experimental work. In the second part of this study, the inviscid bubble train model based on the Bretherton theory was used and coupled with the relative permeability concepts. The phase transformation effects were evaluated by introducing the interfacial mass flux based on the carry-away and precipitation processes of vapor molecules. Results from this model are qualitatively in accordance with our and most earlier experimental measurements. Besides the quantitative investigation, an idealized toroidal throat geometry was used to illustrate the efficient transport that occurs in the steam (vapor) phase. The more efficient substitution transport may occur when steam bubbles are transported through the pore throats. This may be another characteristic contributing to the enhancement of steam-phase relative permeabilities.

The experimental investigation of steam-water flow showed that the steam-water flow behavior in fractures is different from that of air-water flow in the aspects of relative permeability, flow structure and residual/immobile phase saturations. In fractures, steam phase relative permeabilities surpass air phase relative permeabilities. The enhanced steam phase relative permeabilities are due to the effects of phase transformation, which

is consistent with our theoretical study and (most) earlier studies in porous media. By modifying the Brooks-Corey relative permeability functions to expressions for fractured media ($\lambda \rightarrow \infty$), the steam-water relative permeability in the HR and RR fracture seems to be represented acceptably by such expressions; however the smooth-walled result and some published results could not. The generation of nucleated steam clusters is one distinct feature observed during steam-water flow in the rough-walled fractures, and it appears to explain the similar relative permeability behavior in porous media obtained by earlier investigators. By characterizing these immobile steam clusters using nucleated steam saturation (S_{gn}), we incorporated the S_{gn} in the previously suggested tortuous-channel model for air-water flow. This modified tortuous-channel model could describe not only the steam-water relative permeabilities from three fractures studied currently, but also those results from earlier investigations for consolidated and unconsolidated porous media.

Finally, we scaled up the laboratory results to verify and enhance a field-scale method suggested by earlier investigators. The verification was conducted using laboratory measurement in the steam-water flow experiments. The estimates using the field-scale method showed good agreement with the relative permeabilities measured in the laboratory. The steam and water relative permeabilities at The Geysers and Salton Sea geothermal reservoirs were investigated from available production data. The estimated values of relative permeability in The Geysers geothermal field behave close to the results from the rough-walled fractures and viscous-coupling model, while the values from Salton Sea geothermal field conform mostly to the viscous-coupling model. After correcting to static saturation and denormalizing water saturations using reported minimum and maximum residual water saturations in the Geysers field, the possible lower and upper bounds of relative permeabilities in The Geysers geothermal field were suggested. The lower bound result appears to agree with our laboratory investigation of the rough-walled fractures. In addition, both limits show a steep trend of steam phase relative permeabilities, which is consistent with our laboratory investigations.

8.2 Future Work

1. Two-phase flow in real fractures

From this work, the concept of the tortuosity coefficient may allow modeling two-phase flow in a fracture, whatever the flow configuration. To this end, the tortuosity coefficient τ_c must be related physically to the shear stress at the surface between the two fluids and to the interface area. Unfortunately, up to now there is no model that allows us to predict flow structures in fractures. As mentioned in Chapter 2, the method of evaluating the coefficient of tortuosity and modeling two-phase flow in fractures were only validated in specific artificial fractures up to this point. To account for the complexity and heterogeneity of natural rock fractures, the algorithm to evaluate τ_c and the methodology to characterize the flow-based heterogeneity may have to be developed further. Characterizing the flow-based heterogeneity of the fractures is believed to be the most important challenge for the future. The characteristics of heterogeneity in natural fractures are certainly much more complex and variable. Therefore more studies of the relationship between tortuosity and fracture geometry may be needed to gain rigorous models for predicting fracture relative permeabilities accurately. To this end, some tomography techniques have to be utilized to image the two-phase flow field, which are believed to be a major challenge for the future research. The fine resolution X-ray CT scanner may be a good candidate for this future work. If such work can be achieved, perhaps the relative permeabilities of natural fractures can be predicted simply by measuring S_{wr} and determining the coefficient of channel tortuosity using tomographic technology.

2. CO₂-water relative permeability in fractures

In gas-injection and geological CO₂ sequestration technologies, the CO₂-water relative permeabilities in fractures play important roles in forecasting the performance. Similar to the steam-water relative permeability studied in this work, the phase transformation occurs in CO₂-water flow, but is poorly understood. This work has suggested a possible

experimental technique to study the CO₂-water flow behavior. However, to simulate the high reservoir pressure conditions, the apparatus would have to be modified to minimize fracture dilation.

Nomenclature

A =	cross-section area of fractures, L ²
b =	fracture aperture, L
b_c =	contacting aperture, L
b_h =	hydraulic aperture of rough fractures, L
b_{open} =	opening aperture; completely separation distance, L
Ca =	capillary number (Chapter 4); bubble capillary number (Chapter 5)
Ca^* =	water capillary number (Chapter 5)
d =	hydraulic diameter, L
En =	enhancement coefficient due to phase transformations
f_w =	water fractional flow
f_g =	gas fractional flow
F_m =	film flow corrector
h =	hydraulic head, L
h_L =	liquid specific enthalpy, Energy/m
H_w =	water film thickness, L
K =	hydraulic conductivity, L/t
k =	absolute permeability, L ²
\bar{k} =	average (absolute) permeability, L ²
K_w =	effective hydraulic conductivity of water, L/t
k_{rg} =	relative permeability of gas phase
k_{rs} =	relative permeability of steam phase
k_{rw} =	relative permeability of water phase
L =	fracture length, L

L_c =	correlation length or range of variogram, L
L_T =	latent heat of vaporization, Energy/m
m_{in} =	input mass, m
MAE =	mean absolute error; data unit
N_b =	number of bubbles
N_{Re} =	Reynolds number
p =	pressure, m/Lt ²
p' =	pressure gradient, m/L ² t ²
P_c =	capillary pressure; m/Lt ²
Q =	mass flow rate; m/t
Q^* =	inferred mass flow rate; m/t
q =	volumetric flow rate, L ³ /t
r =	radius, L
\bar{R} =	gas constant; Energy/mole-K
S_g =	gas saturation
S_g^* =	normalized gas saturation
S_{gr} =	residual gas saturation
S_s =	steam saturation
S_{si} =	initial immobile steam saturation
S_w =	water saturation
S_{wf} =	flowing water saturation = f_w
S_{wr} =	residual water saturation
S_w^* =	normalized water saturation
u =	superficial (Darcy) velocity; L/t
v =	interstitial or particle velocity; L/t
ν =	specific volume; L ³ /m
w =	fracture width, L
x =	space coordinate
X =	steam quality; mass fraction of steam

Greek Letters

ϕ =	porosity
μ =	fluid dynamic viscosity, m/Lt
ν =	kinematic viscosity; L ² /t
λ =	pore size distribution index
σ =	interfacial tension; F/L
σ_b =	standard deviation of aperture distribution, L
$\hat{\sigma}$ =	accommodation coefficient
ρ =	density, m/L ³
ε =	ratio of water to steam velocities
τ_c =	channel tortuosity
τ_{ip} =	in-place tortuosity
ω =	velocity increasing factor

Subscripts

b =	bubble
f =	fracture or flowing phase
g =	gas phase
i =	input
nw =	nonwetting phase
o =	output
r =	residual or ratio
s =	steam phase
t =	total
w =	water or wetting phase

References

- [1] Adamson, A.W., Gast, A.P.: *Physical Chemistry of Surfaces*, 6th Edition, Wiley-Interscience, (Aug. 1997), ISBN: 0471148733.
- [2] Akhatov I., Lindau O., Topolnikov A., et al.: “Collapse and Rebound of a Laser-Induced Cavitation Bubble,” *Physics of Fluids* (2001), Vol. 13, pp. 2805-2819.
- [3] Ambusso, W.J.: *Experimental Determination of Steam-Water Relative Permeability Relations*, MS thesis, Stanford University, Stanford, California (1996).
- [4] Arihara, N.: *A Study of Non-Isothermal Single and Two-Phase Flow Through Consolidated Sandstones*, Ph.D. dissertation, Stanford University, Stanford, California (1976).
- [5] Arihara, N., Ramey, J. and Brigham, W.E.: “Non-Isothermal Single and Two-Phase Flow Through Consolidated Sandstones,” *Society of Petroleum Engineers Journal* (June 1976), pp. 137-146.
- [6] Babchin, A.J. and Yuan, J.-Y.: “On the Capillary Coupling Between Two Phases in a Droplet Train Model,” *Transport in Porous Media* (1997), Vol. 26, pp. 225-228.
- [7] Barree, R.D. and Conway, M.W.: “Beyond Beta Factors: A Complete Model for Darcy, Forchheimer, and Trans-Forchheimer Flow in Porous Media,” paper SPE 89325, presented in SPE 2004 Annual Technical Conference and Exhibition, Houston, TX, USA, Sept. 26-29, 2004b.
- [8] Bear, J.: *Dynamics of Fluids in Porous Media*, American Elsevier publisher, New York, USA (1972).

- [9] Belen, R.P., Jr. and Horne, R.N.: "Inferring In-Situ and Immobile Water Saturations from Field Measurements," *Geothermal Resources Council Transactions* (2000), Vol. 24.
- [10] Benjamin, R.J. and Balakrishnan, A.R.: "Nucleation Site Density in Pool Boiling of Saturated Pure Liquids: Effect of Surface Microroughness and Surface and Liquid Physical Properties," *Experimental Thermal and Fluid Science* (July 1997), Vol. 15, Issue 1, pp. 32-42.
- [11] Bretherton, F.P.: "The Motion of Long Bubbles in Tubes," *J. Fluid Mech.* (1961), Vol. 10, pp. 166-188.
- [12] Brooks, R.H. and Corey, A.T.: "Properties of Porous Media Affecting Fluid Flow," *J. Irrig. And Drain. Div.*, Proc. ASCE, IR2 (1966), Vol. 92, pp. 61-88.
- [13] Brown, S.R.: "Fluid Flow Through Rock Joints: The Effect of Surface Roughness," *Journal of Geophysical Research* (1987), Vol. 92, No. B2, pp. 1337-1347.
- [14] Buckingham, E.: "Studies of the Movement of Soil Moisture," Bureau of Soils-Bulletin No. 38, US-DOA, Government printing office, Washington D.C. USA, 1907.
- [15] CAMTEL: "Cleanliness Measurements Using Contact Angles," Application Notes, August 14, 2000. (<http://www.camtel.co.uk/Tn008.pdf>)
- [16] Carey, V.P., *Liquid-Vapor Phase-Change Phenomena*, Hemisphere Publishing Corporation, New York, NY (Feb. 1992).
- [17] Chen, C.-Y., Diomampo, G., Li, K. and Horne, R.N.: "Steam-Water Relative Permeability in Fractures," *Geothermal Resources Council Transactions* (2002), Vol. 26, pp. 87-94.
- [18] Chen, C.-Y., Li, K. and Horne, R.N.: "Difference Between Steam-Water and Air-Water Relative Permeabilities in Fractures," *Geothermal Resources Council Transactions* (2003), Vol.27, pp. 793-800.

- [19] Chen, C.-Y., Horne, R.N., and Fourar, M.: "Experimental Study of Liquid-Gas Flow Structure Effects on Relative Permeabilities in a Fracture," *Water Resources Research* (Aug 2004a), Vol. 40, No.8, W08301.
- [20] Chen, C.-Y., Li, K., and Horne, R.N.: "Experimental Study of Phase Transformation Effects on Relative Permeabilities in Fractures," paper SPE 90233, presented in SPE 2004 Annual Technical Conference and Exhibition, Houston, TX, USA, September.26-29, 2004b.
- [21] Chen, H.K.: *Measurement of Water Content in Porous Media Under Geothermal Fluid Flow Conditions*, Ph.D. dissertation, Stanford University, Stanford, California (1976).
- [22] Chen, H.K., Council, J.R., and Ramey, H.J., Jr.: "Experimental Steam-Water Permeability Curves," *Geothermal Resources Council Transactions* (1978), Vol.2, pp. 102-104.
- [23] Cloos, E.: "Experimental Analysis of Fracture Patterns," *Geol. Soc. Am. Bull.* (1955), Vol. 66, pp. 241-256.
- [24] Clossman, P.J., and Vinegar, J.J.: "Relative Permeability to Steam and Water at Residual Oil in Natural Cores; CT Scan Saturation," SPE paper 17449.
- [25] Corey, A.T.: "The Interrelation between Gas and Oil Relative Permeabilities," *Prod. Mon.* (1954), Vol. 19, pp. 38-41.
- [26] Corey, A.T.: *Mechanics of Immiscible Fluids in Porous Media*, Water Resources Publications, Littleton, Colorado (1986).
- [27] Council, J.R.: *Steam-Water Relative Permeability*, Ph.D. dissertation, Stanford University, Stanford, California (1979).
- [28] Council, J.R., and Ramey, H.J., Jr.: "Drainage Relative Permeabilities Obtained from Steam-Water Boiling Flow and External Gas Drive Experiments," *Geothermal Resources Council Transactions* (1979), Vol. 3, pp. 141-143.

- [29] Darcy, H.P.G.: *The Public Fountains of the City Dijon* (appendix), Bookseller of the Imperial Corps of Bridges, Highways and Mines, Quay of Augustins, 49, 1856; English translation: <http://biosystems.okstate.edu/darcy/>
- [30] Diomampo, G.P.: *Relative Permeability through Fractures*, MS thesis, Stanford University, Stanford, California (2001).
- [31] Ehrlich, R.: “Viscous Coupling in Two-phase Flow in Porous Media and Its Effect on Relative Permeabilities,” *Transport in Porous Media* (1993), Vol. 11, pp. 201.
- [32] Faust, C.R. and Mercer, J.W.: “Geothermal Reservoir Simulation II: Numerical Solution Techniques for Liquid- and Vapor- Dominated Hydrothermal Systems,” *Water Resources Research* (1979), Vol.15, No. 1, pp. 31-46.
- [33] Forchheimer, P.: Wasserbewegung durch Boden, Zeits. V. Deutsch. Ing. (1901), Vol. 45, pp. 1781.
- [34] Foulser, R.W.S., Goodyear, S.G. and Sims, R.J.: “New Concepts in Relative Permeabilities at High Capillary Numbers for Surfactant Flooding,” *Transport in Porous Media* (1991), Vol. 6, pp. 223–240.
- [35] Fourar, M. and Bories, S.: “Experimental Study of Air-Water Two-Phase Flow Through a Fracture (Narrow Channel),” *Int. J. Multiphase Flow* (1995), Vol. 21, No. 4, pp. 621-637.
- [36] Fourar, M., Bories, S., Lenormand, R., and Persoff, P.: “Two-Phase Flow in Smooth and Rough Fractures: Measurement and Correlation by Porous-Medium and Pipe Flow Models,” *Water Resources Research* (1993), Vol. 29, No. 11, pp. 3699-3708.
- [37] Fourar, M., and Lenormand, R.: “A Viscous Coupling Model for Relative Permeabilities in Fractures,” SPE 49006, paper presented at the SPE Annual Technical Conference and Exhibition, New Orleans, Louisiana, USA, September 27-30, 1998.

- [38] Fourar M., and Lenormand R.: "A New Model for Two-Phase Flows at High Velocities through Porous Media and Fractures," *Journal of Petroleum Science and Engineering* (2001), Vol. 30, pp. 121-127.
- [39] Fujikawa, S., and Maerefat, M.: "A Study of the Molecular Mechanism of Vapor Condensation," *JSME International Journal* (Nov. 1990), Vol. 2, No. 33, pp. 634-641.
- [40] Gilman, J.R. and Kazemi, H.: "Improvements in Simulation of Naturally Fractured Reservoirs," *Society of Petroleum Engineers Journal* (1983), Vol. 23, No. 4, pp. 695-707.
- [41] Grant, M.A.: "Permeability Reduction Factors at Wairakei," Proceedings, AIChE-ASME Heat Transfer Conference, Salt Lake City, Utah, pp. 15-17, Aug. 1977.
- [42] Grant, M.A., Donaldson I.G., and Bixley P.F.: *Geothermal Reservoir Engineering*, Academic Press Inc., New York (1982).
- [43] Honarpour, M., Koederitz, L.F., and Harvey, A.H.: "Empirical Equations for Estimating Two-Phase Relative Permeability in Consolidated Rock," *JPT* (Dec. 1982), pp. 2905-2909.
- [44] Horne, R.N., and Ramey, H.J., Jr.: "Steam/Water Relative Permeability from Production Data," *Geothermal Resources Council Transactions* (1978), Vol. 2.
- [45] Horne, R.N., Satik, C., Mahiya, G., Li, K., Ambusso, W., Tovar, R., Wang, C. and Nassori, H.: "Steam-Water Relative Permeability," Proceedings of the World Geothermal Congress, Kyushu-Tohoku, Japan, May 28-June 10, 2000.
- [46] Hubbert, M.K.: "Darcy Law and Fluid Equations for the Flow of Underground Fluids," *Trans AIME* (1956), Vol. 207, pp. 222-239.
- [47] Huitt, J.L.: "Fluid Flow in Simulated Fracture," *Journal American Institution Chemical Engineering* (1956), Vol. 2, pp. 259-264.

- [48] Hunt, A.G., and Manga, M.: "Effects of Bubbles on the Hydraulic Conductivity of Porous Materials – Theoretical Results," *Transport in Porous Media* (2003), Vol. 52, pp. 51-65.
- [49] Iwai, K.: "Fundamental Studies of Fluid Flow through a Single Fracture," Ph.D. dissertation, Univ. of Calif. Berkeley, California (1976).
- [50] Johnson, E.F., Bossler, D.P. and Nauman, V.O.: "Calculation of Relative Permeability from Displacement Experiments", *Trans. AIME* (1959), Vol. 216, pp. 370-376.
- [51] Kazemi, H.: *Naturally Fractured Reservoirs*, Third International Forum on Reservoir Simulation, Baden, Austria (1990).
- [52] Kazemi, H. and Merrill, L.S.: "Numerical Simulation of Water Imbibition in Fractured Cores," *Society of Petroleum Engineers Journal* (June 1979), pp. 175-182.
- [53] Kovscek, A.R., Tretheway, D.C., Radke C.J. and Persoff, P.: "Foam Flow Through a Single Rough-Walled Rock Fracture," *Journal of Petroleum Science and Engineering* (1995), Vol. 13, pp. 75-86.
- [54] Kucherov, R.Y. and Rikenglaz, L.E.: "The Problem of Measuring the Condensation Coefficient," *Doklady Akad. Nauk. SSSR* (1960), Vol. 133, No.5, pp. 1130-1131.
- [55] Kucherov, R.Y., and Rikenglaz, L.E, Zh. Eksperim. i Teor. Fiz. 37, 125 (1959) [English Transl.: Sov. Phys.- JETP 10, 88 (1960)].
- [56] Li, K. and Horne, R.N.: "Experimental Verification of Methods to Calculate Relative Permeability Using Capillary Pressure Data," paper SPE76757 presented at the 2002 SPE Western Regional Meeting, Anchorage, Alaska, May 20-22.
- [57] Lomize, G.M.: *Flow in Fractured Rocks*, (Gosenergoizdat, Moscow, 1951).
- [58] Louis, C.: "A Study of Ground Water Flow in Jointed Rock and Its Influence on the Stability of Rock Masses," Rock Mechan. Res. Rep., 10, Imperial College of Science and Technology, London UK, 1969.

- [59] Mahiya, G.: *Experimental Measurement of Steam-Water Relative Permeability*, MS thesis, Stanford University, Stanford, California (1999).
- [60] Mann M., Stephan K. and Stephan P.: "Influence of Heat Conduction in The Wall on Nucleate Boiling Heat Transfer," *International Journal of Heat and Mass Transfer* (June 2000), Vol. 43, Issue 12, pp. 2193-2203.
- [61] Meheust, Y. and Schmittbuhl, J.: "Geometrical Heterogeneities and Permeability Anisotropy of Rough Fractures," *Journal of Geophysical Research* (Feb. 2001); Vol. 106, No. B2, pp. 2089-2102.
- [62] Mendoza, C.A. and Sudicky, E.A.: "Hierarchical Scaling of Constitutive Relationships Controlling Multi-Phase Flow in Fractured Geologic Media," paper presented at the NIPER/DOE Third Int. Conf. on Reservoir Characterization Requirements for Different Stages of Development, Dept. of Energy, Tulsa, Okla., 1991.
- [63] Miller, F.G.: "Steady Flow of Two-Phase Single-Component Fluids Through Porous Media," *Trans. AIME* (1951), Vol. 192, pp. 205.
- [64] Monsalve, A., Schechter, R.S. and Wade, W.H.: "Relative Permeabilities of Surfactant/Steam/Water Systems," Paper SPE/DOE 12661, presented at the Society of Petroleum Engineers Symposium on Enhanced Oil Recovery, Tulsa, Oklahoma, April 1984.
- [65] Murphy, J.R. and Thomson, N.R.: "Two-Phase Flow in a Variable Aperture," *Water Resources Research* (1993), Vol. 29, No 10, pp. 3453-3476.
- [66] Neuzil, C.E., and Tracy, J.V.: "Flow Through Fractures," *Water Resources Research* (1981), Vol. 17, No. 1, pp. 191-199.
- [67] Nicholl, M.J., Glass, R.J. and Nguyen, H.A.: "Gravity-Driven Fingering in Unsaturated Fractures," Proc. High Level Radioactive Waste Management Conference, Las Vegas, NV, 1992

- [68] Nicholl, M.J., Glass, R.J. and Nguyen, H.A.: "Small-Scale Behavior of Single Gravity-Driven Fingers in an Initially Dry Fracture," Proc. High Level Radioactive Waste Manag. Conf., Las Vegas, NV, 1993.
- [69] Nicholl, M.J. and Glass, R.J.: "Wetting Phase Permeability in A Partially Saturated Horizontal Fracture," Proc. 5th Ann. Int. Conf. On High Level Rad. Waste Mgmt., 2007-19, American Nuclear Society, Las Vegas, Nevada, May 22-26, 1994.
- [70] Nicholl, M.J., Rajaram, H. and Glass, R.J.: "Factors Controlling Saturated Relative Permeability in a Partially Saturated Horizontal Fracture," *Geophysical Research Letters* (Feb. 2000), Vol.27, No.3, pp. 393-396.
- [71] O'Connor, P.: *Constant-Pressure Measurement of Steam-Water Relative Permeability*, MS thesis, Stanford University, Stanford, California (2001).
- [72] Olbricht, W.L.: "Pore-Scale Prototypes of Multiphase Flow in Porous Media," *Ann. Rev. Fluid Mech.* (1996), Vol. 28, pp. 187-213.
- [73] Olson, K.E., Haidar, S., Milton, D. and Olsen, E.: "Multiphase Non-Darcy Pressure Drop in Hydraulic Fracturing," paper SPE 90406, presented in SPE 2004 Annual Technical Conference and Exhibition, Houston, TX, USA, September.26-29, 2004b.
- [74] Oseen, C.W.: "Ueber die Stokes'sche Formel, und über eine verwandte Aufgabe in der Hydrodynamik," *Ark. Math. Astronom. Fys.* (1910), Vol. 6, No. 29.
- [75] Osoba, J.S., Richardson, J.G., Kerner, J.K., Hanford, J.A. and Blair, P.M.: "Laboratory Measurement of Relative Permeability," *Pet. Trans, AIME* (1951), Vol. 192, pp. 47-55.
- [76] Pan, X., Wong, R.C. and Maini, B.B.: "Steady State Two-Phase Flow in a Smooth Parallel Fracture," presented at the 47th Annual Technical Meeting of the Petroleum Society in Calgary, Alberta, Canada, June 10-12, 1996.
- [77] Persoff, P.K., Pruess, K. and Myer, L.: "Two-Phase Flow Visualization and Relative Permeability Measurement in Transparent Replicas of Rough-Walled

- Rock Fractures," Proc. 16th Workshop on Geothermal Reservoir Engineering, Stanford University, Stanford, California, January 23-25, 1991.
- [78] Persoff, P. and Pruess, K.: "Two-Phase Flow Visualization and Relative Permeability Measurement in Natural Rough-Walled Rock Fractures," *Water Resources Research* (May 1995), Vol. 31, No. 5, pp. 1175-1186.
- [79] Piquemal, J.: "Saturated Steam Relative Permeabilities of Unconsolidated Porous Media," *Transport in Porous Media* (1994), Vol. 17, pp. 105-120.
- [80] Pruess, K., Bodvarsson, G.S., Schroeder, R.C. and Witherspoon, P.A.: "Model Studies of the Depletion of Two-Phase Geothermal Reservoirs," *Society of Petroleum Engineers Journal* (Apr. 1982), Vol. 22, No. 2, pp. 280-290.
- [81] Pruess, K. and Tsang, Y.W.: "On Two-Phase Relative Permeability and Capillary Pressure of Rough-Walled Rock Fractures," *Water Resources Research* (Sept. 1990), Vol. 26, No. 9, pp. 1915-1926.
- [82] Pyrak-Nolte, L.J., Helgeston, D., Haley, G.M. and Morris, J.W.: "Immiscible Fluid Flow in Fracture," Proceeding of the 33rd U.S. Rock Mech. Symp., edited by Tillersson and Wawersik, pp. 571-578, A. A. Balkema, Rotterdam, Netherlands, 1992.
- [83] Qi, Y., Klausner J.F. and Mei, R.: "Role of Surface Structure in Heterogeneous Nucleation," *International Journal of Heat and Mass Transfer* (July 2004), Vol. 47, Issues 14-16, pp. 3097-3107.
- [84] Rangel-German, E., Akin, S. and Castanier, L.M.: "Multiphase Flow Properties of Fractured Porous Media," paper SPE 54591, presented at the SPE Western Regional Meeting, Anchorage, AK, May 26-28, 1999.
- [85] Ranjith, P.G.: *Analytical and Experimental Modeling of Coupled Water and Air Flow through Rock Joints*, PhD dissertation, University of Wollongong, Australia (2000).

- [86] Rasmussen, T.C. and Evans, D.D.: "Water Infiltration into Exposed Fractured Rock Surfaces," *Soil Sci. Soc. Am. J.* (1993), Vol. 57, pp. 324-329.
- [87] Ratulowski, J. and Chang, H.-C.: "Transport of Gas Bubbles in Capillaries," *Phys. Fluids A* (1989), Vol. 1, pp. 1642–1655.
- [88] Reyes, J.L.P.: *Estimating Water Saturation at The Geysers Based on Historical Pressure and Temperature Production Data*, MS thesis, Stanford University, Stanford, California (Jane 2003).
- [89] Reyes, J.L.P., Li, K., and Horne, R.N.: "Estimating Water Saturation at The Geysers Based on Historical Pressure and Temperature Production Data and By Direct Measurement," *Geothermal Resources Council Transactions* (2003), Vol. 27, pp. 715-726.
- [90] Reyes, J.L.P., Chen C.-Y., Li, K., and Horne, R.N.: "Calculation of Steam and Water Relative Permeabilities Using Field Production Data, WITH Laboratory Verification," *Geothermal Resources Council Transactions* (2004), Vol. 28, pp. 609-615.
- [91] Romm, E.S.: *Fluid Flow in Fractured Rocks*, "Nedra" Publishing House, Moscow (Translated from the Russian) (1966), [English translation, Blake, W.R., Bartlesville, OK, 1972].
- [92] Rossen, W.R., and Kumar A.T.A.: "Single and Two-Phase Flow in Natural Fractures," SPE 24195, the 67th SPE Annual Technical Conference and Exhibition, Washington D.C., Oct. 4-7, 1992.
- [93] Rossen, W.R. and Kumar, A.T.A: "Effect of Fracture Relative Permeabilities on Performance of Naturally Fractured Reservoirs," paper SPE 28700 in proceedings of the 1994 SPE International Petroleum Conference and Exhibition, Veracruz, Mexico, October.

- [94] Saidi, A.M.: "Simulation of Naturally Fractured Reservoirs," paper SPE 12270 in proceedings of the 1983 Symposium on Reservoir Simulation, San Francisco, CA, November.
- [95] Satik, C.: "A Study of Steam-Water Relative Permeability," paper SPE 46209 presented at the 1998 SPE Western Regional Meeting, Bakersfield, California, May. 10-13, 1998.
- [96] Sanchez, J.M and Schechter, R.S.: "A Comparison of the Two-Phase Flow of Steam/Water and Nitrogen/Water Through an Unconsolidated Permeable Medium," SPE 16967, paper presented at the 62nd SPE Annual Technical Conference and Exhibition, Dallas, Texas, USA, September 27-30, 1987.
- [97] Scheidegger, A.E.: *The Physics of Flow through Porous Media*, 3rd ed., University of Toronto, Toronto, Canada (1974).
- [98] Shinohara, K.: *Calculation and Use of Steam/Water Relative Permeabilities in Geothermal Reservoirs*, MS thesis, Stanford University, Stanford, California (1978).
- [99] Silver, R.S. and Simpson, H.C.: "The Condensation of Superheated Steam," Proc. of a conference held at the National Engineering Laboratory, Glasgow, Scotland, 1961.
- [100] Singh, A.B.: "Study of Rock Fracture by Permeability Method," *J. Geotech. and Geoenvir. Eng.* (1997), Vol. 123, pp. 601-608.
- [101] Snow, D. T.: *A Parallel Plate Model of Fractured Permeable Media*, Ph.D. thesis. Univ. of Calif., Berkeley (1965).
- [102] Stark, J. and Manga, M.: "The Motion of Long Bubbles in a Network of Tubes," *Transport in Porous Media* (2000), Vol. 40, pp. 201-218.
- [103] Su, G.W., Geller, J.T., Pruess, K. and Wen, F.: "Experimental Studies of Water Seepage and Intermittent Flow in Unsaturated, Rough-Walled Fractures," *Water Resources Research* (Apr. 1999), Vol. 35, No. 4, pp. 1019-1037.

- [104] Thomas, L.K., Dixon, T.N. and Pierson, R.G.: "Fractured Reservoir Simulation," *Society of Petroleum Engineers Journal* (Feb. 1983), pp. 42-54.
- [105] Thompson, M.E. and Brown, S.R.: "The Effect of Anisotropic Surface Roughness on Flow and Transport in Fractures," *Journal of Geophysical Research* (1991), Vol. 96, pp. 21923-21932.
- [106] Tokunaga, T.K. and Wan, J.M.: "Water Film Flow along Fracture Surfaces of Porous Rock," *Water Resources Research* (Jun. 1997), Vol. 33, No. 6, pp. 1287-1295.
- [107] Trimble, A.E., and Menzie, D.E.: "Steam Mobility in Porous Media," Paper SPE 5571, presented at the 50th Annual Fall Meeting, SPE of AIME, Dallas, Texas, September 1975.
- [108] van Genuchten, M.T.: "A Closed Form Equation for Predicting the Hydraulic Conductivity of Unsaturated Soils," *Soil Science Society of America Journal*, (1980), Vol. 44, No. 5, pp. 892-898.
- [109] van Golf-Racht, T.D.: *Fundamentals of Fractured Reservoir Engineering*, Elsevier Scientific Publishing Company, Amsterdam (1982).
- [110] Verma, A.K.: *Effects of Phase Transformation of Steam-Water Two-Phase Relative-Permeability*, Ph.D. dissertation, University of California, Berkeley (1986).
- [111] Verma, A.K. and Pruess, K.: "Enhancement of Steam Phase Relative Permeability Due to Phase Transformation Effects in Porous Media," Proceedings of 11th Workshop on Geothermal Reservoir Engineering, Stanford University, Stanford, California, 1986.
- [112] Walker, W.R., Sabey, J.D. and Hampton, D.R.: "Studies of Heat Transfer and Water Migration in Soils," U.S. DOE Report, Colorado State University, Fort Collins, Colorado, April 1981.

- [113] Walsh, J.B.: "Effect of Pore Pressure and Confining Pressure on Fracture Permeability," *Int. J. Rock Mech., Min. Sci. & Geomech. Abstr.* (1981), Vol. 18, pp. 429-435.
- [114] Willhite, G.P.: *Waterflooding*, SPE Textbook Series, Richardson Taxes (1986).
- [115] Witherspoon, P.A., Wang, J.S.W., Iwai, K. and Gale, J.E.: "Validity of Cubic Law for Fluid Flow in a Deformable Rock Fracture," *Water Resources Research*, (1980), Vol. 16, No. 6, pp. 1016-1024.
- [116] Wong, H., Radke, C.J. and Morris, S.: "The Motion of Long Bubbles in Polygonal Capillaries. 1. Thin Films," *J. Fluid Mech.* (1995a), Vol. 292, pp. 71–94.
- [117] Wong, H., Radke, C.J. and Morris, S.: "The Motion of Long Bubbles in Polygonal Capillaries. 2. Drag, Fluid Pressure and Fluid flow," *J. Fluid Mech.* (1995b), Vol. 292, pp. 95–110.
- [118] Wyckoff, R.D. and Botset, H.G.: "The Flow of Gas-Liquid Mixtures through Unconsolidated Sands," *Physics* (1936), Vol. 7, pp. 325-345. (A Journal of General and Applied Physics, published for the American Physical Society and the Society of Rheology by the American Institute of Physics)
- [119] Yih, C.S.: *Fluid Mechanics*, McGraw-Hill, New York (1969).
- [120] Zhilenkov, V.N.: *Manual for the Determination of Percolation and Suffusive Properties of Rock Beds of Hydraulic Structures*, Leningrad, Energia Publishers (in Russian) (1975).
- [121] Zimmerman, R.W. and Bodvarsson, G.S.: "Hydraulic Conductivity of Rock Fractures," *Transport in Porous Media* (Apr 1996), Vol.23, No.1, pp. 1-30.